TU Delft

Delft University of Technology

On the creation, coherence and entanglement of multi-defect quantum registers in diamond

Degen, M.J.

DOI
10.4233/uuid:e0b20592-a0ce-4ec4-8df0-a5aa25084301

Publication date
2021

Document Version
Final published version

Citation (APA)
Degen, M. J. (2021). *On the creation, coherence and entanglement of multi-defect quantum registers in diamond*. [Dissertation (TU Delft), Delft University of Technology]. https://doi.org/10.4233/uuid:e0b20592-a0ce-4ec4-8df0-a5aa25084301

Important note
To cite this publication, please use the final published version (if applicable).
Please check the document version above.

Copyright
Other than for strictly personal use, it is not permitted to download, forward or distribute the text or part of it, without the consent of the author(s) and/or copyright holder(s), unless the work is under an open content license such as Creative Commons.

Takedown policy
Please contact us and provide details if you believe this document breaches copyrights.
We will remove access to the work immediately and investigate your claim.

This work is downloaded from Delft University of Technology.
For technical reasons the number of authors shown on this cover page is limited to a maximum of 10.

On the creation, coherence and entanglement of multi-defect quantum registers in diamond

Proefschrift

ter verkrijging van de graad van doctor
aan de Technische Universiteit Delft,
op gezag van de Rector Magnificus Prof.dr.ir. T.H.J.J. van der Hagen,
voorzitter van het College voor Promoties
in het openbaar te verdedigen op maandag 12 april 2021 om 15:00 uur

door

Maarten Johannes DEGEN

Master of Science in Nanoscience,
Rijksuniversiteit Groningen, Nederland
geboren te Zutphen, Nederland.

Dit proefschrift is goedgekeurd door de promotoren.

Samenstelling promotiecommissie:

Rector Magnificus,	voorzitter
Prof. dr. ir. R. Hanson,	Technische Universiteit Delft, promotor
Dr. ir. T. H. Taminiau,	Technische Universiteit Delft, copromotor
Onafhankelijke leden:	
Prof. dr. A. F. Otte	Technische Universiteit Delft
Prof. dr. Y. M. Blanter	Technische Universiteit Delft
Prof. dr. M. Atatüre	Universiteit van Cambridge
Prof. dr. ir. C. H. van der Wal	Rijksuniversiteit Groningen

Copyright © 2021 by Maarten Degen

Cover design: Lucy Matthes-Buck, Joe Randall, Maarten Degen

An electronic version of this dissertation is available at
http://repository.tudelft.nl/.

Contents

Summary

Due to its long spin coherence and coherent spin-photon interface the nitrogen vacancy (NV) center in diamond has emerged as a promising platform for quantum science and technology, including quantum networks, quantum computing and quantum sensing. In recent years larger quantum systems have been demonstrated by using optical entanglement links between distant NV centers. These systems were based on high-quality NV centers that exhibit good optical coherence. State-of-the-art experiments with such systems have shown deterministic delivery of entanglement across a two-node quantum network as well as genuine multi-partite entanglement across a three-node quantum network. The additional capability to create larger quantum registers by direct magnetic coupling between high-quality NV centers and to other nearby defects would provide new opportunities for quantum memories in quantum networks but also for enhanced sensing protocols and spin chains for quantum computation architectures. In this thesis, we investigate methods to create larger quantum registers based on magnetic coupling and develop techniques to address and control individual defects in a system consisting of multiple defects. The results provide new insights for extended quantum registers based on magnetically coupled defects.

Firstly, we investigate nitrogen implantation, a widely employed strategy to create NV centers at precisely controlled positions and also a proven technique to create magnetically coupled NV centers. We study the optical coherence of implanted NV centers created via a procedure of ion implantation followed by high-temperature annealing. By distinguishing between implanted and naturally occurring NV centers through their isotope, we find that implanted NV centers exhibit predominantly broadened optical transitions (>1 GHz). Moreover, we find that implanted NV centers reveal higher strain than naturally occurring ones, indicating local lattice damage. Our data also shows that the poor optical coherence is not due to an intrinsic effect related to the diamond or isotope. These results implicate that this NV creation technique needs to be re-investigated, addressing local lattice damage. Additionally other approaches can be further explored, such as employing 2D nitrogen-doped layers combined with vacancy production via laser writing or electron irradiation.

Secondly, we explore another path towards magnetically coupled defects by controlling so-called dark spin defects in the environment of a single optically addressable NV center. These dark spin defects are associated to multiple P1 centers (substitutional nitrogen), which are part of a spin bath surrounding the NV. For this system, we demonstrate the heralded initialisation, control and entanglement of individual P1 centers. We realize projective measurements to prepare the multiple

degrees of freedom of P1 centers - their Jahn-Teller axis, nuclear spin and charge state - and exploit these to selectively address multiple P1s in the bath. We develop control and single-shot readout of the nuclear and electron spin, and use this to demonstrate an entangled state of two P1 centers. These results demonstrate an alternative approach to obtain multi-defect quantum registers and provide a proof-of-principle towards using dark electron-nuclear spin defects as qubits for quantum sensing, computation and networks.

Lastly, we explore nuclear spins and the ^{14}N nuclear spin in particular for their potential as quantum memories. First, we experimentally investigate the host ^{14}N spin of a single NV center and observe a coherence time >60 s, the longest reported for a single solid-state qubit at the time of writing. This demonstrates that such nuclear spins can be excellent quantum memories. Second, we develop a precision spectroscopy method to characterize the hyperfine and quadrupole interaction of a host ^{14}N and electron spin of the NV. Finally, we theoretically show that in a system of two NV centers, one of the ^{14}N spins can be used as a robust memory for quantum networks.

Together, the work presented in this thesis advances magnetically coupled defect spins to a promising system for extended quantum registers. The results provide insight in creation methods, demonstrate control over coupled defect spins and establish a defect nuclear spin as excellent quantum memory. The developed techniques provide new possibilities for magnetically coupled defects in quantum sensing, quantum networks and quantum information processing.

Samenvatting

Door zijn lange spin coherentie tijd en coherente spin-foton koppeling, is het stikstofgat defect (nitrogen vacancy, NV) in diamant naar voren gekomen als een veelbelovend platform voor quantum wetenschap en technologie zoals quantum netwerken, quantum computers en quantum sensoren. In de afgelopen jaren zijn grotere quantum systemen gedemonstreerd door optisch verstrengelde verbindingen tussen NVs op afstand te genereren. Deze systemen zijn gebaseerd op hoge kwaliteits NV centers gekenmerkt door goede optische coherentie. Met de nieuwste technieken hebben experimenten met zulke systemen het deterministisch leveren van verstrengeling over een tweepunts netwerk aangetoond en ook verstrengeling over een driepunts network. Het vermogen om daarnaast ook grotere quantum processors te creëren via directe magnetische koppeling tussen hoge kwaliteits NV centers en andere dichtbijzijnde defecten zal nieuwe mogelijkheden bieden voor quantum geheugens voor quantum netwerken maar ook voor de verbetering van quantum sensoren en spin schakelingen voor quantum computer architecturen. In dit proefschrift onderzoeken we methodes om grotere systemen gebaseerd op magnetische koppeling te creëren en ontwikkelen we technieken om individuele defecten te adresseren en controleren, binnen een systeem van meerdere defecten. De resultaten verschaffen nieuwe inzichten voor het uitbreiden van quantum processors gebaseerd op magnetisch gekoppelde defecten.

Eerst onderzoeken we stikstof implantatie, een veelgebruikte strategie om NV centers te creëren op gecontroleerde posities en een bewezen techniek voor het creëren van magnetisch gekoppelde defecten. We bestuderen de optische coherentie van geïmplanteerde NV centers die geproduceerd zijn door middel van ionenimplantatie gevolgd door verwarming tot hoge temperaturen. Door geïmplanteerde en natuurlijk voorkomende NV centers te onderscheiden op basis van isotoop, concluderen we dat geïmplanteerde NV centers voornamelijk verbrede optische transities hebben (>1 GHz). Bovendien observeren we bij geïmplanteerde NV centers hogere vervorming van het kristalrooster, hetgeen duidt op schade aan het lokale kristalrooster. Onze data laat ook zien dat de slechte optische coherentie niet veroorzaakt wordt door een intrinsiek effect gerelateerd aan de diamant of de isotoop. Deze resultaten impliceren dat deze methode van het creëren van NV centers moet worden heronderzocht, en er gericht moet worden gekeken naar schade aan het lokale kristalrooster. Daarnaast kunnen andere technieken verder worden verkend, zoals het gebruik van stikstof gedoteerde 2D lagen in combinatie met het produceren van gaten in het kristalrooster door middel van laser pulsen of elektron bestraling.

Ten tweede onderzoeken we een ander pad naar magnetisch gekoppelde defecten door het controleren van zogenaamde donkere spin defecten in de omgeving

van een enkel optisch adresseerbaar NV center. Deze donkere spin defecten zijn meerdere P1 centers (substitutionele stikstof atomen) die onderdeel zijn van een spin bad omliggend aan het NV. Voor dit systeem demonstreren we initialisatie, controle en verstrengeling van individuele P1 centers. We realizeren projectieve metingen om de meerdere vrijheidsgraden van P1 centers te initialiseren - de Jahn-Teller as, kernspin toestand en lading - en gebruiken deze om verschillende P1s selectief te adresseren. We ontwikkelen controle en uitleestechnieken van de kern- en elektronspin, en gebruiken dit om een verstrengelde toestand van twee P1 centers te demonstreren. Deze resultaten demonstreren een alternatieve manier voor het verkrijgen van quantum processors bestaande uit meerdere defecten, en tonen de principiële bruikbaarheid aan van donkere elektronspin-kernspin defecten als qubits voor quantum sensoren, quantum berekeningen en quantum netwerken.

Ten slotte, onderzoeken we kernspins en met name de stikstof kernspin als potentiële quantum geheugens. Eerst doen we experimenteel onderzoek naar de stikstof kernspin van een enkel NV center en observeren een coherentie tijd >60 s, de langst gerapporteerde voor een enkele qubit in de vaste stof op het moment van schrijven. Dit demonstreert dat zulke kernspins excellente quantum geheugens kunnen vormen. Ten tweede ontwikkelen we een precisie spectroscopie methode om de hyperfijn en quadrupool interactie tussen de eigen stikstof kernspin en de elektronspin van een NV te karakterizeren. Als laatste, laten we theoretisch zien dat in een systeem van twee NV centers, een van de stikstof kernspins gebruikt kan worden as een robuust quantum geheugen.

Tezamen demonstreert het werk in dit proefschrift een vooruitgang van gekoppelde defecten naar een beloftevol systeem voor uitgebreidere quantum processors. De resultaten geven inzicht in productie methodes, laten controle over gekoppelde spin defecten zien en bevestigen kernspins as uitstekende quantum geheugens. De ontwikkelde technieken verschaffen nieuwe mogelijkheden voor magnetisch gekoppelde defecten in quantum sensoren, quantum netwerken en quantum processors.

1

Introduction

1

1.1. Quantum science and technology

The theory of quantum mechanics has described and predicted physical phenomena that have been experimentally verified with great accuracy. Non-classical features of quantum mechanics, such as quantum superposition, quantum entanglement and quantum measurement, go strongly against classical intuition and have been subject of debate since their introduction [1–5]. Still, even with great technological advancements in preparing and controlling quantum states since the introduction of quantum mechanics, experimental tests of the theory remain accurate [6–9].

Many scientists and engineers study and realize applications of quantum mechanics in the fields of quantum sensing [10], quantum simulation [11], quantum computing [12] and quantum networks [13]. Current state-of-the-art technological abilities, allows them to create quantum technology composed of controllable and well-isolated quantum systems. In the field of information science, envisioned quantum technologies promise far-reaching advantages over their classical counterparts. For instance, algorithms on a quantum computing machine were proposed by Peter Shor and others to efficiently solve mathematical problems for which no efficient algorithm[1] is known on classical computers [14–16]. The non-classical features of quantum mechanics in quantum technology, are at the basis of many quantum advantages. Entanglement, for instance, is at the basis of factorizing large numbers using Shor's algorithm on a quantum computer, and also recent exciting work builds on entanglement for their claim of quantum supremacy: the point where quantum computers can do things that classical computers can't [17, 18].

The quantum technology needed to exploit quantum advantages, requires a high level of control over quantum systems. Such quantum technology typically consists of building blocks called qubits: quantum systems with a binary level structure. Qubits can be encoded in single photons [19], states of atoms, ions [20] or superconducting systems [21, 22] and solid-state spins [23–25], among other platforms. One of the challenges in quantum information processing is to protect quantum information against errors. Protecting against such errors is challenging because a quantum state cannot be copied, has a continuous computational basis but requires finite precision operations and irreversibly projects upon measurement. Among other methods, quantum error correcting algorithms were developed to detect and correct errors and proof-of-concept experiments have been performed on a variety of quantum information processor systems [21, 22, 24, 26–28]. The achievements in improved and larger quantum information processors over the recent years, have demonstrated steady progress towards quantum advantages using quantum computing.

In analogy with the internet that we now use worldwide, the vision of a quantum network is to connect nodes consisting of qubits or quantum processors over macroscopic distances using entanglement links. Achieving such a network is a cru-

[1] running on a polynomial space or in a polynomial time with the problem size

cial step for distributed quantum computing, in which remote quantum processors can communicate and cooperate. Such an architecture also enables the distribution of many-body quantum states over macroscopic length scales for fundamental tests of quantum mechanics [29], and can establish certifiable secure quantum communication channels [13, 30]. Elementary nodes of quantum networks can be entangled via photonic links. Photons are suitable mediators as they can easily be transported over large distances and exhibit little decoherence. Quantum networks have been established with several different quantum systems and entanglement across three elementary nodes has been demonstrated [31–36].

Quantum systems can also function as precision measurement devices. Such so-called quantum sensors use the commonly considered weakness of quantum systems, their strong sensitivity to external disturbances, to their advantage. Some quantum sensors can combine high sensitivity with very high spatial resolution due to the typical atomic scale size of the sensors [10, 37, 38].

1.2. This thesis: multi-defect quantum registers in diamond

Optically active defects in solids provide promising qubits for a variety of quantum technologies. The NV center in diamond is one of such defects and consists of a substitutional nitrogen atom with an adjacent vacancy. In recent years, several key aspects of NV centers have established it as a promising defect for quantum sensing and quantum information processing. It has long-lived electron spin ground states with coherence times of over a second [39]. Furthermore, at cryogenic temperatures it has a coherent spin-photon interface [40], that provides optical initialisation and single-shot readout [41]. Moreover, multiple nuclear spins in the vicinity of NVs can be sequentially addressed using known techniques for NV-^{13}C two-qubit gates [42–46]. This has enabled quantum computations, such as quantum error correction protocols [24, 28], a quantum fourier transform and Grover's search algorithm [23, 41, 47]. Larger-scale systems can been realized by entangling more NV centers through long-range entanglement links [9, 36, 48], and through direct magnetic coupling to other defects. An envisioned quantum network based on spins in diamond is shown in Fig. 1.1. In recent years, great progress has been made towards increasing entanglement rates [31, 36, 49, 50], and control of nearby ^{13}C nuclear spins [23, 46, 47]. However, an open challenge remains to create magnetically coupled defects for quantum network nodes or advanced quantum processors.

Direct magnetic coupling between multiple electron defect spins for extended quantum registers will provide new opportunities not only for quantum networks [13, 51–54], but also for enhanced sensing protocols [47, 55, 56] or spin chains for quantum computation architectures [57–60]. Such magnetically coupled defects are potentially powerful multi-qubit systems consisting of multiple nuclear and electron spins that can fulfill different roles. For instance, coupling an NV to

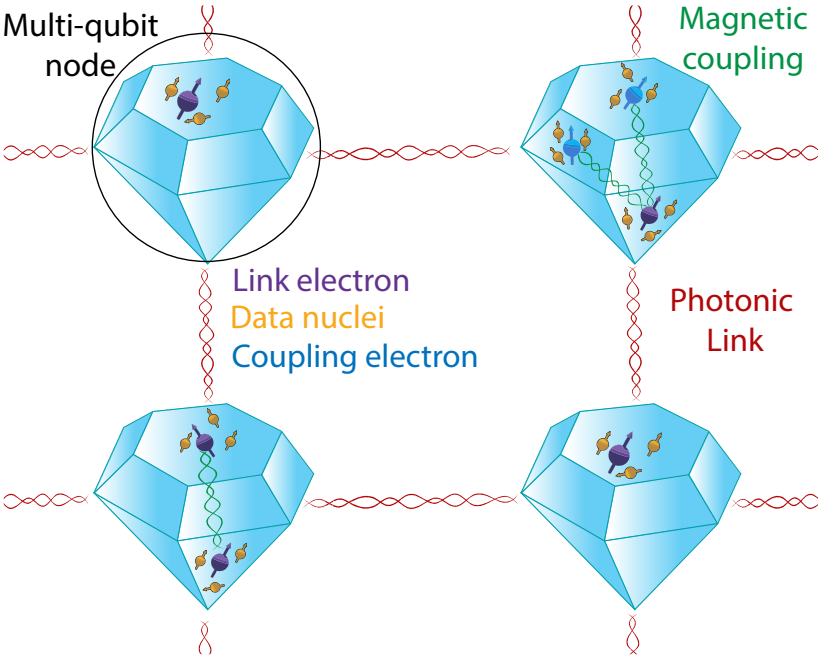

Figure 1.1: **A quantum network with spins in diamond.** Building networks based on defect centers is a promising approach towards distributed quantum computing and secure quantum communication. The envisioned network consists of multi-qubit nodes with NV center electrons as link qubits (purple spins), other defect electrons spin qubits (blue spins) and data qubits (yellow spins) in the form of nuclear spins. Link qubits are used to connect different nodes via photons, and data qubits in the nodes can store and process quantum states. Magnetic coupling (green wiggled lines) between NV centers or between an NV and other defect electron spins (blue spins) form extended quantum registers that can allow fast access to isolated nuclear data qubits for robust quantum memories or provide multiple link qubits within one node. In this thesis we focus on creating magnetically coupled defects within one node for such extended quantum registers. Fig. adapted from C.E. Bradley.

other defect electron spins can provide access to more distant nuclear spins by using the coupling between their electron spins as a quantum bus between defects. As these more distant nuclear spins only interact weakly with the NV, they are potentially well-isolated and robust quantum memories. Also, spectrally distinct and magnetically coupled NV centers could, in addition to robust nuclear memories, provide multiplexed control of nuclear spins surrounding the NV centers. To realize selective quantum control, different types of defects, crystal orientations [61], super-resolution optical focusing [62] or Stark tuning using electric fields [63] can be exploited for distinguishability. Such magnetically coupled NV-NV or NV-defect systems are promising quantum network nodes if they can be created with properties alike naturally occurring NVs in bulk diamond, and are also of interest as stand-alone systems for quantum information processing.

In this thesis, we pursue the creation of a system consisting of magnetically coupled defects that can be employed for novel quantum information processing tasks. In particular, we focus on coupled NV centers or NV centers in combination with other defects in diamond. A first approach is ion implantation to create coupled NV systems with properties that are alike those of naturally occurring NVs in bulk diamond. Implantation has already shown to enable the creation of closely-spaced defects that are magnetically coupled [54, 64], and even room-temperature entanglement has been demonstrated for a pair of ion-implanted NV centers [61, 65]. Yet, the combination of direct magnetic coupling and maintaining good optical NV properties like coherent optical transitions remains to be demonstrated. A second approach towards multi-defect systems using the NV center, is by coupling selectively to individual spins within a surrounding bath of the defects. If the capabilities are developed to selectively initialize, control and readout electron spins within a bath of defects, such defects can be harnessed for multi-defect quantum registers.

1.3. Outline of this thesis

In **chapter 2** of this thesis we describe the used experimental framework and introduce the properties of NV centers at cryogenic temperatures. Moreover, we provide an overview of standard control techniques and introduce systems of defects and nuclei that can form the environment around the NV. In particular, we discuss the P1 center, a substitutional nitrogen defect that is investigated this thesis.

In **Chapter 3**, we investigate ion implantation. In order to reliably obtain magnetically coupled defects via ion implantation, that also have good optical properties, the implantation technique must yield narrow-optical-linewidth NV centers with high yield. In this chapter we correlate the optical linewidth and strain associated with single NVs, with the origin of the nitrogen atom (native or implanted in the diamond). We find significantly broadened optical linewidths for implanted NVs in contrast to narrow optical linewidths for native NV centers. These results show that improvements in quality of implanted NVs are required to obtain coupled NVs for quantum networks using ion implantation.

Chapter 4 presents another approach towards multi-defect systems: control techniques are developed to selectively control P1 center defects which are part of a spin bath surrounding an NV in diamond. We use projective measurements to initialize multiple degrees of freedom of P1 centers, and exploit these to selectively access several P1s in the bath. Developed control and single-shot readout techniques are used to demonstrate an entangled state of two P1 centers. These results provide a proof-of-principle towards using dark electron-nuclear spin defects (P1 centers) as qubits for quantum sensing, computation and networks.

Lastly, in **chapter 5** we show that the ^{14}N nuclear spin is a promising quantum memory for quantum networks. Firstly we show that the ^{14}N spin has the longest reported coherence time for a single solid-state qubit at the time of writing (>60 s). Secondly, we develop a precision spectroscopy method to characterize the hyperfine and quadrupole interactions of the ^{14}N with the electron spin of the NV. Finally, we theoretically show that in a system of two NV centers, one of the ^{14}N spins can be used as a robust memory for quantum networks.

1

References

[1] Einstein, A., Podolsky, B. & Rosen, N., *Can quantum-mechanical description of physical reality be considered complete?* Physical review **47**, 777 (1935).

[2] Bohr, N., *Can quantum-mechanical description of physical reality be considered complete?* Physical review **48**, 696 (1935).

[3] Bell, J. S., *On the einstein podolsky rosen paradox,* Physics Physique Fizika **1**, 195 (1964).

[4] Clauser, J. F., Horne, M. A., Shimony, A. & Holt, R. A., *Proposed experiment to test local hidden-variable theories,* Physical review letters **23**, 880 (1969).

[5] Schlosshauer, M., Kofler, J. & Zeilinger, A., *A snapshot of foundational attitudes toward quantum mechanics,* Studies in History and Philosophy of Science Part B: Studies in History and Philosophy of Modern Physics **44**, 222 (2013).

[6] Giustina, M. *et al.*, *Significant-loophole-free test of bell's theorem with entangled photons,* Physical review letters **115**, 250401 (2015).

[7] Shalm, L. K. *et al.*, *Strong loophole-free test of local realism,* Physical review letters **115**, 250402 (2015).

[8] Rosenfeld, W. *et al.*, *Event-ready bell test using entangled atoms simultaneously closing detection and locality loopholes,* Physical review letters **119**, 010402 (2017).

[9] Hensen, B. *et al.*, *Loophole-free bell inequality violation using electron spins separated by 1.3 kilometres,* Nature **526**, 682 (2015).

[10] Degen, C. L., Reinhard, F. & Cappellaro, P., *Quantum sensing,* Reviews of modern physics **89**, 035002 (2017).

[11] Georgescu, I. M., Ashhab, S. & Nori, F., *Quantum simulation,* Reviews of Modern Physics **86**, 153 (2014).

[12] Nielsen, M. & Chuang, I. L., *Quantum computation and quantum information* (Cambridge University Press, Cambridge, 2000).

[13] Wehner, S., Elkouss, D. & Hanson, R., *Quantum internet: A vision for the road ahead,* Science **362** (2018).

[14] Shor, P. W., *Algorithms for quantum computation: discrete logarithms and factoring,* in *Proceedings 35th annual symposium on foundations of computer science* (Ieee, 1994) pp. 124–134.

[15] Grover, L. K., *A fast quantum mechanical algorithm for database search,* in *Proceedings of the twenty-eighth annual ACM symposium on Theory of computing* (1996) pp. 212–219.

[16] Deutsch, D. & Jozsa, R., *Rapid solution of problems by quantum computation,* Proceedings of the Royal Society of London. Series A: Mathematical and Physical Sciences **439**, 553 (1992).

[17] Arute, F. *et al.*, *Quantum supremacy using a programmable superconducting processor,* Nature **574**, 505 (2019).

[18] Preskill, J., *Quantum computing and the entanglement frontier,* arXiv preprint arXiv:1203.5813 (2012).

[19] Liao, S.-K. *et al.*, *Satellite-to-ground quantum key distribution,* Nature **549**, 43 (2017).

[20] Reiserer, A. & Rempe, G., *Cavity-based quantum networks with single atoms and optical photons,* Reviews of Modern Physics **87**, 1379 (2015).

[21] Andersen, C. K. *et al.*, *Repeated quantum error detection in a surface code,* Nature Physics **16**, 875 (2020).

[22] Riste, D. *et al.*, *Detecting bit-flip errors in a logical qubit using stabilizer measurements,* Nature communications **6**, 1 (2015).

[23] Van Dam, S. B., Cramer, J., Taminiau, T. H. & Hanson, R., *Multipartite Entanglement Generation and Contextuality Tests Using Nondestructive Three-Qubit Parity Measurements,* Phys. Rev. Lett. **123** (2019).

[24] Cramer, J. *et al.*, *Repeated quantum error correction on a continuously encoded qubit by real-time feedback,* Nat. Commun. **7**, 1 (2016).

[25] Hendrickx, N. *et al.*, *A four-qubit germanium quantum processor,* arXiv preprint arXiv:2009.04268 (2020).

[26] Linke, N. M. *et al.*, *Fault-tolerant quantum error detection,* Science advances **3**, e1701074 (2017).

[27] Kelly, J. *et al.*, *State preservation by repetitive error detection in a superconducting quantum circuit,* Nature **519**, 66 (2015).

[28] Waldherr, G. *et al.*, *Quantum error correction in a solid-state hybrid spin register,* Nature **506**, 204 (2014).

[29] Erhard, M., Krenn, M. & Zeilinger, A., *Advances in high-dimensional quantum entanglement,* Nature Reviews Physics **2**, 365 (2020).

[30] Ekert, A. & Renner, R., *The ultimate physical limits of privacy,* Nature **507**, 443 (2014).

[31] Pompili, M. *et al.*, *Realization of a multi-node quantum network of remote solid-state qubits,* arXiv preprint arXiv:2102.04471 (2021).

[32] Jing, B. *et al.*, *Entanglement of three quantum memories via interference of three single photons,* Nature Photonics **13**, 210 (2019).

[33] Stephenson, L. *et al.*, *High-rate, high-fidelity entanglement of qubits across an elementary quantum network,* Physical Review Letters **124**, 110501 (2020).

[34] Yan, Z. *et al.*, *Establishing and storing of deterministic quantum entanglement among three distant atomic ensembles,* Nature Communications **8**, 1 (2017).

[35] Stockill, R. *et al.*, *Phase-tuned entangled state generation between distant spin qubits,* Physical review letters **119**, 010503 (2017).

[36] Humphreys, P. C. *et al.*, *Deterministic delivery of remote entanglement on a quantum network,* Nature **558**, 268 (2018).

[37] Grinolds, M. *et al.*, *Subnanometre resolution in three-dimensional magnetic resonance imaging of individual dark spins,* Nature nanotechnology **9**, 279 (2014).

[38] DeVience, S. J. *et al.*, *Nanoscale nmr spectroscopy and imaging of multiple nuclear species,* Nature nanotechnology **10**, 129 (2015).

[39] Abobeih, M. H. *et al.*, *One-second coherence for a single electron spin coupled to a multi-qubit nuclear-spin environment,* Nat. Commun. **9**, 1 (2018).

[40] Robledo, L., Bernien, H., Van Weperen, I. & Hanson, R., *Control and coherence of the optical transition of single nitrogen vacancy centers in diamond,* Physical review letters **105**, 177403 (2010).

[41] Robledo, L. *et al.*, *High-fidelity projective read-out of a solid-state spin quantum register,* Nature **477**, 574 (2011).

[42] Taminiau, T. *et al.*, *Detection and control of individual nuclear spins using a weakly coupled electron spin,* Physical review letters **109**, 137602 (2012).

[43] Kolkowitz, S., Unterreithmeier, Q. P., Bennett, S. D. & Lukin, M. D., *Sensing distant nuclear spins with a single electron spin,* Physical review letters **109**, 137601 (2012).

[44] Zhao, N. *et al.*, *Sensing single remote nuclear spins,* Nature nanotechnology **7**, 657 (2012).

[45] Taminiau, T. H., Cramer, J., van der Sar, T., Dobrovitski, V. V. & Hanson, R., *Universal control and error correction in multi-qubit spin registers in diamond,* Nature nanotechnology **9**, 171 (2014).

[46] Bradley, C. E. *et al.*, *A ten-qubit solid-state spin register with quantum memory up to one minute,* Phys. Rev. X **9**, 031045 (2019).

[47] Vorobyov, V. *et al.*, *Quantum fourier transform for quantum sensing,* arXiv preprint arXiv:2008.09716 (2020).

[48] Sipahigil, A. *et al.*, *An integrated diamond nanophotonics platform for quantum-optical networks,* Science **354**, 847 (2016).

[49] Kalb, N. *et al.*, *Entanglement distillation between solid-state quantum network nodes,* Science **356**, 928 (2017).

[50] Ruf, M., Weaver, M. J., van Dam, S. B. & Hanson, R., *Resonant excitation and purcell enhancement of coherent nitrogen-vacancy centers coupled to a fabry-perot microcavity,* Physical Review Applied **15**, 024049 (2021).

[51] Nickerson, N. H., Li, Y. & Benjamin, S. C., *Topological quantum computing with a very noisy network and local error rates approaching one percent,* Nature communications **4**, 1 (2013).

[52] Nickerson, N. H., Fitzsimons, J. F. & Benjamin, S. C., *Freely scalable quantum technologies using cells of 5-to-50 qubits with very lossy and noisy photonic links,* Physical Review X **4**, 041041 (2014).

[53] Childress, L., Taylor, J., Sørensen, A. S. & Lukin, M. D., *Fault-tolerant quantum repeaters with minimal physical resources and implementations based on single-photon emitters,* Physical Review A **72**, 052330 (2005).

[54] Scarabelli, D., Trusheim, M., Gaathon, O., Englund, D. & Wind, S. J., *Nanoscale engineering of closely-spaced electronic spins in diamond,* Nano Letters **16**, 4982 (2016).

[55] Cooper, A., Kyu, W., Sun, C., Jaskula, J.-C. & Cappellaro, P., *Environment-assisted Quantum-enhanced Sensing with Electronic Spins in Diamond,* Phys. Rev. Appl. **10**, 44047 (2019).

[56] Goldstein, G. *et al.*, *Environment-assisted precision measurement,* Phys. Rev. Lett. **106**, 140502 (2011).

[57] Yao, N. Y. *et al.*, *Scalable architecture for a room temperature solid-state quantum information processor,* Nat. Commun. **3**, 1 (2012).

[58] Ping, Y., Lovett, B. W., Benjamin, S. C. & Gauger, E. M., *Practicality of spin chain wiring in diamond quantum technologies,* Phys. Rev. Lett. **110** (2013).

[59] Yao, N. Y. *et al.*, *Quantum logic between remote quantum registers,* Phys. Rev. A **87**, 22306 (2013).

[60] Schlipf, L. *et al.*, *A molecular quantum spin network controlled by a single qubit,* Sci. Adv. **3**, e1701116 (2017).

[61] Dolde, F. *et al.*, *High-fidelity spin entanglement using optimal control,* Nat. Commun. **5**, 1 (2014).

[62] Kim, D. & Englund, D. R., *Quantum reference beacon–guided superresolution optical focusing in complex media,* Science **363**, 528 (2019).

[63] Bersin, E. *et al.*, *Individual control and readout of qubits in a sub-diffraction volume,* npj Quantum Information **5**, 1 (2019).

[64] Jakobi, I. *et al.*, *Efficient creation of dipolar coupled nitrogen-vacancy spin qubits in diamond,* in *Journal of Physics: Conference Series*, Vol. 752 (2016) p. 012001.

[65] Dolde, F. *et al.*, *Room-temperature entanglement between single defect spins in diamond,* Nat. Phys. **9**, 139 (2013).

2

Background and methods

This chapter describes the NV center and its environment in diamond. We introduce the ground and excited states of the NV and the transitions between these states that are used as optical interface. We give an overview of surrounding defects and nuclei, including the substitutional nitrogen atom (P1 center) which is studied and controlled in this thesis. Furthermore, we provide a description of the experimental setup and methods used throughout this thesis.

2.1. The NV center in diamond

The nitrogen-vacancy (NV) center is a common lattice defect in diamond. It consists of a substitutional nitrogen atom (replacing a carbon atom) next to a vacant lattice site (Fig. 2.1a). This defect can naturally occur in the diamond, or can be grown in doped δ-layers [1, 2]. Moreover, NV centers can be formed at specific locations through ion implantation [3–6], whereas electron irradiation [7–9] or direct laser writing can be used to create additional vacancies to convert N to NV [10–12]. The NV center mainly exists in one of two charge states: neutrally-charged (NV^0) and negatively-charged (NV^-) [13]. In the neutral charge state, there are 5 unbound electrons from the nearby nuclei (2 from the nitrogen and 3 from the carbons) [13]. The negatively charged state, NV^-, is formed when an additional electron is captured from a charge trap in the environment [13]. In this thesis we work almost exclusively with NV^-, which we denote as NV hereafter. Particularly in its negative charge state, the NV is an interesting and versatile platform for quantum science and technologies [14] with many applications ranging from quantum sensing [15–21] to quantum information processing [22–25], and quantum networks and communication [14, 26–30].

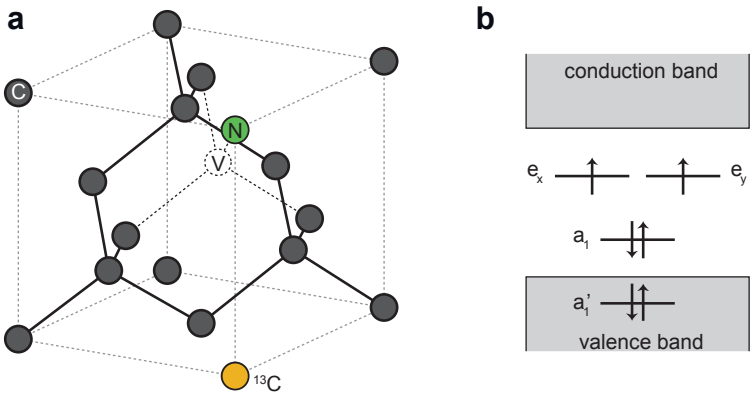

Figure 2.1: **The nitrogen-vacancy (NV) center in diamond.** a) The crystal structure of diamond. The NV center is formed by a substitutional nitrogen atom next to a vacant lattice side. The carbon atoms in the diamond lattice consist for ~1.1% of ^{13}C isotopes with nuclear spin-1/2 (yellow). b) The NV molecular orbitals and their occupation in the electronic ground state. Figures adapted from Pfaff [31], Bernien [32].

The electronic level structure of the NV center is shown in Fig. 2.1b. The electronic wave function can be approximated by a linear combination of the available atomic orbitals from the neighbouring nitrogen and carbon atoms [33–35]. In the ground state, the six electrons are distributed among molecular orbitals as shown in Fig. 2.1b. The two lowest-energy orbitals (a_1' and a_1) are doubly occupied, and the orbitals $e_{x,y}$ have one electron each. In the excited state, one electron from the orbital a_1 is promoted to one of the e orbitals [33–35]. Important to note is that both the ground and first excited state levels have unoccupied orbital levels only inside the diamond band gap. Figure 2.2 shows the energy level diagram of the ground and excited states. The available molecular orbitals and six electrons provide a good approximation of the electronic level structure: the orbital ground state is a spin-triplet that couples optically to the first excited orbital doublet, spin-triplet states [33, 36].

Excitation of the NV from the spin-triplet ground state to one of the six excited states can occur by resonant optical excitations, or off-resonantly via the phonon-sideband. The relaxation can occur in a similar manner by emitting photons resonantly through the zero phonon line (ZPL), or off-resonantly via the phonon-sideband or singlet states (Fig. 2.2). Because both the ground and the excited states have all unoccupied orbital levels within the band gap, the optical transitions are accessible albeit the NV is embedded in a diamond solid-state environment.

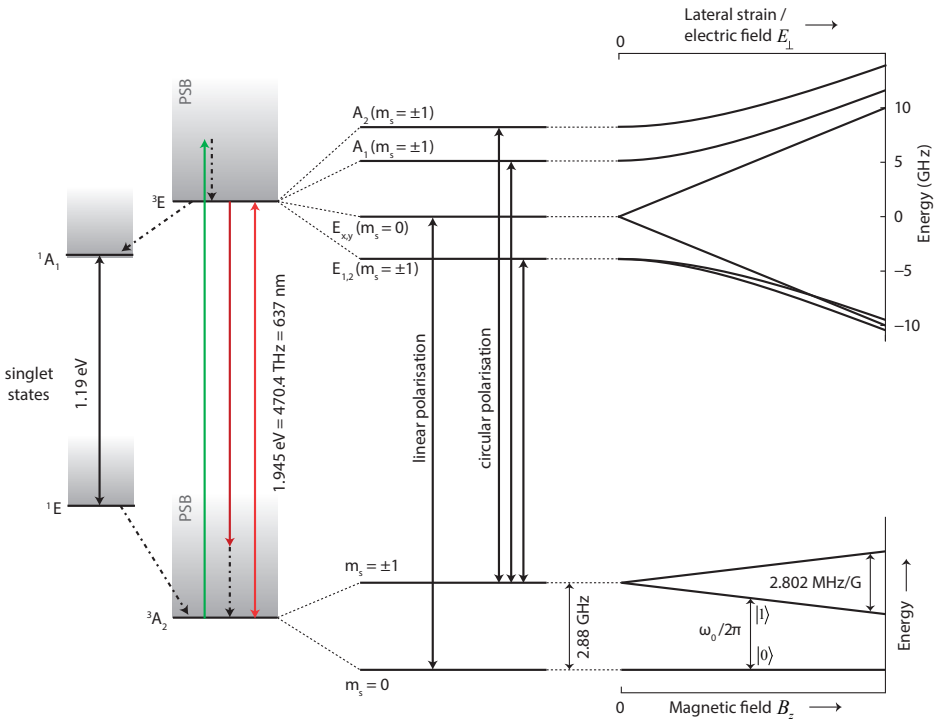

Figure 2.2: Energy level diagram of the negatively charged NV center (ground and excited states). **Bottom center**: The NV ground state is a spin triplet ($S = 1$). The zero field splitting ($\Delta \approx 2\pi \cdot$ 2.88 GHz) separates the $m_s = 0$ state and the two degenerate states $m_s = \pm1$. **Bottom right**: An external magnetic field along the NV axis can lift this degeneracy by Zeeman splitting. **Top center**: The fine structure of the excited states. Spin-spin and spin-orbit interactions split the excited state into four levels. Two of these levels, $E_{x,y}$ and $E_{1,2}$, are doubly degenerate and correspond to $m_s = 0$ and $m_s = \pm1$ respectively. Levels $A_{1,2}$ correspond to $m_s = \pm1$. **Top right**: First order effect of lateral strain (or equivalently of lateral electric field) on the excited state levels. The lateral strain has no effect on the ground state levels to first order. Longitudinal strain (or electric field) only changes the splitting between ground and excited states and thus offsets the whole spectrum. **Left**: Excitation of the NV from the ground state to one of the six excited states can occur by optical excitations resonantly (light red line), or off-resonantly via the phonon-sideband (green lines). The relaxation can also occur in a similar manner by emitting photons resonantly through the zero-phonon line (ZPL), or off-resonantly via the phonon-sideband (dark red line) or the singlet states. Figure adapted from Hensen [36].

2.2. The NV and surrounding defects and nuclei

In its ground orbital state, the NV electron spin and its host ^{14}N nuclear spin form the basis electron-nuclear spin system that is used throughout this thesis. Additionally the NV can couple to surrounding ^{13}C nuclear spins, and electron spins of defects such as P1 centers (nitrogen impurities) as shown in Fig. 2.3. The concentration of surrounding P1 centers and nuclei depends on the diamond growth conditions. It has been shown that, to some extend, the concentration of ^{13}C spins can be controlled via isotope engineering [38, 39]. P1 centers have been introduced in diamond via doping or occur naturally during diamond growth [1, 2]. In this thesis we have studied the NV surrounded by two type of systems: 1) P1 centers (~75 ppb) within isotopically purified diamond (~0.01% ^{13}C), and 2) ^{13}C spins with a natural abundance (~1.1%). In this section, we first discuss the ground state spin structure of the NV, followed by these two type of systems and their interaction with the NV.

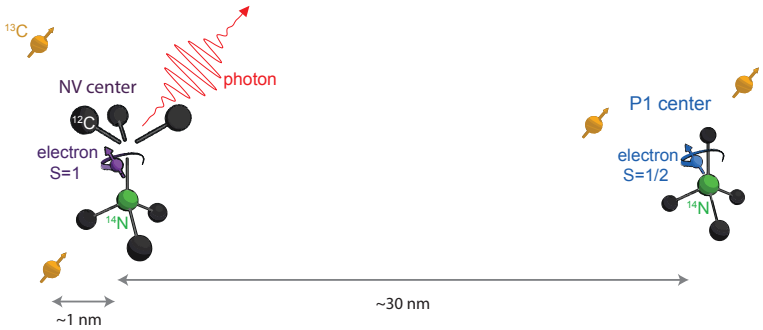

Figure 2.3: **NV center and surrounding spins.** The optically active NV center (left) and additional spins such as ^{13}C nuclear spins (yellow) or electrons spins of P1 center defects (right). The length scales illustrate an order ~kHz coupling between electron-nuclear and electron-electron spins.

2.2.1. Ground-state spin structure of the NV center

The NV electron spin ground state is a spin triplet ($S = 1$) and its Hamiltonian, neglecting second order spin-orbit interactions, is given by [36, 40]:

$$H_{\mathrm{e}} = \Delta\, J_z^2 + \gamma_e \vec{B} \cdot \vec{J}, \tag{2.1}$$

where $\Delta \approx 2\pi \cdot 2.88$ GHz is the zero field splitting, $\gamma_e \approx 2\pi \cdot 2.802$ MHz/G the electron gyromagnetic ratio, $\vec{B} = (B_x, B_y, B_z)$ the magnetic field vector and $\vec{J} = (J_x, J_y, J_z)$ the electron spin-1 operator vector. The $m_s = \pm 1$ levels are split from $m_s = 0$ by Δ at zero magnetic field due to spin-spin interactions. Applying a magnetic field lifts the degeneracy of the $m_s = \pm 1$ levels due to the Zeeman effect. This allows the

definition of a qubit within two of the three spin levels, for instance one can assign $m_s = 0$ (= $|0\rangle$) and $m_s = -1$ (= $|-1\rangle$).

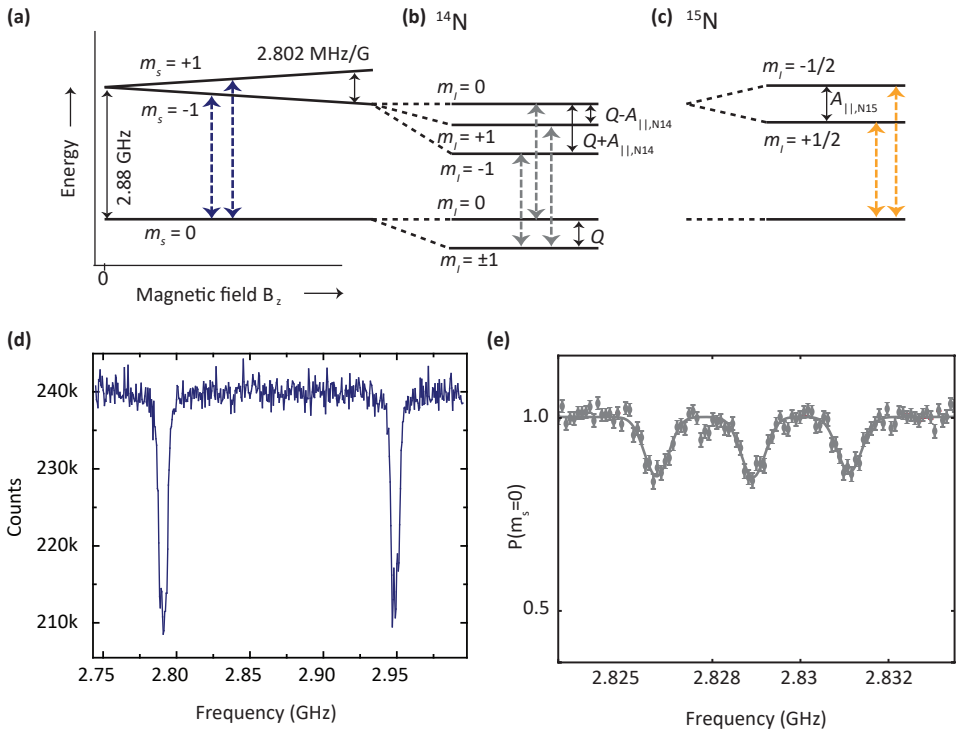

Figure 2.4: **NV ground state spin structure. a)** In a magnetic field, the $m_s = \pm 1$ levels are separated due to the Zeeman effect. **b)** Hyperfine coupling to the ^{14}N nuclear spin 1 causes an additional splitting. Double sided grey arrows show three hyperfine-splitted electron-spin transitions. The splitting between these transitions is parametrized by the hyperfine parameter ($A_{\parallel,14N}$). **c)** In contrast to (b), for the ^{15}N nuclear spin 1/2 there is a splitting into two levels due to the hyperfine coupling. The two hyperfine-splitted transitions are shown by double sided orange arrows. The splitting is parametrized by $A_{\parallel,15N}$. **d,e)** ODMR measurement showing the transitions between $m_s = 0$ and the $m_s = \pm 1$ levels separated in an applied external magnetic field (d), and (e) the hyperfine splitting due to the nitrogen atom (here a three-fold splitting due the ^{14}N spin). Figure adapted from Van Dam [41].

All NV centers have a host nuclear spin associated with the nitrogen atom of the defect. Hyperfine coupling to the nitrogen nucleus gives rise to an additional level splitting. This level splitting is dependent on the nitrogen isotope. The ^{14}N isotope has a 99.6% natural abundance and is most common in naturally occurring NV centers. Both ^{15}N (0.4% natural abundance) and ^{14}N isotopes can be implanted in diamond to form NVs. Often the ^{15}N isotope is used for implantation to distinguish an implanted atom from naturally occurring atoms that have a high abundance of ^{14}N isotopes. The Hamiltonian of the ^{14}N nuclear spin and its hyperfine interaction with the NV electron is given as [13, 42]:

$$H_{14N} = QI_z^2 + \gamma_n \vec{B} \cdot \vec{I} - A_{\parallel,14N} J_z I_z - A_{\perp,14N}(J_x I_x + J_y I_y), \tag{2.2}$$

where (I_x, I_y, I_z) are the nuclear spin 1 operators, $Q \approx -2\pi \cdot$ 4.95 MHz is the quadrupole splitting, $\gamma_n \approx -2\pi \cdot$ 0.3077 kHz/G the gyromagnetic ratio of the nitrogen spin and A_{14N} parametrizes the hyperfine coupling, which is separated in a perpendicular and parallel component. In the secular approximation, the hyperfine interaction can be approximated to $A_{\parallel,14N} J_z I_z$ as the off-diagonal terms are neglected. This is often a valid approximation at magnetic fields (B_z) chosen such that the S_z term is dominant due to the large value of $\Delta \pm \gamma_e B_z$. Moreover, for low magnetic field ($B_z \sim$10 G), nuclear Zeeman terms are small compared to quadrupole and hyperfine interactions.

The Hamiltonian for the ^{15}N nuclear spin and its hyperfine interaction with the NV is given as [13, 43]:

$$H_{15N} = \gamma_n \vec{B} \cdot \vec{I} + A_{\parallel,15N} J_z I_z + A_{\perp,15N}(J_x I_x + J_y I_y). \tag{2.3}$$

The ^{15}N nitrogen atom has spin 1/2 and thus here (I_x, I_y, I_z) are the nuclear spin-1/2 operators. Moreover, the spin-1/2 ^{15}N does not have a quadrupole splitting. The hyperfine level structure of the ^{14}N and ^{15}N are shown in Fig. 2.4. Under the secular approximation, the hyperfine splitting for the two nitrogen isotopes are parameterized by $A_{\parallel,14N} \approx$ 2.2 MHz and $A_{\parallel,15N} \approx$ 3.1 MHz. The difference in hyperfine parameters and the characteristic triplet (^{14}N) and doublet splitting (^{15}N) allows to distinguish both isotopes in optically detected magnetic resonance measurements (ODMR).

2.2.2. P1 centers

A P1 center is a defect that consists of a nitrogen atom that substitutes a carbon atom in the diamond lattice (Fig. 2.5). P1 centers are one of the most common defects in natural type Ib and certain CVD grown diamonds [44–46]. There are three known charge states of P1 centers: neutral, negative and positive [47–49]. Here we will discuss P1 centers in the neutral charge state (referred to as P1 centers unless otherwise stated), which were first detected in 1959 in electron paramagnetic resonance (EPR) [44, 50] and were also indirectly measured in ODMR experiments using NV centers [51–53]. Early electrical resistance measurements of nitrogen rich (∼200 ppm) type Ib diamonds as a function of temperature indicate a thermal ionization energy of 1.7 eV [54]. This suggests a donor level of ∼1.7 eV below the conduction band for P1 centers, in close agreement with several density-functional theory calculations (DFT) [55–57]. Photoconductivity experiments indicate an optical ionization energy within 1.9-2.2 eV [54, 58–60]. Furthermore, in absorption spectroscopy experiments a sharp feature at 4.059 eV (305 nm) and a broader feature at 4.6 eV (270 nm) have been associated with P1 centers [59, 61, 62]. The feature at 4.6 eV has also been correlated with the spin-calibrated intensity of the EPR spectrum or infrared (IR) absorption at 1344 cm^{-1}, that is associated with P1 centers [49, 63, 64]. Although the origin of the 4.6 eV absorption peak is still under

debate, it has been proposed that this feature is associated with the excitation from the valence band maximum to create a negatively charged P1 center and a valence band hole [47]. For a review on the work of the defect its level structure in the diamond band gap, we refer to Ashfold et al. [65].

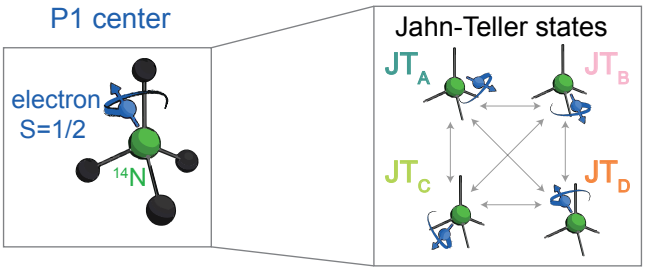

Figure 2.5: **P1 center in diamond.** Left: the P1 center surrounded by four carbon atoms in the diamond lattice. Right: the P1 center exhibits a Jahn-Teller distortion along one of the four ^{14}N - C bonds (labelled as $\{A, B, C, D\}$) that can vary over time.

Electron spin resonance studies have revealed a spin level structure of P1 centers that is now well studied and understood [44, 50–53]. The nitrogen atom of the P1 center has a nuclear spin $I = 1$ (^{14}N, 99.6% natural abundance) and an unpaired electron with spin $S = 1/2$. The unpaired electron likely resides in an antibonding orbital of s and p character [57, 66]. Moreover, the P1 center exhibits a Jahn-Teller distortion along one of its four ^{14}N-C bonds [67, 68]. This ^{14}N-C axis (JT axis) has a bond length that has been calculated to be between 5-36% elongated when comparing to the regular C-C bond length in diamond [67]. The energy barrier for reorientation of the P1 center's JT axis has been experimentally obtained and calculated to be ≈0.7 eV [67, 69, 70]. The reorientation rate at cryogenic temperatures (3.3 K) is below ∼25 mHz and its dependence on temperature has been studied by several groups [45, 69, 71]. The spin Hamiltonian that describes the unpaired electron spin and the ^{14}N spin is given as:

$$H_{\mathbf{i},\mathrm{P1}} = \gamma_e \vec{B} \cdot \vec{S} + \gamma_n \vec{B} \cdot \vec{I} + \vec{I} \cdot \mathbf{P_i} \cdot \vec{I} + \vec{S} \cdot \mathbf{A_i} \cdot \vec{I}, \tag{2.4}$$

where the subscript $\mathbf{i} \in \{A, B, C, D\}$ denotes different JT axes, $\vec{S} = (S_x, S_y, S_z)$ the electron spin-1/2 operator vector, $\vec{I} = (I_x, I_y, I_z)$ the nuclear spin-1 operator vector, $\mathbf{P_i}$ the quadrupole tensor and $\vec{B}$ the applied magnetic field. The tensor $\mathbf{A_i}$ describes the hyperfine interaction between electron spin and nitrogen spin, and includes both the isotropic Fermi contact term as well as the anisotropic dipole-dipole interaction associated with the s and p character of the orbital wave function respectively. Note that for different JT axes given by subscript $\mathbf{i}$, only the quadrupole and hyperfine tensors differ given the same reference frame. Figure 2.6 schematically shows the

energy level structure of a P1 center for all four JT axes and a magnetic field aligned along the $\hat{z}$ axis. The direction of the Jahn-Teller distortion is along $\hat{z}$ for JT axis D.

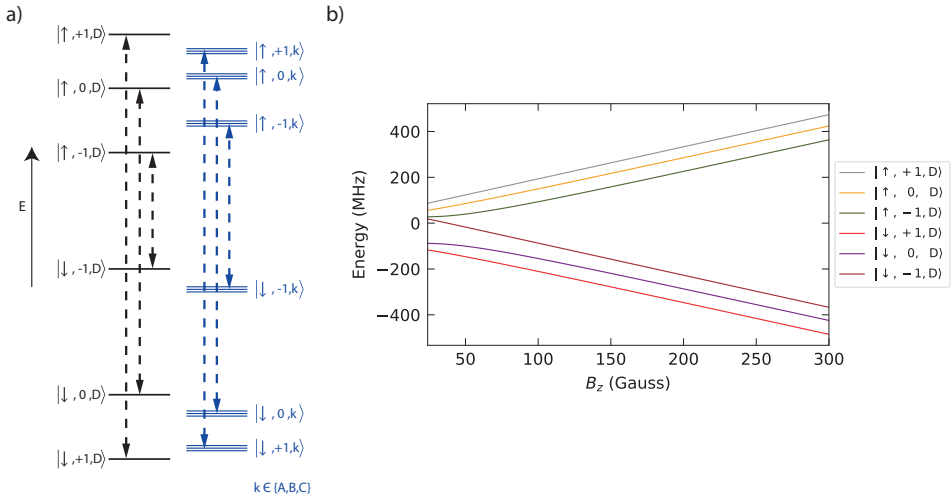

Figure 2.6: **P1 center spin levels. a)** Schematic of the ground state spin energy levels for all four JT axes ($i \in \{A, B, C, D\}$). The eigenenergies are labelled by their electron spin state ↑/↓, ^{14}N spin state $m_I = \{+1, 0, -1\}$ and JT axis $i \in \{A, B, C, D\}$. For convenience, we use the spin eigenstates as labels, while the actual eigenstates are, to some extent, mixtures of the spin eigenstates. Black levels (left) show JT axis D, whereas the blue levels (right) correspond to JT axis A,B and C which are degenerate in energy. **b)** Energy levels for the P1 center in JT axis D as a function of the magnetic field along $\hat{z}$. At magnetic field values where the hyperfine components $A_\parallel \approx 2\pi{\cdot}114$ MHz, $A_\perp \approx 2\pi{\cdot}81$ MHz and magnetic field component $\gamma_e B_z$ are of comparable strength (at $B_z <$ 100 G), the eigenstates become, to a great extent, mixtures of spin eigenstates. At larger magnetic fields ($B_z >$ 100 G) this effect is diminished and the eigenstates become, to a great extent, the spin eigenstates.

Due to the large difference in electron and nitrogen gyromagnetic ratio, the electron-electron dipolar coupling between the NV and a P1 is roughly ~9000 times stronger than their electron-nuclear dipolar coupling. For the work in this thesis, the electron-nuclear coupling between the two defects can be neglected and we describe their interaction as electron-electron dipolar only. This interaction between the NV and the P1, separated by a vector $\vec{r}$ is given as:

$$H_{NV-\mathrm{P1}} = \nu_{dip} \cdot (3(\vec{J} \cdot \hat{r})(\vec{S} \cdot \hat{r}) - \vec{J} \cdot \vec{S}), \tag{2.5}$$

where $\nu_{dip} = \frac{-\mu_0 \gamma_e \gamma_e \hbar}{4\pi r^3}$, $r = |\vec{r}|$ and $\hat{r} = \vec{r}/r$.

2.2.3. ^{13}C spins

Interestingly, ^{13}C spins surrounding the NV have been considered an inconvenience that inhibit the coherence time of NV centers. However, techniques have been developed to characterize and control these nuclear spins [72–74]. This has been further developed such that tailored dynamical decoupling protocols allow for uni-

versal control [75]. In current state-of-the-art experiments, ^{13}C spins have been used for multi-qubit quantum registers, enhanced sensing schemes, entanglement distillation and quantum error correction [25, 76–80]. Moreover, knowledge on the microscopic surrounding of the NV center in combination with tailored decoupling has shown coherence times of over a second for the electron spin of the NV [81], and recently we have demonstrated tens of seconds long quantum memory and atomic scale imaging using ^{13}C spins [82, 83]. The spin Hamiltonian and hyperfine interaction with the electron spin for multiple ^{13}C spins can be written as:

$$H_c = \sum_{i=1}^{n} (\vec{J} \cdot \mathbf{C_i} \cdot \vec{I_i} + \gamma_c \vec{B} \cdot \vec{I_i}), \tag{2.6}$$

where $\vec{I_i}$ is the nuclear spin 1/2 operator vector, $\mathbf{C_i}$ the hyperfine interaction tensor between NV electron spin and ^{13}C spin with index i and γ_c the ^{13}C gyromagnetic ratio. In addition to their interactions with the NV electron spin, the nuclear spins in the environment interact with each other via a dipolar coupling. For some of the work in this thesis these interactions can be neglected.

2.3. Experimental setup

All the experimental work presented in this thesis is performed on setups with closed cycle cryostats operating at cryogenic temperatures (~3.5 K), necessary for resonant optical excitation of the NV [84]. The framework used for experimental control and readout of electron and nuclear spins consists of four main parts. 1) The control electronics are used to run the control cycle and to communicate between different components of the setup. 2) We use optical addressing for initialization and readout of the NV electron spin. 3) Microwave (MW) and radio-frequency (RF) signals are used for spin manipulation of nuclear and electron spins. 4) An external magnetic field is applied using permanent magnets to create Zeeman splittings. In Fig. 2.7, a more detailed schematic is shown of the experimental framework.

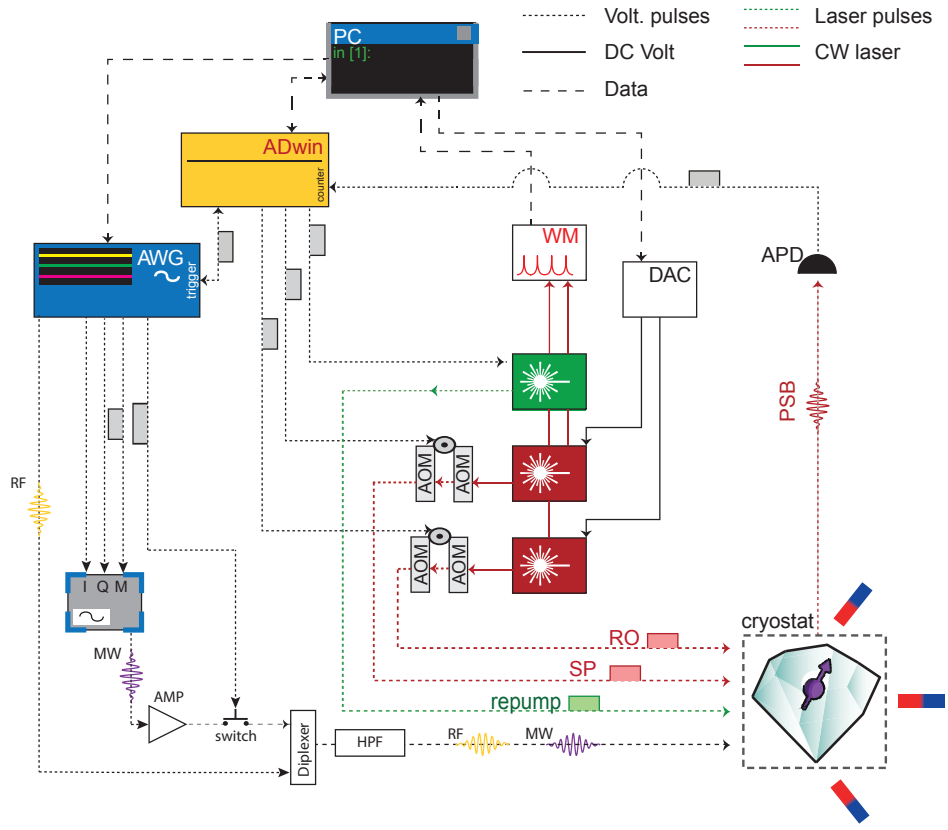

Figure 2.7: Schematic of one of the experimental setups used in this thesis. **Control electronics**: A PC programs the control cycle onto a micro-controller (ADwin) and the pulse sequence with nanosecond resolution onto an arbitrary waveform generator (AWG; Tektronix AWG 5014). The communication between the different components of the setup is mainly done by the ADwin, including triggering the AWG to start the pulse sequence. **Optics**: We use a green laser (515 nm or 532 nm) for charge state control and two resonant lasers (Toptica DL Pro and New Focus Velocity) for initialization and readout. The New Focus Velocity laser is also used as a tunable laser for photoluminescence excitation spectra (as performed in chapter 3). To generate optical pulses we use Acousto-optic modulators (AOM) for the resonant (637 nm) lasers and either an AOM (for 532 nm, not shown) or direct modulation (515 nm) for the green laser. The frequencies of the two resonant lasers are measured using a wavemeter (HF-ANGSTROM WS/U-10U) and stabilized using a PC-controlled feedback loop (PID loop). We use a home-built confocal microscope to focus light onto the sample and to collect the phonon sideband emission of the NV. The microscope objective is mounted on three piezo scanners (PI) that can be used to make 3-dimensional scans and align the NV center to the optical path. **Microwave and RF**: Microwave pulses are generated using a vector source. Via IQ- and pulse-modulation using the AWG, we control the frequencies, timings, shapes and phases of these pulses. The signal is amplified by a microwave amplifier (AR 25S1G6). A fast microwave switch (TriQuint TGS2355-SM, suppression ratio of 40 dB, controlled by the AWG) is used to protect the NV from the amplifier noise while idling. Video leakage noise generated by the switch is filtered with a high pass filter (HPF). RF signals to address P1 centers and nuclear spins are generated directly by an AWG (Tektronix 5014, 4.5V pk-pk). The MW and RF signals are combined using a diplexer and the output is then fed through the HPF to the diamond sample. **External magnetic field**: For the experiments described in chapters 3 and 5, we apply a static magnetic field using a single permanent room-temperature neodymium magnet (one out of the three shown). While in chapter 4 we use three permanent room-temperature neodymium magnets placed along three approximately orthogonal directions, to generate an arbitrary magnetic field direction. **Cryogenics**: The sample is held in a closed cycle cryostat (Montana Cryostation) at a temperature of ~3.5 K. Figure adapted from Pfaff [31].

2.4. Diamond devices

In the experimental work in this thesis we report on 174 NV centers. For 172 of these NV centers, we have used diamond samples that are described in chapter 3. The remaining NV centers were measured in two separate diamond devices that we will describe here.

The first diamond is used for the experimental work described in chapter 4. This is a chemical-vapor-depositioned (CVD) homoepitaxially grown diamond, that is isotopically purified with an estimated 0.01% ^{13}C abundance and a nitrogen concentration of ~75 ppb. The diamond is grown along the ⟨100⟩ crystal direction and has not been cut or polished post growth (sample is obtained from Element Six). In this diamond we have used a naturally occurring NV center. Due to the ⟨100⟩ growth direction, the symmetry axis of the NV does not lie perpendicular to the diamond surface. Therefore three permanent magnets are used to allow an arbitrary magnetic field direction for alignment with respect to the NV axis.

The second diamond is used for the experimental work that is described in chapter 5. This is a CVD homoepitaxially grown diamond with a natural abundance of ^{13}C atoms (1.1%) and an estimated nitrogen concentration of <5 ppb (sample is obtained from Element Six). It has been grown along the ⟨100⟩ direction and post-growth cut perpendicular to the ⟨111⟩ crystal direction. In this diamond we have used a naturally occuring NV center that has starred in numerous experiments [25, 81–83, 85]. Due to the ⟨111⟩ crystal direction, a single permanent magnet on xyz steppers has been used for alignment of the magnetic field.

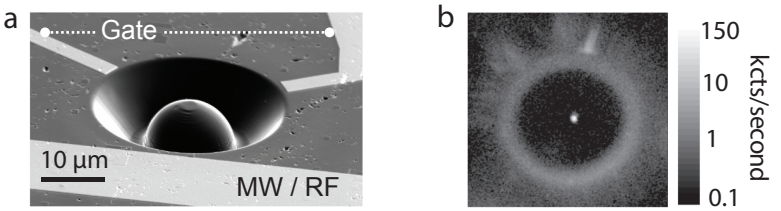

Figure 2.8: a) Scanning electron microscope image of a fabricated device around an NV center. The dome shaped feature in diamond (grey) is a solid immersion lens, that has been fabricated around the NV center. The stripline is fabricated close to the SIL to apply MW and RF pulses for electron and nuclear spin control. The gate electrodes can be used for applying static electric fields. b) Confocal scan over the area of the SIL. The circular shaped feature corresponds to the edges of the SIL and the bright spot near its center is fluorescence from a single NV center. Figure adapted from Bernien [32].

For both diamonds, a solid immersion lens (SIL) is fabricated around the NV center using focused ion beam milling to enhance photon collection efficiency [84, 86]. An example of such a typical diamond device is shown in Fig. 2.8. Using standard lithography techniques, on-chip gold striplines are fabricated next to the SIL to apply MW and RF pulses for fast electron and nuclear spin control (peak rabi frequency ~26 MHz for the electron spin). In the same lithography step, golden gate electrodes are deposited to apply static electric fields. These electrodes can

be used for DC stark tuning of optical transitions of NV centers [36], however, they have not been used for the work in this thesis. Furthermore, an Al_2O_3 anti-reflection coating is deposited on the diamond to further improve photon collection efficiency by reducing internal reflections.

2.5. Optical transitions and single-shot readout

The excited state structure of the NV consists of six levels. As described in section 2.1, in case of no strain (or electric fields) the excited states of the NV center are degenerate for the states E_x/E_y and E_1/E_2. Up to first order, lateral strain ($\xi_\perp$) splits these transitions, while longitudinal strain ($\xi_\parallel$) shifts all excited states levels either up or down in energy.

The optical transitions between ground and excited states above cryogenic temperature (>10 K) are subject to phonon-induced mixing, which leads to averaging of the excited states and strong broadening of the ZPL linewidth [87]. At cryogenic temperatures (~3.5 K), this effect is suppressed and in a high purity IIa diamond, low in nitrogen defects (<5 ppb), the optical transitions are discernible, coherent and their linewidths approach the lifetime-limited value of 13 MHz [88].

Although linewidths of ~140 MHz have been reported for nitrogen rich (~200 ppm, type Ib) nanodiamonds, their linewidth under alternating <532 nm laser and red laser pulses has been observed to broaden to ~30 GHz [88, 89]. This effect has been associated with photoexcitation of P1 centers, which changes the local charge distribution around the NV center [88, 89]. Here we report on the linewidths of an NV in diamond with ~75 ppb nitrogen concentration, used for the experimental work in chapter 4, and find that its optical transitions can be discernible (Fig. 2.9a). Due to the overlap of the E_x and A_1 transitions in our strain regime, we use the $E_{1,2}$ transitions and E_y transition for initialization and single-shot readout of the spin state of the NV respectively. We find a linewidth of 354(8) MHz for E_y (Fig. 2.9b). On the side of the prominent peaks of the E_y and $E_{1,2}$ transitions (Fig. 2.9b, bottom), we observe two lower intensity satellite peaks that are likely caused by an electric field due to a charge reconfiguration in the nearby environment of the NV.

We typically initialize the NV electron spin in the $m_s = 0$ state through a spin pumping process. By using a resonant laser we excite the ground states $m_s = \pm 1$ into the optically excited states $E_{1,2}$, where spin flips occur so that the spin gets prepared in $m_s = 0$. The electron spin state of this NV is read out in a single shot by using a laser in resonance with the E_y transition. Ideally, this leads to one or more photons if the electron spin is in the $m_s = 0$ or no photons if the state is $m_s = \pm 1$. The average readout fidelity that we obtain is ≈85%, which is lower than earlier reported values of ≈93% or higher [84]. Likely causes for this lower fidelity are diminished photon collection counts due to an off-centered position of this NV in its SIL, broader linewidth or a worsened cyclicity of the E_y transition compared to the E_x transition due larger spin-mixing of the E_y excited state for our strain values [90]. Further optimization by including DC stark tuning could provide an accessible

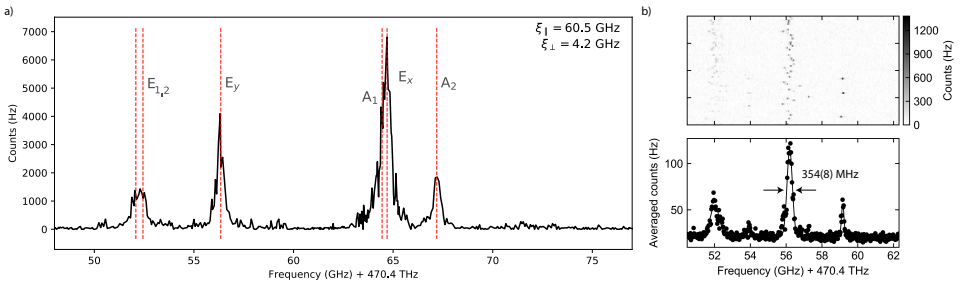

Figure 2.9: **Photoluminescence excitation spectra.** a) Photoluminescence excitation spectrum with alternating green (515 nm) and red laser pulses while sweeping the frequency of the latter. Longitudinal ($\xi_{\parallel}$) and lateral ($\xi_{\perp}$) strain components are obtained from a fit of the excited state NV Hamiltonian. b) Top: 60 individual scans around the frequency range of the E_y and $E_{1,2}$ transitions. Individual scans use a single green (515 nm) laser pulses at the start of each trace followed by a frequency sweep of red laser pulses. Continuous MW driving on the spin resonances was used to prevent optical pumping into a dark spin state during each frequency sweep. Bottom: integration of all 60 individual scans. A linewidth of 354(8) MHz is found for the E_y transition. Besides the prominent transitions of $E_{1,2}$ and E_y at ~52 GHz and ~56 GHz, satellite peaks are observed at ~54 GHz and ~59 GHz. During individual scans (top) the appearance of these satellite peaks are correlated with the disappearance of the prominent transitions, which indicates that these are not different transitions but a discrete shift of the same transitions.

E_x transition and potentially a higher single-shot readout fidelity (this has not been explored in this thesis).

The NV center that is used for the work in chapter 5 of this thesis, has an accessible E_x transition that we use for spin readout of the $m_s = 0$ state. Also here we use the $E_{1,2}$ transitions for NV electron spin initialisation in $m_s = 0$ via spin pumping on these transitions. For this NV, we obtain an average readout fidelity of ≈94.5%, similar to reported values on comparable NV centers [84].

2.6. Double electron-electron resonance

To sense electron spins surrounding a central spin such as the NV center, a commonly used technique is double electron-electron resonance spectroscopy [91]. This technique is illustrated in Fig. 2.10a and consists of a Hahn echo on the NV center, plus a simultaneous π pulse that selectively recouples electron spins. Due to the Hahn echo on the NV, its coherence is extended while remaining sensitive to resonant electron spins. Repetitive application of this sequence can improve the signal-to-noise ratio but is a trade-off with the disturbance of the measured state due to a combination of natural relaxation, effects of the MW pulse sequence and effects of laser-based NV readout. The double electron-electron resonance technique is used extensively in chapter 4 of this thesis.

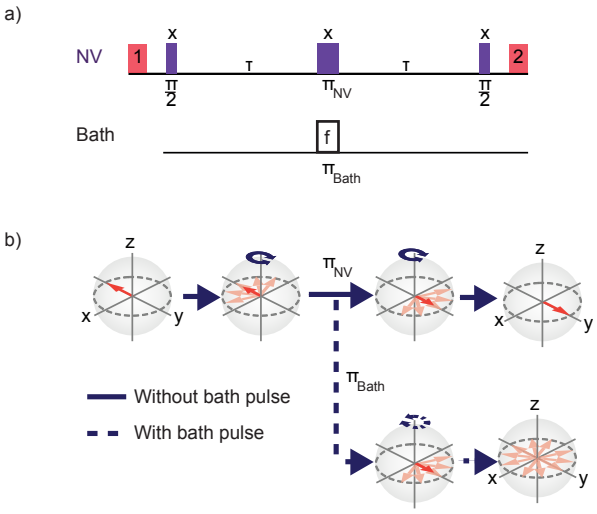

Figure 2.10: **Double electron-electron resonance.** a) The sequence starts with initialising the NV in $m_s = 0$ via spin-pumping (1). Next, a Hahn echo sequence is performed on the NV center. Simultaneously with the π pulse on the NV, a π pulse is applied on surrounding spins at frequency f. Finally the $m_s = 0$ spin state of the NV is read out (2). b) Schematic illustration of spin trajectories of the NV on the Bloch sphere during the sequence in (a). Figure adapted from Van der Sar [92].

References

[1] Ohno, K. *et al.*, *Engineering shallow spins in diamond with nitrogen delta-doping,* Appl. Phys. Lett. **101**, 082413 (2012).

[2] Myers, B. A. *et al.*, *Probing surface noise with depth-calibrated spins in diamond,* Physical Review Letters **113**, 027602 (2014).

[3] Naydenov, B. *et al.*, *Enhanced generation of single optically active spins in diamond by ion implantation,* App. Phys. Lett. **96**, 163108 (2010).

[4] Pezzagna, S., Naydenov, B., Jelezko, F., Wrachtrup, J. & Meijer, J., *Creation efficiency of nitrogen-vacancy centres in diamond,* New J. Phys. **12**, 065017 (2010).

[5] De Oliveira, F. F. *et al.*, *Tailoring spin defects in diamond by lattice charging,* Nature communications **8**, 1 (2017).

[6] Antonov, D. *et al.*, *Statistical investigations on nitrogen-vacancy center creation,* Applied Physics Letters **104**, 012105 (2014).

[7] Ruf, M. *et al.*, *Optically coherent nitrogen-vacancy centers in micrometer-thin etched diamond membranes,* Nano letters **19**, 3987 (2019).

[8] Davies, G., Lawson, S. C., Collins, A. T., Mainwood, A. & Sharp, S. J., *Vacancy-related centers in diamond,* Physical Review B **46**, 13157 (1992).

[9] Twitchen, D. *et al.*, *Electron paramagnetic resonance (EPR) and optical absorption studies of defects created in diamond by electron irradiation damage at 100 and 350 k,* PHYSICA B **273**, 628 (1999).

[10] Chen, Y.-C. *et al.*, *Laser writing of coherent colour centres in diamond,* Nat. Photon. **11**, 77 (2017).

[11] Chen, Y.-C. *et al.*, *Laser writing of individual nitrogen-vacancy defects in diamond with near-unity yield,* Optica **6**, 662 (2019).

[12] Smith, J. M., Meynell, S. A., Jayich, A. C. B. & Meijer, J., *Colour centre generation in diamond for quantum technologies,* Nanophotonics **8**, 1889 (2019).

[13] Doherty, M. W. *et al.*, *The nitrogen-vacancy colour centre in diamond,* Phys. Rep. **528**, 1 (2013).

[14] Awschalom, D., Hanson, R., Wrachtrup, J. & Zhou, B., *Quantum technologies with optically interfaced solid-state spins,* Nat. Photonics **12**, 516 (2018).

[15] Maze, J. R., Taylor, J. M. & Lukin, M. D., *Electron spin decoherence of single nitrogen-vacancy defects in diamond,* Phys. Rev. B **78**, 094303 (2008).

[16] Taylor, J. *et al.*, *High-sensitivity diamond magnetometer with nanoscale resolution,* Nat. Phys. **4**, 810 (2008).

[17] De Lange, G., *Quantum control and coherence of interacting spins in diamond* (PhD Thesis, Delft, University of Technology, 2012).

[18] Schirhagl, R., Chang, K., Loretz, M. & Degen, C. L., *Nitrogen-vacancy centers in diamond: nanoscale sensors for physics and biology,* Annu. Rev. Phys. Chem. **65**, 83 (2014).

[19] Degen, C. L., Reinhard, F. & Cappellaro, P., *Quantum sensing,* Rev. Mod. Phys. **89**, 035002 (2017).

[20] Aslam, N. *et al.*, *Nanoscale nuclear magnetic resonance with chemical resolution,* Science **357**, 67 (2017).

[21] Glenn, D. R. *et al.*, *High-resolution magnetic resonance spectroscopy using a solid-state spin sensor,* Nature **555**, 351 (2018).

[22] Wrachtrup, J. & Jelezko, F., *Processing quantum information in diamond,* J. Condens. Matter Phys. **18**, S807 (2006).

[23] Taminiau, T. H., Cramer, J., van der Sar, T., Dobrovitski, V. V. & Hanson, R., *Universal control and error correction in multi-qubit spin registers in diamond,* Nat. Nanotech. **9**, 171 (2014).

[24] Waldherr, G. *et al.*, *Quantum error correction in a solid-state hybrid spin register,* Nature **506**, 204 (2014).

[25] Cramer, J. *et al.*, *Repeated quantum error correction on a continuously encoded qubit by real-time feedback,* Nat. Commun. **7**, 11526 (2016).

[26] Bernien, H. *et al.*, *Heralded entanglement between solid-state qubits separated by three metres,* Nature **497**, 86 (2013).

[27] Pfaff, W. *et al.*, *Unconditional quantum teleportation between distant solid-state quantum bits,* Science **345**, 532 (2014).

[28] Hensen, B. *et al.*, *Loophole-free Bell inequality violation using electron spins separated by 1.3 kilometres,* Nature **526**, 682 (2015).

[29] Gao, W. B., Imamoglu, A., Bernien, H. & Hanson, R., *Coherent manipulation, measurement and entanglement of individual solid-state spins using optical fields,* Nat. Photon. **9**, 363 (2015).

[30] Wehner, S., Elkouss, D. & Hanson, R., *Quantum internet: A vision for the road ahead,* Science **362** (2018).

[31] Pfaff, W., *Quantum measurement and entanglement of spin quantum bits in diamond* (PhD Thesis, Delft, University of Technology, 2013).

[32] Bernien, H., *Control, measurement and entanglement of remote quantum spin registers in diamond* (PhD Thesis, Delft, University of Technology, 2014).

[33] Doherty, M. W., Manson, N. B., Delaney, P. & Hollenberg, L. C. L., *The negatively charged nitrogen-vacancy centre in diamond: the electronic solution,* New J. Phys. **13**, 025019 (2011).

[34] Hensen, B., *Measurement-based quantum computation with the nitrogen-vacancy centre in diamond* (MSc Thesis, Delft, University of Technology, 2011).

[35] Maze, J. R. *et al.*, *Properties of nitrogen-vacancy centers in diamond: the group theoretic approach,* New J. Phys. **13**, 025025 (2011).

[36] Hensen, B., *Quantum nonlocality with spins in diamond* (PhD Thesis, Delft, University of Technology, 2016).

[37] Kalb, N., *Diamond-based quantum networks with multi-qubit nodes* (PhD Thesis, Delft, University of Technology, 2018).

[38] Balasubramanian, G. *et al.*, *Ultralong spin coherence time in isotopically engineered diamond,* Nature materials **8**, 383 (2009).

[39] Mindarava, Y. *et al.*, *Synthesis and coherent properties of 13c-enriched submicron diamond particles with nitrogen vacancy color centers,* Carbon **165**, 395 (2020).

[40] Doherty, M. *et al.*, *Theory of the ground-state spin of the nv- center in diamond,* Phys. Rev. B **85**, 205203 (2012).

[41] Van Dam, S., *Optical cavities, coherent emitters, and protocols for diamond-based quantum networks* (PhD Thesis, Delft, University of Technology, 2019).

[42] Yavkin, B., Mamin, G. & Orlinskii, S., *High-frequency pulsed endor spectroscopy of the nv- centre in the commercial hpht diamond,* Journal of Magnetic Resonance **262**, 15 (2016).

[43] Gali, A., *Identification of individual c 13 isotopes of nitrogen-vacancy center in diamond by combining the polarization studies of nuclear spins and first-principles calculations,* Physical Review B **80**, 241204 (2009).

[44] Smith, W., Sorokin, P., Gelles, I. & Lasher, G., *Electron-spin resonance of nitrogen donors in diamond,* Phys. Rev. **115**, 1546 (1959).

[45] Ammerlaan, C. A. & Burgemeister, E. A., *Reorientation of nitrogen in type-Ib diamond by thermal excitation and tunneling,* Phys. Rev. Lett. **47**, 954 (1981).

[46] Eichhorn, T. R., McLellan, C. A. & Jayich, A. C. B., *Optimizing the formation of depth-confined nitrogen vacancy center spin ensembles in diamond for quantum sensing,* Physical Review Materials **3**, 113802 (2019).

[47] Ulbricht, R. *et al.*, *Single substitutional nitrogen defects revealed as electron acceptor states in diamond using ultrafast spectroscopy,* Phys. Rev. B **84**, 165202 (2011).

[48] Deák, P., Aradi, B., Kaviani, M., Frauenheim, T. & Gali, A., *Formation of nv centers in diamond: A theoretical study based on calculated transitions and migration of nitrogen and vacancy related defects,* Phys. Rev. B **89**, 075203 (2014).

[49] Lawson, S. C., Fisher, D., Hunt, D. C. & Newton, M. E., *On the existence of positively charged single-substitutional nitrogen in diamond,* Journal of Physics: Condensed Matter **10**, 6171 (1998).

[50] Cook, R. & Whiffen, D. H., *Electron nuclear double resonance study of a nitrogen centre in diamond,* Proceedings of the Royal Society of London. Series A. Mathematical and Physical Sciences **295**, 99 (1966).

[51] De Lange, G. *et al.*, *Controlling the quantum dynamics of a mesoscopic spin bath in diamond,* Sci. Rep **2**, 1 (2012).

[52] Knowles, H. S., Kara, D. M. & Atatüre, M., *Observing bulk diamond spin coherence in high-purity nanodiamonds,* Nat. Mater. **13**, 21 (2014).

[53] Knowles, H. S., Kara, D. M. & Atatüre, M., *Demonstration of a Coherent Electronic Spin Cluster in Diamond,* Phys. Rev. Lett. **117**, 1 (2016).

[54] Farrer, R., *On the substitutional nitrogen donor in diamond,* Solid State Communications **7**, 685 (1969).

[55] Deák, P., Aradi, B., Kaviani, M., Frauenheim, T. & Gali, A., *Formation of nv centers in diamond: A theoretical study based on calculated transitions and migration of nitrogen and vacancy related defects,* Physical Review B **89**, 075203 (2014).

[56] Jones, R., Goss, J. & Briddon, P., *Acceptor level of nitrogen in diamond and the 270-nm absorption band,* Physical Review B **80**, 033205 (2009).

[57] Ferrari, A. M., Salustro, S., Gentile, F. S., Mackrodt, W. C. & Dovesi, R., *Substitutional nitrogen in diamond: A quantum mechanical investigation of the electronic and spectroscopic properties,* Carbon **134**, 354 (2018).

[58] Heremans, F., Fuchs, G., Wang, C., Hanson, R. & Awschalom, D., *Generation and transport of photoexcited electrons in single-crystal diamond,* Appl. Phys. Lett. **94**, 152102 (2009).

[59] Van Enckevort, W. & Versteegen, E., *Temperature dependence of optical absorption by the single-substitutional nitrogen donor in diamond,* Journal of Physics: Condensed Matter **4**, 2361 (1992).

[60] Rosa, J., Vaněček, M., Nesladek, M. & Stals, L., *Photoionization cross-section of dominant defects in cvd diamond,* Diamond and related materials **8**, 721 (1999).

[61] Dyer, H., Raal, F., Du Preez, L. & Loubser, J., *Optical absorption features associated with paramagnetic nitrogen in diamond,* Philosophical Magazine **11**, 763 (1965).

[62] Sumiya, H. & Satoh, S., *High-pressure synthesis of high-purity diamond crystal,* Diamond and Related Materials **5**, 1359 (1996).

[63] De Weerdt, F. & Collins, A., *Determination of the c defect concentration in hpht annealed type iaa diamonds from uv–vis absorption spectra,* Diamond and related materials **17**, 171 (2008).

[64] Manson, N. B. *et al.*, *Nv—n+ pair centre in 1b diamond,* New Journal of Physics **20**, 113037 (2018).

[65] Ashfold, M. N. *et al.*, *Nitrogen in diamond,* Chemical reviews **120**, 5745 (2020).

[66] Loubser, J. & van Wyk, J., *Electron spin resonance in the study of diamond,* Reports on Progress in Physics **41**, 1201 (1978).

[67] Breuer, S. & Briddon, P., *Energy barrier to reorientation of the substitutional nitrogen in diamond,* Physical Review B **53**, 7819 (1996).

[68] Jahn, H. A. & Teller, E., *Stability of polyatomic molecules in degenerate electronic states-i—orbital degeneracy,* Proceedings of the Royal Society of London. Series A-Mathematical and Physical Sciences **161**, 220 (1937).

[69] Shul'man, L. A., Zaritskii, M. I. & Podzyarei, G. A., *Reorientation of the Jahn-Teller distortion in nitrogen impurity centers in diamond,* Sov. phys., Solid State **8**, 1842 (1967).

[70] Loubser, J. & Van Ryneveld, W., *The dynamic jahn-teller and other effects in the high-temperature electron spin resonance spectrum of nitrogen in diamond,* British Journal of Applied Physics **18**, 1029 (1967).

[71] Zaritskii, I. M. *et al.*, *Spin-lattice relaxation of a Jahn-Teller nitrogen center in diamond,* Sov. phys., Solid state **18**, 1883 (1976).

[72] Taminiau, T. *et al.*, *Detection and control of individual nuclear spins using a weakly coupled electron spin,* Physical review letters **109**, 137602 (2012).

[73] Kolkowitz, S., Unterreithmeier, Q. P., Bennett, S. D. & Lukin, M. D., *Sensing distant nuclear spins with a single electron spin,* Physical review letters **109**, 137601 (2012).

[74] Zhao, N. *et al.*, *Sensing single remote nuclear spins,* Nature nanotechnology **7**, 657 (2012).

[75] Taminiau, T. H., Cramer, J., van der Sar, T., Dobrovitski, V. V. & Hanson, R., *Universal control and error correction in multi-qubit spin registers in diamond,* Nature nanotechnology **9**, 171 (2014).

[76] Kalb, N. *et al.*, *Entanglement distillation between solid-state quantum network nodes,* Science **356**, 928 (2017).

[77] van Dam, S. B., Cramer, J., Taminiau, T. H. & Hanson, R., *Multipartite entanglement generation and contextuality tests using nondestructive three-qubit parity measurements,* Physical review letters **123**, 050401 (2019).

[78] Unden, T. K., Louzon, D., Zwolak, M., Zurek, W. H. & Jelezko, F., *Revealing the emergence of classicality using nitrogen-vacancy centers,* Physical review letters **123**, 140402 (2019).

[79] Vorobyov, V. *et al.*, *Quantum fourier transform for quantum sensing,* arXiv preprint arXiv:2008.09716 (2020).

[80] Waldherr, G. *et al.*, *Quantum error correction in a solid-state hybrid spin register,* Nature **506**, 204 (2014).

[81] Abobeih, M. H. *et al.*, *One-second coherence for a single electron spin coupled to a multi-qubit nuclear-spin environment,* Nature communications **9**, 1 (2018).

[82] Bradley, C. E. *et al.*, *A ten-qubit solid-state spin register with quantum memory up to one minute,* Phys. Rev. X **9**, 031045 (2019).

[83] Abobeih, M. *et al.*, *Atomic-scale imaging of a 27-nuclear-spin cluster using a quantum sensor,* Nature **576**, 411 (2019).

[84] Robledo, L. *et al.*, *High-fidelity projective read-out of a solid-state spin quantum register,* Nature **477**, 574 (2011).

[85] Kalb, N. *et al.*, *Experimental creation of quantum zeno subspaces by repeated multi-spin projections in diamond,* Nature communications **7**, 1 (2016).

[86] Hadden, J. *et al.*, *Strongly enhanced photon collection from diamond defect centers under microfabricated integrated solid immersion lenses,* Appl. Phys. Lett. **97**, 241901 (2010).

[87] Fu, K.-M. C. *et al.*, *Observation of the dynamic jahn-teller effect in the excited states of nitrogen-vacancy centers in diamond,* Physical Review Letters **103**, 256404 (2009).

[88] Tamarat, P. *et al.*, *Stark shift control of single optical centers in diamond,* Physical review letters **97**, 083002 (2006).

[89] Jelezko, F. *et al.*, *Single spin states in a defect center resolved by optical spectroscopy,* Applied physics letters **81**, 2160 (2002).

[90] Loenen, S., *Improving single-shot readout for diamond quantum processors* (MSc Thesis, Delft, University of Technology, 2019).

[91] Slichter, C., *Principles of Magnetic Resonance* (Springer-Verlag, New York, 1990).

[92] Van der Sar, T., *Quantum control of single spins and single photons in diamond* (PhD Thesis, Delft, University of Technology, 2012).

3

Optical coherence of diamond nitrogen-vacancy centers formed by ion implantation and annealing

S. B. van Dam*, M. Walsh*, M. J. Degen, E. Bersin, S. L. Mouradian, A. Galiullin, M. Ruf, M. IJspeert, T. H. Taminiau, R. Hanson, and D. R. Englund

The advancement of quantum optical science and technology with solid-state emitters such as nitrogen-vacancy (NV) centers in diamond critically relies on the coherence of the emitters' optical transitions. A widely employed strategy to create NV centers at precisely controlled locations is nitrogen ion implantation followed by a high-temperature annealing process. We report on experimental data directly correlating the NV center optical coherence to the origin of the nitrogen atom. These studies reveal low-strain, narrow-optical-linewidth (< 500 *MHz) NV centers formed from naturally-occurring* ^{14}N *atoms. In contrast, NV centers formed from implanted* ^{15}N *atoms exhibit significantly broadened optical transitions (*> 1 *GHz) and higher strain. The data show that the poor optical coherence of the NV centers formed from implanted nitrogen is not due to an intrinsic effect related to the diamond or isotope. These results have immediate implications for the positioning accuracy of current NV center creation protocols and point to the need to further investigate the influence of lattice damage on the coherence of NV centers from implanted ions.*

The results in this chapter have been published in Phys. Rev. B, **99**, 161203 (2019).
*Equally contributing authors.

3.1. Introduction

Coherent optical control over solid-state quantum emitters has enabled new advances in quantum science [1–3] and may lead to technologies such as quantum networks [4]. A quantum network crucially relies on entanglement connections that can be established through a coherent spin-photon interface. The nitrogen-vacancy (NV) defect center in diamond is a well-suited candidate owing to a spin ground state with a long coherence time [5, 6], nearby nuclear spins for quantum memories [7] or algorithms [8–10], and spin-selective optical transitions allowing for efficient optical spin initialization and readout [11]. Moreover, at low strain and low temperature (< 10 K), effects from phonon mixing in the excited state are small [12, 13], and the optical transition can be coherent. Indeed, narrow-linewidth, coherent optical transitions [14–16] have been used for the generation of indistinguishable photons suited for two photon quantum interference [17, 18] and entanglement generation between remote NV centers [19].

To date, all experiments employing coherent photons from NV centers have been performed with NV centers that were formed during diamond growth. Key to their optical coherence is that these NV centers experience an environment with few defects, since the stability of optical transitions (as with many solid-state systems) suffers from unwanted interactions with nearby bulk and surface defects leading to changes in the strain and electric field environment [20–24]. For NV centers with a broadened linewidth below ≈ 200 MHz dominated by slow spectral diffusion, protocols using resonant charge repumping [25] and real-time monitoring of the transition frequency [26] have been used to reduce the broadened linewidth to an effective linewidth of below 50 MHz, suitable for quantum optical experiments. However, such protocols are challenging for NV centers with greater spectral diffusion.

3.2. Nitrogen ion implantation

Instead of being limited to NV centers formed during diamond growth, they can be created, for example by nitrogen ion implantation [27]. Nitrogen ion implantation provides an NV positioning accuracy that enables integration with on-chip photonics [28, 29] and coupling between nearby NV centers [30–32]. Precise positioning of NV centers or accurately registering their location is also a prerequisite for optimal overlap of the dipole with the electric field mode of diamond optical cavities, for engineering and enhancing light-matter interaction [24, 33–38]. Moreover, ion implantation allows for the creation of single NV centers in high purity diamond, providing a potentially low-defect environment [22].

However, the bombardment of the diamond with nitrogen ions creates crystal damage that can deteriorate spin and optical coherence properties of NV centers [21, 22]. High-temperature annealing can mitigate some of these issues by repairing the diamond lattice [39–42]. A procedure including a low implantation dose, careful cleaning, and high-temperature annealing was reported by Chu et al. [43],

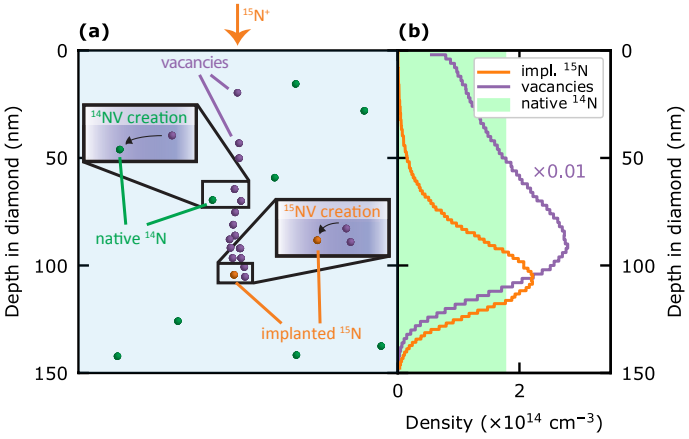

Figure 3.1: **NV creation via nitrogen-ion implantation. a**, Schematic showing implanted $^{15}N^+$ ions (orange) leaving a trail of vacancies (purple) until settling into a final position. Naturally abundant ^{14}N ions (green) are shown randomly distributed throughout the diamond lattice. Vacancies (implantation-induced or native) mobilized by annealing can bind to a nitrogen atom (implanted or native). **b**, A SRIM simulation using the parameters in sample A show the distribution of implanted nitrogen (orange) and created vacancies (purple). The shaded green area indicates the range of the estimated natural ^{14}N concentration reported by Element Six.

leading to the creation of narrow-linewidth NV centers. These narrow-linewidth NV centers can result from implanted nitrogen atoms, or from native nitrogen atoms, combined with for example implantation-induced vacancies (Figure 3.1a). In principle, the source of nitrogen can be verified by implanting ^{15}N isotopes (natural abundance 0.37%) and resolving the hyperfine structure of the NV magnetic spectrum [44], as done in studies of the spin coherence [41, 45] and creation efficiency [30, 46–49] of NVs formed from implanted nitrogen. However, in Chu et al. [43] the isotope of the narrow-linewidth NV centers was not investigated [50]. In a later study with similar results [38], ^{14}N isotopes were implanted, so that the origin of the NV center's nitrogen atom could not be determined. Here we report on a study that enables us to directly correlate the optical linewidth of NV transitions to the NV formation mechanism.

To distinguish NVs formed by implanted nitrogen atoms from those formed by native nitrogen atoms, we implanted ^{15}N isotopes [44]. We then experimentally correlated the optical linewidth to the nitrogen isotope. The study was carried out on two separate samples (see sec. 3.7). Sample A (processed at MIT) is a bulk $\langle 100 \rangle$ CVD grown diamond (Element Six), prepared with the same implantation and annealing procedure as presented in Chu et al. [43]: it was implanted with $^{15}N^+$ at 85 keV with a fluence of 10^9 N/cm^2 and subsequently annealed at a maximum temperature of 1200 °C. Sample B (Delft) is a membrane (thickness ≈ 14 µm) obtained from a bulk $\langle 100 \rangle$ CVD grown diamond (Element Six), implanted with $^{15}N^+$ at 400 keV (fluence 10^8 N/cm^2), and subsequently annealed at a maximum tem-

perature of 1100 °C.

During implantation, nitrogen ions penetrate the diamond to a depth determined by the implantation energy (Figure 3.1). As implanted nitrogen atoms track through the crystal, they displace carbon atoms from their lattice sites creating vacancies. The nitrogen atoms create damage along the entire trajectory, but the damage is greatest near the stopping point [51]. We performed SRIM [52] simulations to predict the stopping point of implanted ^{15}N atoms, in addition to the locations of vacancies created along the trajectory (Figure 3.1b). At temperatures > 600 °C, vacancies become mobile [53]. These vacancies can form an NV center, recombining with the implanted ^{15}N that created the damage or with a native ^{14}N in the lattice. The resulting ^{15}NV and ^{14}NV formation yields can vary significantly [30, 45–48] depending on several factors, including the initial nitrogen concentration, the implantation fluence and energy, the number of vacancies created during the implantation process, and the duration and temperature of annealing.

3.3. NV densities and host isotopes

A representative confocal fluorescence map at the implantation depth in sample A is shown in Figure 3.2a. Confocal fluorescence scans at foci deeper into the diamond show a significantly lower density of fluorescent spots (Figure 3.2a, inset), indicating that the emitters near the surface were predominantly created by the implantation and annealing process (see sec. 3.7.4). We identified emitters using different protocols in the two samples. In sample A, automated spot-recognition was performed on a fluorescence scan. For each detected spot we identified an NV center based on its characteristic zero-phonon line (ZPL) emission around 637 nm using a spectrograph from a photoluminescence measurement at 4 K under 532 nm excitation. This protocol identified 120 fluorescent spots as NV centers in a ~ 400 μm^2 area. In sample B, spots in a fluorescence scan were detected visually, after which an automated protocol identified NV centers based on the presence of a resonance in an optically detected magnetic resonance (ODMR) spectrum around the characteristic NV center zero-field splitting of 2.88 GHz. In this way, 52 out of a total 57 inspected spots in a ≈ 75 μm^2 area in the implantation layer were identified as NV centers.

We next determined the nitrogen isotope of each NV center by observing the hyperfine structure of the ODMR spectra. A weak external magnetic field ($B_\parallel \approx$ 5-10 G) was applied to separate the $m_s = -1$ and $m_s = +1$ electron spin transitions. We found NV centers with the characteristic triplet splitting of the ^{14}NV (with hyperfine splitting, $A = 2.2$ MHz) as well as with the ^{15}NV doublet ($A = 3.1$ MHz) [54], as indicated in Figure 3.2b. Of the 120 NVs identified on sample A, an ODMR signal was detected in 50, out of which 18 were ^{15}NV, 18 ^{14}NV, and there were 14 in which the isotope could not be reliably determined from the ODMR spectra. Similarly, of the 52 NVs identified on sample B, 34 were ^{15}NV, 3 were ^{14}NV, and the isotope could not be determined in 15 NVs. We attribute the different isotope occurrence ratios in sample A and B to different native ^{14}N content and different

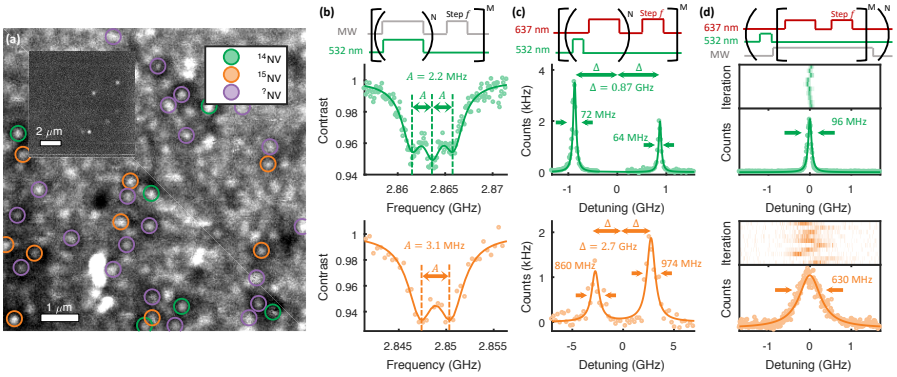

Figure 3.2: **Isotope characterization and optical measurements of NV centers from ^{14}N and ^{15}N. a**, A fluorescent confocal scan of sample A taken at 4 K, with labels indicating NV centers characterized as ^{14}NV, ^{15}NV, and a set with unresolvable hyperfine lines, labeled as $^{?}$NV. A scan a few microns below the implanted layer (inset) shows a lower NV density. **b-d**, Pulse sequences (top row) used for isotope characterisation and optical measurements, and representative measurement results for each isotope (green, middle row: ^{14}NV; orange, bottom row: ^{15}NV). **b**, Continuous wave (CW) ODMR measurements reveal the NV isotope. The ^{14}NV is characterized by $S = 1$ hyperfine transitions; the ^{15}NV by $S = 1/2$ hyperfine transitions. **c**, Interleaved red and green excitation probe the combined effect of short-timescale fluctuations and laser-induced spectral diffusion. The E_x and E_y ZPL transitions are visible for both isotopes; the ^{14}NV linewidths are narrower and show a smaller strain splitting than the ^{15}NV. **d**, Individual line scans of the ZPL in sample B reveal the linewidth free from laser-induced spectral diffusion. The summation of many repeated scans is broadened as a result of repump-laser-induced spectral diffusion.

implantation fluence.

3.4. Linewidth of optical transitions

Subsequently, we measured the linewidth of optical transitions of identified NV centers, recording photoluminescence excitation (PLE) spectra at low temperature (≈ 4 K). A tunable laser with a wavelength near 637 nm was scanned over the optical transition while detecting emitted photons in the phonon-sideband. We performed two types of measurements. First, a scan was made in which resonant excitation (637 nm) and green illumination (532 nm) were rapidly interleaved at each data point. The red excitation causes rapid optical spin pumping and ionization of the NV center. The green excitation provides repumping into the negative charge state and the $m_s = 0$ spin state. This measurement reveals the combined effect of short-time scale fluctuations and repump-laser-induced spectral diffusion in broadening the transition linewidth. Examples of the resulting traces are seen in Figure 3.2c.

Second, in sample B, an additional scan was performed to isolate the effect of short timescale fluctuations from repump-laser-induced diffusion. A single off-resonant repump was applied before sweeping the resonant laser at low power, as seen in Figure 3.2d. We applied microwaves on the spin resonances to prevent

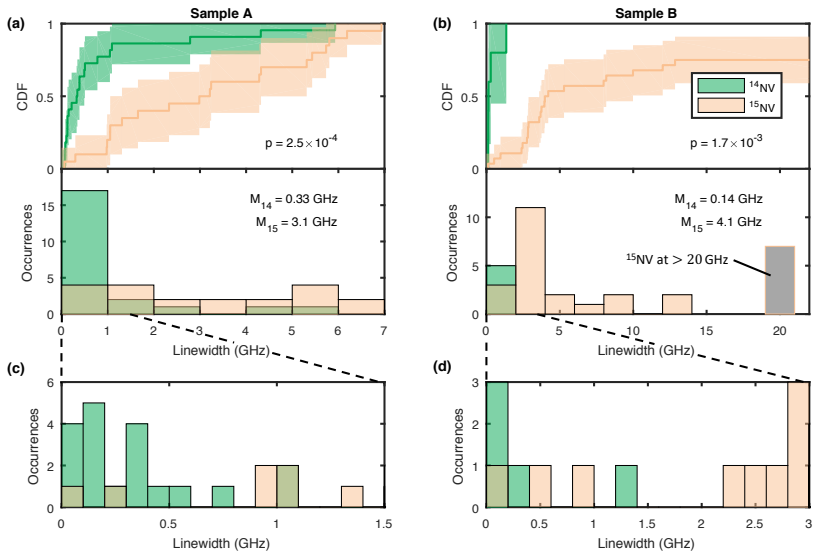

Figure 3.3: **Optical linewidths per isotope. a-b**, A summary of the optical linewidths identified in sample A (**a**) and sample B (**b**) from scans at the implantation depth. For sample B, that has comparatively few ^{14}NV centers at the implantation depth, we included three ^{14}NV centers found deeper in the diamond to enable a comparison between NVs formed from implanted versus native nitrogen. The distribution is represented as a cumulative distribution function (CDF, top), with the corresponding histogram shown below. The shaded region in the CDF indicates a 95% confidence interval calculated using Greenwood's formula. These data show that both diamonds supported narrow-linewidth NV centers, the majority of which originated from ^{14}NVs. While ^{15}NV do exhibit narrow lines, their median linewidth (M) is higher than for the ^{14}NV centers in both samples. We evaluate the probability to obtain the observed linewidths for ^{14}NV centers and ^{15}NV centers if the samples are drawn from the same distribution with a Wilcoxon Rank Sum test, finding a p-value of 2.5×10^{-4} in sample A and 1.7×10^{-3} in sample B. **c-d**, A magnification of the histograms shown in **a** and **b**.

optical pumping into a dark spin state during the sweeps [55]. Remaining traces in which the NV center ionized were excluded by applying a second scan over the resonance to check the charge state. If no resonance was observed, the preceding trace was disregarded. This scanning protocol was repeated many times to probe spectral diffusion through the resulting spread of the observed lines [12]. To extract the linewidth free from repump-laser-induced spectral diffusion, we performed a weighted average of linewidth values found from Lorentzian fits to each individual scan.

Figures 3.2c and d display representative resonant optical scans for the ^{14}NV and ^{15}NV centers, each showing two resonances corresponding to the two $m_s = 0$ orbital transitions E_x and E_y. Notably, while the ^{14}NV center (green, top row) exhibits a narrow optical linewidth with a full-width-at-half-maximum (FWHM) of 64 ± 4 MHz, the ^{15}NV linewidth (orange, bottom row) is broad, with a FWHM of 860 ± 236 MHz. The dynamics in the second scan type (Figure 3.2d) indicate that

both repump-induced fluctuations and a short-timescale mechanism broaden the ^{15}NV linewidth, but that repump-induced fluctuations are dominant in broadening beyond 200 MHz (see sec. 3.7.3).

To correlate the occurrence of narrow optical linewidths with the N isotope of the NV centers, we acquired an extensive data set using the data accumulation procedures described above. The resulting distributions of optical linewidths for both N isotopes are shown in Figure 3.3. Narrow optical linewidths in both samples can be attributed almost exclusively to NVs with a native ^{14}N host. In contrast, ^{15}NV centers exhibiting narrow optical linewidths are extremely rare, with a median linewidth for ^{15}NV centers of 3.1 GHz in sample A and 4.1 GHz in sample B.

Notably, in both datasets one NV center with a ^{15}N host was found that showed narrow optical linewidths (< 100 MHz). Given their low occurrence and the non-zero natural abundance of ^{15}N, the creation mechanism of these narrow-linewidth ^{15}NVs cannot be conclusively determined. Nevertheless, their presence demonstrates that ^{15}NV centers can exhibit coherent optical transitions. Therefore, we conclude that the difference in distribution of optical linewidths between ^{14}NVs and ^{15}NVs is not due to an intrinsic effect related to the isotope itself, but due to differences in the local environment resulting from the implantation process.

3.5. Local strain fields

Damage due to implantation may cause local strain fields. Axial strain results in an overall shift of the optical transition, while transverse strain will split the E_x and E_y transitions [54]. The distributions characterizing the strain for both NV isotopes are shown in Figure 3.4. The spread of the distribution in ZPL detuning representing axial strain for ^{15}NVs (44 GHz for sample A, 60 GHz for sample B) is wider than for ^{14}NVs (13 GHz for sample A, 5.6 GHz for sample B). Further, we found that ^{15}NVs exhibit higher transverse strain, manifested by greater splitting with a median of 5.4 GHz (10 GHz) compared to 1.7 GHz (4.3 GHz) for ^{14}NVs in sample A (B). Assuming a similar strain susceptibility for both isotopes, these results indicate that local damage around the implanted ^{15}NVs creates a more strained environment, providing further evidence that implantation-induced local damage is responsible for the broadened ^{15}NV linewidth. In addition, in both samples we observed a shift of the average ZPL frequency for ^{15}NV compared to ^{14}NV ZPLs, possibly due to an intrinsic dependency of the energy levels on the isotope as observed in other color centers [56, 57].

The data show indications of an increase in ^{14}NV density in the implantation layer in both samples (see sec. 3.7.4). We hypothesize that these ^{14}NV centers can be formed from naturally occurring nitrogen combining with vacancies created during implantation. Since they can be at greater distance from the main damage center near the stopping point of the nitrogen, these NV centers may be coherent and usable for quantum information purposes; more work is needed for a statistically significant correlation. However, these NVs would have worse positioning

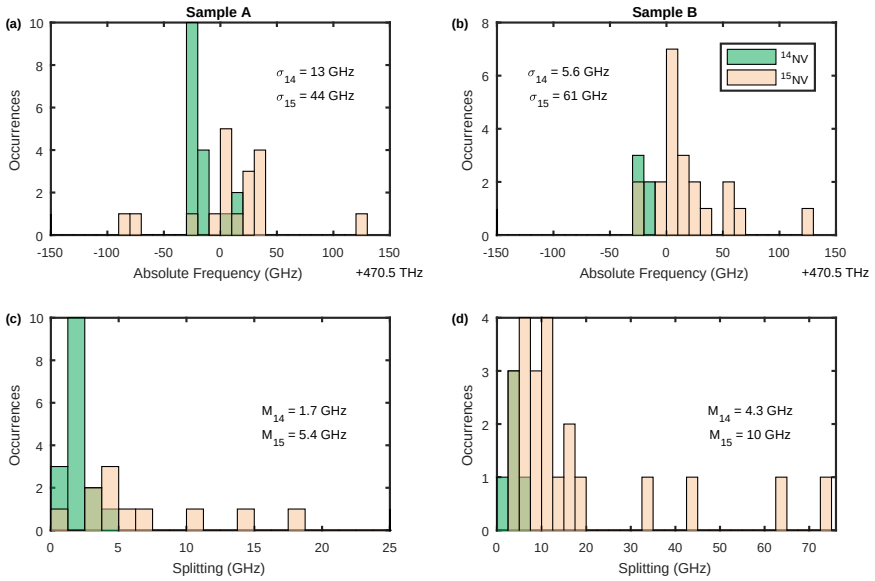

Figure 3.4: **Strain analysis. a-b**, The distribution of axial strain (measured by absolute average ZPL frequency) in NVs acquired from analysis of sample A (**a**) and sample B (**b**). The ^{15}NV ZPLs exhibit a larger spread in axial strain (standard deviation, σ) than the ^{14}NV ZPLs. **c-d**, The distribution of transverse strain (measured by half the splitting between E_x and E_y frequencies) in NV centers of sample A (**c**) and sample B (**d**). The ^{15}NV ZPLs show a greater median splitting (M) in both samples.

accuracy as their spatial distribution is set by arbitrarily positioned naturally occurring nitrogen in combination with the diffusion length of the vacancies generated during implantation.

3.6. Conclusions

In summary, the implanted nitrogen atoms in our study yield NV centers with predominantly broad optical lines (> 1 GHz) and substantially higher strain than NV centers formed from native nitrogen. These results indicate that implanted nitrogen atoms combined with an annealing process at high temperatures do not routinely produce NV centers with narrow optical linewidths. Vacancies produced in the implantation process may combine with existing nitrogen atoms to produce narrow NVs, but more work is needed for a statistically significant correlation. It is clear from this work that recipes for generating implanted NV centers should be reinvestigated, addressing local lattice damage associated with implanted nitrogen. In addition, other approaches for precisely controlling the NV centers' positions while causing minimal local damage can be further explored, such as employing 2D nitrogen-doped diamond layers combined with electron irradiation or ion implantation for vacancy production [58, 59] or laser writing strategies for creating

vacancies with 3D accuracy [60, 61].

3.7. Supplementary information and Methods

3.7.1. Samples and processing

Sample A

Sample A and the data-set for sample A were acquired and prepared at MIT. We used a type IIa chemical-vapour-deposition (CVD) grown diamond (Element Six), with a ⟨100⟩ crystal orientation. The nitrogen content is specified to be less than 5 ppb and is typically less than 1 ppb. The diamond contains a natural abundance of carbon isotopes. This sample was implanted with $^{15}N^{+}$ (minimum purity 98%) at 85 keV (fluence of 10^{9} N/cm^{2}) by Innovion Corporation. After implantation, the diamond underwent cleaning involving a tri-acid clean (boiling sulfuric, nitric and perchloric acids [1:1:1] for one hour) followed by a Piranha clean (sulfuric acid and hydrogen peroxide in a ratio of [3:1]). The sample was subsequently annealed at high temperatures [43]. During the annealing process the temperature was increased at a rate of 1 °C/min and held constant for 2 hours when temperatures reached 400 °C, 800 °C and 1200 °C respectively. The sample underwent the same acid treatment sequence following the annealing process.

Sample B

Sample B was prepared at Delft, with exception of an annealing procedure specified below. The data-set for sample B was acquired at Delft. As with sample A, we used a type IIa CVD grown diamond (Element Six), with a ⟨100⟩ crystal orientation. The diamond was cut, thinned and polished by Delaware Diamond Knives (DDK) into thin (∼14 μm) membranes, one of which is sample B. The membrane was implanted with $^{15}N^{+}$ at 400 keV (fluence of 10^{8} N/cm^{2}) by Innovion Corporation. For these ions, the stopping range is approximately 400 nm, as simulated using SRIM [52]. Subsequently, the sample underwent an acid clean in boiling sulfuric, nitric and perchloric acids [1:1:1] for one hour, and 15 minutes in a Piranha solution. Following cleaning, the sample was annealed at high temperatures [43] at Harvard University. During the annealing process the temperature was increased from room temperature to 400 °C over a 4 hours period, and then the temperature was held constant for 8 hours. Subsequently, the temperature was further increased to 800 °C over a 12 hours period, and held constant for 8 hrs. Finally, the temperature was further increased to 1100 °C and held constant for 2 hours. After annealing, the sample underwent the same acid treatments as before annealing. The sample was bonded to a fused silica substrate via Van der Waals forces [62]. The fused silica substrate contains integrated gold MW striplines for spin control as detailed in Ref. [62].

3.7.2. Methods

Sample A

Experiments were performed using a home-built scanning confocal microscope. The samples were cooled to 4 K using a closed-cycle helium cryostat (Montana Instru-

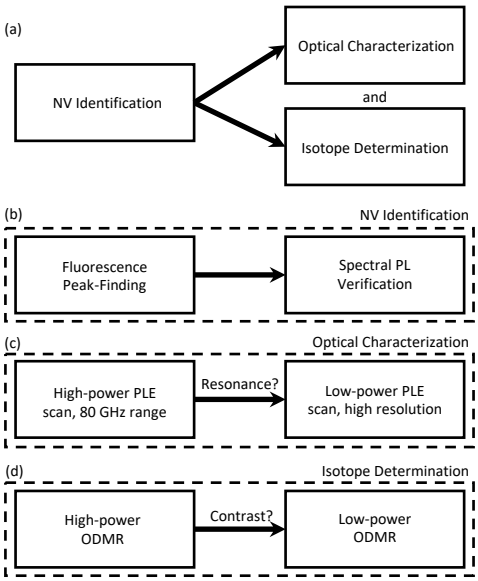

Figure 3.5: **Measurement sequence for sample A. (a)** The three parts of the experimental sequence: NV identification, optical characterization and isotope recognition are executed by an automated protocol. **(b)** Fluorescent peaks are identified after processing the image with a spatial band-pass filter and taking peaks above a certain threshold (more detail in the text). This yields many NV candidates that are tested for the presence of PL between 636-639 nm using a spectrometer to confirm the peak is from an NV. **(c)** Using the wavelength of the peak identified in **(b)**, we coarsely tune the resonant laser to the emitter and scan over the entire range allowed by the cavity (82 GHz) with high power to assure we do not miss the transition peak. Once found, we repeat the measurement with higher resolution and low enough power to avoid power-broadening. **(d)** For each NV center a low-power continuous wave (CW) ODMR spectrum is taken, to find the N isotope.

ments) and were imaged through a 0.9 NA vacuum objective. A Coherent Verdi G5 laser was used to generate 532 nm light and resonant red light tunable around 637 nm was generated by a New Focus Velocity tunable diode laser. Microwave (MW) signals were generated by a Rohde & Schwarz SMIQ06B signal generator and sent through a high-power amplifier (Mini-Circuits ZHL-16W-43+) before delivery to the sample via a wire soldered (15 µm diameter) across the surface. An Excelitas avalanche photodiode (APD) served as our single photon detector. Wavelength/frequency measurements were made with a Princeton Instruments Isoplane SCT 320 spectrometer and/or a WS7 HighFinesse wavelength meter (these two devices were calibrated relative to each other by scanning the Velocity laser through the wavelengths of interest). All digital signals used to produce pulse sequences were generated on a PulseBlaster ESR-Pro from SpinCore; additional analog control and photon counting were performed on a USB NI6343 from National Instruments. The automated measurement sequence for sample A is shown in Figure 3.5 in detail.

1. NV identification

	no ODMR contrast	no resolvable hyperfine	hyperfine resolved	failed	
PLE signal	59	14	36	1	**110**
no PLE signal	5	2	0	3	**10**
	64	**16**	**36**	**4**	**120**

Table 3.1: **Table summarizing all data for sample A.** This table has the numeric breakdown of all NVs reported. The bold numbers indicate a particular column or row summation. NVs that resulted in an error were either due to a hardware failure during the automated protocol or a peak that was detected in one scan but could not be found again (likely due to a false-positive originally).

Fluorescent spots were identified using a peak-detection algorithm on a confocal scan. The image was first filtered using a spatial band-pass filter (constructed with a "low-pass" Gaussian kernel with a full-width at half-maximum (FWHM) of 235 nm and a "high-pass" Gaussian kernel with a spatial FWHM of 700 nm). A peak is defined as a pixel that is greater than or equal to its 4 nearest neighbors and greater than the 4 second nearest neighbors. A threshold was calculated to be 1-2 standard deviations above the median pixel value. Only peaks that carried an intensity value above the calculated threshold were used in the experiment. Each image was inspected, and the threshold fine-tuned before continuing the experiment to ensure that every visible peak was located.

The fluorescent spots were validated by examining a PL spectrum under 532 nm excitation for a peak between 636 nm and 639 nm (the range in which we can tune our resonant laser). No peaks were found out of this range. We illuminated the sample with 300 µW of power while the spectrometer acquired a measurement with an exposure of 10 seconds (a relatively short amount of time compared to the optical characterization). Peaks were detected after noise removal using a similar technique as described above for the fluorescent spot detection.

2. Optical characterization

All photoluminescence excitation (PLE) measurements in this section will refer to a pulse sequence described in Figure 3.2c of the main text. The duration of the green repump was 2 µs with a power of about 300 µW. The collection bin was 10 µs with 3 µW of resonant illumination power that could be attenuated with optical-density (OD) filters. The frequency of the excitation was monitored continuously using the wavelength meter.

The first step in optical characterization was a PLE scan at high power (no attenuation with OD filters). For each ZPL peak identified, the laser was coarsely tuned to the ZPL frequency, then tuned across the full range of the Velocity laser's

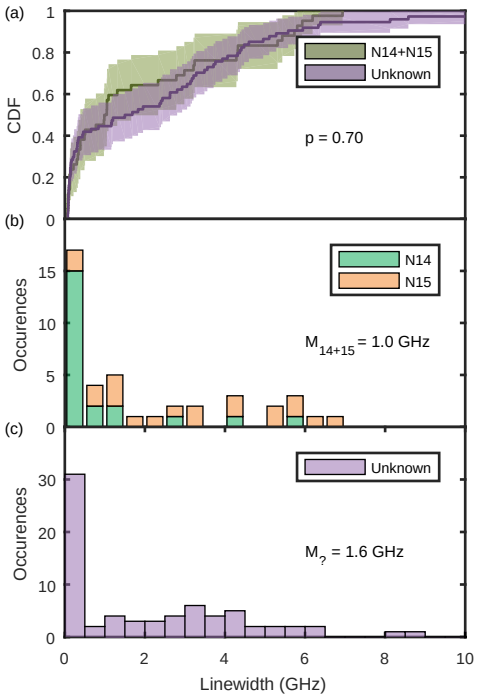

Figure 3.6: **Summary of all data for sample A. (a)** A CDF representing the distributions of unknown isotope to known isotope ZPL linewidths. A similar shape indicates that both sample sets are drawn from the same distribution indicating there is no inherent bias towards sampling ^{14}NV or ^{15}NV. The probability to obtain these results if the samples are drawn from the same distribution (p) is evaluated by a Wilcoxon rank-sum test. **(b)** A stacked histogram showing all the ^{14}NV and ^{15}NV ZPL linewidths. The median linewidth (M) is indicated. **(c)** A histogram showing the linewidths for the set of ZPLs with an unknown host isotope.

external cavity range (82 GHz) with a resolution of 275 MHz. This sequence was averaged 10^4 times at each frequency to ensure that the SNR is large enough to find an NV signal (Table 3.1 shows the statistics corresponding to optical and isotope recognition of our NV set). The automated protocol roughly identified statistically relevant peaks (nearly all locations that were NVs revealed two such peaks; one for E_x and E_y). A sum of Gaussian lineshapes were fit to the data-set based on the number of peaks detected. The location and width of the peak were all recorded for use in the high-resolution scans.

Next, the high-resolution scans were performed using a low power red excitation (300 nW, obtained with an OD filter) to avoid power-broadening. To account for the lower excitation power, we performed 10^6 averages. The scan range and resolution were determined by the location and width of the previous high-power

scan. Gaussian lineshapes were fit to the final low-power, high-resolution scans in the same manner as for the high-power scans. The center ZPL position is midway between the E_x and E_y transitions, and the splitting is half the distance between them.

3. Isotope recognition

The final step in the measurement protocol is to measure a continuous-wave (CW) optically-detected magnetic resonance (ODMR) that probes the NV fine structure. We determined the emitter's orientation by sweeping a strong MW field over each of the 4 possible orientations (pre-characterized prior to each run). Once determined, we iteratively lowered the MW power until the ODMR signal had resolvable hyperfine transitions (up to 10 dB lower than the power used to determine the orientation). The NV isotope was determined by inspection of the multiplicity of the number of dips in the ODMR spectrum. Almost half of the NVs identified (showing both PLE and ODMR signals) had unidentifiable ODMR spectra. Figure 3.6 shows a summary of all identified emitters. It is important to note that the distribution of both categorized (^{14}NV and ^{15}NV) and un-categorized NVs follow the same distribution (as seen by the overlapping CDF in Figure 3.6a and the same shape of histograms in Figure 3.6b-c).

Sample B

Sample B is maintained at a temperature of 4 K in a closed-cycle cryostation (Montana Instruments). The optical and electronic elements of the experimental setup are as previously described in Ref. [63]. We describe the measurement sequence for sample B, schematically presented in Figure 3.7, in detail.

1. NV identification

Fluorescent spots were identified by inspection of a confocal scan. On these spots a spatial optimization in three dimensions was performed. The automated protocol proceeded if the spot could be fit with a Gaussian shape. Next, a CW ODMR measurement was performed at high microwave power. The high power was used to maximize the visibility of an ODMR dip. The dip was fit with a Gaussian curve to find the resonance frequency that was used in the remainder of the protocol for microwave driving. If spatial optimization was successful and an ODMR dip observed, a spot was marked as an NV center. Out of 52 spots identified as an NV center following this protocol, five contained two NV centers. Because a unique link between ODMR for isotope-recognition and the optical linewidth was not made, these NVs were left out of the final analysis. NVs with both narrow and broad optical linewidths were identified in these five spots, as well as at least one ^{14}NV.

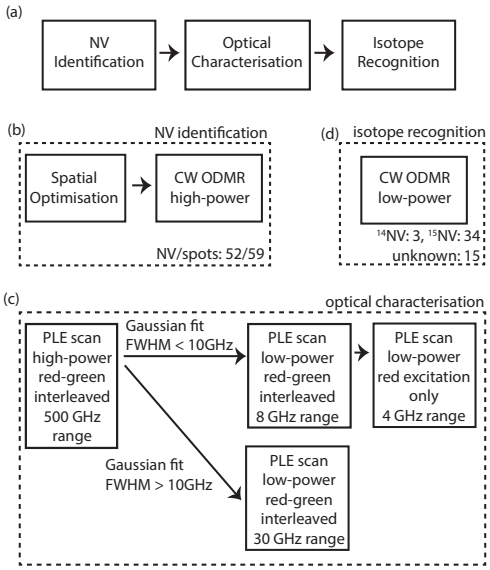

Figure 3.7: **Measurement sequence for sample B. (a)** The three parts of the experimental sequence: NV identification, optical characterization and isotope recognition are executed by an automated protocol. **(b)** Out of a total of 64 fluorescent spots at the implantation depth and deeper in the sample, 57 were identified as NV centers, based on a Gaussian spatial profile and the presence of an ODMR dip. 52 of these spots contained single NV centers **(c)** After a broad range scan to determine the position of the optical resonances, separate sequences are performed for very broad linewidths (> 10 GHz) and the other linewidths, to restrict measurement time. Measurements probing the linewidth free from spectral diffusion (refered to as low-power red excitation only) are performed only if the linewidth was not very broad. **(d)** For each NV center a low-power CW ODMR spectrum is taken, to find the N isotope.

2. Optical characterization

In this section we detail the optical characterization for sample B as described in Figure 3.2c-d of the main text. The first step in optical characterization was a PLE scan at high power, with red and green excitation interleaved for each step. We applied 100 nW of red power (measured before the objective) for 100 µs, followed by 100 µW green power for 10 µs and a 10 µs wait time. This sequence was repeated for a total integration time of 10 ms for each data point. The scan was carried out over a range of 500 GHz, with a resolution of approximately 10 MHz. The laser wavelength was monitored after each laser frequency step using a wavelength meter. During all optical scans microwave driving was applied to observe optical lines for all spin projections in the red-green interleaved scan, and to prevent optical pumping in the scans probing short-timescale dynamics. Automated protocols were used to fit a Gaussian lineshape to the peaks, determining the location of the two highest peaks. The center ZPL position is midway between the highest peaks, and the strain splitting is the half distance. For four NVs no optical resonances were found in the 500 GHz range scanned in the automated protocol (between 470.3 THz and 470.8 THz). For three of these, optical resonances were

	PLE signal	no PLE signal	
ODMR isotope resolvable	35	0	**35**
ODMR isotope unresolvable	16	1	**17**
no ODMR contrast	1	4	**5**
	51	**5**	**57**

Table 3.2: **Table summarizing all data for sample B.** This table has the numeric breakdown of all fluorescent spots reported, at the implantation depth (52 spots) and deeper in the diamond (5 NVs). Not included are two data-points for which spatial optimization was not successful, and 5 spots that contained more than one NV. The bold numbers indicate a particular column or row summation.

found manually outside this range (around 469.7 THz, 470.2 THz, and 471.1 THz). For one NV no optical lines were found in a range from 469.4 THz to 471.4 THz.

We continued with scans around the resonances, using a low power red excitation (12 nW) to avoid any power-broadening. To restrict measurement time, the performed measurements depend on the fitted linewidth in the large-range scan as follows. If the fitted linewidth in the broad-range scan was very broad (> 10 GHz), a PLE scan with interleaved red and green was subsequently carried out over a range of approximately 30 GHz. The resolution of this scan was 30 MHz. The timing of the sequence is as described for the broad-range scan. If the fitted linewidth was < 10 GHz, we performed a single PLE scan interleaving red and green excitation for each data point over a range of 8 GHz (resolution 4 MHz, same timings as the broad-range scan). Next, we proceeded with 30 scans with red excitation, with repumping only in between each scan. The range of these scans was 4 GHz, with a resolution of approximately 4 MHz. The integration time for each pixel was 20 ms, and the total scan time over the full 4 GHz range was approximately 40 seconds. After each scan we performed a second scan over the resonance to determine if the NV ionized during the original scan. We fit a Lorentzian to the non-ionized traces, and extract the FWHM, $\bar{\gamma}$, from their weighted average:

$$\bar{\gamma} = \frac{\sum_i \gamma_i \sigma_i^{-2}}{\sum_i \sigma_i^{-2}}, \tag{3.1}$$

where γ_i are the fitted FWHM of the individual traces, and σ_i the corresponding standard error of the fit parameter.

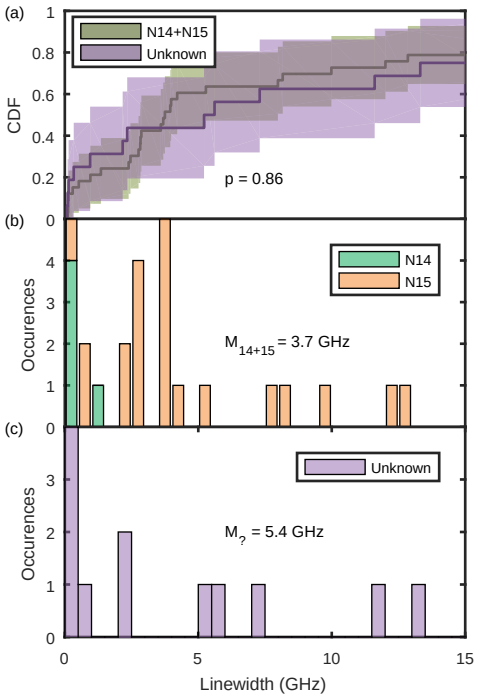

Figure 3.8: **Summary of all data for sample B. (a)** A CDF representing the distributions of unknown isotope to known isotope ZPL linewidths. A similar shape indicates that both sample sets are drawn from the same distribution indicating there is no inherent bias towards sampling ^{14}NV or ^{15}NV. The probability to obtain these results if the samples are drawn from the same distribution (p) is evaluated by a Wilcoxon rank-sum test. **(b)** A stacked histogram showing the all ^{14}NV and ^{15}NV ZPL linewidths. The median linewidth (M) is indicated. **(c)** A histogram showing the linewidths for the set of ZPLs with an unknown host isotope. The histograms in **(c)** and **(d)** do not show data for 7 ^{15}NV and 4 NVs with unknown isotope as they are out of the range (> 15 GHz).

3. Isotope recognition

The final step in the measurement protocol was an ODMR measurement probing the NV fine structure, scanning around the resonance detected during the NV identification (step 1). This ODMR measurement was performed at 7 dB attenuation relative to the ODMR measurement during NV characterization, to avoid power-broadening. The NV isotope was determined by inspection of the multiplicity of the number of dips in the ODMR spectrum, and confirmed by the best goodness of fit out of fits with Gaussian dips with hyperfine splittings fixed to the ^{14}NV or ^{15}NV values. The isotope could not be reliably identified by inspection in 15 NV centers located at the implantation depth. We note that these contained both NV centers with broad (> 500 MHz, 13 NVs) and narrow (< 500 MHz, 2 NVs) linewidths. Table

3.2 shows a summary of the PLE and ODMR contrast for spots at the implantation depth and deeper in the diamond. In Fig. 3.8 a summary of the optical linewidths is shown, including the NVs with unknown isotopes. Similar to the observations for sample A, we find that the cumulative density function for the unknown isotopes and the combined ^{14}NV and ^{15}NV data overlap.

3.7.3. Characterization of repump laser-induced spectral diffusion

On sample B we performed scans to isolate short timescale fluctuations from repump laser-induced spectral diffusion (Figure 3.2(d) of the main text). For each NV center we performed 30 consecutive scans, with a green repump laser pulse applied only in between the scans. The scans in which the NV center did not ionize are selected. We fit a Lorentzian curve to the resonance in each scan and calculate the weighted average for each NV center (see Eq. 3.1). We also fit the sum of the scans with a Gaussian curve, extracting the FWHM including repump laser-induced spectral diffusion. When correlating the two analyses, as shown in Figure 3.9, we find that the Lorentzian linewidths are mostly less than 200 MHz, while further broadening in the linewidth can be attributed to laser-induced spectral diffusion.

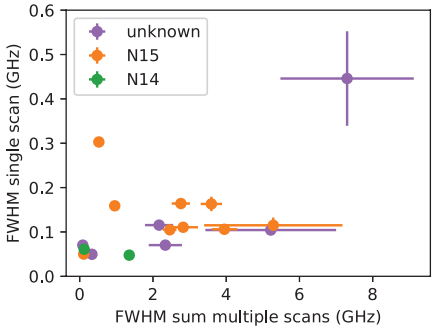

Figure 3.9: **Optical linewidths from scans with red excitation only.** Consecutive scans over a single resonance are performed as described in the text. The FWHM of the optical linewidth in individual scans (y-axis) is correlated to the FWHM of the summed scans including repump laser-induced spectral diffusion (x-axis). We conclude that the Lorentzian linewidths are mostly less than 200 MHz, while further broadening in the linewidth can be attributed to laser-induced spectral diffusion. This figure contains data for NV centers at the implantation depth with linewidths < 10 GHz (Figure 3.7).

Protocols using resonant charge repumping [25] and real-time monitoring of the transition frequency [26] have been used to reduce linewidths broadened to <200 MHz by slow spectral diffusion. However, for larger broadening, and especially for the very broad (>1 GHz) linewidths for ^{15}NVs, such a repump scheme is challenging as after each remaining frequency jump the resonances shift significantly, complicating the locating of the new resonances within an acceptable time.

3.7.4. NV densities

In sample A (see confocal scans in Figure 3.2a of the main text), the NV areal densities estimated from the verified isotopes at the implantation depth are at least 3.9×10^{-2} ^{14}NVs/μm^2 and 3.5×10^{-2} ^{15}NVs/μm^2. When assuming that the isotope distribution over the NVs with unknown isotope follows the same distribution as for the known NVs (this assumption is supported by the overlapping linewidth distributions in Figure 3.6), the areal density estimates are 5.1×10^{-2} ^{14}NVs/μm^2 and 4.7×10^{-2} ^{15}NVs/μm^2. This corresponds to a conversion efficiency of implanted ^{15}N to NV of approximately 3.5%-4.7%. At a scan deeper in the sample over the same area (Figure 2a, inset) we found 3 NVs, that we assume to be ^{14}NV given their location in the diamond well below the implantation depth. The native areal density of ^{14}NVs that we estimate from this is 3×10^{-2} ^{14}NVs/μm^2.

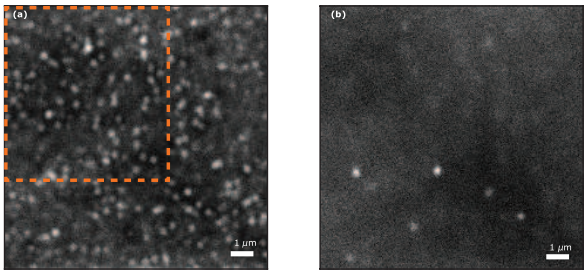

Figure 3.10: **Confocal scans of sample B (a)** at the implantation depth and **(b)** at ≈5 μm under the diamond surface. The orange box indicates the approximate region at the implantation depth in which fluorescent spots were characterized.

Confocal scans of sample B are shown in Figure 3.10, at the implantation depth and deeper into the sample to illustrate the change in NV density due to implantation. The confocal scan at the implantation depth (∼ 400 nm, Figure 3.10a) displays around ~ 180 fluorescent spots. We characterized 59 of these spots from the highlighted region in Figure 3.10a, identifying 57 NV centers (47 single NVs in a confocal spot and 5 spots with two NVs). We are able to determine the isotope for 37 NVs, 3 out of which are ^{14}NVs, and 34 are ^{15}NVs. From this, a lower-bound estimate of the ^{14}NV areal density after implantation is 4×10^{-2} ^{14}NVs/μm^2. We estimate the ^{15}NV areal density to be at least 5×10^{-1} ^{15}NVs/μm^2. When assuming that the unknown isotopes follow the distribution of isotopes for the known isotopes (as for sample A, this is supported by the overlapping linewidth distributions in Figure 3.8), the areal density estimates are 6×10^{-2} ^{14}NVs/μm^2 and 7×10^{-1} ^{15}NVs/μm^2. This corresponds to an estimated conversion efficiency of implanted ^{15}N to NV of approximately 50%-70%. We attribute differences in conversion efficiencies between sample A and sample B to the difference in implantation parameters [64].

We characterized 5 out of 6 bright fluorescent spots in the deep scan (≈ 5 μm depth (Figure 3.10b). All 5 spots were identified as NVs, and all displayed narrow

linewidths in the red-green interleaved scan. The isotope were found to be ^{14}N for 3 out of 5 NVs, whereas the isotope could not be reliably determined from the ODMR measurement for 2 NVs (this is a comparable ratio of known versus undetermined isotopes as at the implantation depth). Because their location in the diamond was well below the implantation depth, these findings strongly suggest that these fluorescent spots are naturally occurring ^{14}NV. A best estimate of the ^{14}NV areal density before implantation is therefore 3×10^{-2} ^{14}NVs/μm^2. Although the sample sizes are small, comparing the estimated ^{14}NV densities at the implantation depth and deeper in the diamond we find indications that ^{14}NVs at the implantation depth are created during implantation in both sample A and B.

Author contributions

On the side of the TU Delft: SBD, MJD, THT and RH devised the project and experiments. SBD and MJD performed the experiments. SBD, MJD, THT and RH analysed the data. SBD, MJD, MR, MIJ developed software for the experiments. MJD and MR fabricated samples. SBD and AG performed initial measurements. MW, EB and SLM and DRE performed the work on the side of MIT. SBD, MW wrote the manuscript with help from MJD, EB and input from all authors.

References

[1] Aharonovich, I., Englund, D. & Toth, M., *Solid-state single-photon emitters,* Nat. Photonics **10**, 631 (2016).

[2] Awschalom, D. D., Hanson, R., Wrachtrup, J. & Zhou, B. B., *Quantum technologies with optically interfaced solid-state spins,* Nat. Photonics **12**, 516 (2018).

[3] Lodahl, P., *Quantum-dot based photonic quantum networks,* Quantum Sci. Technol. **3**, 13001 (2018).

[4] Wehner, S., Elkouss, D. & Hanson, R., *Quantum Internet: a vision for the road ahead,* Science **362**, 303 (2018).

[5] Bar-Gill, N., Pham, L. M., Jarmola, A., Budker, D. & Walsworth, R. L., *Solid-state electronic spin coherence time approaching one second,* Nat. Commun. **4**, 1743 (2013).

[6] Abobeih, M. H. *et al.*, *One-second coherence for a single electron spin coupled to a multi-qubit nuclear-spin environment,* Nat. Commun. **9**, 2552 (2018).

[7] Kalb, N. *et al.*, *Entanglement Distillation between Solid-State Quantum Network Nodes,* Science **356**, 928 (2017).

[8] Waldherr, G. *et al.*, *Quantum error correction in a solid-state hybrid spin register,* Nature **506**, 204 (2014).

[9] Cramer, J. *et al.*, *Repeated quantum error correction on a continuously encoded qubit by real-time feedback,* Nat. Commun. **7**, 11526 (2016).

[10] Lovchinsky, I. *et al.*, *Nuclear magnetic resonance detection and spectroscopy of single proteins using quantum logic,* Science **351**, 836 (2016).

[11] Robledo, L. *et al.*, *High-fidelity projective read-out of a solid-state spin quantum register,* Nature **477**, 574 (2011).

[12] Fu, K.-M. C. *et al.*, *Observation of the Dynamic Jahn-Teller Effect in the Excited States of Nitrogen-Vacancy Centers in Diamond,* Phys. Rev. Lett. **103**, 256404 (2009).

[13] Goldman, M. L. *et al.*, *State-selective intersystem crossing in nitrogen-vacancy centers,* Phys. Rev. B **91**, 165201 (2015).

[14] Tamarat, P. *et al.*, *Stark shift control of single optical centers in diamond,* Phys. Rev. Lett. **97**, 083002 (2006).

[15] Batalov, A. *et al.*, *Temporal coherence of photons emitted by single nitrogen-vacancy defect centers in diamond using optical rabi-oscillations,* Phys. Rev. Lett. **100**, 077401 (2008).

[16] Robledo, L., Bernien, H., van Weperen, I. & Hanson, R., *Control and coherence of the optical transition of single nitrogen vacancy centers in diamond,* Phys. Rev. Lett. **105**, 177403 (2010).

[17] Bernien, H. *et al.*, *Two-photon quantum interference from separate nitrogen vacancy centers in diamond,* Phys. Rev. Lett. **108**, 043604 (2012).

[18] Sipahigil, A. *et al.*, *Quantum Interference of Single Photons from Remote Nitrogen-Vacancy Centers in Diamond,* Phys. Rev. Lett. **108**, 143601 (2012).

[19] Bernien, H. *et al.*, *Heralded entanglement between solid-state qubits separated by three metres.* Nature **497**, 86 (2013).

[20] Manson, N. B., Harrison, J. P. & Sellars, M. J., *Nitrogen-vacancy center in diamond: Model of the electronic structure and associated dynamics,* Phys. Rev. B **74**, 104303 (2006).

[21] Fu, K.-M. C., Santori, C., Barclay, P. E. & Beausoleil, R. G., *Conversion of neutral nitrogen-vacancy centers to negatively charged nitrogen-vacancy centers through selective oxidation,* Appl. Phys. Lett. **96**, 121907 (2010).

[22] Orwa, J. O. *et al.*, *Engineering of nitrogen-vacancy color centers in high purity diamond by ion implantation and annealing,* J. Appl. Phys. **109**, 083530 (2011).

[23] Santori, C. *et al.*, *Nanophotonics for quantum optics using nitrogen-vacancy centers in diamond,* Nanotechnology **21**, 274008 (2010).

[24] Faraon, A., Santori, C., Huang, Z., Acosta, V. M. & Beausoleil, R. G., *Coupling of nitrogen-vacancy centers to photonic crystal cavities in monocrystalline diamond,* Phys. Rev. Lett. **109**, 033604 (2012).

[25] Siyushev, P. *et al.*, *Optically controlled switching of the charge state of a single nitrogen-vacancy center in diamond at cryogenic temperatures,* Phys. Rev. Lett. **110**, 167402 (2013).

[26] Hensen, B. *et al.*, *Loophole-free bell inequality violation using electron spins separated by 1.3 kilometres,* Nature **526**, 682 (2015).

[27] Pezzagna, S., Rogalla, D., Wildanger, D., Meijer, J. & Zaitsev, A., *Creation and nature of optical centres in diamond for single-photon emission-overview and critical remarks,* New J. Phys. **13**, 035024 (2011).

[28] Mouradian, S. L. *et al.*, *Scalable integration of long-lived quantum memories into a photonic circuit,* Phys. Rev. X **5**, 031009 (2015).

[29] Schröder, T. *et al.*, *Review Article: Quantum Nanophotonics in Diamond,* J. Opt. Soc. Am. B **33**, 65 (2016).

[30] Gaebel, T. *et al.*, *Room-temperature coherent coupling of single spins in diamond,* Nat. Phys. **2**, 408 (2006).

[31] Dolde, F. *et al.*, *Room-temperature entanglement between single defect spins in diamond,* Nat. Phys. **9**, 139 (2013).

[32] Yamamoto, T. *et al.*, *Strongly coupled diamond spin qubits by molecular nitrogen implantation,* Phys. Rev. B **88**, 201201 (2013).

[33] Faraon, A., Barclay, P. E., Santori, C., Fu, K.-M. C. & Beausoleil, R. G., *Resonant enhancement of the zero-phonon emission from a colour centre in a diamond cavity,* Nat. Photonics **5**, 301 (2011).

[34] Hausmann, B. J. M. *et al.*, *Coupling of NV centers to photonic crystal nanobeams in diamond,* Nano Lett. **13**, 5791 (2013).

[35] Lee, J. C. *et al.*, *Deterministic coupling of delta-doped nitrogen vacancy centers to a nanobeam photonic crystal cavity,* Appl. Phys. Lett. **105**, 261101 (2014).

[36] Li, L. *et al.*, *Coherent spin control of a nanocavity-enhanced qubit in diamond.* Nat. Comm. **6**, 6173 (2015).

[37] Riedrich-Möller, J. *et al.*, *Nanoimplantation and Purcell enhancement of single nitrogen-vacancy centers in photonic crystal cavities in diamond,* Appl. Phys. Lett. **106**, 221103 (2015).

[38] Riedel, D. *et al.*, *Deterministic enhancement of coherent photon generation from a nitrogen-vacancy center in ultrapure diamond,* Phys. Rev. X **7**, 031040 (2017).

[39] Lea-Wilson, M. A., Lomer, J. N. & Van Wyk, J. A., *Electron spin resonance of the R4/W6 defect in irradiated diamond,* Philos. Mag. B **72**, 81 (1995).

[40] Naydenov, B. *et al.*, *Increasing the coherence time of single electron spins in diamond by high temperature annealing,* Appl. Phys. Lett. **97**, 242511 (2010).

[41] Yamamoto, T. *et al.*, *Extending spin coherence times of diamond qubits by high-temperature annealing,* Phys. Rev. B **88**, 075206 (2013).

[42] Deák, P., Aradi, B., Kaviani, M., Frauenheim, T. & Gali, A., *Formation of NV centers in diamond: A theoretical study based on calculated transitions and migration of nitrogen and vacancy related defects,* Phys. Rev. B **89**, 075203 (2014).

[43] Chu, Y. *et al.*, *Coherent optical transitions in implanted nitrogen vacancy centers.* Nano Lett. **14**, 1982 (2014).

[44] Rabeau, J. R. *et al.*, *Implantation of labelled single nitrogen vacancy centers in diamond using15N,* Appl. Phys. Lett. **88**, 023113 (2006).

[45] Ofori-Okai, B. K. *et al.*, *Spin properties of very shallow nitrogen vacancy defects in diamond,* Phys. Rev. B **86**, 081406 (2012).

[46] Naydenov, B. *et al.*, *Enhanced generation of single optically active spins in diamond by ion implantation,* Appl. Phys. Lett. **96**, 163108 (2010).

[47] Toyli, D. M., Weis, C. D., Fuchs, G. D., Schenkel, T. & Awschalom, D. D., *Chip-scale nanofabrication of single spins and spin arrays in diamond.* Nano Lett. **10**, 3168 (2010).

[48] Yamamoto, T. *et al.*, *Isotopic identification of engineered nitrogen-vacancy spin qubits in ultrapure diamond,* Phys. Rev. B **90**, 081117 (2014).

[49] Becker, S., Raatz, N., Jankuhn, S., John, R. & Meijer, J., *Nitrogen implantation with a scanning electron microscope,* Sci. Rep. **8**, 1 (2018).

[50] Y. Chu, private communication.

[51] De Oliveira, F. F. *et al.*, *Tailoring spin defects in diamond by lattice charging,* Nat. Commun. **8**, 15409 (2017).

[52] Ziegler, J. F., Ziegler, M. & Biersack, J., The Stopping and Range of Ions in Matter (SRIM-2013, http://www.srim.org/).

[53] Davies, G., Lawson, S. C., Collins, A. T., Mainwood, A. & Sharp, S. J., *Vacancy-related centers in diamond,* Phys. Rev. B **46**, 13157 (1992).

[54] Doherty, M. W. *et al.*, *The nitrogen-vacancy colour centre in diamond,* Phys. Rep. **528**, 1 (2013).

[55] Tamarat, P. *et al.*, *Spin-flip and spin-conserving optical transitions of the nitrogen-vacancy centre in diamond,* New J. Phys. **10**, 045004 (2008).

[56] Dietrich, A. *et al.*, *Isotopically varying spectral features of silicon-vacancy in diamond,* New J. Phys. **16**, 113019 (2014).

[57] Ekimov, E. A. *et al.*, *Germanium–vacancy color center in isotopically enriched diamonds synthesized at high pressures,* JETP Lett. **102**, 701 (2015).

[58] Ohno, K. *et al.*, *Engineering shallow spins in diamond with nitrogen delta-doping,* Appl. Phys. Lett. **101**, 82413 (2012).

[59] Ohno, K. *et al.*, *Three-dimensional localization of spins in diamond using 12 C implantation,* Appl. Phys. Lett. **105**, 052406 (2014).

[60] Chen, Y. C. *et al.*, *Laser writing of coherent colour centres in diamond,* Nat. Photonics **11**, 77 (2017).

[61] Chen, Y.-C. *et al.*, *Laser writing of individual atomic defects in a crystal with near-unity yield,* arXiv:1807.04028 (2018).

[62] Bogdanovic, S. *et al.*, *Robust nano-fabrication of an integrated platform for spin control in a tunable microcavity,* APL photonics **2**, 126101 (2017).

[63] Blok, M. S. *et al.*, *Manipulating a qubit through the backaction of sequential partial measurements and real-time feedback,* Nat. Phys. **10**, 189 (2014).

[64] Pezzagna, S., Naydenov, B., Jelezko, F., Wrachtrup, J. & Meijer, J., *Creation efficiency of nitrogen-vacancy centres in diamond,* New J. Phys. **12**, 065017 (2010).

4

Entanglement of dark electron-nuclear spin defects in diamond.

M. J. Degen*, S. J. H. Loenen*, H. P. Bartling, C. E. Bradley, A. L. Meinsma, M. Markham, D. J. Twitchen, T. H. Taminiau

A promising approach for multi-qubit quantum registers is to use optically addressable spins to control multiple dark electron-spin defects in the environment. While recent experiments have observed signatures of coherent interactions with such dark spins, it is an open challenge to realize the individual control required for quantum information processing. Here we demonstrate the heralded initialisation, control and entanglement of individual dark spins associated to multiple P1 centers, which are part of a spin bath surrounding a nitrogen-vacancy center in diamond. We realize projective measurements to prepare the multiple degrees of freedom of P1 centers - their Jahn-Teller axis, nuclear spin and charge state - and exploit these to selectively access multiple P1s in the bath. We develop control and single-shot readout of the nuclear and electron spin, and use this to demonstrate an entangled state of two P1 centers. These results provide a proof-of-principle towards using dark electron-nuclear spin defects as qubits for quantum sensing, computation and networks.

The results in this chapter have been submitted for publication; arXiv:2011.09874.
*Equally contributing authors.

4.1. Introduction

Optically active defects in solids provide promising qubits for quantum sensing [1], quantum-information processing [2–4], quantum simulations [5, 6] and quantum networks [7–9]. These defects, including the nitrogen-vacancy (NV) and silicon-vacancy (SiV) centers in diamond and various defects in silicon-carbide [10–12], combine long spin coherence times [4, 13–18], high-quality control and readout [2–4, 14, 19–21], and a coherent optical interface [7–9, 15, 19, 22].

Larger-scale systems can be realized by entangling multiple defects together through long-range optical network links [7–9] and through direct magnetic coupling, as demonstrated for a pair of ion-implanted NV centers [23, 24]. The number of available spins can be further extended by controlling nuclear spins in the vicinity. Multi-qubit quantum registers [4, 24–27], quantum error correction [2, 3], enhanced sensing schemes [28], and entanglement distillation [29] have been realized using nuclear spins.

The ability to additionally control dark electron-spin defects that cannot be directly detected optically would open new opportunities. Examples are studying single defect dynamics [30], extended quantum registers, enhanced sensing protocols [28, 31, 32] and spin chains for quantum computation architectures [33–36]. Two pioneering experiments reported signals consistent with an NV center coupled to a single P1 center (a dark substitutional nitrogen defect) [37, 38], but the absence of the expected P1 electron-spin resonance signal [39] and later results revealing identical signals due to NV-^{13}C couplings in combination with an excited state anti-crossing [40], make these assignments inconclusive. Recent experiments have revealed signatures of coherent interactions between NV centers and individual dark electron-spin defects, including P1 centers [41–43], N2 centers [44] and not-yet-assigned defects [31, 45–49]. Those results have revealed the prospect of using dark spin defects as qubits. However, high-quality initialisation, measurement and control of multi-qubit quantum states is required to exploit such spins as a quantum resource.

Here we demonstrate the control and entanglement of individual P1 centers that are part of a bath surrounding an NV center in diamond (Fig. 4.1a). A key property of the P1 center is that, in addition to its electron spin, it exhibits three extra degrees of freedom: the Jahn-Teller axis, a nuclear spin, and the charge state [50–52]. Underlying our selective control of individual centers is the heralded preparation of specific configurations of these additional degrees of freedom for multiple P1 centers through projective measurements. In contrast, all previous experiments averaged over these additional degrees of freedom [41, 42, 53]. We use this capability to develop initialisation, single-shot readout and control of the electron and nuclear spin states of multiple P1s, and investigate their spin relaxation and coherence times. Finally, we demonstrate the potential of these dark spins as a qubit platform by realizing an entangled state between two P1 electron spins through their direct magnetic-dipole coupling.

4.2. A spin bath with multiple degrees of freedom.

We consider a bath of P1 centers surrounding a single NV center at 3.3 K (Fig. 4.1a). The diamond is isotopically purified with an estimated ^{13}C concentration of 0.01%. The P1 concentration is estimated to be $\sim$ 75 ppb (see section 4.9.4). Three P1 charge states are known [51, 52]. The experiments in this work detect the neutral charge state and do not generate signal for the positive and negative charge states. In addition to an electron spin ($S = 1/2$), the P1 center exhibits a ^{14}N nuclear spin ($I = 1$, 99.6% natural abundance) and a Jahn-Teller (JT) distortion, which results in four possible symmetry axes due to the elongation of one of the four N-C bonds [54]. Both the ^{14}N state and the JT axis generally fluctuate over time [55–57]. The Hamiltonian for a single neutrally-charged P1 defect in one of the four JT axis $i \in$ {A,B,C,D} is [50]:

$$H_{\mathbf{i},\mathrm{P1}} = \gamma_e \vec{B} \cdot \vec{S} + \gamma_n \vec{B} \cdot \vec{I} + \vec{I} \cdot \mathbf{P_i} \cdot \vec{I} + \vec{S} \cdot \mathbf{A_i} \cdot \vec{I}, \tag{4.1}$$

where γ_e (γ_n) is the electron (^{14}N) gyromagnetic ratio, $\vec{B}$ the external magnetic field vector, $\vec{S}$ and $\vec{I}$ are the electron spin-1/2 and nuclear spin-1 operator vectors, and $\mathbf{A_i}$ ($\mathbf{P_i}$) the hyperfine (quadrupole) tensor. We label the ^{14}N ($m_I \in -1, 0, +1$) and JT states as $|m_I, i\rangle$, and the electron spin states as $|\uparrow\rangle$ and $|\downarrow\rangle$. For convenience, we use the spin eigenstates as labels, while the actual eigenstates are, to some extent, mixtures of the ^{14}N and electron spin states.

We probe the bath surrounding the NV by double electron-electron resonance (DEER) spectroscopy [41, 42, 45, 47, 53]. The DEER sequence consists of a spin echo on the NV electron spin, which decouples it from the environment, plus a simultaneous π-pulse that selectively recouples resonant P1 centers. Figure 4.1b reveals a complex spectrum. The degeneracy of three of the JT axes is lifted by a purposely slightly tilted magnetic field with respect to the NV axis ($\theta \approx 4°$). In combination with the long P1 dephasing time ($T_2^* \sim 50$ µs, see Fig 4.6d) this enables us to resolve all 12 main P1 electron-spin transitions – for four JT axes and three ^{14}N states – and selectively address at least one transition for each JT axis.

Several additional transitions are visible due to mixing of the electron and nuclear spin in the used magnetic field regime ($\gamma_e|\vec{B}| \sim A_\parallel, A_\perp$). We select 11 well-isolated transitions to fit the P1 Hamiltonian parameters and obtain $\{A_\parallel, A_\perp, P_\parallel\}$ = {114.0264(9), 81.312(1), -3.9770(9)} MHz and $\vec{B}$ = {2.437(2), 1.703(1), 45.5553(5)} G (see section 4.9.3), closely matching ensemble ESR measurements [58]. The experimental spectrum is well described by the 60 P1 transitions for these parameters. No signal is observed at the bare electron Larmor frequency ($\approx$ 128 MHz), confirming that the P1 centers form the dominant electron spin bath.

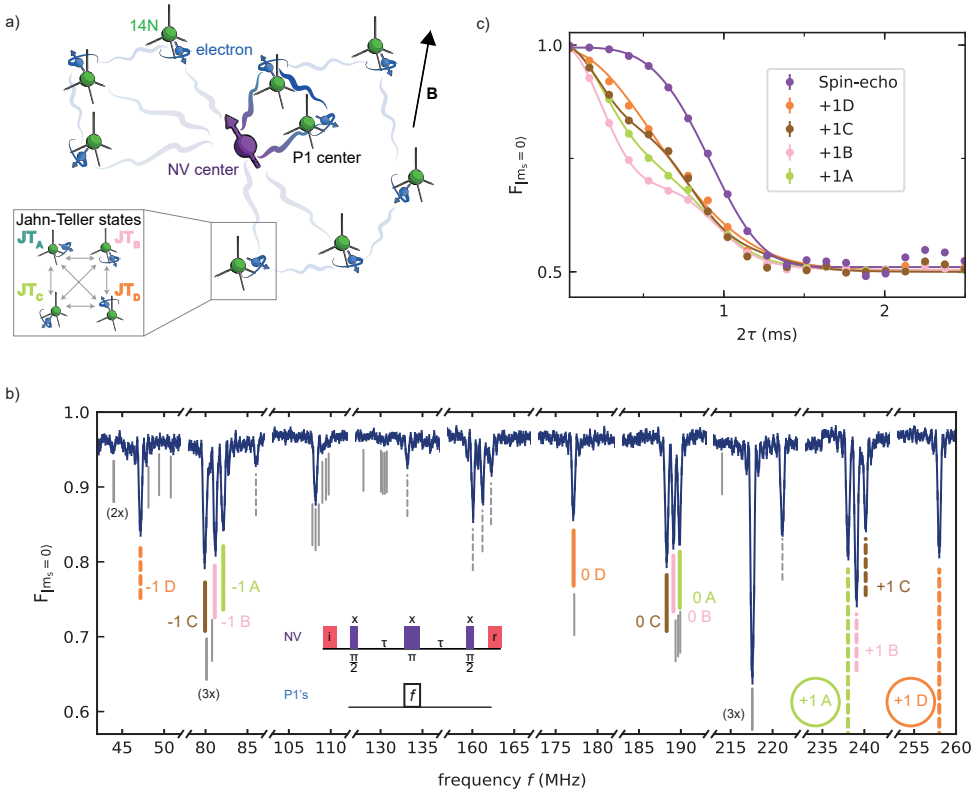

Figure 4.1: **DEER spectroscopy of a P1 spin bath. a)** We study a bath of P1 centers surrounding a single NV center. The state of each P1 center is defined by an electron spin (blue), a ^{14}N nuclear spin (green), and one of four JT axis, which can vary over time (see inset). **b)** DEER spectrum obtained by varying the frequency f (see inset). The NV is initialized in $m_s = 0$ via optical spin-pumping (i) and optically read out (r) at the end of the sequence (Methods). $F_{|m_s=0\rangle}$ is the fidelity of the final NV state with $m_s = 0$. The 12 main P1 electron-spin transitions are labelled by their nitrogen nuclear spin state and JT axis (colored lines). 11 isolated transitions (dashed lines) are used to fit the P1 Hamiltonian and all predicted transition frequencies are indicated (solid lines). In this work, we mainly use the circled transitions corresponding to $|+1, \mathrm{D}\rangle$ and $|+1, \mathrm{A}\rangle$. **c)** We apply a calibrated π pulse (Rabi frequency Ω = 250 kHz) at a fixed frequency f, to selectively couple to P1 centers in the $|+1, i\rangle$ state ($i \in \{\mathrm{A,B,C,D}\}$) and vary the interaction time 2τ (see inset in b). From the fits we obtain a dephasing time $T_{2,DEER}$ of 0.767(6), 0.756(7), 0.802(6) and 0.803(5) ms for the $|+1, i\rangle$ state with i corresponding to A,B,C and D respectively. A spin-echo (no pulse on P1 centers) is added for reference from which we obtain $T_{2,NV}$ = 0.992(4) ms. Error bars are one standard deviation (Methods), with a typical value 4×10^{-3}, which is smaller than the data points. See Methods for the fit functions.

To probe the coupling strength of the P1 bath to the NV, we sweep the interaction time in the DEER sequences (Fig. 4.1c). The curves for the different $|+1, i\rangle$ states show oscillatory features, providing a first indication of an underlying microscopic structure of the P1 bath. However, like all previous experiments [41, 42, 53], these measurements are a complex averaging over ^{14}N, JT and charge states for all the P1 centers, which obscures the underlying structure and hinders control over individual spins.

4.3. Detecting and preparing single P1 centers.

To investigate the microscopic structure of the bath we repeatedly apply the DEER sequence and analyze the correlations in the measurement outcomes [30]. Figure 4.2a shows a typical time trace for continuous measurement, in which groups of K=820 measurements are binned together (see Fig. 4.2b for the sequence). We observe discrete jumps in the signal that indicate individual P1 centers jumping in and out of the $|+1, \mathrm{D}\rangle$ state. The resulting histogram (Fig. 4.2a) reveals multiple discrete peaks that indicate several P1 centers with different coupling strengths to the NV center, as schematically illustrated in Fig. 4.2c. We tentatively assign four P1 centers S1, S2, S3 and S4 to these peaks.

We verify whether these peaks originate from single P1 centers by performing cross-correlation measurements. We first apply a DEER measurement on $|+1, \mathrm{D}\rangle$ followed by a measurement on $|+1, \mathrm{A}\rangle$ (Fig. 4.2d). For a single P1, observing it in $|+1, \mathrm{D}\rangle$ would make it unlikely to subsequently also find it in state $|+1, \mathrm{A}\rangle$. We observe three regions of such anti-correlation (red rectangles in Fig. 4.2d). We define the correlation:

$$C = \frac{P(N_A^{min} \leq N_{|+1,\mathrm{A}\rangle} \leq N_A^{max} \big| N_D^{min} \leq N_{|+1,\mathrm{D}\rangle} \leq N_D^{max})}{P(N_A^{min} \leq N_{|+1,\mathrm{A}\rangle} \leq N_A^{max})} \tag{4.2}$$

where N_A^{min}, N_A^{max}, N_D^{min} and N_D^{max} define the region, and where $P(X)$ is the probability that X is satisfied. Assuming that the states of different P1 centers are uncorrelated, a value $C < 0.5$ indicates that the signal observed in both the DEER sequences on $|+1, \mathrm{A}\rangle$ and $|+1, \mathrm{D}\rangle$ is associated to a single P1 center, while $C < 2/3$ indicates 1 or 2 centers (see section 4.9.7).

For the three areas we find $C = 0.40(5)$, $0.22(4)$ and $0.47(5)$ for S1, S2 and S3/S4 respectively. These correlations corroborate the assignments of a single P1 to both S1 and S2 and one or two P1s for S3/S4 (the result is within one standard deviation from 0.5). Additionally, these results reveal which signals for different $|+1, i\rangle$ states belong to which P1 centers. This is non-trivial because the NV-P1 dipolar coupling varies with the JT axis, as exemplified in Fig. 4.2d (see section 4.9.2 for a theoretical treatment).

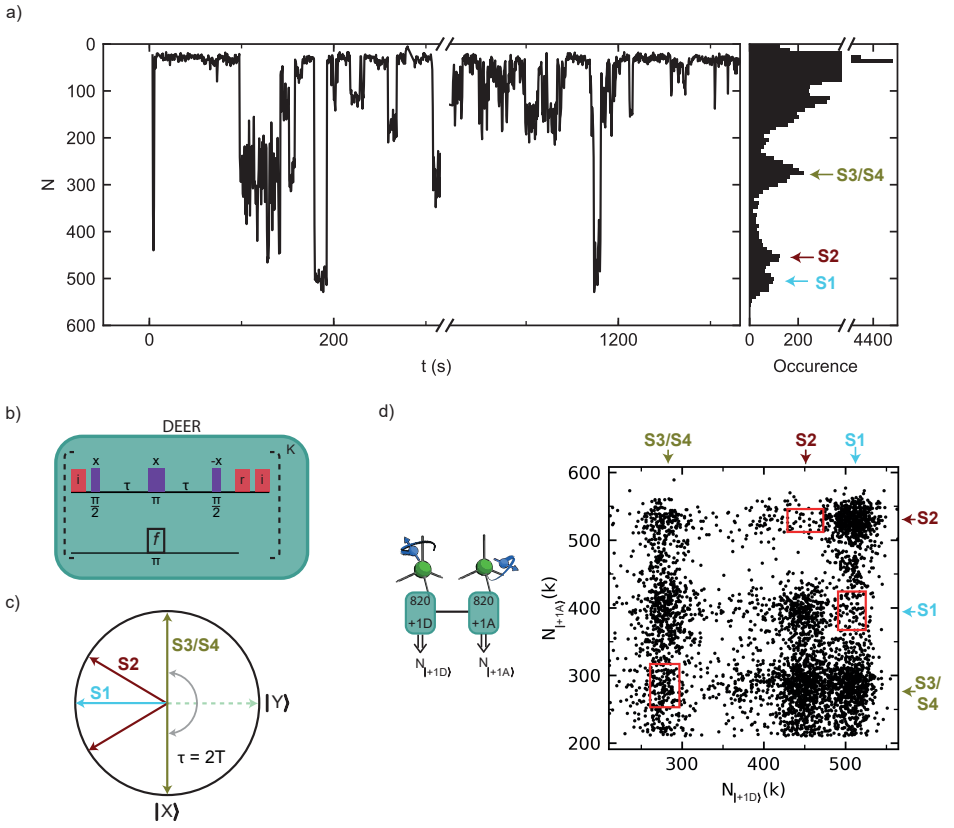

Figure 4.2: **Detection and preparation of single P1 centers. a)** Typical time trace for the DEER signal for $|+1,\mathrm{D}\rangle$. N is the total number of $m_s = 0$ NV readout outcomes in $K = 820$ repetitions of the sequence (see (b)). The discrete jumps and corresponding peaks in the histogram of the full time trace ($\sim$ 6 h, right) indicate that several individual P1s are observed (S1, S2 and S3/S4). **b)** Sequence for K repeated DEER measurements. Note that the phase of the final $\pi/2$ pulse is along -x and thus the signal is inverted as compared to Fig. 4.1b. Optical initialisation (i) and readout (r) of the NV electron are indicated with red pulses. **c)** XY-plane of the NV-spin Bloch sphere before the second $\pi/2$ pulse of a DEER measurement, with the NV initialised along +z at the start. The NV spin picks up phase depending on which nearby P1 centers are in the targeted $|+1,\mathrm{D}\rangle$ state. Because the NV spin is effectively measured along the y-axis, this sequence is insensitive to the P1 electron spin state. We discuss the case of two P1 centers simultaneously in the same state, which happens with a small probability and yields a distinct signal, in section 4.9.1. **d)** Cross-correlation of two consecutive DEER measurements for $|+1,\mathrm{D}\rangle$ (K=820) and $|+1,\mathrm{A}\rangle$ (K=820). Three areas (red boxes, section 4.9.7) show an anti-correlation associated to S1, S2, and S3/S4, in agreement with the assignment of discrete P1 centers. Left: sequence for the two consecutive DEER measurements (green blocks). Double lined arrows indicate measurement outcomes.

Next, we develop single-shot readout and heralded initialisation of the ^{14}N and JT state of individual P1 centers. For this, we represent the time trace data (Fig. 4.2a) as a correlation plot between subsequent measurements k and $k+1$ (Fig. 4.3a) [59–61]. We bin the outcomes using K=820 repetitions, where K is chosen as a trade-off between the ability to distinguish S1 from S2 and the disturbance of the state due to the repeated measurements (1/e value of $\sim 1.5 \times 10^4$ repetitions, see section 4.9.5). Separated regions are observed for the different P1 centers. Therefore, by setting threshold conditions, one can use the DEER measurement as a projective measurement to initialize or readout the $|m_I, i\rangle$ state of selected P1 centers, which we illustrate for S1.

First, we set an initialisation condition $N(k) > N_{S1}$ (blue dashed line) to herald that S1 is initialized in the $|+1, \mathrm{D}\rangle$ state and that S2, S3/S4 are not in that state. We use $N(k) \leq N_{notS1}$ to prepare a mixture of all other other possibilities. The resulting conditional probability distributions of $N(k+1)$ are shown in Fig. 4.3b. Second, we set a threshold for state readout N_{RO} to distinguish between the two cases. We then optimize N_{S1} for the trade-off between the success rate and signal contrast, and find a combined initialisation and readout fidelity F = 0.96(1) (see Methods). Other states can be prepared and read out by setting different conditions (section 4.9.7).

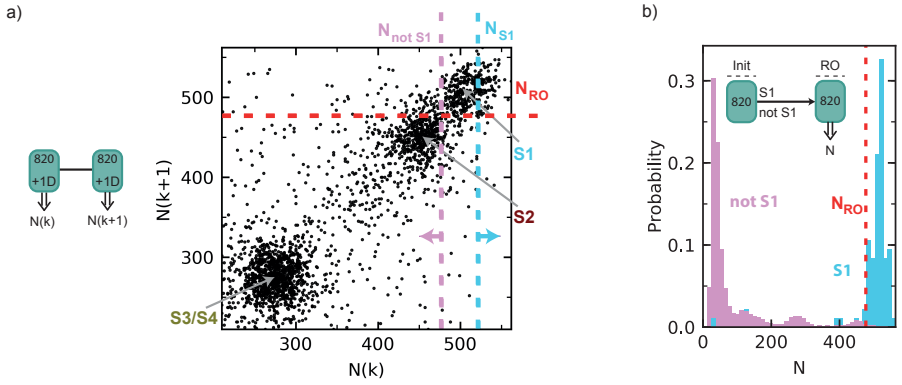

Figure 4.3: **Single-shot readout and initialisation of the ^{14}N and JT state. a)** Correlation plot for consecutive measurement outcomes $N(k)$ and $N(k+1)$, both for $|+1, \mathrm{D}\rangle$. Dashed lines are the thresholds used to prepare (vertical) and read out (horizontal) the JT and ^{14}N state in panel b. We use $N_{S1} > 522$ to prepare S1 in $|+1, \mathrm{D}\rangle$, and S2 and S3/S4 in any other state. The condition $N_{notS1} \leq 477$ prepares a mixture of all other possibilities. A threshold $N_{RO} = 477$ distinguishes between those two cases in readout. **b)** Conditional probability distributions for both preparations, demonstrating initialisation and single-shot readout of the ^{14}N and JT state of S1. Inset: experimental sequence. Labelled horizontal arrows indicate conditions for passing the initialisation measurement (init).

4.4. Control of the electron and nuclear spin.

To control the electron spin of individual P1 centers, we first determine the effective dipolar NV-P1 coupling. We prepare, for instance, S1 in $|+1,\mathrm{D}\rangle$ and perform a DEER measurement in which we sweep the interaction time (Fig. 4.4a). By doing so, we selectively couple the NV to S1, while decoupling it from S2 and S3/S4, as well as from all bath spins that are not in $|+1,\mathrm{D}\rangle$. By applying this method we find effective dipolar coupling constants ν of $2\pi\cdot1.910(5)$, $2\pi\cdot1.563(6)$ and $2\pi\cdot1.012(8)$ kHz for S1, S2 and S3/S4 respectively. Note that, if the signal for S3/S4 originates from two P1 centers, the initialisation sequence prepares either S3 or S4 in each repetition of the experiment.

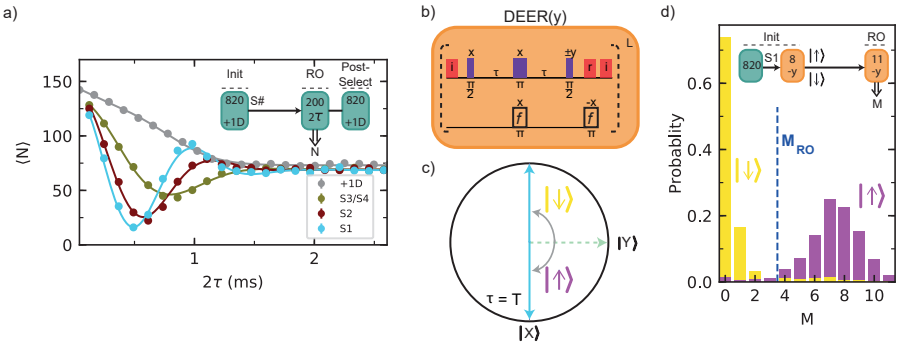

Figure 4.4: **Electron spin initialisation and readout. a)** Measuring the NV-P1 coupling strength. We initialize S1, S2, or S3/S4 in $|+1,\mathrm{D}\rangle$ and vary the interaction time 2τ of a DEER sequence. $\langle N\rangle$ is the mean of the number of NV $m_s = 0$ outcomes for K=200 repetitions. To improve the signal, the results are post-selected on again obtaining $|+1,\mathrm{D}\rangle$. Error bars are one standard deviation (Methods), with a typical value 1, which is smaller than the data points. Grey: without P1 initialisation (data from Fig. 4.1c). **b)** DEER(y) sequence with the readout basis rotated by $\pi/2$ compared to the DEER sequence and $\tau = \pi/2\nu$. An additional π pulse is added to revert the P1 electron spin. Optical initialisation (i) and readout (r) of the NV electron are indicated with red pulses. **c)** XY-plane of the NV Bloch sphere before the second $\pi/2$ pulse, illustrating that the DEER(y) sequence measures the P1 electron spin state (shown for positive NV-P1 coupling). **d)** Single-shot readout of the S1 electron spin. After preparation in $|+1,\mathrm{D}\rangle$, the electron spin is initialized through a DEER(y) measurement (L=8) with thresholds $M_{|\uparrow\rangle}$ (> 6) and $M_{|\downarrow\rangle}$ (≤1). Shown are the conditional probability distributions for a subsequent DEER(y) measurement with L=11 and the readout threshold M_{RO}.

We initialize and measure the electron spin state of the P1 centers through a sequence with a modified readout axis that we label DEER(y) (Fig. 4.4b). Unlike the DEER sequence, this sequence is sensitive to the P1 electron spin state. After initializing the charge, nuclear spin and JT axis, and setting the interaction time $\tau \approx \pi/(2\cdot\nu)$, the DEER(y) sequence projectively measures the spin state of a selected P1 center (Fig. 4.4c). We first characterize the P1 electron spin relaxation under repeated application of the measurement and find a 1/e value of ~250 repetitions (section 4.9.5). We then optimize the number of repetitions and the initialisation and readout thresholds to obtain a combined initialisation and single-shot readout fidelity for the S1 electron spin of $F_{|\uparrow\rangle/|\downarrow\rangle}$ = 0.95(1) (Fig. 4.4d).

We now show that we can coherently control the P1 nitrogen nuclear spin (Fig. 4.5a). To speed up the experiment, we choose a shorter initialisation sequence that prepares either S1 or S2 in the $|+1,\mathrm{D}\rangle$ state (K=420, Methods). We then apply a radio-frequency (RF) pulse that is resonant with the $m_I = +1 \leftrightarrow 0$ transition if the electron spin is in the $|\uparrow\rangle$ state. Varying the RF pulse length reveals a coherent Rabi oscillation. Because the P1 electron spin is not polarized, the RF pulse is on resonance 50% of the time and the amplitude of the Rabi oscillation is half its maximum.

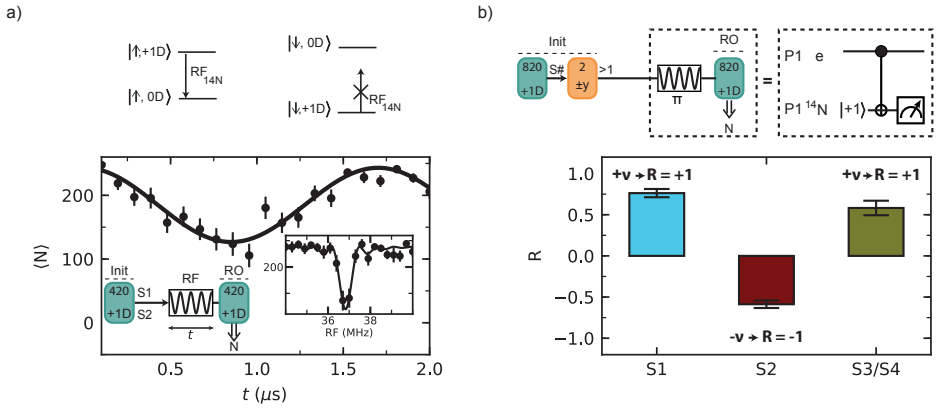

Figure 4.5: **Nitrogen nuclear spin control and NV-P1 coupling sign. a)** ^{14}N Rabi oscillation. Top: energy levels of the P1 electron spin in the $\{0\mathrm{D},+1\mathrm{D}\}$ subspace. Bottom: either S1 or S2 is prepared in $|+1,\mathrm{D}\rangle$ and the length t of a pulse at frequency $RF = RF_{14N} = 36.8$ MHz is varied. The nitrogen nuclear spin is driven conditionally on the electron spin state. Inset: NMR spectrum obtained by varying the frequency RF for a fixed pulse duration t. **b)** We use the ^{14}N spin to determine the sign of the NV-P1 coupling. First, we prepare a selected P1 center (K=820) and initialise its electron spin (L=2). Second, we apply a π pulse at RF_{14N}, which implements an electron controlled CNOT$_{\mathrm{e,N}}$ (see level structure in (a)). The coupling sign to the NV determines the P1 electron-spin state, and, in turn, the final ^{14}N state. Finally, we measure the fidelity with the ^{14}N $|+1\rangle$ state for two opposite electron spin initialisations (+y and -y final $\pi/2$ pulse of DEER(y)). The normalized difference R of these measurements reveals the sign of the coupling (see Methods). All error bars indicate one statistical standard deviation.

We use the combined control over the electron and nuclear spin to determine the sign of the NV-P1 couplings (Fig. 4.5b). First, we initialize the ^{14}N, JT axis and electron spin state of a P1 center. Because the DEER(y) sequence is sensitive to the sign of the coupling (Fig. 4.4c), the sign affects whether the P1 electron spin is prepared in $|\uparrow\rangle$ or $|\downarrow\rangle$. Second, we measure the P1 electron spin through the ^{14}N nuclear spin. We apply an RF pulse, which implements an electron-controlled CNOT gate on the nuclear spin (see Fig. 4.5a). Subsequently reading out the ^{14}N spin reveals the electron spin state and therefore the sign of the NV-P1 coupling. We plot the normalized difference R (Methods) for two different initialisation sequences that prepare the electron spin in opposite states. The results show that NV-P1 coupling is positive for the cases of S1 and S3/S4, but negative for S2 (Fig. 4.5b). If S3/S4 consists of two P1 centers, then they have the same coupling sign to the NV.

4.5. Spin coherence and relaxation.

To assess the potential of P1 centers as qubits, we measure their coherence times. First, we investigate the relaxation times. We prepare either S1 or S2 in $|+1,\mathrm{D}\rangle$, the NV electron spin in $m_s = 0$, and vary the waiting time t before reading out the same state (Fig. 4.6a). This sequence measures the relaxation of a combination of the nitrogen nuclear spin state, JT axis and charge state, averaged over S1 and S2. An exponential fit gives a relaxation time of $T_{|+1,\mathrm{D}\rangle}$ = 40(4) s (Fig. 4.6b, green).

We measure the longitudinal relaxation of the electron spin by preparing either $|\uparrow\rangle$ (S1) or $|\downarrow\rangle$ (S2) (Fig. 4.6a). We post-select on the $|+1,\mathrm{D}\rangle$ state at the end of the sequence to exclude effects due to relaxation from $|+1,\mathrm{D}\rangle$, and find T_{1e} = 21(7) s. The observed electron spin relaxation time is longer than expected from the typical P1-P1 couplings in the bath (order of 1 kHz). A potential explanation is that flip-flops are suppressed due to couplings to neighbouring P1 centers, which our heralding protocol preferentially prepares in other $|m_I, i\rangle$ states. Below, we will show that S1 and S2 have a strong mutual coupling, which could shift them off resonance from the rest of the bath.

Second, we investigate the electron and nitrogen nuclear spin coherence via Ramsey and spin-echo experiments (Figs. 4.6c and d). We find T_{2e}^{*} = 50(3) μs and T_{2e} = 1.00(4) ms for the electron spin, and T_{2N}^{*} = 0.201(9) ms and T_{2N} = 4.2(2) ms for the nitrogen nuclear spin. The ratio of dephasing times for the electron and nitrogen nuclear spins is ~4, while the difference in bare gyromagnetic ratios is a factor ~9000. The difference is partially explained by electron-nuclear spin mixing due to the large value of $A_{\perp}$, which changes the effective gyromagnetic ratios of the nitrogen nuclear spin and electron spin. Based on this, a ratio of dephasing times of 12.6 is expected (see section 4.9.8). The remaining additional decoherence of the nitrogen nuclear spin is currently not understood.

The electron Ramsey experiment shows a beating frequency of 21.5(1) kHz (Fig. 4.6d). As the data is an average over S1 and S2, this suggests an interaction between these two P1 centers. Note that, whilst the signal is expected to contain 11 frequencies due to the different Jahn-Teller and nitrogen nuclear spin state combinations, the observation of a single beating frequency indicates that these are not resolved. Next, we will confirm this hypothesis and use the coupling between S1 and S2 to demonstrate an entangled state of two P1 centers.

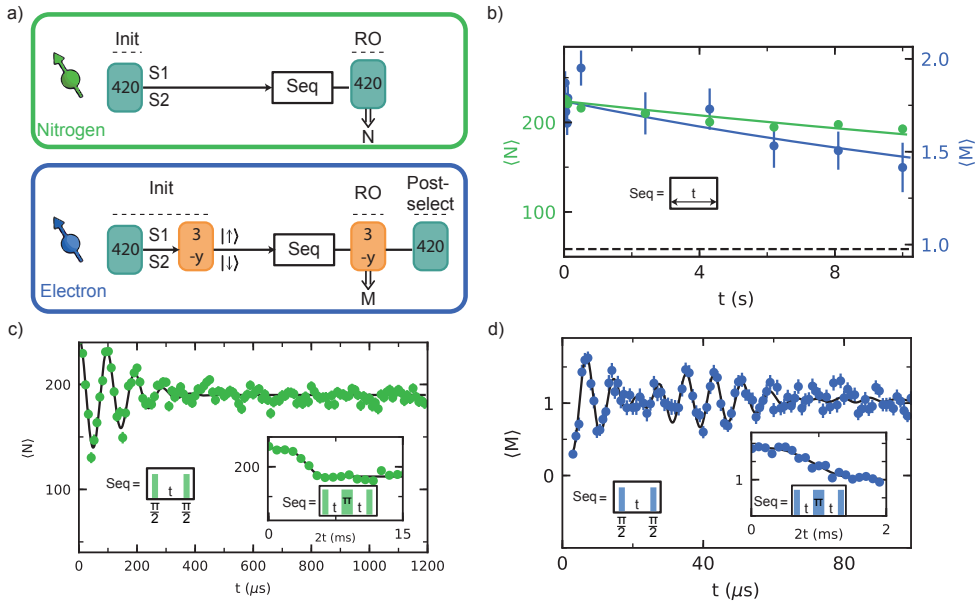

Figure 4.6: **Coherence and timescales. a)** Sequence for initialisation of either S1 or S2 in $|+1,\mathrm{D}\rangle$ (top). Sequence for initializing all degrees of freedom of either S1 or S2, including the electron spin state (bottom). These sequences are used in b, c and d. **b)** Relaxation of a combination of: the nitrogen nuclear spin state, JT axis and charge state (green), and only the electron spin state (blue). We fit (solid lines) both curves to $o + A_0 e^{-t/T}$, where o is fixed to the uninitialized mean value (dashed line) and obtain $T{=}T_{|+1,\mathrm{D}\rangle}$ = 40(4) s and $T{=}T_1$ = 21(7) s. **c)** Ramsey experiment on the nitrogen nuclear spin. We fit the data (solid line) and obtain T^*_{2N} = 0.201(9) ms. (inset) Nitrogen nuclear spin-echo experiment. From the fit we obtain T_{2N} = 4.2(2) ms. **d)** Ramsey experiment on the electron spin. A Gaussian decay (T^*_{2e} = 50(3) μs) with a single beating is observed, suggesting a dipolar coupling between S1 and S2. (inset) Electron spin-echo experiment. From the fit we obtain T_{2e} = 1.00(4) ms. See Methods for complete fit functions and obtained parameters. All error bars indicate one statistical standard deviation.

4.6. Entanglement of two dark electron spins

Thus far we have shown selective initialisation, control and single-shot readout of individual P1 centers within the bath. We now combine all these results to realize coherent interactions and entanglement between the electron spins of two P1 centers.

We first sequentially initialize both P1 centers (Fig. 4.7a). We prepare S1 in the $|+1, \mathrm{D}\rangle$ state and S2 in the $|+1, \mathrm{A}\rangle$ state. To overcome the small probability for both P1 centers to be in the desired state, we use fast logic to identify failed attempts in real-time and actively reset the states (Methods). By initializing the two P1 centers in these different states, we ensure that the spin transitions are strongly detuned, so that mutual flip-flops are suppressed and the interaction is effectively of the form $S_z S_z$. We then sequentially initialize both electron spins to obtain the initial state $|\uparrow\rangle_{S1}|\downarrow\rangle_{S2}$. As consecutive measurements can disturb the previously prepared degrees of freedom, the number of repetitions in each step is optimized for high total initialisation fidelity and success rate (section 4.9.11).

Next, we characterize the dipolar coupling J between S1 and S2 (Fig. 4.7b). We apply two $\pi/2$ pulses to prepare both spins in a superposition. We then apply simultaneous echo pulses on each spin. This double echo sequence decouples the spins from all P1s that are not in $|+1, \mathrm{D}\rangle$ or $|+1, \mathrm{A}\rangle$, as well as from the ^{13}C nuclear spin bath and other noise sources. This way, the coherence of both spins is extended from T_2^* to T_2, while their mutual interaction is maintained. We determine the coupling J by letting the spins evolve and measuring $\langle XZ\rangle$ as a function of the interaction time $2t$ through a consecutive measurement of both electron spins (Fig. 4.7b). From this curve we extract a dipolar coupling $J = -2\pi \cdot 17.8(5)$ kHz between S1 in $|+1, \mathrm{D}\rangle$ and S2 in $|+1, \mathrm{A}\rangle$.

Finally, we create an entangled state of S1 and S2 using the sequence in Fig. 4.7a. We set the interaction time $2t = \pi/|J|$ so that a 2-qubit CPHASE gate is performed. The final state is (see section 4.9.10):

$$|\Psi\rangle = \frac{|\uparrow\rangle_{S1}|-\rangle_{S2} + |\downarrow\rangle_{S1}|+\rangle_{S2}}{\sqrt{2}}, \tag{4.3}$$

with $|\pm\rangle = \frac{|\uparrow\rangle \pm |\downarrow\rangle}{\sqrt{2}}$. We then perform full 2-qubit state tomography and reconstruct the density matrix as shown in Fig. 4.7c. The resulting state fidelity with the ideal state is $F = (1 + \langle XZ\rangle - \langle ZX\rangle - \langle YY\rangle)/4 = 0.81(4)$. The fact that $F > 0.5$ is a witness for two-qubit entanglement [62]. The coherence time during the echo sequence (~ 700 μs, see Methods) is long compared to $\pi/|J|$ (~ 28 μs), and thus the dephasing during the 2-qubit gate is estimated to be at most 2%. Therefore we expect the main sources of infidelity to be the final sequential single-shot readout of the two electron spin states – no readout correction is made – and the sequential initialisation of the two electron spins (section 4.9.11).

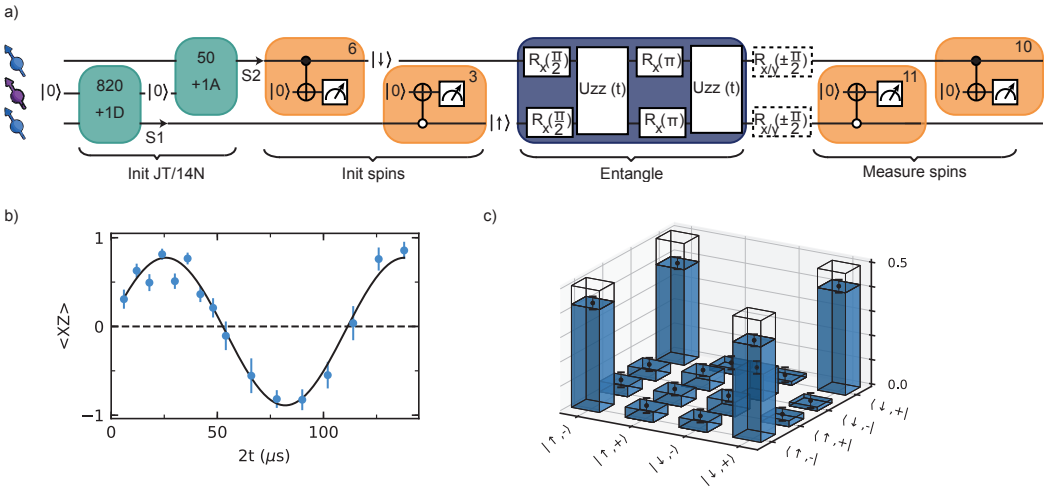

Figure 4.7: **Entanglement between two P1s. a)** Experimental sequence to measure coupling and generate entanglement between S1 and S2. DEER measurements initialize the JT axis and nitrogen state of S1 and S2 (K=820, 50 and $f = f_{+1D}$, f_{+1A}), followed by DEER(y) measurements to initialize their electron spin states (L=6, 3). Two $\pi/2$ pulses and an evolution for time $2t$ under a double echo implements the S_zS_z interaction with both spins in the equatorial plane of the Bloch sphere. This is followed by single qubit gates (dashed boxes) for full 2-qubit state tomography and two final DEER(y) measurements for electron spin readout. We apply an additional initial sequence (K = 5, f_{+1A}) to speed up the experiment (not shown in sequence, see section 4.9.11). **b)** The coherent oscillation of the $\langle XZ\rangle$ as a function of interaction time $2t$ demonstrates a dipolar coupling J = -2π·17.8(5) kHz between S1 and S2. **c)** Density matrix of the S1 and S2 electron spins after applying the sequence as shown in (a) for $2t = \pi/J$. The fidelity with the target state is F = 0.81(5). Transparent bars indicate the density matrix for the target state $|\Psi\rangle$. All error bars indicate one statistical standard deviation.

4.7. Conclusions

In conclusion, we have developed initialisation, control, single-shot readout, and entanglement of multiple individual P1 centers that are part of a bath surrounding an NV center. These results establish the P1 center as a promising qubit platform. Our methods to control individual dark spins can enable enhanced sensing schemes based on entanglement [28, 31, 32], as well as electron spin chains for quantum computation architectures [33–36]. Larger quantum registers might be formed by using P1 centers to control nearby ^{13}C nuclear spins with recently developed quantum gates [4]. Such nuclear spin qubits are connected to the optically active defect only indirectly through the P1 electron spin, and could provide isolated robust quantum memories for quantum networks [63]. Finally, these results create new opportunities to investigate the physics of decoherence, spin diffusion and Jahn-Teller dynamics [30] in complex spin baths with control over the microscopic single-spin dynamics.

4.8. Methods

Sample.
We use a single nitrogen vacancy (NV) center in a homoepitaxially chemical-vapor-deposition (CVD) grown diamond with a $\langle 100 \rangle$ crystal orientation (Element Six). The diamond is isotopically purified to an approximate 0.01% abundance of ^{13}C. The nitrogen concentration is ~75 parts per billion, see section 4.9.4. To enhance the collection efficiency a solid-immersion lens was fabricated on top of the NV center [64, 65] and a single-layer aluminum-oxide anti-reflection coating was deposited [66, 67].

Setup.
The experiments are performed at 3.3 Kelvin (Montana Cryostation) with the magnetic field $\vec{B}$ applied using three permanent magnets on motorized linear translation stages (UTS100PP) outside of the cryostat housing. We realize a long relaxation time for the NV electron spin ($T_1 > 30$ s) in combination with fast NV spin operations (peak Rabi frequency $\sim$ 26 MHz) and readout/initialisation ($\sim$ 40 μs/100 μs), by minimizing noise and background from the microwave and optical controls [13]. Amplifier (AR 20S1G4) noise is suppressed by a fast microwave switch (TriQuint TGS2355-SM). Video leakage noise generated by the switch is filtered with a high pass filter.

Error analysis.
The data presented in this work is either a probability derived from the measurements, the mean of a distribution, or a quantity derived from those. For probabilities, a binomial error analysis is used, where p is the probability and $\sigma = \sqrt{p \cdot (1-p)/Q}$, Q being the number of measured binary values. For the mean μ of a distribution, σ_μ is calculated as $\sigma/\sqrt{Q}$, where σ is the square root average of the squared deviations from the mean and Q is the number of measurements. Uncertainties on all quantities derived from a probability or a mean are calculated using error propagation.

NV spin control and readout.
We use Hermite pulse envelopes [68, 69] to obtain effective microwave pulses without initialisation of the intrinsic ^{14}N nuclear spin of the NV. We initialize and read out the NV electron spin through spin selective resonant excitation (F = 0.850(5)) [64]. Laser pulses are generated by acoustic optical modulators (637 nm Toptica DL Pro, for spin pumping and New Focus TLB-6704-P for single-shot spin readout) or by direct current modulation (515 nm laser, Cobolt MLD - for charge state control, and scrambling the P1 center state, see section 4.9.6). We place two modulators in series (Gooch and Housego Fibre Q) for an improved on/off ratio for the 637 nm lasers.

Magnetic field stabilization.
During several of the experiments we actively stabilize the magnetic field via a feedback loop to one of the translation stages. The feedback signal is obtained

from interleaved measurements of the NV $|0\rangle \leftrightarrow |-1\rangle$ transition frequency. We use the P1 bath as a three-axis magnetometer to verify the stability of the magnetic field during this protocol (see Appendix A.5), and find a magnetic field that is stable to <3 mG along $\hat{\mathbf{z}}$ and <20 mG along the $\hat{\mathbf{x}}, \hat{\mathbf{y}}$ directions.

Heralded initialization protocols

Initialisation of the P1 ^{14}N spin, JT axis, charge and electron spin states is achieved by heralded preparation. Before starting an experimental sequence, we perform a set of measurements that, given certain outcomes, signals that the system is in the desired state.

A challenge is that the probability for the system to be in a given desired state is low, especially in experiments with multiple P1 centers (e.g. Fig. 4.7). We realize fast initialization by combining the heralded preparation with fast logic (ADwin-Pro II) to identify unsuccessful attempts in real time and then actively "reset" the system to a random state. This way each step is performed only if all previous steps were successful, and one avoids being trapped in an undesired state.

To reset the P1 centers to a random state, we use photoexcitation [70] of the P1s. We apply a ∼5 μs 515 nm laser pulse to scramble the ^{14}N, JT and charge states of P1 centers. See section 4.9.6 for details and the optimization procedure.

The most time-consuming step is the selective initialization of the Jahn-Teller and ^{14}N spin states, as $K = 820$ repetitions are required to distinguish the signals from the P1 centers (S1, S2 and S3/S4). However, cases for which none of these P1 centers are in the desired state can be identified already after a few repetitions (section 4.9.6). So after $K = 5$ repetitions we infer the likelihood for the desired configuration and use fast logic to determine whether to apply a new optical reset pulse or continue with the full sequence ($K = 820$). This procedure significantly speeds up the experiments (section 4.9.6). For creating the entangled state (Fig. 4.7) we use a more extensive procedure, which is detailed in section 4.9.11.

In the experiments in Figs. 4.5a and 4.6, we take an alternative approach to speed up the experiments by using a shorter initialisation sequence ($K = 420$) that does not distinguish between S1 and S2. Such a sequence prepares either S1 or S2, and the resulting data is an average over the two cases. Note that this method cannot be used in experiments where a selective initialization is required (e.g. Fig 4.4, Fig 4.5b, Fig. 4.7).

The optimization of the heralded initialization fidelities are discussed in section 4.9.11.

Initialisation and single-shot readout fidelity.

We define the combined initialisation and readout fidelity for S1 in $|+1, \mathrm{D}\rangle$ and S2, S3/S4 not in that state as

$$F_{S1} = P(N(k+1) > N_{RO} | N(k) > N_{S1}), \tag{4.4}$$

whereas for a mixture of all other possibilities we define

$$F_{notS1} = P(N(k+1) \leq N_{RO} | N(k) \leq N_{notS1}). \tag{4.5}$$

In both cases $P(X|Y)$ is the probability to obtain X given Y. We then take the average fidelity of these two cases:

$$F = \frac{F_{S1} + F_{notS1}}{2}. \tag{4.6}$$

We initialize and measure the electron spin state of P1 centers through a DEER(y) sequence following initialisation of the $|+1, \mathrm{D}\rangle$ state. Similarly, we use the correlation of consecutive measurements $M(k)$ and $M(k+1)$ to determine the combined initialisation and readout fidelity $F_{|\uparrow\rangle/|\downarrow\rangle}$. First, we define the fidelity for $|\uparrow\rangle$ as

$$F_{|\uparrow\rangle} = P(M(k+1) > M_{RO} | M(k) > M_{|\uparrow\rangle}), \tag{4.7}$$

and the fidelity for $|\downarrow\rangle$ as

$$F_{|\downarrow\rangle} = P(M(k+1) \leq M_{RO} | M(k) \leq M_{|\downarrow\rangle}). \tag{4.8}$$

Finally, the average combined initialisation and readout fidelity is given as

$$F_{|\uparrow\rangle/|\downarrow\rangle} = \frac{F_{|\uparrow\rangle} + F_{|\downarrow\rangle}}{2}. \tag{4.9}$$

For a description of the optimization of the single-shot readout fidelities, we refer to section 4.9.11.

Data analysis.
The DEER measurements in Fig. 4.1c are fitted to:

$$a_0 + A_0 \cdot \mathrm{Exp}[-(2\tau/T_{2,DEER})^2] \cdot (1 + B_0 \cos(\omega \cdot \tau)) \tag{4.10}$$

from which we find $T_{2,DEER}$ of 0.767(6), 0.756(7), 0.802(6) and 0.803(5) ms for $|+1, \mathrm{A}\rangle$, $|+1, \mathrm{B}\rangle$, $|+1, \mathrm{C}\rangle$ and $|+1, \mathrm{D}\rangle$, respectively. The obtained values for ω are 2π·2.12(5), 2π·2.14(3) and 2π·2.78(6) kHz with corresponding amplitudes B_0 of 0.105(5), 0.218(7), and 0.073(4) for $|+1, \mathrm{A}\rangle$, $|+1, \mathrm{B}\rangle$ and $|+1, \mathrm{C}\rangle$, respectively. For $|+1, \mathrm{D}\rangle$ we fix $B_0 = 0$.

The DEER measurements with P1 initialisation (Fig. 4.4a) and the P1 nitrogen nuclear spin Ramsey (Fig. 4.6c) are fitted to:

$$A_1 \cdot e^{-(t/T)^2} (\cos(\nu \cdot t/2)) + a_1. \tag{4.11}$$

For the dephasing time during the DEER sequence (here $t = 2\tau$) we find T = 0.893(5), 0.763(8) and 0.790(8) ms for S1, S2 and S3/S4 respectively. The obtained respective dipolar coupling constants ν are $2\pi\cdot$1.894(3), $2\pi\cdot$1.572(6) and $2\pi\cdot$1.001(6) kHz. For the P1 nitrogen nuclear spin Ramsey we find a dephasing time of $T = T_{2N}^{*}$ = 0.201(9) ms.

Spin-echo experiments (Fig. 4.1c and Fig. 4.6) are fitted to

$$A_2 \cdot e^{-(t/T)^n} + a_2. \tag{4.12}$$

For the NV spin-echo (Fig. 4.1c), $T = T_2$ = 0.992(4) ms with n = 3.91(7). For the P1 nitrogen nuclear spin and electron (insets of Figure 4.6c,d) T is T_{2N} = 4.2(2) ms or T_{2e} = 1.00(4) ms with the exponents n = 3.9(8) and n = 3.1(5), respectively.

The Ramsey signal for the P1 electron spin in Fig. 4.6d is fitted to a sum of two frequencies with a Gaussian decay according to:

$$a_3 + e^{-(t/T_{2,e}^{*})^2} \cdot \sum_{j=1}^{2} (A_j \cos\big((f_{det} + (-1)^j f_b/2)t\big) + \phi_j))/2, \tag{4.13}$$

which gives a beating frequency $f_b = 2\pi\cdot$21.5(5) kHz.

The value R (Fig. 4.5b) is defined as

$$R = \frac{P_{(+y)} - P_{(-y)}}{P_{(+y)} + P_{(-y)}}, \tag{4.14}$$

where $P_{(+y)}$ ($P_{(-y)}$) is the probability to read out the ^{14}N spin in the $m_I = +1$ state when using a +y (-y) readout basis in the DEER(y) sequence used to initialize the electron spin (Fig. 4.5b and see Appendix A.3).

Two-qubit gate fidelity.
We estimate the dephasing during the two-qubit CPHASE gate in Fig. 4.7 by extrapolation of the measured P1 electron T_{2e} = 1.00(4) ms for a single spin-echo pulse (decoupled from all spins except those in $|+1, \mathrm{D}\rangle$). We use the scaling $T_2 \propto 1/\sqrt{\langle n_{spins}\rangle}$ with $\langle n_{spins}\rangle$ the average number of spins coupled to during the measurement [53]. The two-qubit gate is implemented by a double echo and the two P1s are thus not decoupled from spins in $|+1, \mathrm{D}\rangle$ and $|+1, \mathrm{A}\rangle$, resulting in $T_2 \sim T_{2e}/\sqrt{2} \approx$ 700 μs. Assuming the same decay curve as for T_{2e} ($n = 3.1$) this implies a loss of fidelity due to dephasing of ~0.4%. For a Gaussian decay ($n = 2$) the infidelity would be ~2%.

4.9. Supplementary information

4.9.1. Multiple P1 centers

In this section we discuss multiple coupled P1 centers that simultaneously occupy the same nitrogen nuclear spin- and JT-state. For simplicity we discuss the case of two P1 centers - S1 and S2 - with significant couplings to the NV center, but this can be extended to more P1 centers. Given the measured coupling strengths in $|+1,\mathrm{D}\rangle$ and the chosen interaction time 2τ as shown in Fig. 4.2c of the main text, the NV acquires a phase of approximately $\pm\pi$ ($\pm 4\pi/5$) due to S1 (S2) individually. For the case that both spins occupy the same $|m_I, i\rangle$ state, summation of coupling strengths and the number of repetitive measurements play a role for the observed effective phase. If both spins are in $|+1,\mathrm{D}\rangle$, the total phase is given by the sum or difference of the individual phase contributions and depends on the parity of their electron spins. This results in phases of $\pm 1\pi/5$ or $\pm 9\pi/5$. However, because the P1 electron spin states relax rapidly under repeated measurement (see Fig. 4.13b), for $K = 820$ the measured result is an average of the results generated by the phases of each possible two-spin state. In this case, this gives an effective phase of $1\pi/5$. The resulting signal is well separated from the cases of just S1 or S2, so that cases in which both P1s occupy the same state are removed by the initialization procedures used. Note also that the probability that two of the P1s (S1-S4) are in the same state simultaneously is small.

4.9.2. JT dependent coupling

Mainly due to the anisotropic hyperfine interaction of the P1 center, the effective NV-P1 dipolar coupling ν, which is the interaction observed in a DEER experiment (see Appendix A.2 for detailed description), varies depending on the JT axis. We numerically calculate ν as a function of spherical angles θ and ϕ of the vector $\vec{r}$ between an NV and a P1 using an exemplary case. Figure 4.8a, shows the calculated $\nu/2\pi$ for different states $|m_I, i\rangle$ as a function of angle ϕ (here $\theta = 45°$). This figure demonstrates that the JT state can affect the effective dipolar coupling strength ν. For a P1 center in the states $|+1,\mathrm{A}\rangle$,$|+1,\mathrm{B}\rangle$ and $|+1,\mathrm{C}\rangle$ the principal axis of the hyperfine tensor is rotated 109.5° w.r.t. the $\hat{\boldsymbol{z}}$ axis (NV axis) and thus varying ϕ has a substantial effect on ν. For a P1 center in $|+1,\mathrm{D}\rangle$ the hyperfine tensor's principal axis is along $\hat{\boldsymbol{z}}$ and therefore the dependence on ϕ is small. The observed dependence in the simulation for $|+1,\mathrm{D}\rangle$ is explained by the purposely slightly tilted magnetic field. The tilted magnetic field also explains the differences in maximal and minimal values of ν for the states $|+1,\mathrm{A}\rangle$,$|+1,\mathrm{B}\rangle$ and $|+1,\mathrm{C}\rangle$. The ϕ angles at which ν is at a maximum for these three states are shifted by $\Delta\phi \approx 120°$ w.r.t. each other as is expected from the three-fold rotational symmetry.

Figure 4.8b illustrates that the relative differences of ν for different states are largest near the magic angles $\theta = \pm 54.7°$. Note that information about the P1 positions can be obtained by combining the knowledge of which signal belongs to which P1 center for several $|m_I, i\rangle$ states (Fig. 4.2d main text) and measuring the NV-P1 dipolar coupling. This provides a future opportunity to determine the position

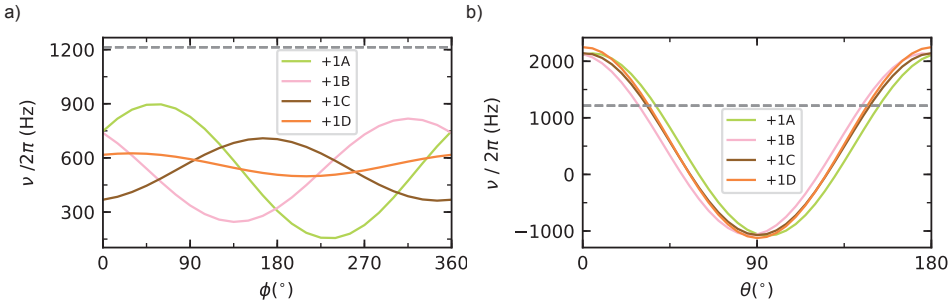

Figure 4.8: **Example showing JT dependent effective dipolar coupling ν. a)** Numerical simulation of $\nu/2\pi$ as a function of angle ϕ of the vector $\vec{r}$ between the NV and a P1. As an example we set θ = 45° and $|\vec{r}|$ = 35 nm. The magnetic field $\vec{B}$ and hyperfine/quadrupole parameters as obtained from the fitted DEER spectrum (main text Fig. 4.1b) are used. Colored curves indicate the P1 center in different states $|+1, i\rangle$. The dashed grey line indicates the value of the prefactor of the dipolar coupling term $\nu_{dip}/2\pi$ (as in eq. A.8 of Appendix A). **b)** Similar to (a) but now as a function of θ (ϕ = 90°).

of P1 centers (up to inversion symmetry) w.r.t. the NV.

4.9.3. Fitting the Hamiltonian parameters

This section describes the fitting procedure used to obtain the Hamiltonian parameters $A_\parallel$, $A_\perp$, $P_\parallel$, B_x, B_y and B_z from the DEER spectroscopy (see Fig. 4.1b and Fig. 4.9). We use parabolic fits of the measured dips to determine their center frequencies, and subsequently use a least squares method to minimize the difference between the measured frequencies and the frequencies resulting from diagonalization of the Hamiltonian (eq. (4.1)) for all 4 JT axes (see Fig. 4.9b). This method requires that we can assign which measured frequency (dips in Fig. 4.9a) belongs to which transition. We use a two step process. First, we take the four highest-energy transitions, which are well separated from any other transition, and use initial values for $A_\parallel$, $A_\perp$, $P_\parallel$ [41] to obtain an estimate of the magnetic field vector. Second, we select 11 well-isolated transitions and corresponding experimental dips to fit $A_\parallel$, $A_\perp$, $P_\parallel$ and the magnetic field vector.

To obtain an initial estimate of B_x, B_y and B_z, we first perform a brute force optimization. We sweep B_x and B_y between $\pm$4 G and B_z between 45 and 46 G in discrete steps and diagonalize the Hamiltonian (eq. (4.1)), where we use γ_e = $2\pi\cdot$ 2.802495 MHz/G and γ_n = - $2\pi\cdot$ 0.3078 kHz/G. For every combination we sort the four highest frequencies (corresponding to $|+1, i\rangle$) and calculate $\Delta = \sum_{i=1}^{4}(f_{i,\mathrm{exp}} - f_{i,\mathrm{theo}})^2$, where $f_{i,\mathrm{theo}}$ is the transition frequency obtained by diagonalization and $f_{i,\mathrm{exp}}$ is the measured frequency. We find a minimum in Δ for $\vec{B} = (2.53, 1.39, 45.37)^T$ G.

We then use 11 dips that we can unambiguously assign to a well-isolated transition and measure these dips with high accuracy, see Fig. 4.9b. We use this data to extract $A_\parallel$, $A_\perp$, $P_\parallel$ and the magnetic field vector using a least squares fit. The fit ob-

tains $\{A_\parallel, A_\perp, P_\parallel\}$ = {114.0264(9), 81.312(1), -3.9770(9)} MHz and $\vec{B}$ = { 2.437(2), 1.703(1), 45.5553(5)} G. The vertical lines in Fig. 4.9b are the 11 transition frequencies calculated with these values. In order to provide a more quantitative comparison we provide the experimentally measured frequencies of the 11 dips in Table 4.1 alongside with their values calculated from equation (4.1). Furthermore, by inspection, we identify 9 other dips in Fig. 4.9a. We determine their center frequency and compare them to their closest transition frequency resulting from the fitted parameters, see Table 4.1.

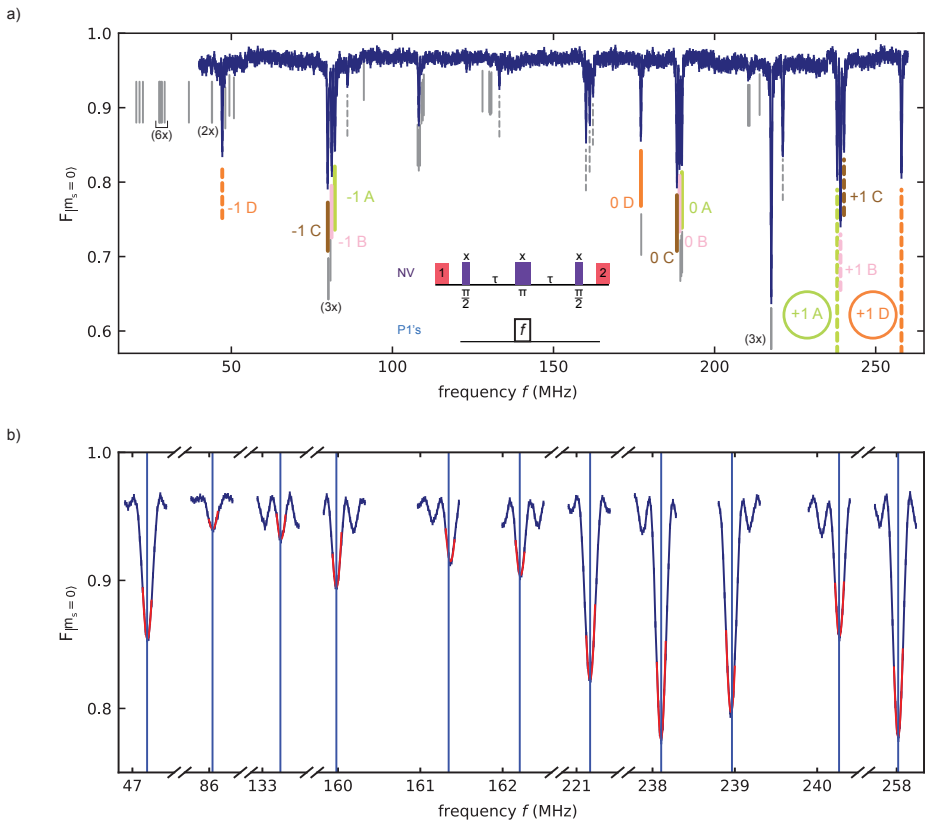

Figure 4.9: **Fitting the P1 Hamiltonian parameters.** a) Complete dataset corresponding to Fig. 4.1b (main text). b) Measurement of 11 dips that are assigned to a well isolated transition (blue lines). Side lobes are due to Rabi oscillations. We fit a parabola (red) and extract the center frequency. Using a least squares fit of the center frequencies and the transitions, we extract the values of $\{A_\parallel, A_\perp, P_\parallel\}$ and $\vec{B}$. Error bars indicate one statistical standard deviation, with a typical value 2×10^{-3}, which is smaller than the data points.

Dip Nr	Experimental value (MHz)	Equation (4.1) (MHz)	$\|m_I, i\rangle$ state
1	47.183(1)	47.179	$\|-1, \mathrm{D}\rangle$
2	86.042(2)	86.040	
3	133.227(2)	133.219	
4	159.9810(4)	159.980	
5	161.367(4)	161.344	
6	162.217(3)	162.208	
7	221.1641(7)	221.1648	
8	238.1027(6)	238.1051	$\|+1, \mathrm{A}\rangle$
9	238.954(1)	238.965	$\|+1, \mathrm{B}\rangle$
10	240.271(1)	240.266	$\|+1, \mathrm{C}\rangle$
11	258.0176(6)	258.018	$\|+1, \mathrm{D}\rangle$
12	79.898(4)	79.961	$\|-1, \mathrm{C}\rangle$
13	81.16(2)	81.10	$\|-1, \mathrm{B}\rangle$
14	82.106(8)	82.119	$\|-1, \mathrm{A}\rangle$
15	108.18(2)	108.20	
16	177.1167(2)	177.1476	$\|0, \mathrm{D}\rangle$
17	188.32(2)	188.32	$\|0, \mathrm{C}\rangle$
18	189.15(6)	189.11	$\|0, \mathrm{B}\rangle$
19	189.88(5)	189.88	$\|0, \mathrm{A}\rangle$
20	217.5783(8)	217.5709	

Table 4.1: Comparison of measured P1 transition frequencies (Fig. 4.9b) with closest values from equation (4.1). We include the 11 frequencies of Fig. 4.9b used in the fitting, as well as 9 other identified dips in Fig. 4.9a, which is taken at a slightly different magnetic field compared to Fig. 4.9b.

4.9.4. Estimate of P1 concentration

In this section we estimate the P1 concentration surrounding the NV center. We calculate an expected concentration (C_d) based on decoherence of the NV electron spin. In the secular approximation the dipolar interaction of a number (N_d) of P1 centers and the NV is given as:

$$H_{int} = J_z \sum_{k=1}^{N_d} 2\pi \cdot \nu_k \cdot (1 - 3\cos^2(\theta)) \cdot S_z = J_z \sum_{k=1}^{N_d} b_k \cdot S_z, \tag{4.15}$$

where $2\pi \cdot \nu_k = \frac{-\mu_0 \gamma_e \gamma_e \hbar}{4\pi r_k^3}$ and θ the polar angle in spherical coordinates. For a given concentration of P1 centers C_d, we consider a sphere around the NV center of radius R:

$$R = \left(\frac{3 \cdot V_{tot}}{4\pi} \right)^{1/3}, \tag{4.16}$$

where $V_{tot} = \frac{N_d \cdot V_{unit}}{C_d \cdot 8}$ with V_{unit} the volume of a diamond crystal unit cell, and 8 denotes the number of atoms within one unit cell. Within such a sphere we

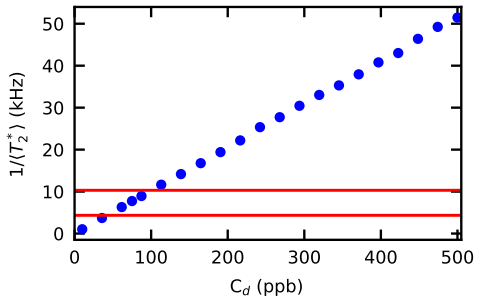

Figure 4.10: Simulated $1/\langle T_2^* \rangle$. Simulation based on m = 10^4 different defect configurations of N_d = 40 defects. The red vertical lines indicate estimated bounds for $1/\langle T_2^* \rangle$.

generate a number of P1 centers (N_d = 40) at random positions and calculate T_2^* due to a Gaussian spin bath [71] as:

$$T_2^* = \frac{\sqrt{2}}{\frac{1}{2}\sqrt{\sum_{k=1}^{N_d} b_k^2}}. \tag{4.17}$$

We repeat this procedure to generate m = 10^4 different spatial configurations of P1 centers and calculate the average, $\langle T_2^* \rangle$.

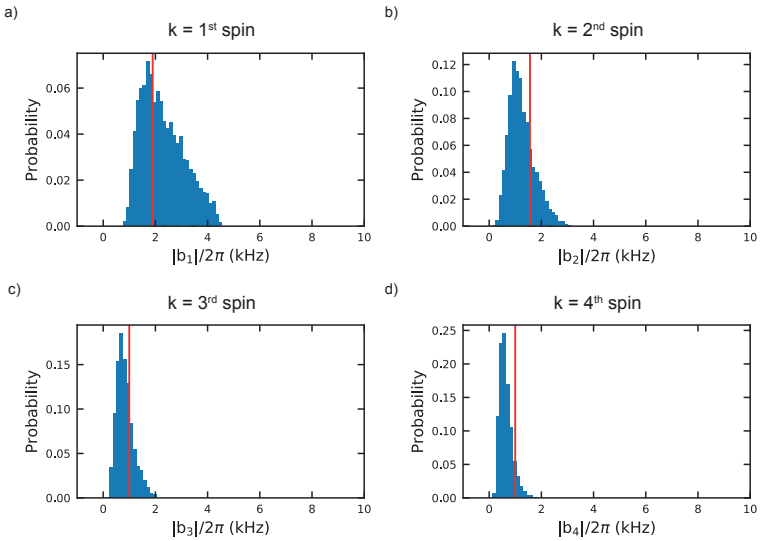

Figure 4.11: **Simulated distributions of the coupling strengths for the most strongly coupled P1 spins.** a),b),c),d) Distributions of $|b_k|/2\pi$ given 4 kHz ≤ $1/T_2^*$ ≤ 10 kHz and a concentration C_d = 75 ppb.

The result of this simulation as a function of P1 concentration C_d is shown in Fig. 4.10. For randomly positioned P1s, $1/\langle T_2^* \rangle$ scales linearly with C_d. Note the difference in scaling with the average number of P1 centers coupled to during a DEER measurement, $\langle n_{spins} \rangle$, which scales as $1/T_{2,DEER} \propto \sqrt{\langle n_{spins} \rangle}$ due to the fixed positions of the P1s [53]. We estimate the NV decoherence time due to coupling to P1s to be within two values (as indicated by the red vertical lines in Fig. 4.10). The first value is the measured $T_{2,NV}^*$ = 97(3) μs ($1/T_{2,NV}^* \approx$ 10 kHz). Here it is assumed that the P1 centers are the dominant spin bath and the effect of the ^{13}C bath, and other magnetic field noise sources, on the NV decoherence is small. The second value is extrapolated from the measured $T_{2,DEER}$ = 0.803(5) ms for $|+1, \mathrm{D}\rangle$ and thus is given by $T_2^* \sim T_{2,DEER}/\sqrt{12} \approx$ 230 μs ($1/T_2^* \approx$ 4 kHz). Here we assume approximately equal coupling strength in all 12 $|m_I, i\rangle$ states and an equal probability of occurrence for each state. The concentration is expected to be within these values and thus we estimate $C_d \sim$ 75 ppb.

Figure 4.11 shows the probability density of $b_k/2\pi$ for the first four P1 spins, given a concentration C_d = 75 ppb and the condition 4 kHz ≤ $1/T_2^*$ ≤ 10 kHz for the NV spin. These distributions demonstrate the expected values of $|b_k|$ to be close to the measured values as stated in Methods (indicated by the vertical red lines). The probability densities without a condition on $1/T_2^*$ are shown in Fig. 4.12. These plots show that given the concentration $C_d \sim$ 75 ppb, a large range of coupling strengths are possible for the nearest spin (including the measured value |17.8(5)| kHz as measured between S1 and S2).

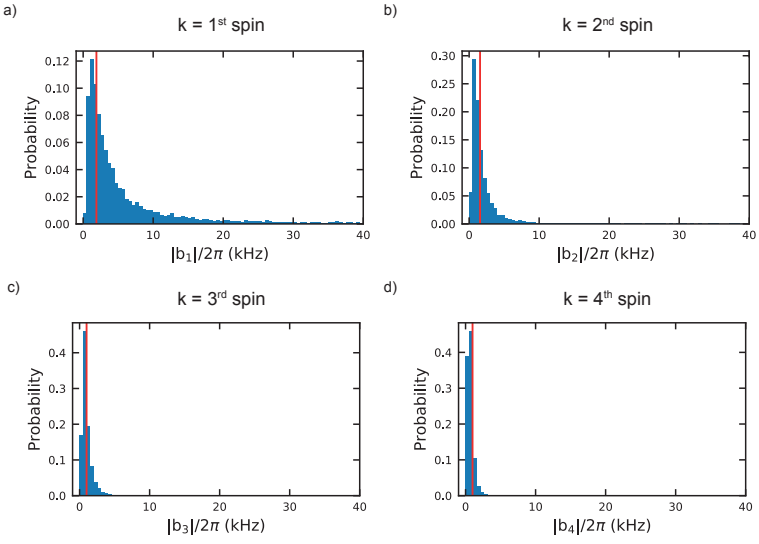

Figure 4.12: **Simulated distributions for the 4 most strongly coupled spins.** a),b),c),d) Distributions of $|b_k|/2\pi$ given a concentration C_d = 75 ppb.

4.9.5. Relaxation times of S1 during repetitive DEER measurements

This section characterizes the relaxation of the P1 $|+1,\mathrm{D}\rangle$ state (Fig. 4.13a) and the P1 electron spin in $|+1,\mathrm{D}\rangle$ (Fig. 4.13b) under repeated measurement sequences. We first prepare spin S1 in $|+1,\mathrm{D}\rangle$ using DEER measurements (K=820) and subsequently apply 5 sequential sets of DEER measurements with K=820. We plot the result of each set in Fig. 4.13a. We obtain a 1/e decay of ~19 sets, showing the $|+1,\mathrm{D}\rangle$ state is stable over $\sim 1.5 \times 10^4$ DEER repetitions (including optical 637 nm pulses).

To investigate the stability of the P1 electron state under repetitive DEER(y) measurements, we initialize S1 in $|+1,\mathrm{D}\rangle$ and prepare its electron state in $|\uparrow\rangle$ using L=8 DEER(y) measurements. Subsequently we apply 51 sequential sets of DEER(y) measurements with L=8 and plot the result of each set in Fig. 4.13b. We extract a 1/e decay for $|\uparrow\rangle$ of ~32 sets, showing a stability over ~250 DEER(y) repetitions. Comparing this with the 1/e decay of $|+1,\mathrm{D}\rangle$ shows that a single sequence is much more destructive for the P1 electron state than for the combined nitrogen nuclear spin and JT state. This limits the amount of DEER(y) sequences L that can be used to initialize the P1 electron spin with high fidelity.

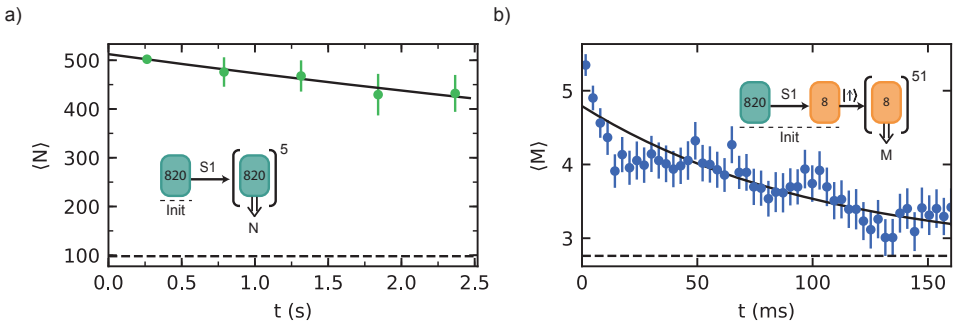

Figure 4.13: **Relaxation during repetitive readout.** a) Relaxation from the $|+1,\mathrm{D}\rangle$ state while continuously performing DEER measurements. We fit (solid line) the curve to $o + A_0 \cdot e^{-t/T_{|+1,\mathrm{D}\rangle rep}}$, where o is fixed to the uninitialized mean value (dashed line) and obtain $T_{|+1,\mathrm{D}\rangle rep}$ = 10(4) s. This timescale corresponds to ~ 19 bins of DEER measurements with K=820 repetitions. b) Relaxation from the $|\uparrow\rangle$ state, we fit (solid line) the curve to $o_1 + A_1 \cdot e^{-t/T_{|\uparrow\rangle rep}}$, where o_1 is fixed to the uninitialized mean value (dashed line) and obtain $T_{|\uparrow\rangle rep}$ = 103(8) ms. This timescale corresponds to ~ 32 bins of DEER(y) measurements with L=8 repetitions.

4.9.6. Preparation of P1 bath configurations by active optical reset

Several of the experiments require initialisation of the charge, nitrogen nuclear spin and JT degrees of freedom for single P1 centers. To be able to distinguish the signals of the different P1 centers a large amount of measurement repetitions K is required, which limits the experimental repetition rate. In this section we describe

how we increase the experimental rate fourfold by dynamically resetting the P1 center states based on outcomes of early measurement repetitions. The key ideas are: (1) cases for which none of the P1 centers start in the desired state can be identified already after a few repetitions, so that the sequence can be aborted, and (2) the state of the P1 centers can be rapidly reset by a laser pulse (515 nm) before re-attempting the initialization.

Optimization to increase experimental rate

In various experiments, we initialize the nitrogen nuclear spin- and JT-state of selected P1 centers by using the outcome of K = 420 or K = 820 DEER measurements to herald the desired state (Fig. 4.3 of the main text and Fig. 4.16). In Fig. 4.14a, we plot the histogram of $\sim 3 \times 10^5$ DEER measurements in bins of K=420 on $|+1, \mathrm{D}\rangle$. In this dataset we define a successful (unsuccessful) initialisation of either S1 or S2 in $|+1, \mathrm{D}\rangle$ if the outcome N of K=420 DEER measurements fulfils $N > 180$ ($N \leq 180$), see the green (red) part of the distribution in Fig. 4.14a. We find ~11% of the distribution in the green region which indicates the probability to find either S1 or S2 in $|+1, \mathrm{D}\rangle$. This differs from a probability of $\sim 2 \cdot \frac{1}{12}$ and suggests that P1 centers occasionally ionize or preferentially occupy specific states. Research on all 12 nitrogen nuclear spin- and JT-states is required to provide more insight on the occupation of such states and provides a potential direction for future research. We note that from Supplementary Fig. 4.16 we extract ~11% of S1 or S2 being in $|+1, \mathrm{A}\rangle$. Because of these low probabilities, the success rate of initialising S1 or S2 is limited. In Supplementary Fig. 4.14b, we inspect the measurement outcome $\mathrm{N1}$ of successful (green) and unsuccessful (red) initialisation attempts after the first K=Θ DEER sequences, where in this figure $\Theta = 5$. This shows that $\mathrm{N1}$ is low for many unsuccessful cases (red), indicating that the experiment can be sped up by aborting the sequence after a few repetitions if $\mathrm{N1}$ is below a threshold.

We implement a Monte Carlo method to determine a good set of parameters to increase the experimental rate. A schematic of the method is depicted in Fig. 4.14d. We sample from the dataset in Fig. 4.14a and check after Θ DEER measurements (DEER 1) whether the outcome $\mathrm{N1}$ is below a threshold Λ. If so, we abort, sample again from the dataset and inspect DEER 1 again. If $\mathrm{N1} \geq \Lambda$, we continue until finishing 420 DEER measurements. If the outcome of the 420 DEER measurements is above 180, we accept it as a successful initialisation. We continuously sample from the dataset until we achieve 1000 successful runs ($\mathrm{N1} + \mathrm{N2} > 180$).

We now sweep Θ and Λ and calculate the average time $\langle \mathrm{T_{avg}} \rangle$ required to finish one of the 1000 runs (see Fig. 4.14d). Here we use that 1 DEER sequence takes 684 μs and we introduce an overhead time of 1 ms for resetting the P1 center states (experimentally done with a laser pulse, see subsection below). Two critical parameters that determine $\langle \mathrm{T_{avg}} \rangle$ are 1) the probability $P(\mathrm{N1} \geq \Lambda)$ to pass the condition in DEER 1, and 2) the probability $P(\mathrm{N1} + \mathrm{N2} > 180 | \mathrm{N1} \geq \Lambda)$ to obtain $\mathrm{N1} + \mathrm{N2} > 180$ conditioned on passing the condition in DEER 1. These probabilities can be extracted from Fig. 4.14a and b and are shown in Fig. 4.14c for the example case of $\Theta = 5$. From Fig. 4.14d we extract that $\Theta = 5$ and $\Lambda = 3$ are parameters

where $\langle T_{avg} \rangle$ is small and we find an increase in experimental rate by a factor $\sim$ 5. This shows that the experiment can be sped up by aborting the sequence after 5 repetitions already if $N1$ is below 3. Note, however, that this method assumes perfect randomization of the P1 center states by drawing random samples from the dataset.

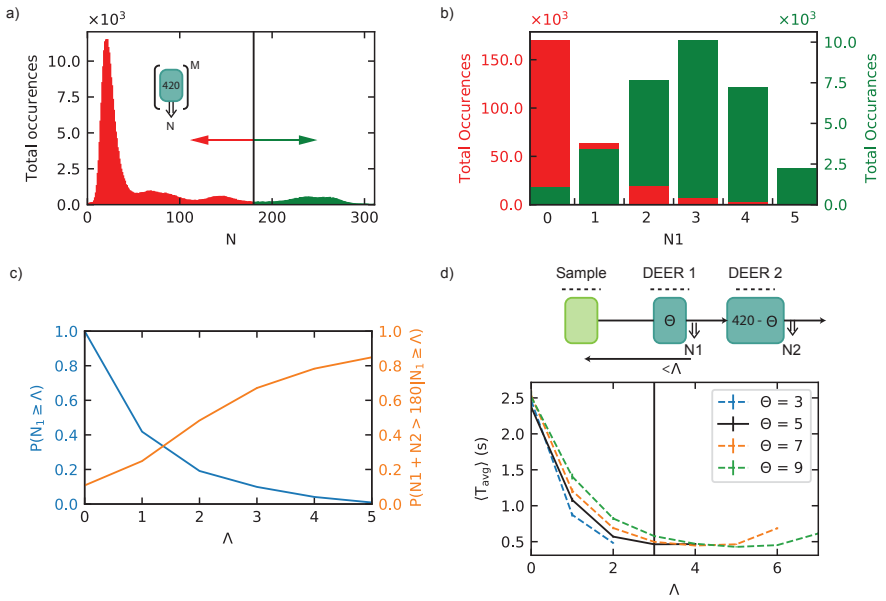

Figure 4.14: **Optimization to increase the experimental rate** a) The distribution of outcomes for $K = 420$ DEER measurements. We define successful (unsuccessful) initializations as $N > 180$ ($N \leq 180$) indicated by the green (red). b) Distribution of outcomes after Θ DEER measurements, where as an example we take $\Theta = 5$. Green (red) bars correspond to the green (red) datasets in (a). c) The probability $P(N1 \geq \Lambda)$ to measure an outcome $N1 \geq \Lambda$ after 5 DEER measurements (blue) and the probability $P(N1 + N2 > 180 | N1 \geq \Lambda)$ to obtain $N > 180$ after 420 DEER measurements, conditioned on having $N1 \geq \Lambda$ in the first 5 DEER measurements. d) The average time ($\langle T_{avg} \rangle$) to complete one successful run of the method shown on top. A run is successful if $N1 + N2 > 180$. We calculate $\langle T_{avg} \rangle$ as a function of Λ for different settings of Θ. We find a factor 5 increase in experimental rate for $\Theta = 5$ and $\Lambda = 3$ compared to no thresholding ($\Lambda = 0$).

Active optical reset

In this section we implement the method devised above to increase the experimental rate. We use photoexcitation [70] to efficiently randomize/reset the P1 center states after failed initialisation attempts. This method results in a fourfold increase of experimental rate. We observe a trade-off for the laser power, with higher laser power decreasing the rate due to spectral diffusion and ionization of the NV [72] and increasing the rate due to resetting the nitrogen nuclear spin and JT configuration of the P1 bath, and find an optimal working point.

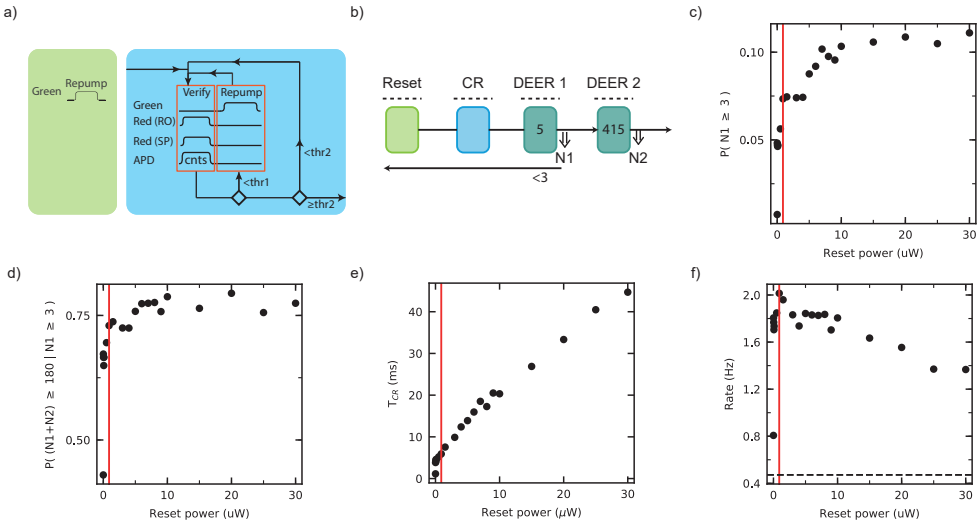

Figure 4.15: **Active optical reset of P1 bath.** a) Illustration of the green (515 nm) optical reset pulse (left). Logical sequence showing the charge and resonance verification (CR) for the NV center (right). We count the number of photons (cnts) while resonantly exciting the NV center simultaneously at its readout (RO) and spin-pump (SP) transitions. If cnts < thr1, the charge state is optically reset (repump, 30 μW). The experimental sequence is continued if cnts ≥ thr2 (thr2 > thr1). If thr1 ≤ cnts < thr2, a new verification step is entered. b) Schematic of the experimental sequence. An initial optical reset is performed (green, 5 μs) to excite the P1 bath [70]. Thereafter, the CR scheme (blue, see (a)) is implemented until the experimental sequence is continued. This scheme is followed by a DEER sequence (K=5, see main text). Based on the outcome of DEER 1 we either continue to DEER 2 (K=415) or go back to the start of the experimental sequence to apply an optical reset pulse. c),d) Plots of the probabilities to pass the desired threshold after DEER 1 and DEER 2, as a function of the optical reset pulse power. e) Average duration of the CR scheme (T_{CR}) as a function of optical reset pulse power. f) Experimental rate given the desired threshold (N1 + N2) ≥ 180. The dashed horizontal line marks the rate without optical reset pulse and without feedback based on the outcome $\mathrm{N1}$. Vertical red lines in c),d),e),f) mark the reset power for maximal experimental rate.

Our experiments require that the NV centre is in the correct negative charge state and that its readout and spin-pump transitions are on resonance with the two 637 nm lasers. This is established by implementing a charge and resonance verification scheme (CR) [64]. Additional to this scheme, we use an optical pulse to reset the P1 center states. Figs. 4.15a and b show the experimental sequence where the optical reset pulse is applied at the beginning. The CR scheme is thereafter implemented, followed by a short DEER sequence (DEER 1). At this point, feedback is implemented as the DEER 1 sequence provides information about the configuration of the P1 bath (see Fig. 4.14b). Based on the method above, we apply an optical reset pulse if $\mathrm{N1} < 3$. In Figs. 4.15c,d), an increase of the probability of passing the desired thresholds for both DEER 1 and DEER 2 as a function of reset pulse power is shown. This demonstrates the reset pulse to be fully effective at a power of ~10 μW.

We observe an increase of the duration of the CR scheme as a function of reset power (Fig. 4.15e), likely due to spectral diffusion caused by photoexcitation of the P1 bath. The trade-off between optical reset and increased CR scheme duration becomes apparent in Fig. 4.15f, where the experimental rate is plotted as a function of optical reset power. The rate initially increases, followed by a decrease as the time required for CR verification becomes dominant. We find over a 4-fold increase of experimental rate at the optimal optical reset power of 0.9 μW. The observed increase in experimental rate here is close to theoretically predicted in the section above.

4.9.7. Correlation measurements for different JT axes

In this section we provide the background for the correlation measurement on different JT axes (Fig. 4.2d, main text), and include an analysis of the complete dataset (additional to the selected data in the main text). We derive the expected correlation value C for a signal originating from a number n of P1 centers in such correlation measurements.

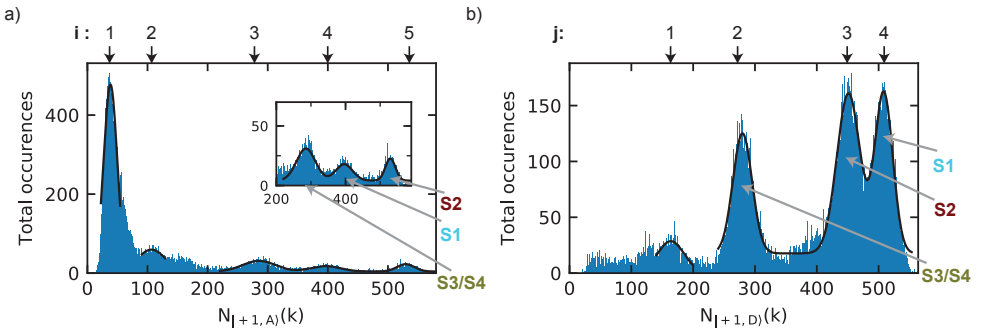

Figure 4.16: **Distributions of total occurrences.** a) All data from the measurement of Fig. 4.2d in the main text. The histogram shows the total occurrences plotted as a function of outcome $N_{|+1,A\rangle}$ (irrespective of the outcome $N_{|+1,D\rangle}$). The black solid line corresponds to the fit. Numbers corresponding to an index, indicate the center of each fitted Gaussian. Inset: enlarged view of the same histogram indicating S2, S1 and S3/S4. b) Similar to (a), but for measurements on $|+1,D\rangle$. The data in (b) is taken with an increased rate using the active optical reset method described in section 4.9.6, explaining why no peak at low counts is observed.

First, we define the regions of interest for the measurement outcomes in both JT axes ($N_{|+1,A\rangle}$ and $N_{|+1,D\rangle}$, see Fig. 4.16). We fit the peaks in both distributions to Gaussian functions of the form $f = O + \sum_{q=1}^{q_{\text{tot}}} A_q \cdot e^{-(N-N_{q,0})^2/2\cdot\sigma_{q,0}^2}$, where N corresponds to either $N_{|+1,A\rangle}$ or $N_{|+1,D\rangle}$ and q_{tot} is either 1 or 3. From these fits (black lines, Fig. 4.16), we obtain the FWHM of each Gaussian, and use these to define the areas of interest as shown in Fig. 4.17. Note that these ranges for $N_{|+1,D\rangle}$

($N_{|+1,\mathrm{A}\rangle}$) are also used in experiments described in the main text and supplementary information for initialisation of S1, S2 and S3/S4 in $|+1,\mathrm{D}\rangle$ ($|+1,\mathrm{A}\rangle$), unless mentioned otherwise.

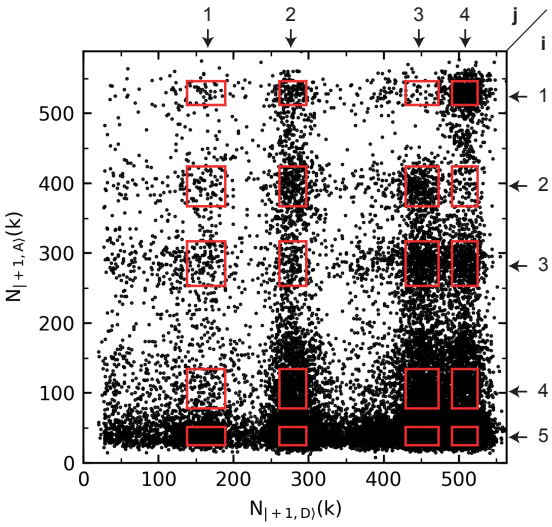

Figure 4.17: **Complete dataset corresponding to the measurement in Fig. 4.2d (main text).** The red rectangular areas illustrate the regions defined by the FWHM as obtained from the fitted curves in Fig. 4.16. We denote each area by indices (i,j). The correlation values C corresponding to these areas are shown in Table 4.2.

Second, we define the required probability functions. For outcome $N_{|+1,\mathrm{D}\rangle}$, the probabilities for obtaining $N_D^{min} \leq N_{|+1,\mathrm{D}\rangle} \leq N_D^{max}$ irrespective of $N_{|+1,\mathrm{A}\rangle}$ are given by:

$$P(N_D^{min} \leq N_{|+1,\mathrm{D}\rangle} \leq N_D^{max}) = P_D\big|_{min}^{max} = \int_{N_D^{min}}^{N_D^{max}} pdf_D \cdot dN_{|+1,\mathrm{D}\rangle}, \tag{4.18}$$

and, for outcome $N_A^{min} \leq N_{|+1,\mathrm{A}\rangle} \leq N_A^{max}$ irrespective of outcome $N_{|+1,\mathrm{D}\rangle}$, this is given as:

$$P(N_A^{min} \leq N_{|+1,\mathrm{A}\rangle} \leq N_A^{max}) = P_A\big|_{min}^{max} = \int_{N_A^{min}}^{N_A^{max}} pdf_A \cdot dN_{|+1,\mathrm{A}\rangle}. \tag{4.19}$$

pdf_D and pdf_A are probability density functions. We additionally define a conditional probability

$$P((N_A^{min} \leq N_{|+1,\mathrm{A}\rangle} \leq N_A^{max})|(N_D^{min} \leq N_{|+1,\mathrm{D}\rangle} \leq N_D^{max})) = \overline{P_A}\big|_{min}^{max} = \int_{N_A^{min}}^{N_A^{max}} \overline{pdf_A} \cdot dN_{|+1,\mathrm{A}\rangle} \tag{4.20}$$

with $\overline{pdf_A}$ the probability density function for outcomes $N_{|+1,\mathrm{A}\rangle}$ given $N_D^{min} \leq N_{|+1,\mathrm{D}\rangle} \leq N_D^{max}$.

Finally, we derive a bound for the correlation function C. Consider n P1 centers, each of which generates signal within $N_D^{min} \leq N_{|+1,\mathrm{D}\rangle} \leq N_D^{max}$ or within $N_A^{min} \leq N_{|+1,\mathrm{A}\rangle} \leq N_A^{max}$ if they are in the corresponding state. The correlation C for consecutive measurements then satisfies:

$$C = \frac{\overline{P_A}\big|_{min}^{max}}{P_A\big|_{min}^{max}} \geq \frac{n-1}{n}. \tag{4.21}$$

The inequality in equation 4.21 is derived as follows. We consider k P1 centers, each with an identical probability p to be in any of the states $|m_I, i\rangle$ (here p is approximately 1/12). We consider two signal regions $N_D^{min} \leq N_{|+1,\mathrm{D}\rangle} \leq N_D^{max}$ and $N_A^{min} \leq N_{|+1,\mathrm{A}\rangle} \leq N_A^{max}$, and assume that there are n ($n \leq k$) P1 centers with a coupling that results in a signal in those regions. Note that no signal is generated in the respective region if more than one P1 center is simultaneously in the state $|+1,\mathrm{D}\rangle$ or $|+1,\mathrm{A}\rangle$, as the NV then accumulates a different phase [1].

From the above, it follows that:

$$P_D\big|_{min}^{max} = P_A\big|_{min}^{max} = n \cdot p \cdot (1-p)^{k-1}. \tag{4.22}$$

The observation of a signal in the region $N_D^{min} \leq N_{|+1,\mathrm{D}\rangle} \leq N_D^{max}$ means that one of the n spins is in state $|+1,\mathrm{D}\rangle$ and thus conditional probability for the second measurement becomes:

$$\overline{P_A}\big|_{min}^{max} = (n-1) \cdot p \cdot (1-p)^{k-2} = \frac{n-1}{n} \cdot \frac{1}{1-p} \cdot P_A\big|_{min}^{max} \geq \frac{n-1}{n} \cdot P_A\big|_{min}^{max}, \tag{4.23}$$

which yields equation 4.21. In a similar way it follows that $\overline{P_A}\big|_{min}^{max} \geq P_A\big|_{min}^{max} \geq \frac{n-1}{n} P_A\big|_{min}^{max}$, if the signal $N_A^{min} \leq N_{|+1,\mathrm{A}\rangle} \leq N_A^{max}$ is generated by m spins that are not necessarily the same as the n spins that generate signal $N_D^{min} \leq N_{|+1,\mathrm{D}\rangle} \leq N_D^{max}$.

The values of C obtained for all areas as indicated in Fig. 4.17 (red rectangles) are shown in Table 4.2. For the areas (i,j) = (1,3) and (2,4) (as in Fig. 4.2d in the

[1] For two P1 centers (out of S1-S4) that simultaneously occupy the same state, summation of coupling strengths and electron spin relaxation play a role for the acquired phase and are discussed in section 4.9.1. Note also that the probability that two or more of the P1s considered here are in the same state simultaneously is small.

main text) we obtain C = 0.22(4) and 0.40(5) respectively, which indicates a single spin. For (i,j) = (3,4) (as in Fig. 4.2d main text), C = 0.47(4) indicating 1 or 2 spins. For areas such as (i,j) = (5,1), (5,2), (5,3) and (5,4) we find C ≈ 1 indicating a large number of spins n. For these areas one would indeed expect a larger number of spins because they correspond to weaker dipolar coupling to the NV. Interestingly, some areas have a C value that is significantly above unity such as (1,4), (2,1) and (2,2). For the area (1,4) the highest value is observed (C = 2.2(2)), this suggests that there might be preferred combinations of $|m_i, i\rangle$ states for $S1$ and $S2$.

i\j	1	2	3	4
1	1.0(2)	1.0(1)	0.22(4)	2.2(2)
2	1.6(2)	1.5(1)	1.20(8)	0.40(5)
3	1.4(1)	0.47(4)	1.14(6)	1.15(6)
4	0.74(7)	1.17(5)	1.0(1)	0.94(4)
5	0.99(4)	0.94(2)	1.00(2)	0.97(2)

Table 4.2: C values for areas as shown in Fig. 4.17

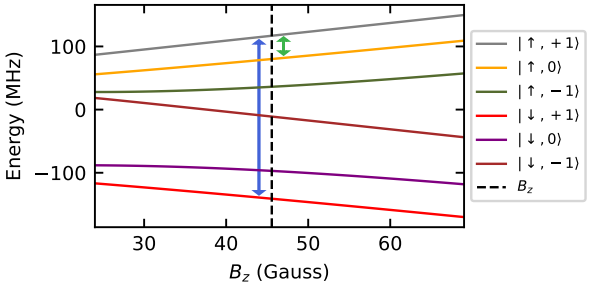

Figure 4.18: **Energy levels for a single P1 center in JT axis D**. Simulation of the six energy levels which are labelled according to their P1 electron and nitrogen nuclear spin state. The black dashed line denotes the experimental magnetic field value. The green (blue) double headed arrow indicates the transition used in the nitrogen (electron) coherence experiments (Fig. 4.6c,d)

4.9.8. Effective gyromagnetic ratio and spin coherence

Here we consider the effect of the electron-nuclear spin mixing due to a relatively large perpendicular hyperfine component ($\gamma_e|\vec{B}| \sim A_\perp$) on the expected coherence times. First we calculate the effective gyromagnetic ratios (labelled $\gamma_{n_{\text{eff}}}$ and $\gamma_{e_{\text{eff}}}$) of the two transitions used in the experiments of Fig. 4.6c, d (main text). We consider the six energy levels of a single P1 center distorted along the JT axis D at the experimental magnetic field, see dashed line Fig. 4.18. Subsequently, we investigate the susceptibility of the energy levels to each component (B_i) of the magnetic field vector ($\vec{B}$). We then determine the tangent of both energy levels connected to the green (blue) double headed arrows at the experimental value of B_i

(see Fig. 4.18) and calculate $\gamma_{n_{\mathrm{eff},i}}$ ($\gamma_{e_{\mathrm{eff},i}}$) as the difference between two tangents. The green (blue) arrow indicates the transition used in Fig. 4.6c, d) in the main text. We find $\gamma_{n_{\mathrm{eff},z}}$ ($\gamma_{e_{\mathrm{eff},z}}$) is more than 10 times larger than $\gamma_{n_{\mathrm{eff},x/y}}$ ($\gamma_{e_{\mathrm{eff},x/y}}$), and therefore we will only consider $\gamma_{n_{\mathrm{eff},z}}$ and $\gamma_{e_{\mathrm{eff},z}}$.

With the approach above, we obtain $\gamma_{n_{\mathrm{eff},z}} = 2\pi\cdot$ 0.206 MHz/G (~$700\gamma_n$) and $\gamma_{e_{\mathrm{eff},z}} = 2\pi\cdot$ 2.60 MHz/G (~$0.93\gamma_e$). Defining $\Gamma = \gamma_{e_{\mathrm{eff},z}}/\gamma_{n_{\mathrm{eff},z}}$, we find $\Gamma = 12.6$. Thus, based on the spin mixing, we would expect the nitrogen nuclear spin coherence to be a factor 12.6 larger than the electron spin coherence. For S3/S4, we find a ratio $T_{2N}^*/T_{2e}^* \sim 12$ between the nitrogen nuclear spin and electron spin coherence (see Table 4.3), which agrees well. However, for spin S1 and S2 we find $T_{2N}^*/T_{2e}^* \sim 4$. The remaining discrepancy by a factor 3 is not yet understood.

4

4.9.9. Coherence times of S3/S4 in $|+1,\mathrm{D}\rangle$

We use the same experimental sequence as in Fig. 4.6 to measure the T_1, T_2^* and T_2 of the electron and nitrogen nuclear spin of S3/S4 (see Fig. 4.19a). The observed coherence times are presented in Table 4.3, where also the coherence times of S1/S2 are shown for completeness.

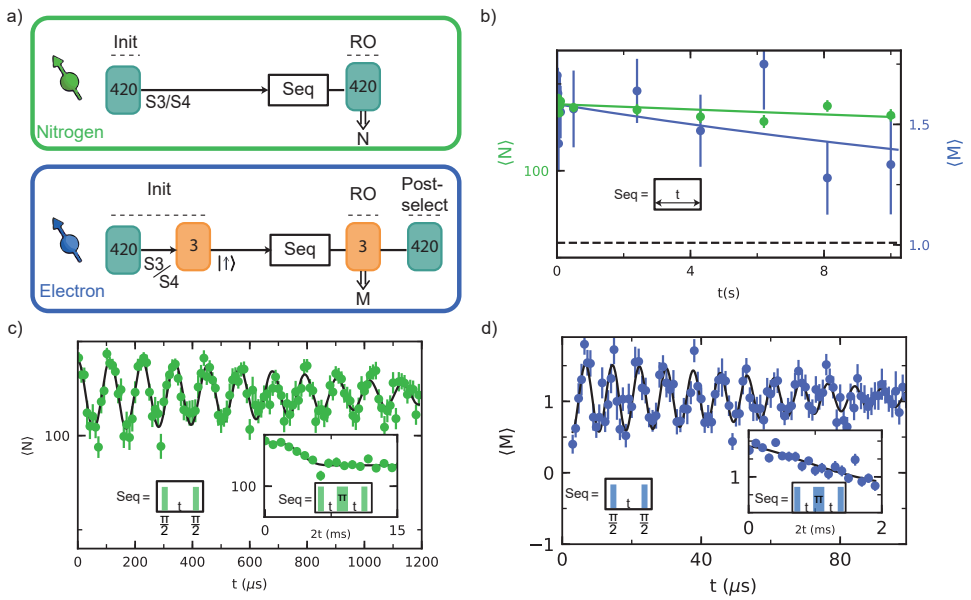

Figure 4.19: **Timescales S3/S4.** (a) Sequence for initialisation of S3/S4 in $|+1,\mathrm{D}\rangle$ (top) and sequence for initialisation of all degrees of freedom of S3/S4 (bottom). These sequences are used in b,c and d. b) Relaxation of a combination of: the nitrogen nuclear spin state, JT axis and charge state (green), and only the electron spin state (blue). We fit (solid lines) both curves to $o + A_0 e^{-t/T}$. c) Ramsey and spin echo (inset) experiments on the nitrogen nuclear spin. d) Ramsey and spin echo (inset) experiments on the electron spin. The obtained coherence times are shown in Table 4.3. See Data analysis (Methods) for the complete fit functions of the Ramsey (equation (4.11)) and spin echo (equation (4.12)) experiments presented in this figure.

	S3/S4	S1/S2
$T_{\|+1,D\rangle}$	104(38) s	40(4) s
T_{1e}	26(20) s	21(7) s
T_{2e}^{*}	82(10) μs	50(3) μs
T_{2N}^{*}	1.06(9) ms	0.201(9) ms
T_{2e}	1.5(1.2) ms	1.00(4) ms
T_{2N}	4.5(4) ms	4.2(2) ms

Table 4.3: Measured coherence and relaxation times of S3/S4 and S1/S2. For experimental data, see Fig. 4.19 and Fig. 4.6 respectively.

4.9.10. Entanglement sequence

In this section the entanglement generation sequence for S1 and S2 is explained in detail. We begin by initializing S1 and S2 in $|\Psi\rangle_{init} = |\uparrow,+1,\mathrm{D}\rangle_{S1}\,|\downarrow,+1,\mathrm{A}\rangle_{S2} = |\uparrow\downarrow\rangle$. Next we apply $U_1 = R_x(\pi/2)_{S1}R_x(\pi/2)_{S2}$, consisting of two $\frac{\pi}{2}$ pulses along x to obtain the state:

$$U_1\,|\Psi\rangle_{init} = \frac{1}{2}\big(-i\,|\uparrow\uparrow\rangle + |\uparrow\downarrow\rangle - |\downarrow\uparrow\rangle - i\,|\downarrow\downarrow\rangle\big) \tag{4.24}$$

This state evolves for time t and accumulates phase due to dipolar coupling J, as $U_{zz}(t) = e^{-i\cdot J\cdot S_z S_z t}$:

$$U_{zz}U_1\,|\Psi\rangle_{init} = \frac{1}{2}e^{i\cdot J\cdot t/4}\big(-i\cdot e^{-i\cdot J\cdot t/2}\,|\uparrow\uparrow\rangle + |\uparrow\downarrow\rangle - |\downarrow\uparrow\rangle - i\cdot e^{-i\cdot J\cdot t/2}\,|\downarrow\downarrow\rangle\big) \tag{4.25}$$

Thereafter, we apply $U_2 = R_x(\pi)_{S1}R_x(\pi)_{S2}$, consisting of two π pulses along X, followed by another free evolution time t:

$$|\Psi\rangle_{final} = U_{zz}U_2U_{zz}U_1\,|\Psi\rangle = \frac{1}{2}e^{i\cdot J\cdot t/2}\big(i\cdot e^{-i\cdot J\cdot t}\,|\uparrow\uparrow\rangle + |\uparrow\downarrow\rangle - |\downarrow\uparrow\rangle + i\cdot e^{-i\cdot J\cdot t}\,|\downarrow\downarrow\rangle\big) \tag{4.26}$$

Rewriting $|S2\rangle$ in the X basis, where $|+\rangle = \frac{|\uparrow\rangle+|\downarrow\rangle}{\sqrt{2}}$ and $|-\rangle = \frac{|\uparrow\rangle-|\downarrow\rangle}{\sqrt{2}}$, results in:

$$|\Psi\rangle_{final} = \tfrac{1}{2}e^{i\cdot J\cdot t/2}\Bigg[\left(\frac{i\cdot e^{-i\cdot J\cdot t}+1}{\sqrt{2}}\right)|\uparrow+\rangle + \left(\frac{i\cdot e^{-i\cdot J\cdot t}-1}{\sqrt{2}}\right)|\uparrow-\rangle + \left(\frac{i\cdot e^{-i\cdot J\cdot t}-1}{\sqrt{2}}\right)|\downarrow+\rangle + \left(\frac{-i\cdot e^{-i\cdot J\cdot t}-1}{\sqrt{2}}\right)|\downarrow-\rangle\Bigg] \tag{4.27}$$

Note that at time $2t = \frac{\pi}{|J|}$, and a negative coupling J, this yields to the entangled state:

$$|\Psi\rangle_{final} = -e^{\frac{-i\pi}{4}}\,\frac{|\uparrow-\rangle + |\downarrow+\rangle}{\sqrt{2}} \tag{4.28}$$

4.9.11. Optimization of initialisation/readout ^{14}N and JT state

Here we explain the optimization of single-shot readout and initialisation of the ^{14}N and JT state of individual P1 centers. We define the fidelity of initialisation of S1 in $|+1,\mathrm{D}\rangle$ and S2, S3/S4 not in that state as

$$F_{S1} = P(N(k+1) > N_{RO} | N(k) > N_{S1}), \tag{4.29}$$

whereas for a mixture of all other possibilities we define

$$F_{notS1} = P(N(k+1) \leq N_{RO} | N(k) \leq N_{notS1}). \tag{4.30}$$

In both cases $P(X|Y)$ is the probability to obtain X given Y. We define the combined initialisation and readout fidelity of these two cases as:

$$F = \frac{F_{S1} + F_{notS1}}{2}. \tag{4.31}$$

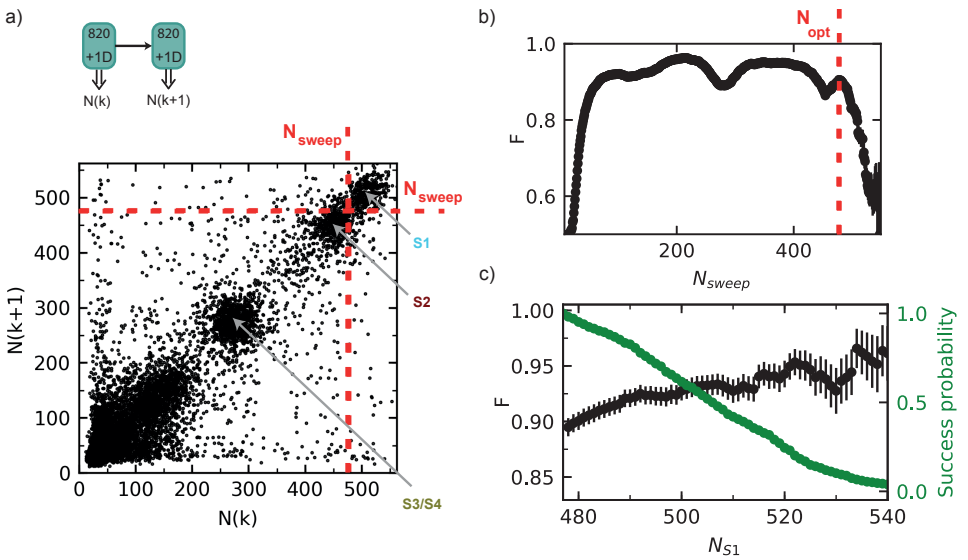

Figure 4.20: **Optimization of combined initialisation and readout of S1 in** $|+1,\mathrm{D}\rangle$. **a)** Full correlation plot for consecutive measurement outcomes $N(k)$ and $N(k+1)$, both for $|+1,\mathrm{D}\rangle$ (same dataset as Fig. 4.3a in the main text). We set the thresholds $N_{S1} = N_{notS1} = N_{RO}$ all equal to N_{sweep} (see main text Fig. 4.3a). Using these thresholds we calculate F as in eq. 4.31 for different values of N_{sweep}. **b)** Fidelity F as a function of N_{sweep}. The red dashed line indicates a local maximum of F (here $N_{sweep} = N_{opt} = 477$) that optimally separates between S1 and S2 under the given constraints ($N_{S1} = N_{notS1} = N_{RO} = N_{sweep}$). The same value ($N_{sweep} = N_{opt}$) is shown by the red dashed lines in (a). **c)** Further improvement of F at the cost of experimental rate is achieved by a stricter initialisation threshold N_{S1}. First we set $N_{notS1} = N_{RO} = N_{opt}$ and vary N_{S1}. The fidelity F is plotted as function of N_{S1} (black). The success probability of initialisation of $S1$ in $|+1,\mathrm{D}\rangle$ as compared to when $N_{S1} = 477$ is plotted in green as a function of N_{S1}.

The correlation plot between two subsequent measurements of K = 820 binned DEER sequences is shown in Fig. 4.20a. First, we find a threshold that separates S1 from other P1 centers by setting N_{S1} = N_{notS1} = N_{RO} all equal to N_{sweep} and calculate the combined initialisation and readout fidelity F while we sweep this parameter. A local maximum N_{opt} = 477 is found separating spins S1 and S2 as shown in Fig. 4.20b (red dashed line). Second, we set N_{RO} = N_{notS1} = N_{opt} to distinguish between *S1* and *not S1* and vary N_{S1} as shown in Fig. 4.20c. As a trade-off between the success rate and fidelity F we choose N_{S1} = 522 to maintain a success probability > 0.2. For Fig. 4.3b in the main text we have thus used N_{notS1} = N_{RO} = 477 and N_{S1} = 522.

Electron spin initialisation and readout

We initialize and measure the electron spin state of P1 centers through a DEER(y) sequence following initialisation of the $|+1, \mathrm{D}\rangle$ or $|+1, \mathrm{A}\rangle$ state. Again, we use the correlation of consecutive measurements $M(k)$ and $M(k+1)$ to determine the combined initialisation and readout fidelity. First, we define the fidelity of preparing $|\uparrow\rangle$ as

$$F_{|\uparrow\rangle} = P(M(k+1) > M_{RO} | M(k) > M_{|\uparrow\rangle}), \tag{4.32}$$

and the fidelity of preparing $|\downarrow\rangle$ as

$$F_{|\downarrow\rangle} = P(M(k+1) \leq M_{RO} | M(k) \leq M_{|\downarrow\rangle}). \tag{4.33}$$

Again, the combined initialisation and readout fidelity is given as

$$F_{|\uparrow\rangle/|\downarrow\rangle} = \frac{F_{|\uparrow\rangle} + F_{|\downarrow\rangle}}{2}. \tag{4.34}$$

We calculate $F_{|\uparrow\rangle/|\downarrow\rangle}$ for a large range of initialisation and readout bin sizes (L) and thresholds ($M_{|\downarrow\rangle}$, $M_{|\uparrow\rangle}$ and M_{RO}). In Fig. 4.21b maximum values of $F_{|\uparrow\rangle/|\downarrow\rangle}$ are shown as a function of success probability. We trade-off $F_{|\uparrow\rangle/|\downarrow\rangle}$ against success probability to obtain a combined initialisation and readout fidelity of $F_{|\uparrow\rangle/|\downarrow\rangle}$ = 0.95(1) while maintaining a success probability above 0.1.

Optimization of sequential initialisation in $|+1, \mathrm{D}\rangle$ and $|+1, \mathrm{A}\rangle$

For entanglement generations of S1 and S2 we optimize for high total initialisation and readout fidelity while maintaining a fast experimental rate. To initialize the P1 centers in the desired $|m_I, i\rangle$ state, we use 4 sequential steps with real time logic. Firstly we use K = 5 DEER measurements on $|+1, \mathrm{A}\rangle$ to quickly assess the likelihood of S2 in this state. If the outcome is below a threshold ($N_{|+1,\mathrm{A}\rangle}$ = 3), we apply fast logic: we abort the sequence, apply an optical reset (section 4.9.6) and start again. If the threshold is passed, we continue. Secondly we repeat this on $|+1, \mathrm{D}\rangle$ to assess the likelihood of S1 in this state. If successful, we continue with DEER repetitions on $|+1, \mathrm{D}\rangle$ and perform a third step after K = 22 to distinguish S1 from S3/S4. To finish the initialization of S1, we continue to K = 820, required to distinguish S1 from S2. Fourthly, we apply DEER sequences on $|+1, \mathrm{A}\rangle$

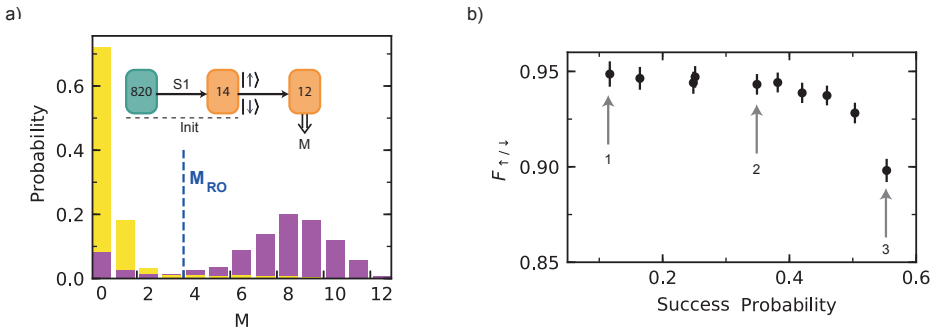

Figure 4.21: **Optimization of combined electron initialisation and readout fidelity.** We trade off fidelity and experimental success rate by setting the thresholds and bin sizes of the DEER(y) sequences used. For optimization, a large range of thresholds and bin sizes are explored. **a)** An exemplary case of probability distributions after initialisation. Here, after preparation of S1 in $|+1,\mathrm{D}\rangle$, the electron spin is initialized through a DEER(y) (L = 14) with thresholds $M_{|\uparrow\rangle}$ (> 1) and $M_{|\downarrow\rangle}$ (≤1) before reading out (L = 12). The parameters in this exemplary case ensure a larger success probability (≈ 0.55) but lower $F_{|\uparrow\rangle/|\downarrow\rangle}$ = 0.90(1) as compared to those in Fig. 4.4d of the main text. **b)** The fidelity $F_{|\uparrow\rangle/|\downarrow\rangle}$ against the success probability of initialisation in $|\uparrow\rangle$. We calculate $F_{|\uparrow\rangle/|\downarrow\rangle}$ for a range of initialisation and readout bin sizes (L) and thresholds $M_{|\downarrow\rangle}$, $M_{|\uparrow\rangle}$ and M_{RO}. Only the maximum fidelities are shown, grouped over 10 intervals between 0.1 and 0.6 success probability. To ensure enough statistics, we only include intervals above 0.1 success probability. Numbered arrows indicate example cases: (1) parameters and probability histogram as shown in Fig. 4.4d in the main text; (2) L = 14 for initialisation, L = 8 for readout, $M_{|\uparrow\rangle}$ (> 8), $M_{|\downarrow\rangle}$ (≤1) and M_{RO} (= 2); (3) corresponds to panel (a).

and hereafter implement fast logic. With S1 initialized in $|+1,\mathrm{D}\rangle$, S2 is more easily distinguished from S3/S4. Therefore we perform the logic after K = 50 DEER sequences. Because consecutive measurements can disturb earlier prepared states, the small number of repetitions for the initialisation of S2 is beneficial for the overall fidelity. The probability to have both P1 centers in the desired state is small, and this limits the experimental rate. By heralding and the use of subsequent fast logic, we significantly speed up because the initialization of S2 is not attempted if the initialization of S1 fails.

After initialisation of the JT and nitrogen state, we perform electron spin initialisation. For electron spin initialisation and readout we optimize in a similar way as described above. However, we now introduce additional measurements in order to take disturbance due to sequential measurements into account and find a best combined initialisation and readout fidelity for both spins. Finally, we optimize the sequential initialisation (S1 in $|\uparrow\rangle$ then S2 in $|\downarrow\rangle$) for a high rate and fidelity but minimal disturbance of the initialized state of the other P1 center.

4.9.12. NV fluorescence rate reference

In this section, we verify that the discrete jumps in the DEER time traces (Fig. 4.2a of the main text) are not due to the changes in the detected fluorescence rate of the NV itself (e.g. due to ionization, spatial or spectral drifts). As shown in Fig. 4.22, we

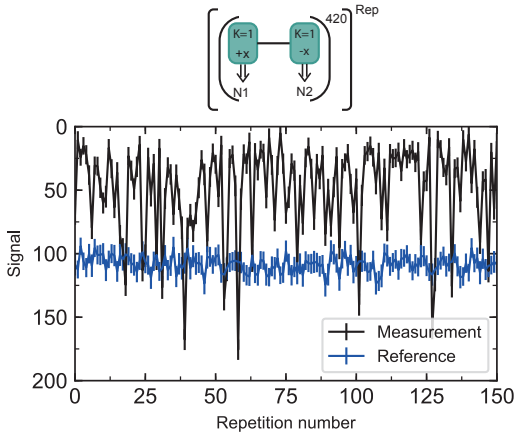

Figure 4.22: **Continuous DEER signal with reference signal.** Top: Experiment in which we alternate between a single DEER sequence (K=1, $f_{+1\mathrm{D}}$ as in main text Fig. 4.2b) with phase $+x$ and one with $-x$ for the final $\pi/2$ pulse. The outcomes N_1 and N_2 are summed in a bin size of 420 to obtain N_{bin1} and N_{bin2}. The reference signal for the NV fluorescence detection rate is defined as N_{ref} = (N_{bin1}+N_{bin2})/2. The measurement signal is given as (2⟨N_{ref}⟩ - N_{bin1} + N_{bin2})/2, here ⟨N_{ref}⟩ is the mean over the full dataset. Bottom: the measurement signal shows similar discrete jumps as in Fig. 4.2a of the main text, while the reference measurement remains approximately constant over time.

repeatedly apply the DEER sequence while alternating between opposite readout bases. We combine these measurements to obtain a continuous DEER signal and a reference of the detected NV fluorescence rate. The DEER signal shows discrete jumps. These jumps are not observed in the reference signal, thus excluding that they are caused by changes in the detected NV fluorescence rate.

Author contributions

MJD, SJHL and THT devised the project and experiments. CEB, MJD, SJHL and HPB constructed the experimental apparatus. MJD and SJHL performed the experiments. MJD, SJHL, HPB, and THT analysed the data. ALM and MJD performed preliminary experiments. MM and DJT grew the diamond sample. MJD, SJHL and THT wrote the manuscript with input from all authors. THT supervised the project.

References

[1] Degen, C. L., Reinhard, F. & Cappellaro, P., *Quantum sensing,* Rev. Mod. Phys. **89**, 035002 (2017).

[2] Waldherr, G. *et al.*, *Quantum error correction in a solid-state hybrid spin register,* Nature **506**, 204 (2014).

[3] Cramer, J. *et al.*, *Repeated quantum error correction on a continuously encoded qubit by real-time feedback,* Nat. Commun. **7**, 1 (2016).

[4] Bradley, C. *et al.*, *A ten-qubit solid-state spin register with quantum memory up to one minute,* Phys. Rev. X **9**, 031045 (2019).

[5] Cai, J., Retzker, A., Jelezko, F. & Plenio, M. B., *A large-scale quantum simulator on a diamond surface at room temperature,* Nat. Phys. **9**, 168 (2013).

[6] Wang, Y. *et al.*, *Quantum Simulation of Helium Hydride Cation in a Solid-State Spin Register,* ACS Nano **9**, 7769 (2015).

[7] Bernien, H. *et al.*, *Heralded entanglement between solid-state qubits separated by three metres,* Nature **497**, 86 (2013).

[8] Hensen, B. *et al.*, *Loophole-free bell inequality violation using electron spins separated by 1.3 kilometres,* Nature **526**, 682 (2015).

[9] Sipahigil, A. *et al.*, *An integrated diamond nanophotonics platform for quantum-optical networks,* Science **354**, 847 (2016).

[10] Awschalom, D. D., Hanson, R., Wrachtrup, J. & Zhou, B. B., *Quantum technologies with optically interfaced solid-state spins,* Nat. Photonics **12**, 516 (2018).

[11] Atatüre, M., Englund, D., Vamivakas, N., Lee, S.-Y. & Wrachtrup, J., *Material platforms for spin-based photonic quantum technologies,* Nat. Rev. Mater. **3**, 38 (2018).

[12] Castelletto, S. & Boretti, A., *Silicon carbide color centers for quantum applications,* J. Phys. Photonics **2**, 022001 (2020).

[13] Abobeih, M. H. *et al.*, *One-second coherence for a single electron spin coupled to a multi-qubit nuclear-spin environment,* Nat. Commun. **9**, 1 (2018).

[14] Sukachev, D. D. *et al.*, *Silicon-vacancy spin qubit in diamond: a quantum memory exceeding 10 ms with single-shot state readout,* Phys. Rev. Lett. **119**, 223602 (2017).

[15] Rose, B. C. *et al.*, *Observation of an environmentally insensitive solid-state spin defect in diamond,* Science **361**, 60 (2018).

[16] Nagy, R. *et al.*, *Quantum properties of dichroic silicon vacancies in silicon carbide,* Phys. Rev. Appl. **9**, 034022 (2018).

[17] Simin, D. *et al.*, *Locking of electron spin coherence above 20 ms in natural silicon carbide,* Phys. Rev. B **95**, 161201 (2017).

[18] Bar-Gill, N., Pham, L. M., Jarmola, A., Budker, D. & Walsworth, R. L., *Solid-state electronic spin coherence time approaching one second,* Nat. Commun. **4**, 1 (2013).

[19] Nagy, R. *et al.*, *High-fidelity spin and optical control of single silicon-vacancy centres in silicon carbide,* Nat. Commun. **10**, 1 (2019).

[20] Koehl, W. F., Buckley, B. B., Heremans, F. J., Calusine, G. & Awschalom, D. D., *Room temperature coherent control of defect spin qubits in silicon carbide,* Nature **479**, 84 (2011).

[21] Maity, S. *et al.*, *Coherent acoustic control of a single silicon vacancy spin in diamond,* Nat. Commun. **11**, 1 (2020).

[22] Green, B. L. *et al.*, *Electronic structure of the neutral silicon-vacancy center in diamond,* Phys. Rev. B **99**, 161112 (2019).

[23] Dolde, F. *et al.*, *Room-temperature entanglement between single defect spins in diamond,* Nat. Phys. **9**, 139 (2013).

[24] Dolde, F. *et al.*, *High-fidelity spin entanglement using optimal control,* Nat. Commun. **5**, 1 (2014).

[25] Van Dam, S. B., Cramer, J., Taminiau, T. H. & Hanson, R., *Multipartite Entanglement Generation and Contextuality Tests Using Nondestructive Three-Qubit Parity Measurements,* Phys. Rev. Lett. **123** (2019), 10.1103/PhysRevLett.123.050401.

[26] Unden, T. K., Louzon, D., Zwolak, M., Zurek, W. H. & Jelezko, F., *Revealing the Emergence of Classicality Using Nitrogen-Vacancy Centers,* Phys. Rev. Lett. **123**, 140402 (2019).

[27] Hou, P. Y. *et al.*, *Experimental Hamiltonian Learning of an 11-Qubit Solid-State Quantum Spin Register,* Chin. Phys. Lett. **36** (2019), 10.1088/0256-307X/36/10/100303.

[28] Vorobyov, V. *et al.*, *Quantum fourier transform for quantum sensing,* arXiv preprint arXiv:2008.09716 (2020).

[29] Kalb, N. *et al.*, *Entanglement distillation between solid-state quantum network nodes,* Science **356**, 928 (2017).

[30] Xiao, X. & Zhao, N., *Proposal for observing dynamic jahn–teller effect by single solid-state defects,* New J. Phys. **18**, 103022 (2016).

[31] Cooper, A., Kyu, W., Sun, C., Jaskula, J.-C. & Cappellaro, P., *Environment-assisted Quantum-enhanced Sensing with Electronic Spins in Diamond,* Phys. Rev. Appl. **10**, 44047 (2019).

[32] Goldstein, G. *et al.*, *Environment-assisted precision measurement,* Phys. Rev. Lett. **106**, 140502 (2011).

[33] Yao, N. Y. *et al.*, *Scalable architecture for a room temperature solid-state quantum information processor,* Nat. Commun. **3**, 1 (2012).

[34] Ping, Y., Lovett, B. W., Benjamin, S. C. & Gauger, E. M., *Practicality of spin chain wiring in diamond quantum technologies,* Phys. Rev. Lett. **110** (2013), 10.1103/PhysRevLett.110.100503.

[35] Yao, N. Y. *et al.*, *Quantum logic between remote quantum registers,* Phys. Rev. A **87**, 22306 (2013).

[36] Schlipf, L. *et al.*, *A molecular quantum spin network controlled by a single qubit,* Sci. Adv. **3**, e1701116 (2017).

[37] Gaebel, T. *et al.*, *Room-temperature coherent coupling of single spins in diamond,* Nat. Phys. **2**, 408 (2006).

[38] Hanson, R., Mendoza, F., Epstein, R. & Awschalom, D., *Polarization and readout of coupled single spins in diamond,* Phys. Rev. Lett. **97**, 087601 (2006).

[39] Hanson, R. & Wrachtrup, J., Private communication.

[40] Dréau, A., Maze, J.-R., Lesik, M., Roch, J.-F. & Jacques, V., *High-resolution spectroscopy of single nv defects coupled with nearby 13 c nuclear spins in diamond,* Phys. Rev. B **85**, 134107 (2012).

[41] Knowles, H. S., Kara, D. M. & Atatüre, M., *Observing bulk diamond spin coherence in high-purity nanodiamonds,* Nat. Mater. **13**, 21 (2014).

[42] Knowles, H. S., Kara, D. M. & Atatüre, M., *Demonstration of a Coherent Electronic Spin Cluster in Diamond,* Phys. Rev. Lett. **117**, 1 (2016).

[43] Belthangady, C. *et al.*, *Dressed-state resonant coupling between bright and dark spins in diamond,* Phys. Rev. Lett. **110**, 157601 (2013).

[44] Shi, F. *et al.*, *Quantum logic readout and cooling of a single dark electron spin,* Phys. Rev. B **87**, 195414 (2013).

[45] Cooper, A., Sun, W. K. C., Jaskula, J.-C. & Cappellaro, P., *Identification and control of electron-nuclear spin defects in diamond,* Phys. Rev. Lett. **124**, 083602 (2020).

[46] Yamamoto, T. *et al.*, *Strongly coupled diamond spin qubits by molecular nitrogen implantation,* Phys. Rev. B **88**, 201201 (2013).

[47] Rosenfeld, E. L., Pham, L. M., Lukin, M. D. & Walsworth, R. L., *Sensing coherent dynamics of electronic spin clusters in solids,* Phys. Rev. Lett. **120**, 243604 (2018).

[48] Grinolds, M. *et al.*, *Subnanometre resolution in three-dimensional magnetic resonance imaging of individual dark spins,* Nat. Nanotechnol. **9**, 279 (2014).

[49] Sun, W. K. C., Cooper, A. & Cappellaro, P., *Improved entanglement detection with subspace witnesses,* Phys. Rev. A **101**, 012319 (2020).

[50] Smith, W., Sorokin, P., Gelles, I. & Lasher, G., *Electron-spin resonance of nitrogen donors in diamond,* Phys. Rev. **115**, 1546 (1959).

[51] Ulbricht, R. *et al.*, *Single substitutional nitrogen defects revealed as electron acceptor states in diamond using ultrafast spectroscopy,* Phys. Rev. B **84**, 165202 (2011).

[52] Deák, P., Aradi, B., Kaviani, M., Frauenheim, T. & Gali, A., *Formation of nv centers in diamond: A theoretical study based on calculated transitions and migration of nitrogen and vacancy related defects,* Phys. Rev. B **89**, 075203 (2014).

[53] De Lange, G. *et al.*, *Controlling the quantum dynamics of a mesoscopic spin bath in diamond,* Sci. Rep **2**, 1 (2012).

[54] Loubser, J. & van Wyk, J., *Electron spin resonance in the study of diamond,* Rep. Prog. Phys. **41**, 1201 (1978).

[55] Zaritskii, I. M. *et al.*, *Spin-lattice relaxation of a Jahn-Teller nitrogen center in diamond,* Sov. phys., Solid state **18**, 1883 (1976).

[56] Shul'man, L. A., Zaritskii, M. I. & Podzyarei, G. A., *Reorientation of the Jahn-Teller distortion in nitrogen impurity centers in diamond,* Sov. phys., Solid State **8**, 1842 (1967).

[57] Ammerlaan, C. A. & Burgemeister, E. A., *Reorientation of nitrogen in type-Ib diamond by thermal excitation and tunneling,* Phys. Rev. Lett. **47**, 954 (1981).

[58] Cook, R. & Whiffen, D. H., *Electron nuclear double resonance study of a nitrogen centre in diamond,* Proc. Math. Phys. Eng. Sci. **295**, 99 (1966).

[59] Dréau, A., Spinicelli, P., Maze, J., Roch, J.-F. & Jacques, V., *Single-shot readout of multiple nuclear spin qubits in diamond under ambient conditions,* Phys. Rev. Lett. **110**, 060502 (2013).

[60] Liu, G.-Q. *et al.*, *Single-shot readout of a nuclear spin weakly coupled to a nitrogen-vacancy center at room temperature,* Phys. Rev. Lett. **118**, 150504 (2017).

[61] Neumann, P. *et al.*, *Single-shot readout of a single nuclear spin,* Science **329**, 542 (2010).

[62] Gühne, O. & Tóth, G., *Entanglement detection,* Phys. Rep. **474**, 1 (2009).

[63] Reiserer, A. *et al.*, *Robust quantum-network memory using decoherence-protected subspaces of nuclear spins,* Phys. Rev. X **6**, 021040 (2016).

[64] Robledo, L. *et al.*, *High-fidelity projective read-out of a solid-state spin quantum register,* Nature **477**, 574 (2011).

[65] Hadden, J. *et al.*, *Strongly enhanced photon collection from diamond defect centers under microfabricated integrated solid immersion lenses,* Appl. Phys. Lett. **97**, 241901 (2010).

[66] Pfaff, W. *et al.*, *Unconditional quantum teleportation between distant solid-state quantum bits,* Science **345**, 532 (2014).

[67] Yeung, T., Le Sage, D., Pham, L. M., Stanwix, P. & Walsworth, R. L., *Anti-reflection coating for nitrogen-vacancy optical measurements in diamond,* Appl. Phys. Lett. **100**, 251111 (2012).

[68] Vandersypen, L. M. & Chuang, I. L., *Nmr techniques for quantum control and computation,* Rev. Mod. Phys. **76**, 1037 (2005).

[69] Warren, W. S., *Effects of arbitrary laser or nmr pulse shapes on population inversion and coherence,* J. Chem. Phys. **81**, 5437 (1984).

[70] Heremans, F., Fuchs, G., Wang, C., Hanson, R. & Awschalom, D., *Generation and transport of photoexcited electrons in single-crystal diamond,* Appl. Phys. Lett. **94**, 152102 (2009).

[71] De Lange, G., Wang, Z., Riste, D., Dobrovitski, V. & Hanson, R., *Universal dynamical decoupling of a single solid-state spin from a spin bath,* Science **330**, 60 (2010).

[72] Robledo, L., Bernien, H., Van Weperen, I. & Hanson, R., *Control and coherence of the optical transition of single nitrogen vacancy centers in diamond,* Physical review letters **105**, 177403 (2010).

5

Nuclear spin coherence

Electron and nuclear spins provide promising qubits for quantum-information processing and quantum networks. Due to their smaller gyromagnetic ratio, nuclear spins provide excellent quantum memories. Here, we first experimentally investigate the host ^{14}N spin of a single NV center and observe a coherence time >60 s, the longest reported for a single solid-state qubit at the time of writing. Secondly, we develop a method of precision spectroscopy to characterize the transverse hyperfine interaction between the ^{14}N spin and the electronic spin of the NV. We show that the same method provides a useful tool for magnetometry of magnetic fields perpendicular to the symmetry axis of the NV, while remaining insensitive to parallel fields. Finally, we provide an outlook on a quantum memory for optical quantum networks that consists of a nuclear spin which is part of a system of coupled defects.

Parts of this chapter have been published in Abobeih et al., Nature **576**, 411 (2019) [1] and Bradley et al., Phys. Rev. X **9**, 031045 (2019) [2]

5.1. Long-lived nuclear quantum memory

Electron and nuclear spins associated with single defects in solids provide promising qubits for quantum-information processing and quantum networks [3, 4]. In these hybrid registers, different types of spins fulfill different roles. Electron spins offer fast control [5–15] and high-fidelity readout [9, 16, 17] and can be used to connect and control nuclear spins [16, 18–23]. Furthermore, electron-electron coupling enables on-chip connectivity between defects [21, 24–27], while coupling to photons [14, 28–32] allows for the realization of long-range entanglement [33–35]. Nuclear spins provide additional qubits with long coherence times that can be used to store and process quantum states [18, 19, 23, 28, 36].

Here we investigate the coherence properties of the host nuclear spin of a single NV center in a diamond containing a natural abundance of ^{13}C spins (1.1%) at cryogenic temperatures (3.7 K). We prepare the ^{14}N spin state using a measurement based initialization technique [17]. Next, we rotate the ^{14}N spin to one of its six cardinal states and initialize the NV electron spin in $|m_s = -1\rangle$. The magnetic field gradient imposed by the electron-nuclear hyperfine interaction induces a frozen core, which suppresses flip-flop interactions between ^{13}C spins and thereby reduces the noise the ^{14}N spin is exposed to. The coherence is investigated under dynamical decoupling.

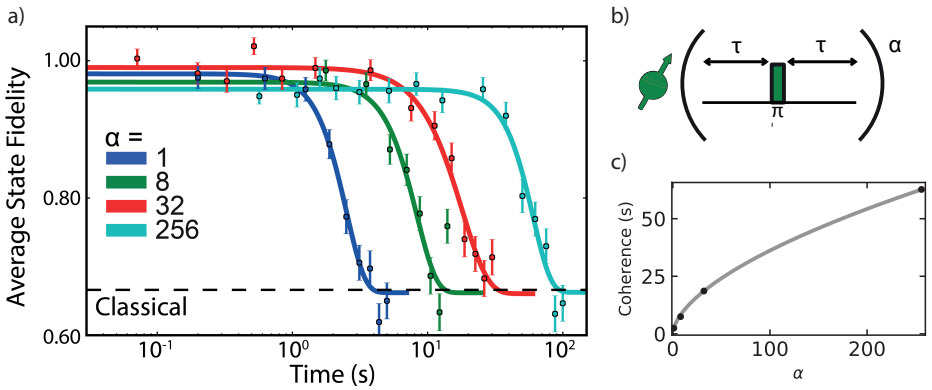

Figure 5.1: **Dynamical decoupling of the ^{14}N spin.** a) For α = 256 pulses, the average state fidelity at 75.3 s is 0.73(3), which is above the bound for a classical memory [37]. b) Dynamical decoupling sequence used in (a). To mitigate pulse errors we alternate the phases of the pulses following the $XY8$ scheme [38]. c) Scaling of the coherence time as a function of the number of pulses α. The solid line is a fit to the power function f(n) = $T_2^{\alpha=1} \cdot \alpha^n$, where $T_2^{\alpha=1}$ is the coherence time for a single pulse. We find n = 0.585(1).

An overview of observed coherence times is shown in table 5.1, with α the number of radio-frequency (rf) pulses. This demonstrates an extension of over three orders of magnitude from the Ramsey decay $T_2^{*,\alpha=0}$ = 23.2(7) ms to $T_2^{\alpha=256}$ = 63(2) s for 256 pulses. This is the longest reported for a single solid-state spin

qubit at the time of writing. The small gyromagnetic ratio of the ^{14}N spin and central position in the frozen core allow for long coherence times. We confirm that arbitrary quantum states can be protected by preparing in the six cardinal states and measuring the average state fidelity under dynamical decoupling. The measured decay curve is shown in Fig. 5.1a. With 256 pulses we measure an average state fidelity exceeding the classical memory bound of $\frac{2}{3}$ [37], at a time of 75.3 s for the ^{14}N spin.

	$T_2^{*,\alpha=0}$ (m_s = -1)	$T_2^{*,\alpha=0}$ (m_s = 0)	$T_2^{\alpha=1}$ (m_s = -1)	$T_2^{\alpha=256}$ (m_s = -1)
^{14}N	23.2(7) ms	25.1(7) ms	2.3(2) s	63(2) s

Table 5.1: Coherence times for the ^{14}N nuclear spin. T_2^* is obtained from a least-squares fit of Ramsey signals, with evolution for the m_s = -1 and m_s = 0 electron spin projections.

For an increasing number of pulses α, we observe a scaling $T_2^\alpha \propto \alpha^n$ with n = 0.585(1) (Fig. 5.1c). For the NV electron in a bath of slowly fluctuating electron spins ($T_2^* \ll \tau_c$, with τ_c the bath correlation time), a scaling of n = 2/3 with the number of dynamical decoupling pulses has been theoretically imposed and experimentally observed by, for example, de Lange et al. [5]. A similar scaling could be expected for a nuclear spin in a nuclear spin bath. However from the central position of the ^{14}N nuclear spin in the frozen core, it is expected that the fluctuating spins it dominantly couples to are at the edge of the core [39]. The coupling strengths to these spins is possibly comparable to the inverse of their correlation time, which could result in a different dephasing mechanism with a scaling that deviates from n = 2/3.

5.2. Thermal echo and its applications

In this section, we investigate applications of an echo sequence that uses the full three level spin-1 manifold of the NV electron and has previously been used in fluorescence thermometry [40]. We will refer to this sequence as the thermal echo. We show that applications beyond thermometry are measurements of non-secular hyperfine terms due to interactions with nuclear spins, and magnetometry of fields perpendicular to the NV symmetry axis. A key property of this sequence is that it extends the NV coherence from T_2^* to T_2 , while remaining susceptible to specific interactions that are usually decoupled from in a Hahn echo using two spin levels. Therefore, information about Hamiltonian terms that describe these interactions can be probed more accurately.

The Hamiltonian of the NV electron is given by [41]:

$$H_e = (\Delta + \Pi_z)J_z^2 + \gamma_e \vec{B} \cdot \vec{J} + \Pi_x(J_y^2 - J_x^2) + \Pi_y(J_x J_y - J_y J_x). \tag{5.1}$$

Here, $\hat{z}$ is the symmetry axis of the NV, J_x, J_y, J_z are the electronic spin-1 operators, $\vec{B}$ the static magnetic field, γ_e the electron gyromagnetic ratio and Δ the zero-field splitting. The terms $\Pi_z = d_\parallel(E_z + \delta_z)$ and $\Pi_{x,y} = d_\perp(E_{x,y} + \delta_{x,y})$ denote the coupling

of the NV to electric fields $\vec{E}$ and crystal strain $\vec{\delta}$, with susceptibilities $d_{\parallel}$ and $d_{\perp}$. Note that crystal strain here has been expressed as an effective electric field [41]. Additionally, the NV center couples to its host ^{14}N spin and surrounding ^{13}C spins via the hyperfine interaction, thus we describe the total system as:

$$H = H_e + \gamma_n \vec{B}\cdot\vec{I} + QI_z^2 + A_{\parallel}J_zI_z + A_{\perp}(J_xI_x + J_yI_y) + \sum_{i=1}^{n}(\vec{J}\cdot\mathbf{C_i}\cdot\vec{I}_i + \gamma_{13C}\vec{B}\cdot\vec{I}_i). \quad (5.2)$$

Here $\vec{I}$ and $\vec{I}_i$ are the nuclear spin-1 and spin-$\frac{1}{2}$ operator vectors, γ_n (γ_{13C}) is the ^{14}N (^{13}C) gyromagnetic ratio, Q the ^{14}N quadrupole splitting, $A_{\parallel}$ ($A_{\perp}$) the parallel (perpendicular) component of the hyperfine interaction with the host ^{14}N spin and $\mathbf{C_i}$ the hyperfine interaction tensor of the NV electron spin with ^{13}C carbon spin with index i.

The thermal echo sequence starts by initializing the host ^{14}N state, then the NV spin is initialized in a superposition (Fig. 5.2). This is followed by two free evolution periods for time τ in between which the superposition state is flipped from $(|0\rangle + |-1\rangle)/\sqrt{2}$ to $(|0\rangle + |+1\rangle)/\sqrt{2}$ by three consecutive pulses $\pi_{+1}\pi_{-1}\pi_{+1}$. At the end of the sequence this phase is converted to population of $|0\rangle$, which is measured. The phase that is accumulated in the laboratory frame during this sequence is given as $e^{-i2\tau\overline{\omega}}$ where $\overline{\omega} = (\omega_- + \omega_+)/2$. Here $\omega_{\pm}$ are the transitions between energy levels $\lambda_{\pm} \leftrightarrow \lambda_0$, labelled according to the NV spin states $m_s = \{0, \pm 1\}$.

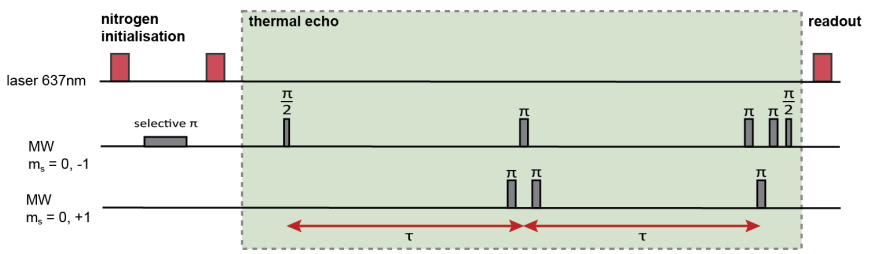

Figure 5.2: **Thermal echo sequence.** Pulse sequence for the thermal echo measurement [40]. The NV center its ^{14}N spin is initialised at the start of the sequence [17]. Thereafter, the electron spin is prepared in a superposition of the states $m_s = 0$ and $m_s = -1$ in the first half of the sequence, and then swapped to a superposition of $m_s = 0$ and $m_s = +1$ for the second half, using a sequence of three closely spaced π pulses. During the evolution time 2τ, phase is accumulated in both the m_s = {0, -1 } as well as in the m_s = {0, +1 } subspace.

Due to the large zero-field splitting ($\Delta \sim 2.88$ GHz) and externally applied magnetic field (~403 G) that is aligned along $\hat{z}$, we consider the unperturbed part of the Hamiltonian in eq. 5.2 to be all terms that are solely along $\hat{z}$ and refer to it as H_0. All off-diagonal terms are small and non-commuting with H_0 and thus non-secular

terms which we refer to as the perturbation Hamiltonian [42]. In the following, for the purpose of simplicity, we consider eq. 5.2 for a single ^{13}C spin (n = 1). This can be generalized to include more spins. From the eigenvalues of H_0, we obtain $\overline{\omega}$ and find:

$$\overline{\omega} = \Delta + \Pi_z, \tag{5.3}$$

indicating linear susceptibility to variations of the zero-field splitting or electric fields along the NV axis. We use perturbation theory to calculate further frequency shifts, $\Delta\overline{\omega}$, of $\overline{\omega}$ due to the perturbation Hamiltonian. We will consider changes in frequency up till second order, and will describe the effect of individual terms of the perturbation Hamiltonian.

First, we consider transverse magnetic and electric fields that directly affect the NV electron spin. We calculate second-order corrections to the eigenvalues of H_0 that emerge from the perturbation Hamiltonian, and use these to obtain $\Delta\overline{\omega}$, which captures the approximated susceptibility to perpendicular magnetic fields B_x, B_y:

$$\Delta\overline{\omega}(m_I, m_C) = \frac{3}{4}\sum_{k=1}^{2} \frac{\gamma_e^2(B_x^2 + B_y^2)}{\Delta + (-1)^k \cdot [m_C \cdot C_{zz} + m_I A_\parallel + \gamma_e B_z]}, \tag{5.4}$$

where m_I, m_C are the spin projections of the host ^{14}N spin and the considered ^{13}C spin respectively. Looking at eq. 5.4 reveals that for our magnetic field regime and the small hyperfine terms (typically C_{zz} ~10 kHz, $A_\parallel$ ~2.16 MHz) differences between nuclear spin projections are negligible. On the other hand, perpendicular fields with magnitudes of ~1 G result in ~1 kHz frequency shifts that can readily be detected. This susceptibility to transverse magnetic fields is useful for directional magnetometry and has been used in our work to accurately align the magnetic field for an atomic-scale imaging method [1]. For transverse electric fields associated with Π_x or Π_y terms we obtain no effect ($\Delta\overline{\omega}$ = 0), these terms are cancelled by the thermal echo.

Second, we consider hyperfine interactions with a nearby ^{13}C spin. From all terms that constitute the hyperfine interaction tensor with the ^{13}C spin, we find a relatively large susceptibility to the C_{zx} term:

$$\Delta\overline{\omega}(m_I, m_C) = m_C \cdot \frac{\gamma_{13C} B_z C_{zx}^2}{4 \cdot (C_{zz}^2 - \gamma_{13C}^2 B_z^2)}. \tag{5.5}$$

This effect is conceptually illustrated in Fig. 5.3. In the large magnetic field regime ($\gamma_{13C}B_z >> C_{zx}, C_{zz}$), the $J_z I_x$ dipolar interaction has little effect on the quantization axis of ^{13}C spins. However, in a moderate magnetic field and given the condition $\gamma_{13C}B_z > C_{zz}$ (as in Fig. 5.3), the quantization axis of ^{13}C spins with spin projection m_C = 1/2, will become more aligned (misaligned for m_C = -1/2) with the NV dipolar field direction. This causes a change in energy of the NV that depends on the ^{13}C state.

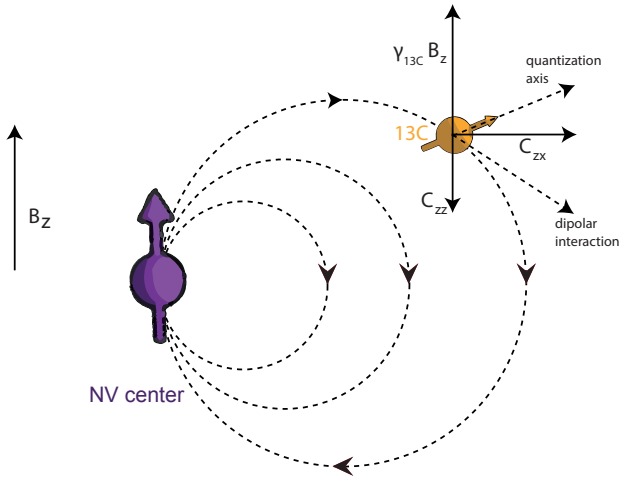

Figure 5.3: **^{13}C spin in a dipole field.** Exemplary case in which the $J_z I_x$ interaction causes its quantization axis to become more aligned with the dipole field direction due to the the NV (m_s = -1) given the condition $C_{zz} < \gamma_{13C} B_z$. The same holds for the NV in m_s = +1, in this case the direction of the dipole field and thus C_{zx} and C_{zz} change to their direct opposite.

The C_{xx} interaction with the ^{13}C spin causes a much smaller frequency shift given by:

$$\Delta\overline{\omega}(m_I, m_C) = \frac{1}{8}\sum_{k=1}^{2} \frac{C_{xx}^2}{\Delta - 2m_C \cdot \gamma_{13C} B_z + (-1)^k \cdot [m_C \cdot C_{zz} - m_I A_\parallel - \gamma_e B_z]} + \frac{1}{16}\sum_{k=1}^{2} \frac{C_{xx}^2}{\Delta + 2m_C \cdot \gamma_{13C} B_z + (-1)^k \cdot [m_C \cdot C_{zz} + m_I A_\parallel + \gamma_e B_z]}. \tag{5.6}$$

Due to our magnetic field regime and the typically small C_{xx} terms of ^{13}C spins (~10 kHz), this results in frequency shifts, $\Delta\overline{\omega}$, of ~mHz which are negligible. The same holds for all other terms of the hyperfine interaction tensor with ^{13}C spins, with the exception of C_{zx} (equation 5.5).

Finally, we consider the host ^{14}N nuclear spin of the NV. Due to its position directly above or below the NV electron spin, the hyperfine interaction does not include $J_z I_x$ but only $J_x I_x$ and $J_y I_y$ nonsecular terms. For this $A_\perp$ interaction, we find:

$$\Delta\overline{\omega}(m_I = \pm 1, m_C) = \frac{A_\perp^2}{\Delta - Q - m_I \cdot \gamma_n B_z + m_C \cdot C_{zz} + \gamma_e B_z} + \frac{1}{2}\frac{A_\perp^2}{\Delta + Q + m_I \cdot \gamma_n B_z - m_C \cdot C_{zz} - m_I A_\parallel - \gamma_e B_z}, \quad (5.7)$$

for $m_I = \pm 1$ and,

$$\Delta\overline{\omega}(m_I = 0, m_C) = \sum_{k=1}^{2} \frac{A_\perp^2}{\Delta + Q - A_\parallel + (-1)^k[\gamma_n B_z - m_C \cdot C_{zz} - \gamma_e B_z]} + \frac{1}{2}\sum_{k=1}^{2} \frac{A_\perp^2}{\Delta - Q + (-1)^k[\gamma_n B_z - m_C \cdot C_{zz} - \gamma_e B_z]} \quad (5.8)$$

for m_I = 0. Because of its proximity to the NV electron, the nonsecular terms are relatively large ($A_\perp$ ~2.6 MHz). In contrast to ^{13}C spins where these terms are negligible, for the ^{14}N spin this interaction results in frequency shifts, $\Delta\overline{\omega}$, of ~kHz. Moreover, we obtain that for m_I = 0 (eq. 5.8) this effect is approximately twice as large as for m_I = ±1 (eq. 5.7). Therefore, up to second order, we expect a ~kHz frequency shift for these different ^{14}N spin states.

5.2.1. Measurement of transverse ^{14}N hyperfine interaction

To probe these frequency shifts we measure $\overline{\omega}$ using the thermal echo sequence, for different ^{14}N states (Fig. 5.4a). Other than a central frequency that shifts for different ^{14}N states, the data shows four equally separated frequencies for each ^{14}N state. Also, the average dephasing time for all ^{14}N states, $\langle T_{2,TE} \rangle$ = 0.27(1) ms, is lower than the measured Hahn echo T_2 = 1.182(5) ms, indicating an additional dephasing mechanism in the thermal echo. We use the knowledge of the previously determined coupling of 27 identified nuclear spins surrounding this NV [1], to find that coupling to surrounding ^{13}C spins with non-negligible C_{zx} hyperfine interaction terms explains the shorter dephasing time. This indicates that other effects such as electric fields, strain or fluctuations of the zero-field splitting Δ due to temperature are not dominant factors for the dephasing. Moreover, from two spins that exhibit strong C_{zx} interactions of 2π·59.21(3) and 2π·41.51(3) kHz [1], we expect four distinct frequencies corresponding to their four two-spin states. For each ^{14}N state the signal fits well to the sum of four frequencies and agrees well with simulated frequency splittings due to these two ^{13}C spins (Fig. 5.4b).

From the average of the four frequencies (Fig. 5.4b, red arrows), we obtain $\overline{\omega}$ which demonstrates a shift for different ^{14}N states due to the $A_\perp$ hyperfine interaction term. For all the other nonsecular terms that we have considered, shifts of $\overline{\omega}$ due to different ^{14}N spin states are negligible. From eqs. 5.7 and 5.8, we only expect the average frequency of the m_I = ±1 states to be shifted with respect to

m_I = 0. However, we note that the m_I = ±1 states are also shifted relative to each other with approximately ~1 kHz. This effect is not captured by eqs. 5.7 and 5.8, and is likely included in higher order perturbation terms. Therefore, to obtain $A_\perp$ we use a least squares fit of the Hamiltonian as given in eq. 5.2 (see sec. 5.5.1). From the fit we obtain $A_\perp$ = -2.652(8) MHz, which is in agreement with Yavkin et al., Chen et al. and Felton et al. [43–46] and provides better precision than previously measured values (see Tab. 5.2).

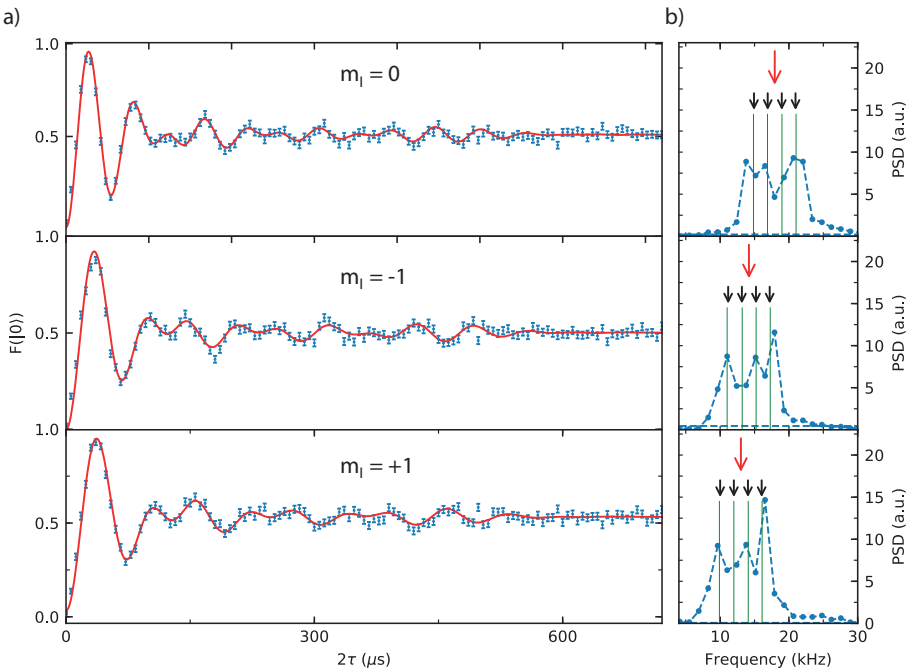

Figure 5.4: **NV electron thermal echo. a)** Thermal echo measurement for different initialized ^{14}N spin states (m_I). The data is fitted to $a - \frac{1}{2}e^{-(2\tau/T_{2,TE})^n} \sum_{j=1}^{j=4} \frac{1}{4} \cos(\omega_j \cdot 2\tau)$. The average of the four fitted frequencies ω_j is defined as $\omega_c = \overline{\omega}$ - $2\pi \cdot$ 2.877658 GHz. We find $T_{2,TE}$ = 0.26(1), 0.27(1) and 0.29(1) ms for m_I = 0,-1 and +1 respectively, all shorter than T_2 = 1.182(5) ms due to coupling to ^{13}C spins. **b)** Fourier transform of (a) with vertical green lines indicating fitted frequencies ω_j. The red arrow demonstrates the average of the four fitted frequencies ω_c. Black arrows demonstrate simulated shifts centered around ω_c due to two ^{13}C spins with a strong $J_z I_x$ interaction.

Ref	$A_\perp$ (MHz)	Temp.
Our measurement	-2.652(8)	3.7 K
2016 Yavkin et al.[43]	-2.7(1)	RT
2015 Chen et al. [44]	-2.62(5)	RT
2009 Felton et al. [45]	-2.70(7)	10-300 K

Table 5.2: Overview of experimentally determined transverse hyperfine parameter.

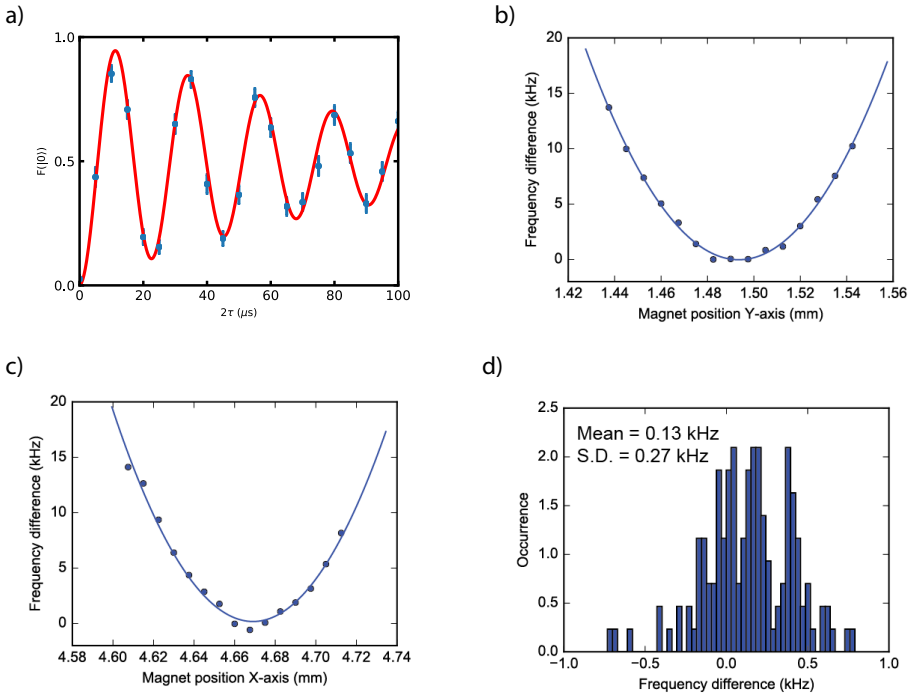

Figure 5.5: **Aligning the magnetic field using a thermal echo sequence. a)** Measurement of the first 100 μs of the thermal echo signal. The signal is fitted to $a\text{-}\frac{1}{2}e^{-(2\tau/T)^n}\cos(\omega_c \cdot 2\tau)$ to obtain a central frequency ω_c, which is minimised when $B_\perp = 0$ (see sec. 5.5.2). The NV ^{14}N spin is initialised in $m_I = 0$ [17]. **b,c)** Magnetic field alignment by scanning the magnet position in two orthogonal directions. The obtained thermal echo frequencies are fitted to a parabolic function to find the optimum position (i.e. minimal ω_c). The plots show the frequency difference $\omega_c/2\pi - 2.877652$ GHz. **d)** Placing the magnet at the optimum position and repeating the measurement 200 times (over a 10-hour period). The obtained average frequency difference is 0.13 kHz, with a standard deviation of 0.27 kHz. Therefore, the total uncertainty for the magnet alignment is estimated to be smaller than ~ 0.4 kHz which corresponds to a perpendicular field of 0.5 Gauss or a misalignment angle of 0.07 degrees.

5.2.2. Directional magnetometry

As described by eq. 5.4, thermal echo measurements are sensitive to transverse magnetic fields. Here we demonstrate directional magnetometry by exploiting this sensitivity to $\hat{x}$,$\hat{y}$ components of the magnetic field. This allows for precise alignment of the external magnetic field which is often desirable for various applications of the NV center. We use a permanent magnet on an XYZ translation stage to control the strength and the direction of a magnetic field of ~403 G. By sweeping the magnet position while implementing the thermal echo sequence we find a minimum of its average frequency at which $B_\perp = \sqrt{B_x^2 + B_y^2} = 0$ (see Supplemen-

tary information sec. 5.5.2 and eq. 5.4). The method is implemented to align the magnetic field via an automatic re-calibration procedure which realizes a misalignment angle <0.07° (Fig. 5.5). We have used this method to help enable the measurement of isolated individual nuclear-nuclear spin interactions to image 27 surrounding nuclear spins with sub-angstrom resolution [1].

5.2.3. ^{14}N thermal echo

Similar as for the NV electron spin, a thermal echo sequence can be applied on the ^{14}N spin-1. We use projective readout of the electronic spin in combination with quantum gate operations (selective π pulses) for initialization and readout of the m_I = 0 nuclear spin state [17]. In between initialization and readout, we implement a thermal echo sequence using rf pulses on the ^{14}N nuclear spin-1 manifold while the NV electron spin is in m_s = -1 (Fig. 5.6).

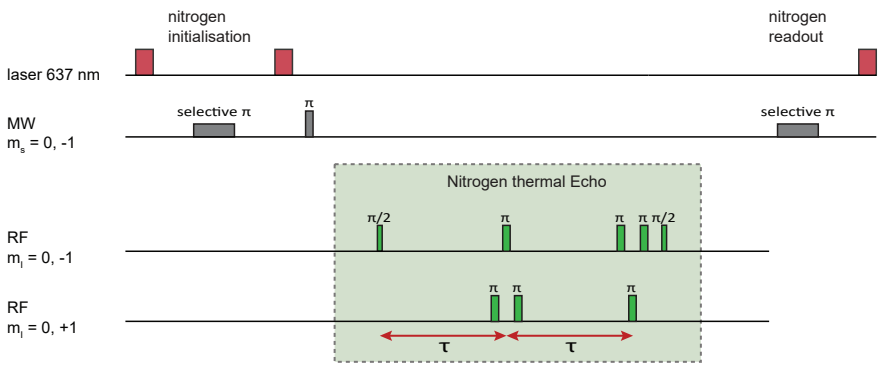

Figure 5.6: **Nitrogen thermal echo sequence.** Pulse sequence for nitrogen thermal echo measurement. The NV ^{14}N spin is initialised and read out via a combination of projective readout of the electronic spin and selective π pulses [17]. After initialisation of the ^{14}N spin, a π pulse rotates the NV electron spin to m_s = -1. The thermal echo prepares a superposition of the states $m_I = 0$ and $m_I = -1$ in the first half of the sequence, and then swaps the state to a superposition of $m_I = 0$ and $m_I = +1$ for the second half, using a sequence of three closely spaced π RF pulses. During the evolution time 2τ, phase is accumulated in both the m_I = {0, -1 } as well as in the m_I = {0, +1 } subspace.

The phase that is accumulated during this sequence is given as $e^{-i2\tau\overline{\nu}}$ where $\overline{\nu} = (\nu_- + \nu_+)/2$. Here $\nu_\pm$ are the transition frequencies between energy levels of the m_I = 0 and $m_I = \pm 1$ ^{14}N spin states. From the unperturbed part of the Hamiltonian, H_0, we find for these transitions that:

$$\overline{\nu} = Q, \tag{5.9}$$

which indicates linear susceptibility to the quadrupole splitting. Furthermore, similar as for the electron thermal echo, this measurement is susceptible to perpendicular magnetic fields. This susceptibility is magnified due to an enhanced gyromagnetic ratio of the ^{14}N spin because of electron-nuclear spin mixing with the NV electron [44].

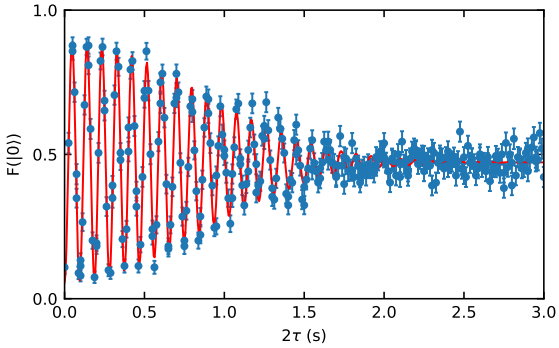

Figure 5.7: **Nitrogen thermal echo.** Nitrogen thermal echo sequence fitted to $a + A \cdot e^{-(2\tau/T_{2,TE})^n} \cos(f_d \cdot 2\tau)$. From the fit we obtain $T_{2,TE}$ = 1.15(2) s, n = 2.1(1) and from the fitted frequency (f_d) and detuning that was set we obtain $|\overline{\nu}|$ = 4951065.683(4) Hz. Using $|\overline{\nu}|$ we obtain the quadrupole splitting Q. The uncertainty in $B_\perp$ during the measurement limits the uncertainty in the obtained Q, and we find Q = -4.95107(1) MHz.

To obtain an accurate measurement of the quadrupole splitting Q, we implement the ^{14}N thermal echo (Fig. 5.7). From the obtained frequency and by taking into account a conservative uncertainty in transverse magnetic field (~1 G), we obtain an estimate of the quadrupole splitting of Q = -4.95107(1) MHz. This closely matches earlier work [45, 46] and provides better precision. Furthermore, we observe a Gaussian dephasing envelope with $T_{2,TE}$ = 1.15(2) s which is shorter than T_2 = 2.3(2) s. The shorter $T_{2,TE}$ with a Gaussian envelope is currently not understood. In contrast to a Gaussian shape, transverse magnetic field noise would result in a nonexponential slow dephasing envelope (see Supplementary Information section 5.5.3). The observed Gaussian shape is likely caused by a linear dependence of frequency $\overline{\nu}$ on the dominant dephasing channel. A possible explanation is direct shifts of the quadrupole splitting Q, due to changes of the electron wave function of the NV under the influence of electric field noise.

5.3. Quantum memories in coupled defects

In this section, we will discuss quantum memories in quantum networks and quantum registers. Elementary nodes of quantum networks contain qubits that are commonly divided in two types: communicators and memories. Communicators are optically active and form elementary links between remote nodes, and can allow readout of quantum states of memory qubits. Memories provide long storage of arbitrary quantum states, and intra-node connectivity with communicator qubits. The NV is naturally surrounded with memory qubits in the form of ^{13}C spins, and its electron spin can selectively address these spins by using two-qubit gates [2, 47]. The NV and surrounding nuclear spins therefore form a versatile multi-qubit node for networks, and state-of-the-art experiments have used ^{13}C spins for entanglement distillation, quantum error correction and three-node entanglement [18, 19, 48, 49].

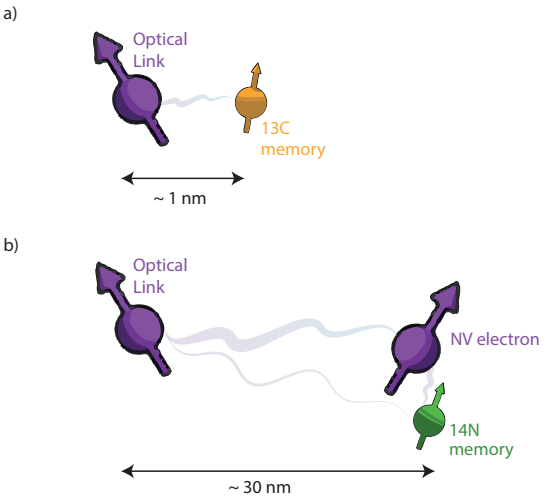

Figure 5.8: **Quantum memories.** a) ^{13}C spin (memory) coupled to an NV center that is used as an optical link (communicator). b) System of coupled NV centers. At ~30 nm, the ^{14}N nuclear spin (memory) is accessible indirectly via a relatively strong (~kHz) electron-electron coupling between NV electrons. The ^{14}N spin is also robust against undesirable changes of the electron state of the optical link NV center (communicator), as the electron-nuclear coupling is much weaker (sub-Hz).

The NV center and surrounding ^{13}C nuclear spins interact via the always-on magnetic hyperfine interaction (Fig. 5.8a). This interaction makes the precession frequency of the ^{13}C memory dependent on the electron spin state of the NV. During remote-entanglement attempts or NV-^{13}C two-qubit gates, multiple electron spin operations are performed. Some imperfections in these operations result in undesirable changes of the NV spin state, which leads to dephasing of ^{13}C spins. Such imperfections include the stochastic nature of the NV electron initialization through spin pumping, initialization infidelity, MW pulse errors and spin flipping due to optical π pulses [50, 51]. Ultimately experiments, such as entanglement distillation and quantum error correction with a single NV and surrounding ^{13}C spins [18, 19, 48], involve an intrinsic trade-off: reducing the hyperfine coupling to the NV center improves the robustness of ^{13}C memories, but reduces gate speeds.

Electron-nuclear defects that are magnetically coupled to an NV provide new opportunities for quantum memories. Figure 5.8b illustrates such a system, which in this case consists of two NV centers that have a separation of ~30 nm. One of the NV centers is a communicator qubit (optical link), whereas the other is dedicated to function as a memory. Because of a difference in gyromagnetic ratio of a factor ~9000 (γ_e/γ_n) between the electron and nitrogen spin, the electron-electron dipolar coupling is nearly four orders of magnitude larger than the electron-nuclear dipolar coupling. At their separation of ~30 nm, the two NVs are magnetically coupled by a relatively strong (~kHz) electron-electron dipolar interaction, while the electron-nuclear interaction is weak. Nevertheless the nitrogen spin on the memory NV is

indirectly accessible for the communicator NV, via the electron spin of the memory NV.

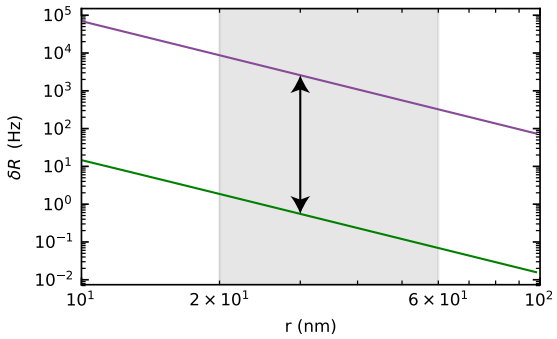

Figure 5.9: **Qubit precession frequency dependence.** Simulated difference of precession frequency (δR) of a ^{14}N spin qubit in the subspace m_I = {0,+1} (green), and the electron spin qubit in the subspace m_s = {0,-1} (purple) of the memory NV upon changing electron state of the optical link NV. δR is plotted as a function of separation distance r between the two NV centers. The black double sided arrow shows nearly four orders of magnitude difference.

Moreover, the weaker electron-nuclear dipolar interaction (sub-Hz) ensures that the nuclear memory is well-isolated and robust against undesirable changes of the electron state of the communicator NV. In Fig. 5.9 we simulate the difference in precession frequency, δR, of the ^{14}N nuclear spin qubit and electron spin qubit of the memory NV, upon changing the electron state of the optical link NV. This simulation is performed for two NV centers with different diamond crystal orientations and at low magnetic field (B_z = 40 G along the communicator NV axis), such that the quantization axes are only slightly tilted from the direction of the zero field splitting Δ and the spin transitions are detuned to suppress mutual spin flip-flops. For separation distances of 20-60 nm, δR is on the order ~kHz for the electron spin, whereas below ~Hz for the nitrogen spin on the memory NV. This indicates an accessible and yet robust nuclear quantum memory in a system of coupled NV centers.

5.4. Conclusions

In conclusion, we have shown a coherence time >60 s for the host ^{14}N spin of a single NV center, which demonstrates it to be an excellent quantum memory. Moreover, we have developed a method for precision spectroscopy of the transverse hyperfine interaction between the host ^{14}N and electron spin of the NV, as well as the quadrupole splitting of the ^{14}N spin. Also, we demonstrate the thermal echo sequence to be a useful tool for magnetometry of perpendicular magnetic fields. Finally, we have provided an outlook for a ^{14}N nuclear quantum memory in a system of coupled NVs. The simulated qubit precession frequency dependence of a ^{14}N spin memory suggests it to be a robust memory in quantum network nodes consisting of magnetically coupled NVs.

5.5. Supplementary information

5.5.1. Obtained frequencies and used parameters

In this section we provide an overview of the used Hamiltonian parameters for the least squares fit of $A_\perp$, as well as the difference frequencies of the electron thermal echo measurements.

Parameter	Estimated value	Ref.
Q	-4.945 MHz	[46]
$A_\parallel$	-2.162 MHz	[46]
γ_e	2.8031 MHz/G	[45]
γ_n	-0.3077 kHz/G	[52]
Δ	2.877652 GHz	-
B_z	403.553 G	-
B_x, B_y	0 G	-

Table 5.3: Overview of parameters used for least squares fit of $A_\perp$ as explained in section 5.2.1.

Difference of $\overline{\omega}$ for ^{14}N states:	Measured (kHz)	Theory (kHz)
$m_{I=0} - m_{I=-1}$	3.75(5)	3.779
$m_{I=0} - m_{I=+1}$	4.92(5)	4.903

Table 5.4: Overview of differences between the measured frequencies $\overline{\omega}$ for the ^{14}N states, as shown in Fig. 5.4.

As the method of obtaining $A_\perp$ (sec. 5.2.1) relies on the difference of $\overline{\omega}$ between different ^{14}N spin states, it does not strongly depend on the parameters given in table 5.3. Up till second order, this is apparent from the calculated shifts of $\overline{\omega}$ (eq. (5.7), (5.8)). Also in the least squares fit, the obtained value and uncertainty for $A_\perp$ = -2.652(8) MHz allow for an uncertainty of individual parameters of 1 G for B_z, B_x, B_y, or a 100 kHz uncertainty of Δ, Q or $A_\parallel$.

5.5.2. Derivation of minimum perpendicular magnetic field

Here we include a derivation following ref. [53], which analytically shows that $B_\perp$ = 0 if the average, $\overline{\omega}$, of the transitions between the ground state energy level λ_0 and λ_{-1},λ_{+1} is minimized. We consider the Hamiltonian of the NV electron spin as in eq. 5.1 but omit electric field dependence and, without loss of generality, have set the perpendicular magnetic field along $\hat{x}$:

$$H_e = \Delta J_z^2 + \gamma_e B_z J_z + \gamma_e B_\perp J_x. \tag{5.10}$$

We consider the regime where $0 < \gamma_e B_z < \Delta$, and diagonalize the Hamiltonian to find the analytical form:

$$\overline{\omega} = 2^{\frac{2}{3}} \frac{2^{\frac{2}{3}} G + H^2}{4H}, \tag{5.11}$$

where we have defined the functions F, G and H as:

$$F(B_z, B_\perp) = \Delta(3^2 \gamma_e^2 (B_\perp^2 - 2B_z^2) + 2\Delta^2) \tag{5.12}$$

$$G(B_z, B_\perp) = 3\gamma_e^2 (B_\perp^2 + B_z^2) + \Delta^2 \tag{5.13}$$

$$H(F, G) = \left(F + \sqrt{F^3 - 4G^2} \right)^{\frac{1}{3}}. \tag{5.14}$$

We take the partial derivative of $\overline{\omega}$ with respect to $B_\perp$ which results in:

$$\frac{\delta \overline{\omega}}{\delta B_\perp} = \frac{2^{\frac{2}{3}}}{4} \left(2^{\frac{2}{3}} \left(\frac{1}{H} \frac{\delta G}{\delta B_\perp} - \frac{G}{H^2} \frac{\delta H}{\delta B_\perp} \right) + \frac{\delta H}{\delta B_\perp} \right) \tag{5.15}$$

We find the partial derivatives are given by:

$$\frac{\delta G}{\delta B_\perp} = 6\gamma_e^2 B_\perp \tag{5.16}$$

$$\frac{\delta F}{\delta B_\perp} = 18\Delta\gamma_e^2 B_\perp \tag{5.17}$$

$$\frac{\delta H}{\delta B_\perp} = \frac{\delta}{\delta B_\perp} \left(F + \sqrt{F^3 - 4G^2} \right)^{\frac{1}{3}} \tag{5.18}$$

$$= \frac{1}{3H^2} \left(\frac{\delta F}{\delta B_\perp} + \frac{1}{\sqrt{F^3 - 4G^2}} \left(3F^2 \frac{\delta F}{\delta B_\perp} - 8G \frac{\delta G}{\delta B_\perp} \right) \right).$$

In the considered regime $0 < \gamma_e B_z < \Delta$ we find for $B_\perp = 0$ that $H \neq 0$ and $\sqrt{F^3 - 4G^2} \neq 0$. Thus we find the partial derivatives in eqs. 5.16,5.17,5.18 to be 0 for $B_\perp = 0$. Therefore the derivative of $\overline{\omega}$ with respect to $B_\perp$ is 0

$$\frac{\delta \overline{\omega}}{\delta B_\perp} = 0, \tag{5.19}$$

and for this regime $\overline{\omega}(B_\perp = 0)$ is at a minimum. As shown in ref. [53], for more elaborate models of the system such as including the host ^{14}N or strain terms, eq. 5.19 holds when using second-order perturbation theory.

5.5.3. Effect of magnetic field noise on ^{14}N thermal echo

In this section, we numerically simulate the thermal echo sequence on the ^{14}N spin-1 under Gaussian distributed quasi-static perpendicular magnetic field noise. This simulation is shown in Fig. 5.10 for $\langle B_\perp \rangle = 0$, and a conservative estimate of 1 G for the standard deviation, σ, of the perpendicular magnetic field. The simulated dephasing envelope resembles a nonexponential slow decay, which is similar as analytically derived for the decay of Rabi oscillations under quasi-static magnetic field noise by Dobrovitski et al. [54]. The simulated envelope shape is in contrast with the measured dephasing envelope which resembles a Gaussian decay (Fig. 5.7). This suggests that quasi-static perpendicular magnetic field noise is not the dominant dephasing mechanism of the ^{14}N thermal echo measurement in Fig. 5.7.

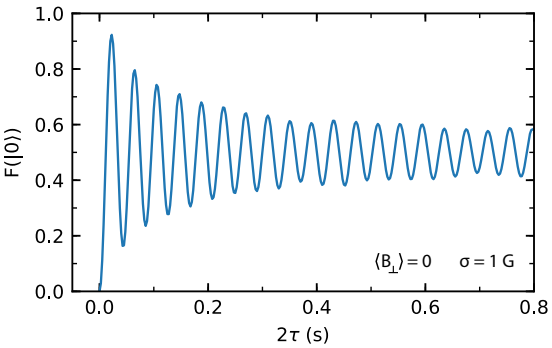

Figure 5.10: **Simulation of the nitrogen thermal echo.** The simulated fidelity of the NV electron spin after a nitrogen thermal echo sequence (see Fig. 5.6), under Gaussian distributed perpendicular magnetic field noise, $\langle B_\perp \rangle = 0$, with standard deviation $\sigma = 1$ G. Numerical simulations of 10^3 sampled $B_\perp$ values from this distribution are performed and averaged to emulate quasi-static Gaussian distributed noise.

Author contributions

M.J. Degen, C.E. Bradley, M.H. Abobeih, J. Randall and T.H. Taminiau devised the experiments in this chapter. M.J. Degen, C.E. Bradley and J. Randall performed the experiments in this chapter. M.J. Degen, C.E. Bradley, M.H. Abobeih, J. Randall and T.H. Taminiau analysed the data. M.J. Degen performed simulations, J. Randall and R. Gharibaan did the derivation in sec. 5.5.2 in this chapter. M.J. Degen wrote this chapter. T. H. Taminiau supervised the project. The results in this chapter have been incorporated in two publications, which are not reproduced here [1, 2].

References

[1] Abobeih, M. *et al.*, *Atomic-scale imaging of a 27-nuclear-spin cluster using a quantum sensor,* Nature **576**, 411 (2019).

[2] Bradley, C. E. *et al.*, *A ten-qubit solid-state spin register with quantum memory up to one minute,* Phys. Rev. X **9**, 031045 (2019).

[3] Awschalom, D. D., Hanson, R., Wrachtrup, J. & Zhou, B. B., *Quantum technologies with optically interfaced solid-state spins,* Nat. Photonics **12**, 516 (2018).

[4] Zwanenburg, F. A. *et al.*, *Silicon quantum electronics,* Reviews of modern physics **85**, 961 (2013).

[5] De Lange, G., Wang, Z., Riste, D., Dobrovitski, V. & Hanson, R., *Universal dynamical decoupling of a single solid-state spin from a spin bath,* Science **330**, 60 (2010).

[6] Fuchs, G. D., Dobrovitski, V. V., Toyli, D. M., Heremans, F. J. & Awschalom, D. D., *Gigahertz dynamics of a strongly driven single quantum spin,* Science **326**, 1520 (2009).

[7] Christle, D. J. *et al.*, *Isolated spin qubits in sic with a high-fidelity infrared spin-to-photon interface,* Phys. Rev. X **7**, 021046 (2017).

[8] Seo, H. *et al.*, *Quantum decoherence dynamics of divacancy spins in silicon carbide,* Nat. Commun. **7**, 12935 (2016).

[9] Sukachev, D. D. *et al.*, *Silicon-vacancy spin qubit in diamond: a quantum memory exceeding 10 ms with single-shot state readout,* Phys. Rev. Lett. **119**, 223602 (2017).

[10] Iwasaki, T. *et al.*, *Germanium-vacancy single color centers in diamond,* Sci. Rep. **5**, 12882 (2015).

[11] Siyushev, P. *et al.*, *Optical and microwave control of germanium-vacancy center spins in diamond,* Phys. Rev. B **96**, 081201 (2017).

[12] Becker, J. N. *et al.*, *All-optical control of the silicon-vacancy spin in diamond at millikelvin temperatures,* Phys. Rev. Lett. **120**, 053603 (2018).

[13] Pingault, B. *et al.*, *Coherent control of the silicon-vacancy spin in diamond,* Nat. Commun. **8**, 15579 (2017).

[14] Trusheim, M. E. *et al.*, *Transform-limited photons from a coherent tin-vacancy spin in diamond,* Phys. Rev. Lett. **124**, 023602 (2020).

[15] Rugar, A. E., Dory, C., Sun, S. & Vučković, J., *Characterization of optical and spin properties of single tin-vacancy centers in diamond nanopillars,* Phys. Rev. B **99**, 205417 (2019).

[16] Pla, J. J. *et al.*, *High-fidelity readout and control of a nuclear spin qubit in silicon,* Nature **496**, 334 (2013).

[17] Robledo, L. *et al.*, *High-fidelity projective read-out of a solid-state spin quantum register,* Nature **477**, 574 (2011).

[18] Cramer, J. *et al.*, *Repeated quantum error correction on a continuously encoded qubit by real-time feedback,* Nat. Commun. **7**, 11526 (2016).

[19] Waldherr, G. *et al.*, *Quantum error correction in a solid-state hybrid spin register,* Nature **506**, 204 (2014).

[20] Wolfowicz, G. *et al.*, *29si nuclear spins as a resource for donor spin qubits in silicon,* New J. Phys. **18**, 023021 (2016).

[21] Tosi, G. *et al.*, *Silicon quantum processor with robust long-distance qubit couplings,* Nat. Commun. **8**, 450 (2017).

[22] Metsch, M. H. *et al.*, *Initialization and readout of nuclear spins via a negatively charged silicon-vacancy center in diamond,* Phys. Rev. Lett. **122**, 190503 (2019).

[23] Hensen, B. *et al.*, *A silicon quantum-dot-coupled nuclear spin qubit,* Nature Nanotechnology **15**, 13 (2020).

[24] Dolde, F. *et al.*, *Room-temperature entanglement between single defect spins in diamond,* Nature Physics **9**, 139 (2013).

[25] Dolde, F. *et al.*, *High-fidelity spin entanglement using optimal control,* Nature Communications **5**, 3371 (2014).

[26] Yamamoto, T. *et al.*, *Strongly coupled diamond spin qubits by molecular nitrogen implantation,* Phys. Rev. B **88**, 201201 (2013).

[27] He, Y. *et al.*, *A two-qubit gate between phosphorus donor electrons in silicon,* Nature **571**, 371 (2019).

[28] Yang, S. *et al.*, *High-fidelity transfer and storage of photon states in a single nuclear spin,* Nat. Photonics **10**, 507 (2016).

[29] Togan, E. *et al.*, *Quantum entanglement between an optical photon and a solid-state spin qubit,* Nature **466**, 730 (2010).

[30] Christle, D. J. *et al.*, *Isolated spin qubits in sic with a high-fidelity infrared spin-to-photon interface,* Phys. Rev. X **7**, 021046 (2017).

[31] Sipahigil, A. *et al.*, *An integrated diamond nanophotonics platform for quantum-optical networks,* Science **354**, 847 (2016).

[32] Evans, R. E. *et al.*, *Photon-mediated interactions between quantum emitters in a diamond nanocavity,* Science **362**, 662 (2018).

[33] Bernien, H. *et al.*, *Heralded entanglement between solid-state qubits separated by three metres,* Nature **497**, 86 (2013).

[34] Hensen, B. *et al.*, *Loophole-free Bell inequality violation using electron spins separated by 1.3 kilometres,* Nature **526**, 682 (2015).

[35] Humphreys, P. C. *et al.*, *Deterministic delivery of remote entanglement on a quantum network,* Nature **558**, 268 (2018).

[36] Maurer, P. C. *et al.*, *Room-temperature quantum bit memory exceeding one second,* Science **336**, 1283 (2012).

[37] Massar, S. & Popescu, S., *Optimal extraction of information from finite quantum ensembles,* Phys. Rev. Lett. **74**, 1259 (1995).

[38] Gullion, T., Baker, D. B. & Conradi, M. S., *New, compensated carr-purcell sequences,* J. Magn. Reson. **89**, 479 (1990).

[39] Bakker, M., *Frozen Core Spin Dynamics in Diamond* (MSc Thesis, Delft University of Technology, 2015).

[40] Toyli, D. M., de las Casas, C. F., Christle, D. J., Dobrovitski, V. V. & Awschalom, D. D., *Fluorescence thermometry enhanced by the quantum coherence of single spins in diamond,* Proc. Natl. Acad. Sci. **110**, 8417 (2013).

[41] Doherty, M. W. *et al.*, *The nitrogen-vacancy colour centre in diamond,* Physics Reports **528**, 1 (2013).

[42] Edén, M., *Zeeman truncation in nmr. i. the role of operator commutation,* Concepts in Magnetic Resonance Part A **43**, 91 (2014).

[43] Yavkin, B., Mamin, G. & Orlinskii, S., *High-frequency pulsed endor spectroscopy of the nv- centre in the commercial hpht diamond,* Journal of Magnetic Resonance **262**, 15 (2016).

[44] Chen, M., Hirose, M. & Cappellaro, P., *Measurement of transverse hyperfine interaction by forbidden transitions,* Phys. Rev. B **92**, 020101 (2015).

[45] Felton, S. *et al.*, *Hyperfine interaction in the ground state of the negatively charged nitrogen vacancy center in diamond,* Physical Review B **79**, 075203 (2009).

[46] Smeltzer, B., McIntyre, J. & Childress, L., *Robust control of individual nuclear spins in diamond,* Physical Review A **80**, 050302 (2009).

[47] Taminiau, T. H. *et al.*, *Detection and control of individual nuclear spins using a weakly coupled electron spin,* Phys. Rev. Lett. **109**, 137602 (2012).

[48] Kalb, N. *et al.*, *Entanglement distillation between solid-state quantum network nodes,* Science **356**, 928 (2017).

[49] Pompili, M. *et al.*, *Realization of a multi-node quantum network of remote solid-state qubits,* arXiv preprint arXiv:2102.04471 (2021).

[50] Kalb, N., Humphreys, P. C., Slim, J. & Hanson, R., *Dephasing mechanisms of diamond-based nuclear-spin memories for quantum networks,* Physical Review A **97**, 062330 (2018).

[51] Beukers, H., *Improving coherence of quantum memory during entanglement creation between nitrogen vacancy centres in diamond* (MSc Thesis, Delft University of Technology, 2019).

[52] Cramer, J., *Quantum error correction with spins in diamond* (PhD Thesis, Delft University of Technology, 2016).

[53] Gharibaan, R., *Parameter estimation of the Hamiltonian of the nitrogen-vacancy center in diamond* (BSc Thesis, Delft, University of Technology, 2019).

[54] Dobrovitski, V., Feiguin, A., Hanson, R. & Awschalom, D., *Decay of rabi oscillations by dipolar-coupled dynamical spin environments,* Physical review letters **102**, 237601 (2009).

6

Conclusion and outlook

In this chapter, we will summarize the results of this thesis. Thereafter, we will give an overview of near-term research and devices that can be explored next. Finally, we will discuss how to move forward towards building larger quantum networks.

6.1. Summary

The work in this thesis is summarized as follows:

- We investigate ion implantation and find that nitrogen implantation and subsequent annealing yields implanted NV centers with predominantly broad optical transitions (>1 GHz) and substantially higher strain than NV centers formed from native nitrogen impurities. This indicates that methods for creating implanted NV centers should be re-investigated, addressing local lattice damage associated with implanted nitrogen. These results thus show that improvements are required to create coupled defects for quantum networks by implantation.

- We demonstrate that single P1 centers can be controlled for multi-defect quantum registers. By using projective measurements we exploit the multiple degrees of freedom of these defects and develop selective control of individual P1 centers that are part of a spin bath surrounding an NV. The developed initialisation, control and single-shot readout techniques are used to demonstrate entanglement between two P1 centers. These results demonstrate an alternative approach to obtain multi-defect quantum registers and provide a proof-of-principle towards using dark electron-nuclear spin defects as qubits for quantum sensing, computation and networks.

- For the host ^{14}N spin of a single NV center we show a coherence time >60 s, which demonstrates it to be an excellent quantum memory. Also, our simulations show that the ^{14}N spin can be used as a robust quantum memory in a system of coupled NVs.

- We demonstrate a precision spectroscopy method to measure specific interactions of the NV such as the transverse hyperfine interaction, quadrupole interaction or its interaction with transverse magnetic fields, while extending coherence from T_2^* to T_2. This method could improve the understanding of the NV center, and its Hamiltonian parameters. Additionally, it provides a technique for magnetic field alignment.

6.2. Future research and quantum devices in diamond

Here we will discuss the implications of our research and other progress for the future of quantum devices in diamond. Among others, we will address the creation óf and near-term future directions fór devices that consist of multiple coupled NVs or an NV coupled to P1 centers for quantum processors and quantum networks.

The development of multi-defect devices that contain NV centers still face challenges towards unlocking their full potential as quantum processors and quantum network nodes. In particular, the need for high fabrication yield of devices with coherent optical transitions, further improvements of control techniques and the demonstration of robustness against optical excitation.

6.2.1. NV center creation

A key challenge for nanoscale diamond devices with embedded NV centers is to reliably obtain spectral stability and long spin coherence times. NV centers in such devices are mainly affected by fabrication procedures [1, 2], surface effects [3–5] and implantation damage [6].

Ion implantation

In this thesis we studied the NV creation method as proposed by Chu et al. [7] that employs implantation followed by high-temperature annealing. We conclude that this method does not routinely produce narrow-optical-linewidth (<500 MHz) NV centers. This conclusion is in line with later work by Kasperczyk et al. [1] and provides the insight that in order to routinely produce narrow-optical-linewidth implanted NV centers, NV engineering procedures should be re-investigated. For example by investigating shallow implantation energies (<12 keV) in combination with diamond overgrowth techniques [8]. With a lower implantation energy there is likely less lattice damage near the stopping point of the nitrogen atom, and overgrowth can be used to increase the distance to surface charges and surface spins that are known to decrease coherence [3–5] and fluorescence contrast [9]. Despite these findings, the work in chapter 3 suggests that narrow-optical-linewidth NV centers may be formed from native nitrogen in diamond after implantation. In other work the mechanism of vacancy creation by electron irradiation followed by recombination with native nitrogen has produced optically coherent NV centers [10], and the same mechanism could be responsible for the generation of NV centers when implanting nitrogen or ^{12}C atoms. Such a mechanism cannot be used to create NVs with high lateral positional accuracy (<50 nm). However, in combination with 2D nitrogen-doped layers, it can provide the capability to embed coherent NVs in well-defined device layers. This is a useful tool that can find several applications, for example for the creation of high-quality NV centers near diamond surfaces for sensing of single molecules or proteins [11, 12].

Laser writing and nitrogen doping

Apart from implantation techniques, in recent years exciting progress has been made in alternative techniques to create NV centers. For example, using diamond growth for doping of defects within 1-2 nm thick layers [13–15], and another the creation of vacancies locally [15–18]. Particularly promising are recently developed laser writing techniques, in which laser pulses are used to create and diffuse vacancies in the diamond lattice to recombine with native nitrogen atoms. Due to the nonlinear interaction of the laser pulse with the diamond lattice, a factor 4.5 higher than the diffraction-limited spatial resolution has been achieved, resulting in an accuracy in the lateral direction of ~40 nm [17]. Furthermore, a yield of ~50% was achieved for narrow-optical-linewidths (<500 MHz) NV centers (from a sample size of 50) [16]. Although more statistics will give better insights in the yield of narrow-optical-linewidth NV centers and reproducibility of this method, this progress highlights a promising path towards controlled engineering of NV centers.

The demonstrated spatial accuracy of this method - if combined with depth positioning using delta doping of nitrogen impurities - suffices for accurate 3D positioning, which could achieve multi-defect devices of several magnetically coupled NV centers or precise placement within photonic cavities. Yet the employability of such devices will depend on the engineering of precisely nitrogen-doped diamond samples, such that the nitrogen concentration is at an appropriate level for conversion to NV centers without the unconverted nitrogen (P1 centers) drastically inhibiting coherence times. In short, it is likely that this path will result in novel devices in the near future with a range of applications in quantum information processing or sensing, yet at the current stage there are still open questions to be answered.

6.2.2. Multi-defect devices with P1 centers

The ability to control dark electron-spin defects that cannot be optically detected but which surround a single optically active defect has gained interest, as harnessing such defects would open new opportunities in quantum information processing and quantum sensing. High-quality initialisation, measurement and control of multi-qubit quantum states are tools which are required to exploit such spins as a resource in multi-defect systems. In chapter 4 of this thesis, we have demonstrated progress towards such tools on dark defects (P1 centers) surrounding an NV. Here we will address challenges and open research questions concerning this system. Some of such are: improvements of initialisation, measurement and control techniques, the robustness of P1 centers under optical excitation, further control techniques for nuclear spins associated with P1s, and understanding of its energy level structure within the diamond band gap. There are several paths that can be explored to address these points, which we will describe below.

Initialisation, readout and control

A straightforward improvement in the initialisation rate and fidelity of single P1 centers can be achieved simply by improving the single-shot NV readout fidelity. Different strain regimes can reduce the excited state spin-mixing and thus improve the cyclicity of the E_y optical transition [19]. This will also grant access to the E_x transition that typically demonstrates better cyclicity than the E_y transition. Such strain regimes can be accessed using DC stark tuning and will likely improve the NV readout fidelity. Moreover, the employed initialisation methods in chapter 4 rely on heralded state preparation. That is, before running each experiment, we perform an initialisation measurement, that given a probabilistic outcome, signals that the system is in a certain state and ready to be used. If techniques for P1 nuclear or electron spin polarization can be developed, the initialisation rates and fidelities of individual P1 centers are likely to improve. Optical polarization via an excited state avoided crossing, or Hartmann-Hahn double resonance polarization techniques are promising approaches to improve the P1 initialisation rates [20]. It is currently not known how JT states can be prepared in a fast and deterministic manner. Further theoretical studies on deterministic initialisation techniques could provide useful tools in this direction. Reducing overhead time needed for initialisation of P1 centers can enable enhanced sensing schemes based on entanglement, via an

increased number of sensing spins and entangled states between them [21, 22]. Moreover, the developed control over spins in the environment potentially allows for the distribution of sensing tasks [23].

Robustness of P1 centers under optical excitation

For applicability of P1 centers in NV based quantum networks or processors, its quantum states are ideally stable against externally applied control fields such as for instance optical excitation laser pulses intended for the NV. In chapter 4 of this thesis, the robustness of quantum states of the P1 center is investigated, yet not exhaustively. By applying repetitive DEER sequences (Fig. 4.13) we find a faster than natural relaxation (Fig. 4.6b), indicating a disturbance due to the sequence. Additionally we find that a single sequence is much more destructive for the P1 electron state than for the combined nitrogen and JT state, however the underlying mechanisms have not yet been thoroughly investigated. The disturbance of the measured states can occur due to a combination of natural relaxation, effects of the MW pulse sequence and laser based NV readout during DEER. As a follow-up, it is interesting to isolate the different effects and gain further insights in the dominant causes of disturbance. Such effects could potentially be mitigated, thereby improving stability of quantum states of P1 centers.

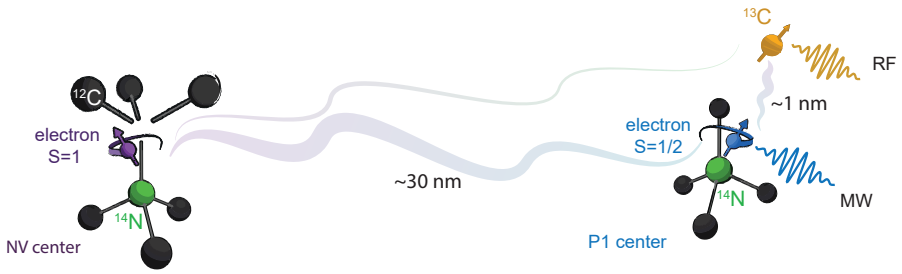

Figure 6.1: **Extending the quantum register.** Schematic of an NV center strongly coupled to a P1 center via the electron-electron coupling. The P1 also couples strongly to a nearby ^{13}C spin that has a negligible coupling to the NV. Control over such a system is envisioned by using a recently developed electron-nuclear two-qubit gate [24], based on phase-controlled selective driving of the ^{13}C spin via RF pulses which are interleaved with dynamical decoupling sequences on the P1 electron spin using MW pulses.

Nuclear spins associated with P1 centers

Nuclear spins associated with the P1 center could provide promising quantum memories that exhibit long coherence and are robust against optical excitation. In chapter 4 we demonstrate that the ratio of dephasing times for the electron (T_{2e}^{*} = 50(3) μs) and nitrogen (T_{2n}^{*} = 201(9) μs) spins is ~4, and lower than expected based on the difference in gyromagnetic ratio of these spins. This effect is mainly attributed

to electron-nuclear spin mixing due to the large perpendicular component of the hyperfine interaction. Spin mixing can be greatly reduced by increasing the magnitude of the external magnetic field along the NV axis, which would increase nuclear spin coherence. Extending the coherence and further exploring the nitrogen spin for use as a qubit is an interesting direction for future research. Besides the host nitrogen spin, ^{13}C spins nearby the P1 center might provide additional useful qubits for larger quantum registers (Fig. 6.1). Control over nearby ^{13}C spins is envisioned by using recently developed electron-nuclear two-qubit gates [24]. The ^{13}C spins are connected to the optically active NV only indirectly through the P1 electron spin, and could provide isolated robust quantum memories for quantum networks (sec. 5.3).

Energy level structure of P1 centers

Although photoconductivity experiments indicate an optical ionization energy of P1 centers within 1.9-2.2 eV [25–28], a more precise measurement of optical ionization energy is preferred in order to design optimal control sequences. The developed control techniques in chapter 4 can be exploited for further study of the energy level structure. Single P1 centers can be prepared in a known nitrogen and Jahn-Teller state while subsequently applying optical laser excitation pulses at varying wavelengths (and/or power). The correlation of excitation wavelength and readout signal of the P1 could provide a more detailed picture of the energy level structure of P1 centers. Additionally, the excited state levels of the NV, and potentially the ground state levels [29], can be used as charge sensors, and in combination with the developed control of single P1 centers, could provide insights in the charge dynamics between NV and P1s.

Also, the electric field susceptibility of the energy levels of P1 centers can be investigated. Due to the four different JT distortions of the P1, the ground-state energy landscape of its electron wave function can be imagined to consist of four potential wells. In the absence of an external magnetic field, four degenerate states exist for different JT distortions with an estimated energy barrier of ~0.7 eV between them [30–32]. In a study by Ammerlaan et al. [33], uniaxial stress was applied to type Ib diamond to lift the fourfold degeneracy of P1 centers, and thereby induce a preferential alignment along the lower-energy distortions. Similar effects can possibly be achieved by applying strong electric fields, which could result in further control over JT states and potentially longer lifetimes of such states. The developed JT initialisation and readout techniques could aid in understanding electric field responses on the single defect level.

Finally, the ability to selectively address transitions that correspond to different nitrogen and JT states provides an interesting avenue for future research on charge-, JT- and nitrogen state occupation and the dynamics of P1 centers. Furthermore, the developed control techniques over P1 centers within the spin bath creates new opportunities to explore the physics of decoherence, spin diffusion, and Jahn-Teller dynamics in complex spin baths with control over the microscopic single spin dynamics [34, 35].

6.3. Future quantum information protocols

A large-scale quantum computer that has far-reaching advantages over their classical counterparts and can efficiently perform quantum algorithms such as Shor's or Grover's algorithm will require millions of qubits which can be interconnected [36]. Although noisy intermediate-scale quantum computers consisting of 50-100 qubits have already demonstrated exciting computational tasks [37, 38], scaling up towards millions of qubits is challenging. A modular approach in which nodes consisting of a smaller number of qubits that are interconnected in a quantum network is a promising way to build larger systems that allow for distributed quantum computation and quantum communication [39–42]. Earlier theoretical work proposes a modular approach, in which each node contains multiple qubits, and stabilizer measurements are repetitively performed on entangled states shared between several nodes to allow for fault-tolerant quantum computations [43, 44]. This modular approach avoids the complexity of a large-scale monolithic architecture by focusing on many identical nodes, in which operations are above error thresholds, and thereby provides a way towards larger structures.

Essential requirements for building large-scale quantum networks are: nodes of quantum registers consisting of multiple qubits that can be controlled with high fidelity, flying qubits that provide an efficient interface for high rate entanglement generation over a network, and robust quantum memories for storing quantum states while remote entanglement is being generated. Several of these requirements have been demonstrated on various platforms ranging from superconducting qubits [45–47], trapped ions and atoms [48, 49], spin qubits in silicon [50, 51] and optically active spin defects in solid state [52–54].

The NV center in diamond is one of the most promising platforms to build such networks. Its coherent spin-photon interface allows for remote entanglement via photonic links [55, 56], and nearby ^{13}C spins can be controlled as quantum memories [24, 57–60]. This has led to the demonstration of entanglement distillation [61], deterministic delivery of remote entanglement [62] and genuine multi-partite entanglement across a three-node network [63]. Despite this remarkable progress there remain several open challenges concerning this platform. One of these is improving the remote entanglement rates, which are low due to poor collection efficiency and because only ∼3% of the emitted NV photons are zero-phonon-line (ZPL) photons - the coherent photons needed for remote entanglement. Moreover, optical fibres are lossy at the optical wavelength of NV centers (∼8 dB/km attenuation at 637 nm) which make it difficult to extend the network to larger distances. Promising solutions are 1) frequency conversion towards the telecom band where optical fibre attenuation is only ∼0.2 dB/km [64], and 2) optical cavities to realize an efficient optical interface. A second challenge is to store and preserve quantum states in memories while generating entanglement. The entanglement generation process is probabilistic (heralded) which means that multiple entanglement attempts have to be made until one is successful. Due to the always-on hyperfine interaction between the NV electron spin and nuclear spin memories, entanglement attempts cause decoherence of current ^{13}C memories. These memories have

shown great progress in robustness over the last years, but still dephase before a new entangled state is generated. In the future it is desirable to protect quantum states stored in memories far beyond the time a new entangled state is generated, such that multiple entangled states can be generated and stored reliably.

6.3.1. Robust quantum memories

An important open challenge is to reliably store quantum states in quantum memories while entanglement links between distant network nodes are generated. Since the first use of ^{13}C memory assisted network protocols [61], progress has been made on the number of entanglement attempts that can be performed before dephasing the memory qubit [65]. Recently a high magnetic field (>0.1 T) has been used to reduce dephasing from coupling to the NV electron spin under network activity, thereby increasing memory robustness [63, 66]. Futher improvements in robustness can be achieved by using diamond with a lower abundance of ^{13}C atoms, thereby reducing the coupling to ^{13}C memories.

A different approach is to use decoherence-protected subspaces of pairs of ^{13}C spins or other spins. Such pairs naturally occur in the diamond lattice and within the decoherence-protected subspace the effective coupling to the NV center is reduced [67]. Moreover, ^{13}C spin pairs can be addressed using dynamical decoupling techniques [68]. Strongly coupled pairs are a good candidate for quantum memories as their precession frequency only weakly depends on the NV electron spin state (∼Hz).

Creating a system of coupled NVs or an NV coupled with another electron-nuclear defect to achieve robust quantum memories has been pursued in this thesis. In such a system, an NV center is used as an optical link, whereas the other defect is dedicated to function as a memory. Because of a large difference in gyromagnetic ratio (factor ∼9000) between the electron and nitrogen nuclear spin, the electron-electron dipolar coupling is nearly four orders of magnitude larger than the electron-nuclear dipolar coupling. At a separation of ∼30 nm, the two defects are magnetically coupled by a relatively strong (∼kHz) electron-electron dipolar interaction, while the interaction between optical link electron and memory nuclear spin is weak. Nevertheless, the nuclear spin on the memory defect is indirectly accessible for the optical link NV, via the electron spin of the memory defect. Moreover, the weaker electron-nuclear dipolar interaction (sub-Hz) ensures that the nuclear memory is well-isolated and robust against undesirable changes of the electron state of the communicator NV. The aforementioned and studied system of an NV and surrounding P1 centers is potentially a promising system for accessing nuclear spins that are well isolated from the optical link NV. However, the challenges concerning this system (as described in sec. 6.2.2) need to be addressed to achieve useful quantum nodes with robust and easily accessible quantum memories. Other promising techniques to obtain a system of coupled defects are using delta-doping in combination with laser writing of NV centers (see section 6.2.1) [13, 14, 16, 17].

6.3.2. Optical cavities and novel defects

As current entanglement rates between remote nodes using NVs are ∼40 Hz [62], an increase in such rates is desirable to achieve large-scale quantum networks. Optical cavities are a promising tool to realize an efficient spin-photon interface, and are an elegant solution as they address both the emission- and collection efficiency simultaneously. Through Purcell enhancement an increase in emission can be achieved [69, 70]. Since the cavity provides preferential emission in a well defined spatial mode, the collection efficiency is also enhanced. Embedding NV centers in optical cavities thus holds great promise for enhancing entanglement rates, however it has been difficult to obtain NV centers with coherent optical transitions in nanostructure devices such as photonic crystal cavities [71]. By embedding NV centers in Fabry Pérot cavities that consist of μm-thick diamond membranes, nanostructure devices can be avoided and promising progress has been made in this direction [72, 73]. Reducing technical limitations in such systems such as length fluctuations of the Fabry Pérot cavity will further increase the emission of ZPL photons.

Alternatively, one could investigate other defects that have more favourable intrinsic emission properties. Recent research on group-IV color centers have shown promising results. Several of these defects have been investigated, each with its own strong points and drawbacks. The SiV^- center, for instance, emits around 80% of its photons into the ZPL [74]. Moreover, due to its inversion symmetry this defect is insensitive to electric field fluctuations up to first order and therefore spectrally stable, even when implanted in nanostructured devices. This provides an opportunity for enhancing photon emission and collection via nano-scale photonic crystal cavities [75]. On the other hand, millikelvin temperatures are required to suppress acoustic-phonon-induced orbital relaxation that leads to dephasing of the electron spin [76]. Also, the SiV^- has a relatively low intrinsic radiative quantum yield (∼0.05) [77]. Recently the observation of the neutrally charged SiV^0 center was reported [78]. In the neutral charge state the defect maintains several of the advantageous properties of the SiV^- center, such as emitting a high percentage in the ZPL and spectral stability even if implanted. Additionally, the relaxation mechanism of the SiV^0 spin-1 system has been reported not to be limited by a single phonon relaxation process, and a T_2 of ∼1 ms has been demonstrated at cryogenic temperatures (∼4 K), thereby combining many favourable properties [78]. The drawback of this defect is that advanced device engineering is needed to obtain charge stable SiV^0; boron doping is necessary to achieve the right Fermi level for a stable charge state, and it has thus far been difficult to engineer this defect.

Other group-IV defects such as GeV^-, PbV^- and SnV^- could be even more promising as they are envisioned to have a larger splitting of the two orbital branches of the ground state than SiV^-, thus enabling higher operation temperatures [77]. These defects are expected to exhibit similar desirable optical properties as the SiV^- defect or even better, for SnV^- for example the quantum efficiency is estimated to be ∼0.8 [52, 79–83]. Although much progress has been made on optical control of

group-IV defects, control of the spin states via applied microwave driving is challenging because in the case of no external strain the two spin (S = 1/2) projections have orthogonal orbital states. Thereby making it difficult to drive the transition between the spin states as both a spin and an orbital state needs to be flipped. This can be mitigated by applying external strain or obtaining strained samples such that the orbital basis mixes, which makes microwave driving of the spin more allowed. However, applying strain could deteriorate the inversion symmetry of the defect and thus its desirable optical properties. A proper balance needs to be found between obtaining the right amount of strain in order to apply MWs without heating effects while maintaining desirable inversion symmetry properties. If good optical and spin control can be combined using group-IV defects, they have great potential to drastically advance the field of quantum networks.

Besides diamond, other wide band gap materials such as for instance silicon carbide (SiC) are suitable for hosting defect emitters. SiC has the advantage of being a wide band gap material with established industrial production methods and controlled doping [84]. In particular VSi^- in SiC shows initial promising properties such as spectral stability, T_2 time of ~ms at cryogenic temperatures (~4 K) and near telecom band emission frequency (861 nm) [85]. Challenges concerning this defect are to enhance photon collection and emission, establish single-shot readout of the spin states and develop nuclear-spin control.

References

[1] Kasperczyk, M. *et al.*, *Statistically modeling optical linewidths of nitrogen vacancy centers in microstructures,* Physical Review B **102**, 075312 (2020).

[2] Tao, Y., Boss, J. M., Moores, B. & Degen, C. L., *Single-crystal diamond nanomechanical resonators with quality factors exceeding one million,* Nature communications **5**, 1 (2014).

[3] Ohno, K. *et al.*, *Engineering shallow spins in diamond with nitrogen delta-doping,* Applied Physics Letters **101**, 082413 (2012).

[4] Rosskopf, T. *et al.*, *Investigation of surface magnetic noise by shallow spins in diamond,* Physical review letters **112**, 147602 (2014).

[5] Bluvstein, D., Zhang, Z., McLellan, C. A., Williams, N. R. & Jayich, A. C. B., *Extending the quantum coherence of a near-surface qubit by coherently driving the paramagnetic surface environment,* Physical Review Letters **123**, 146804 (2019).

[6] De Oliveira, F. F. *et al.*, *Tailoring spin defects in diamond by lattice charging,* Nature communications **8**, 1 (2017).

[7] Chu, Y. *et al.*, *Coherent optical transitions in implanted nitrogen vacancy centers.* Nano Lett. **14**, 1982 (2014).

[8] Unden, T. *et al.*, *Coherent control of solid state nuclear spin nano-ensembles,* npj Quantum Information **4**, 1 (2018).

[9] Yuan, Z. *et al.*, *Charge state dynamics and optically detected electron spin resonance contrast of shallow nitrogen-vacancy centers in diamond,* arXiv preprint arXiv:2005.01142 (2020).

[10] Ruf, M. *et al.*, *Optically coherent nitrogen-vacancy centers in micrometer-thin etched diamond membranes,* Nano letters **19**, 3987 (2019).

[11] Lovchinsky, I. *et al.*, *Nuclear magnetic resonance detection and spectroscopy of single proteins using quantum logic,* Science **351**, 836 (2016).

[12] Abobeih, M. *et al.*, *Atomic-scale imaging of a 27-nuclear-spin cluster using a quantum sensor,* Nature **576**, 411 (2019).

[13] Jaffe, T. *et al.*, *Novel ultra localized and dense nitrogen delta-doping in diamond for advanced quantum sensing,* Nano Letters (2020).

[14] Myers, B. A. *et al.*, *Probing surface noise with depth-calibrated spins in diamond,* Physical Review Letters **113**, 027602 (2014).

[15] Ohno, K. *et al.*, *Three-dimensional localization of spins in diamond using 12c implantation,* Applied Physics Letters **105**, 052406 (2014).

[16] Chen, Y.-C. *et al.*, *Laser writing of coherent colour centres in diamond,* Nature Photonics **11**, 77 (2017).

[17] Chen, Y.-C. *et al.*, *Laser writing of individual nitrogen-vacancy defects in diamond with near-unity yield,* Optica **6**, 662 (2019).

[18] McLellan, C. A. *et al.*, *Patterned formation of highly coherent nitrogen-vacancy centers using a focused electron irradiation technique,* Nano letters **16**, 2450 (2016).

[19] Loenen, S., *Improving single-shot readout for diamond quantum processors* (MSc Thesis, Delft, University of Technology, 2019).

[20] Knowles, H. S., Kara, D. M. & Atatüre, M., *Demonstration of a Coherent Electronic Spin Cluster in Diamond,* Phys. Rev. Lett. **117**, 1 (2016).

[21] Cooper, A., Kyu, W., Sun, C., Jaskula, J.-C. & Cappellaro, P., *Environment-assisted Quantum-enhanced Sensing with Electronic Spins in Diamond,* Phys. Rev. Appl. **10**, 44047 (2019).

[22] Goldstein, G. *et al.*, *Environment-assisted precision measurement,* Phys. Rev. Lett. **106**, 140502 (2011).

[23] Vorobyov, V. *et al.*, *Quantum fourier transform for quantum sensing,* arXiv preprint arXiv:2008.09716 (2020).

[24] Bradley, C. *et al.*, *A ten-qubit solid-state spin register with quantum memory up to one minute,* Phys. Rev. X **9**, 031045 (2019).

[25] Heremans, F., Fuchs, G., Wang, C., Hanson, R. & Awschalom, D., *Generation and transport of photoexcited electrons in single-crystal diamond,* Appl. Phys. Lett. **94**, 152102 (2009).

[26] Farrer, R., *On the substitutional nitrogen donor in diamond,* Solid State Communications **7**, 685 (1969).

[27] Van Enckevort, W. & Versteegen, E., *Temperature dependence of optical absorption by the single-substitutional nitrogen donor in diamond,* Journal of Physics: Condensed Matter **4**, 2361 (1992).

[28] Rosa, J., Vaněček, M., Nesladek, M. & Stals, L., *Photoionization cross-section of dominant defects in cvd diamond,* Diamond and related materials **8**, 721 (1999).

[29] Mittiga, T. *et al.*, *Imaging the local charge environment of nitrogen-vacancy centers in diamond,* Physical review letters **121**, 246402 (2018).

[30] Shul'man, L. A., Zaritskii, M. I. & Podzyarei, G. A., *Reorientation of the Jahn-Teller distortion in nitrogen impurity centers in diamond,* Sov. phys., Solid State **8**, 1842 (1967).

[31] Breuer, S. & Briddon, P., *Energy barrier to reorientation of the substitutional nitrogen in diamond,* Physical Review B **53**, 7819 (1996).

[32] Loubser, J. & Van Ryneveld, W., *The dynamic jahn-teller and other effects in the high-temperature electron spin resonance spectrum of nitrogen in diamond,* British Journal of Applied Physics **18**, 1029 (1967).

[33] Ammerlaan, C. A. & Burgemeister, E. A., *Reorientation of nitrogen in type-Ib diamond by thermal excitation and tunneling,* Phys. Rev. Lett. **47**, 954 (1981).

[34] Xiao, X. & Zhao, N., *Proposal for observing dynamic jahn–teller effect by single solid-state defects,* New J. Phys. **18**, 103022 (2016).

[35] Hall, L. T., Cole, J. H. & Hollenberg, L. C., *Analytic solutions to the central-spin problem for nitrogen-vacancy centers in diamond,* Physical Review B **90**, 075201 (2014).

[36] Van Meter, R. & Horsman, C., *A blueprint for building a quantum computer,* Communications of the ACM **56**, 84 (2013).

[37] Arute, F. *et al.*, *Quantum supremacy using a programmable superconducting processor,* Nature **574**, 505 (2019).

[38] Zhang, J. *et al.*, *Observation of a many-body dynamical phase transition with a 53-qubit quantum simulator,* Nature **551**, 601 (2017).

[39] Van Meter, R. & Devitt, S. J., *The path to scalable distributed quantum computing,* Computer **49**, 31 (2016).

[40] Kimble, H. J., *The quantum internet,* Nature **453**, 1023 (2008).

[41] Wehner, S., Elkouss, D. & Hanson, R., *Quantum internet: A vision for the road ahead,* Science **362** (2018).

[42] Vandersypen, L. *et al.*, *Interfacing spin qubits in quantum dots and donors—hot, dense, and coherent,* npj Quantum Information **3**, 1 (2017).

[43] Nickerson, N. H., Fitzsimons, J. F. & Benjamin, S. C., *Freely scalable quantum technologies using cells of 5-to-50 qubits with very lossy and noisy photonic links,* Physical Review X **4**, 041041 (2014).

[44] Nickerson, N. H., Li, Y. & Benjamin, S. C., *Topological quantum computing with a very noisy network and local error rates approaching one percent,* Nature communications **4**, 1 (2013).

[45] Magnard, P. *et al.*, *Microwave quantum link between superconducting circuits housed in spatially separated cryogenic systems,* Physical Review Letters **125**, 260502 (2020).

[46] Dickel, C. *et al.*, *Chip-to-chip entanglement of transmon qubits using engineered measurement fields,* Physical Review B **97**, 064508 (2018).

[47] Narla, A. *et al.*, *Robust concurrent remote entanglement between two superconducting qubits,* Physical Review X **6**, 031036 (2016).

[48] Hucul, D. *et al.*, *Modular entanglement of atomic qubits using photons and phonons,* Nature Physics **11**, 37 (2015).

[49] Wright, K. *et al.*, *Benchmarking an 11-qubit quantum computer,* Nature communications **10**, 1 (2019).

[50] Borjans, F., Croot, X., Mi, X., Gullans, M. & Petta, J., *Resonant microwave-mediated interactions between distant electron spins,* Nature **577**, 195 (2020).

[51] Samkharadze, N. *et al.*, *Strong spin-photon coupling in silicon,* Science **359**, 1123 (2018).

[52] Trusheim, M. E. *et al.*, *Transform-limited photons from a coherent tin-vacancy spin in diamond,* Physical review letters **124**, 023602 (2020).

[53] Sukachev, D. D. *et al.*, *Silicon-vacancy spin qubit in diamond: a quantum memory exceeding 10 ms with single-shot state readout,* Physical review letters **119**, 223602 (2017).

[54] Bhaskar, M. K. *et al.*, *Experimental demonstration of memory-enhanced quantum communication,* Nature **580**, 60 (2020).

[55] Robledo, L. *et al.*, *High-fidelity projective read-out of a solid-state spin quantum register,* Nature **477**, 574 (2011).

[56] Bernien, H. *et al.*, *Heralded entanglement between solid-state qubits separated by three metres,* Nature **497**, 86 (2013).

[57] van Dam, S. B., Cramer, J., Taminiau, T. H. & Hanson, R., *Multipartite entanglement generation and contextuality tests using nondestructive three-qubit parity measurements,* Physical review letters **123**, 050401 (2019).

[58] Kolkowitz, S., Unterreithmeier, Q. P., Bennett, S. D. & Lukin, M. D., *Sensing distant nuclear spins with a single electron spin,* Physical review letters **109**, 137601 (2012).

[59] Zhao, N. *et al.*, *Sensing single remote nuclear spins,* Nature nanotechnology **7**, 657 (2012).

[60] Taminiau, T. H., Cramer, J., van der Sar, T., Dobrovitski, V. V. & Hanson, R., *Universal control and error correction in multi-qubit spin registers in diamond,* Nature nanotechnology **9**, 171 (2014).

[61] Kalb, N. *et al.*, *Entanglement distillation between solid-state quantum network nodes,* Science **356**, 928 (2017).

[62] Humphreys, P. C. *et al.*, *Deterministic delivery of remote entanglement on a quantum network,* Nature **558**, 268 (2018).

[63] Pompili, M. *et al.*, *Realization of a multi-node quantum network of remote solid-state qubits,* arXiv preprint arXiv:2102.04471 (2021).

[64] Tchebotareva, A. *et al.*, *Entanglement between a diamond spin qubit and a photonic time-bin qubit at telecom wavelength,* Physical review letters **123**, 063601 (2019).

[65] Kalb, N., Humphreys, P. C., Slim, J. & Hanson, R., *Dephasing mechanisms of diamond-based nuclear-spin memories for quantum networks,* Physical Review A **97**, 062330 (2018).

[66] Beukers, H., *Improving coherence of quantum memory during entanglement creation between nitrogen vacancy centres in diamond* (MSc Thesis, Delft University of Technology, 2019).

[67] Reiserer, A. *et al.*, *Robust quantum-network memory using decoherence-protected subspaces of nuclear spins,* Physical Review X **6**, 021040 (2016).

[68] Abobeih, M. H. *et al.*, *One-second coherence for a single electron spin coupled to a multi-qubit nuclear-spin environment,* Nature communications **9**, 1 (2018).

[69] Purcell, E. M., *Spontaneous emission probabilities at radio frequencies,* in *Confined Electrons and Photons* (Springer, 1995) pp. 839–839.

[70] Faraon, A., Barclay, P. E., Santori, C., Fu, K.-M. C. & Beausoleil, R. G., *Resonant enhancement of the zero-phonon emission from a colour centre in a diamond cavity,* Nature Photonics **5**, 301 (2011).

[71] Faraon, A., Santori, C., Huang, Z., Acosta, V. M. & Beausoleil, R. G., *Coupling of nitrogen-vacancy centers to photonic crystal cavities in monocrystalline diamond,* Physical review letters **109**, 033604 (2012).

[72] Ruf, M., Weaver, M. J., van Dam, S. B. & Hanson, R., *Resonant excitation and purcell enhancement of coherent nitrogen-vacancy centers coupled to a fabry-perot microcavity,* Physical Review Applied **15**, 024049 (2021).

[73] Riedel, D. *et al.*, *Deterministic enhancement of coherent photon generation from a nitrogen-vacancy center in ultrapure diamond,* Physical Review X **7**, 031040 (2017).

[74] Pingault, B. *et al.*, *Coherent control of the silicon-vacancy spin in diamond,* Nature communications **8**, 1 (2017).

[75] Nguyen, C. *et al.*, *Quantum network nodes based on diamond qubits with an efficient nanophotonic interface,* Physical review letters **123**, 183602 (2019).

[76] Nguyen, C. *et al.*, *An integrated nanophotonic quantum register based on silicon-vacancy spins in diamond,* Physical Review B **100**, 165428 (2019).

[77] Bradac, C., Gao, W., Forneris, J., Trusheim, M. E. & Aharonovich, I., *Quantum nanophotonics with group iv defects in diamond,* Nature communications **10**, 1 (2019).

[78] Rose, B. C. *et al.*, *Observation of an environmentally insensitive solid-state spin defect in diamond,* Science **361**, 60 (2018).

[79] Trusheim, M. E. *et al.*, *Lead-related quantum emitters in diamond,* Physical Review B **99**, 075430 (2019).

[80] Bhaskar, M. K. *et al.*, *Quantum nonlinear optics with a germanium-vacancy color center in a nanoscale diamond waveguide,* Physical review letters **118**, 223603 (2017).

[81] Iwasaki, T. *et al.*, *Germanium-vacancy single color centers in diamond,* Scientific reports **5**, 1 (2015).

[82] Rugar, A. E. *et al.*, *Narrow-linewidth tin-vacancy centers in a diamond waveguide,* ACS Photonics **7**, 2356 (2020).

[83] Iwasaki, T. *et al.*, *Tin-vacancy quantum emitters in diamond,* Physical review letters **119**, 253601 (2017).

[84] Son, N. T. *et al.*, *Developing silicon carbide for quantum spintronics,* Applied Physics Letters **116**, 190501 (2020).

[85] Nagy, R. *et al.*, *High-fidelity spin and optical control of single silicon-vacancy centres in silicon carbide,* Nature communications **10**, 1 (2019).

A

Appendix Chapter 4

This appendix complements the results reported in chapter 4, which presents entanglement of dark electron-nuclear spin defects in diamond.

A

A.1. System Hamiltonian

In this section we describe the Hamiltonian of a system consisting of a P1 center and an NV center in diamond.

P1 center

The Hamiltonian of the P1 center is given by [1]:

$$H_{\mathbf{i},\mathrm{P1}} = \gamma_e \vec{B} \cdot \vec{S} + \vec{S} \cdot \mathbf{A_i} \cdot \vec{I} + \gamma_n \vec{B} \cdot \vec{I} + \vec{I} \cdot \mathbf{P_i} \cdot \vec{I}, \tag{A.1}$$

where γ_e ($\approx 2\pi \cdot 2.802$ MHz/G) and γ_n ($\approx -2\pi \cdot 0.3078$ kHz/G) are the electron and ^{14}N gyromagnetic ratio respectively. $\vec{B}$ is the external magnetic field vector and $\vec{S}$ and $\vec{I}$ are the electron spin-1/2 and nuclear spin-1 operator vectors. The P1 center exhibits a JT distortion along the axis of one of the four carbon-nitrogen bonds (denoted by $i \in \{\mathrm{A,B,C,D}\}$). This JT axis defines the principal axis of the hyperfine interaction and the quadrupole interaction.

The hyperfine tensor ($\mathbf{A_i}$) and quadrupole tensor ($\mathbf{P_i}$) can be obtained in any coordinate frame via a transformation of the diagonal hyperfine tensor, $\mathbf{A_{diag}}$ = diag$[A_{xx}, A_{yy}, A_{zz}]$ and diagonal quadrupole tensor, $\mathbf{P_{diag}}$ = diag$[P_{xx}, P_{yy}, P_{zz}]$:

$$\mathbf{A_i} = R^T \cdot \mathbf{A_{diag}} \cdot R \tag{A.2}$$

and

$$\mathbf{P_i} = R^T \cdot \mathbf{P_{diag}} \cdot R. \tag{A.3}$$

Here R is the rotation matrix from the principal axis of the P1 center to any other coordinate frame defined by Euler angles $\{\alpha, \beta, \gamma\}$:

$$R(\alpha,\beta,\gamma) =$$

$$\begin{pmatrix} \cos(\gamma)\cos(\beta)\cos(\alpha) - \sin(\gamma)\sin(\alpha) & \cos(\gamma)\cos(\beta)\sin(\alpha) + \sin(\gamma)\cos(\alpha) & -\cos(\gamma)\sin(\beta) \\ -\sin(\gamma)\cos(\beta)\cos(\alpha) - \cos(\gamma)\sin(\alpha) & -\sin(\gamma)\cos(\beta)\sin(\alpha) + \cos(\gamma)\cos(\alpha) & \sin(\gamma)\sin(\beta) \\ \sin(\beta)\cos(\alpha) & \sin(\beta)\sin(\alpha) & \cos(\beta) \end{pmatrix}$$

Due to the axial symmetry of the P1 center in its principal axis coordinate frame ($A_\perp = A_{xx} = A_{yy}$ and $P_\perp = P_{xx} = P_{yy}$), this can be reduced to:

$$R(\beta,\alpha) = \begin{pmatrix} \cos(\beta)\cos(\alpha) & \cos(\beta)\sin(\alpha) & -\sin(\beta) \\ -\sin(\alpha) & \cos(\alpha) & 0 \\ \sin(\beta)\cos(\alpha) & \sin(\beta)\sin(\alpha) & \cos(\beta) \end{pmatrix}. \tag{A.4}$$

For any of the four JT axes, the hyperfine (quadrupole) tensor $\mathbf{A_i}$ ($\mathbf{P_i}$) in the coordinate frame of the symmetry axis of the NV center is obtained via a transformation with angles $(\beta,\alpha)_i \in \{(109.5°, 240°)_\mathrm{A}, (109.5°, 120°)_\mathrm{B}, (109.5°, 0°)_\mathrm{C}, (0°, 0°)_\mathrm{D}\}$.

NV-P1 system

The Hamiltonian of a coupled NV-P1 system (in the frame of the symmetry axis of the NV center) is given by the terms corresponding to the NV, the P1 and the terms describing their dipolar coupling:

$$H_{\text{tot}} = H_{\text{NV}} + H_{\text{P1}} + H_{\text{dipole}}. \tag{A.5}$$

For the NV we only consider the electron spin of the NV center:

$$H_{\text{NV}} = \Delta J_z^2 + \gamma_e \vec{B} \cdot \vec{J}. \tag{A.6}$$

where $\Delta = 2\pi \cdot 2.877$ GHz is the zero-field splitting and $\vec{J}$ is the electron spin 1 vector.

If we consider a point dipole coupling between the NV and the electron spin of the P1 center, separated by a vector $\vec{r}$, the dipole term can be written as:

$$H_{\text{dipole}} = \nu_{dip} \cdot \left(3(\vec{J} \cdot \hat{r})(\vec{S} \cdot \hat{r}) - \vec{J} \cdot \vec{S}\right), \tag{A.7}$$

where $\nu_{dip} = \frac{-\mu_0 \gamma_e \gamma_e \hbar}{4\pi r^3}$, $r = |\vec{r}|$ and $\hat{r} = \vec{r}/r$. Transforming to spherical coordinates using the definitions $r_x = r\sin(\theta)\cos(\varphi)$, $r_y = r\sin(\theta)\sin(\varphi)$ and $r_z = r\cos(\theta)$, gives

$$\begin{aligned} H_{\text{dipole}} = \nu_{dip} \cdot \Big[& J_x S_x \left(3\sin^2(\theta)\cos^2(\varphi) - 1\right) + J_y S_y \left(3\sin^2(\theta)\sin^2(\varphi) - 1\right) \\ & + J_z S_z \left(3\cos^2(\theta) - 1\right) + (J_y S_x + J_x S_y) 3\sin^2(\theta)\cos(\varphi)\sin(\varphi) \\ & + (J_z S_x + J_x S_z) 3\cos(\theta)\sin(\theta)\cos(\varphi) \\ & + (J_z S_y + J_y S_z) 3\cos(\theta)\sin(\theta)\sin(\varphi) \Big]. \end{aligned} \tag{A.8}$$

Due to the large difference between electron and ^{14}N gyromagnetic ratio ($\gamma_e/\gamma_n \sim 9000$) we expect the electron-nuclear NV-P1 dipolar coupling to be negligible and omit this term in the Hamiltonian.

Orientation in the crystal lattice

In the diamond lattice, the P1 defect is located in a tetrahedral geometry with four surrounding carbon atoms. A single carbon atom can be positioned either directly above (orientation 1) or below (orientation 2) the P1 center's nitrogen atom, and the other three carbon atoms at 109.5° bond angles below or above respectively.

If we consider the JT distortions along the $\hat{\mathbf{z}}$ axis (JT axis D) for these two orientations, the nitrogen atom either distorts in the -$\hat{\mathbf{z}}$ direction or the +$\hat{\mathbf{z}}$ direction. Therefore, these two orientations correspond to two spin Hamiltonians as in eq. A.5: $H_{tot,1}$ with $\mathbf{A_D} = \mathbf{A_{diag}}$ and $H_{tot,2}$ with $\mathbf{A_D} = R(180°, 0°)^T \cdot \mathbf{A_{diag}} \cdot R(180°, 0°)$

A

(similar for $\mathbf{P_D}$). From eq. A.4 it is evident that $R(180°,0°)^T \cdot \mathbf{A_{diag}} \cdot R(180°,0°) = \mathbf{A_{diag}}$, and thus $H_{tot,1} = H_{tot,2}$. Therefore, in the experiments performed in this work, we cannot distinguish between these two different orientations of P1 centers.

A.2. DEER and DEER(y) sequence

Here a more detailed description is given for the experimental sequences shown in Figs. 4.2b and 4.4b of chapter 4. We consider an idealized case of a single NV, a single P1 center and their magnetic dipolar coupling. In a diagonalized frame, the energy eigenstates and eigenvalues of the system are labelled as $|m_s, m_{\uparrow/\downarrow}, m_I\rangle$ and $\lambda_{m_s,m_{\uparrow/\downarrow},m_I}$ respectively. The eigenstates form a 12-dimensional Hilbert space (the subspace m_s = {0,-1} of the NV, the electron spin 1/2 of the P1 center and its ^{14}N spin 1).

DEER

We consider the sequence of unitary operations as applied during a DEER sequence with a single repetition K=1 (see Fig. 4.2b in chapter 4). First we apply $U_{NV,1} = R_x(\pi/2)_{NV} \otimes \mathbb{1}_{P1}$, a $\pi/2$ rotation on the NV with phase x, followed by an evolution time $U_{evo}(\tau)$, which is given by diag[$e^{-i\lambda_{0,\uparrow,+1}\cdot\tau}$, $e^{-i\lambda_{0,\uparrow,0}\cdot\tau}$, ... ,$e^{-i\lambda_{m_s,m_{\uparrow/\downarrow},m_I}\cdot\tau}$, ... ,$e^{-i\lambda_{-1,\downarrow,-1}\cdot\tau}$]. This is followed by a π pulse on the NV; $U_{NV,2} = R_x(\pi)_{NV} \otimes \mathbb{1}_{P1}$. Simultaneously, we apply a π pulse on the P1 electron spin conditional on its ^{14}N state $|m_I\rangle = |+1\rangle$. This operation is described by $U_{P1} = \mathbb{1}_{NV} \otimes R_x(\pi)_{P1,e} \otimes |+1\rangle\langle+1| + \mathbb{1}_{NV} \otimes \mathbb{1}_{P1,e} \otimes |0\rangle\langle 0| + \mathbb{1}_{NV} \otimes \mathbb{1}_{P1,e} \otimes |-1\rangle\langle -1|$. Then there is another evolution time $U_{evo}(\tau)$ and finally a $\pi/2$ pulse $U_{NV,3} = R_{-x}(\pi/2)_{NV} \otimes \mathbb{1}_{P1}$ with phase $-x$. We assume perfect π and $\pi/2$ pulses between energy eigenstates. For an initial state ρ_1, we obtain a final state given by:

$$\rho_{f,1}(\tau) = U_{NV,3}U_{evo}(\tau)U_{P1}U_{NV,2}U_{evo}(\tau)U_{NV,1}\rho_1 U_{NV,1}^{\dagger}U_{evo}(\tau)^{\dagger}U_{NV,2}^{\dagger}U_{P1}^{\dagger}U_{evo}(\tau)^{\dagger}U_{NV,3}^{\dagger} \tag{A.9}$$

For the NV initialized in $|0\rangle$ but mixed P1 electron and ^{14}N spin states, the initial density matrix is given as:

$$\rho_1 = \frac{1}{6}|0\rangle\langle 0| \otimes \mathbb{1}_{P1} \tag{A.10}$$

The reduced density matrix of the NV as a function of interaction time is given by:

$$\rho_{NV}(\tau) = \sum_{m_{\uparrow,\downarrow},m_I} \langle m_{\uparrow,\downarrow}, m_I|\, \rho_{f,1}(\tau)\, |m_{\uparrow,\downarrow}, m_I\rangle = \frac{1}{6}\cos(\nu\cdot\tau)\big[\,|-1\rangle\langle -1| - |0\rangle\langle 0|\,\big] + \frac{1}{6}|0\rangle\langle 0| + \frac{5}{6}|-1\rangle\langle -1|. \tag{A.11}$$

Here the effective NV-P1 dipolar coupling (ν) is given as

$$\nu = \lambda_{-1,\downarrow,+1} - \lambda_{0,\downarrow,+1} - (\lambda_{-1,\uparrow,+1} - \lambda_{0,\uparrow,+1}). \tag{A.12}$$

Note that at $\tau = \pi/|\nu|$ we obtain the highest probability of measuring $|0\rangle_{NV}$. Upon measurement of $|0\rangle_{NV}$ we obtain the state:

$$\rho_{m_s=0} = \frac{|0\rangle\langle 0|\,\rho_{f,1}(\tau)\,|0\rangle\langle 0|}{\mathrm{Tr}\big(|0\rangle\langle 0|\,\rho_{f,1}(\tau)\big)} = \frac{1}{2}\,|0\rangle\langle 0| \otimes \mathbb{1}_{P1,e} \otimes |+1\rangle\langle +1|\,, \tag{A.13}$$

and thus initialize the ^{14}N state of the P1 center in $|+1\rangle$.

DEER(y)

Now we consider DEER(y) (see chapter 4, Fig. 4.4b), which is sensitive to the P1 electron spin state. This sequence is the DEER sequence with the phase of the final $\pi/2$ pulse changed from $-x \rightarrow -y$, or $-x \rightarrow +y$. For an initial state ρ_2 and the phase of the final $\pi/2$ pulse as $-y$, we obtain the final state $\rho_{f,2}$ by:

$$\rho_{f,2}(\tau) = U_{NV,4}U_{evo}(\tau)U_{P1}U_{NV,2}U_{evo}(\tau)U_{NV,1}\rho_2 U_{NV,1}^{\dagger}U_{evo}(\tau)^{\dagger}U_{NV,2}^{\dagger}U_{P1}^{\dagger}U_{evo}(\tau)^{\dagger}U_{NV,4}^{\dagger}. \tag{A.14}$$

Note that the final operator has been changed to $U_{NV,4} = R_{-y}(\pi/2)_{NV} \otimes \mathbb{1}_{P1}$ with phase $-y$. If we consider the NV initialized in $|0\rangle$ and the ^{14}N state of the P1 in $|+1\rangle$, the initial density matrix is given as:

$$\rho_2 = \frac{1}{2}\,|0\rangle\langle 0| \otimes \mathbb{1}_{P1,e} \otimes |+1\rangle\langle +1|\,. \tag{A.15}$$

The reduced density matrix of the NV as a function of interaction time is now given by:

$$\rho_{NV}(\tau) = \sum_{m_{\uparrow,\downarrow},m_I} \langle m_{\uparrow,\downarrow}, m_I|\,\rho_{f,2}(\tau)\,|m_{\uparrow,\downarrow}, m_I\rangle = \frac{1}{2}\cos(\nu\cdot t)\big[\,|0\rangle\langle -1| + |-1\rangle\langle 0|\,\big] + \frac{1}{2}\,|0\rangle\langle 0| + \frac{1}{2}\,|-1\rangle\langle -1|\,. \tag{A.16}$$

Upon measurement of $|0\rangle_{NV}$ we obtain the state:

$$\rho_{m_s=0} = \frac{|0\rangle\langle 0|\,\rho_{f,2}(\tau)\,|0\rangle\langle 0|}{\mathrm{Tr}\big(|0\rangle\langle 0|\,\rho_{f,2}(\tau)\big)} = \frac{1}{2}(1+\sin(\nu\cdot\tau))\,|0,\uparrow,+1\rangle\langle 0,\uparrow,+1| + \frac{1}{2}(1-\sin(\nu\cdot\tau))\,|0,\downarrow,+1\rangle\langle 0,\downarrow,+1|\,. \tag{A.17}$$

Note that at interaction time $\tau = \pi/(2|\nu|)$, the initialized state is either $|0,\downarrow,+1\rangle$ or $|0,\uparrow,+1\rangle$ depending on the sign of ν. Applying a phase $+y$ instead of $-y$ in the final $\pi/2$ pulse effectively changes the signs in front of the $\sin(\nu\cdot\tau)$ terms in equation (A.17), which is used in Fig. 4.5b.

A

A.3. NV-P1 dipolar coupling sign in $|+1,\mathrm{A}\rangle$

This section demonstrates coherent control of the ^{14}N spin and extracts the sign of the NV-P1 dipolar coupling for the electron spin of S1, S2 and S3/S4 in the $|+1,\mathrm{A}\rangle$ state (similar as in Fig. 4.5b of chapter 4 for $|+1,\mathrm{D}\rangle$). First, we choose an initialisation sequence with a low K (K=6), which with high probability prepares either S1, S2 or S3/S4 in $|+1,\mathrm{A}\rangle$. Then we calibrate a π pulse that implements a CNOT between the electron (control) and nitrogen nuclear spin (target) for a P1 in the $|+1,\mathrm{A}\rangle$ state, see Fig. A.1a. This pulse is only resonant with the $m_I = +1 \leftrightarrow 0$ transition, if the P1 electron spin is in the $|\uparrow\rangle$ state.

We use the same experimental procedure as in chapter 4 for $|+1,\mathrm{D}\rangle$, to determine the NV-P1 coupling signs (Fig. A.1b). The value R is defined as:

$$R = \frac{P_{(+y)} - P_{(-y)}}{P_{(+y)} + P_{(-y)}}, \tag{A.18}$$

with $P_{(+y)}$ ($P_{(-y)}$) the probability that the outcome of the DEER readout sequence is within the FWHM range corresponding to S1, S2 or S3/S4 (see section 4.9.7), and the subscript +y (-y) indicates the readout basis of the DEER(y) sequence used to initialize the electron spin. The result shows that spin S1 and S3/S4 have a positive coupling sign, whereas it is negative for S2. Note that S1, S2 and S3/S4 have the same NV coupling sign in $|+1,\mathrm{A}\rangle$ and $|+1,\mathrm{D}\rangle$.

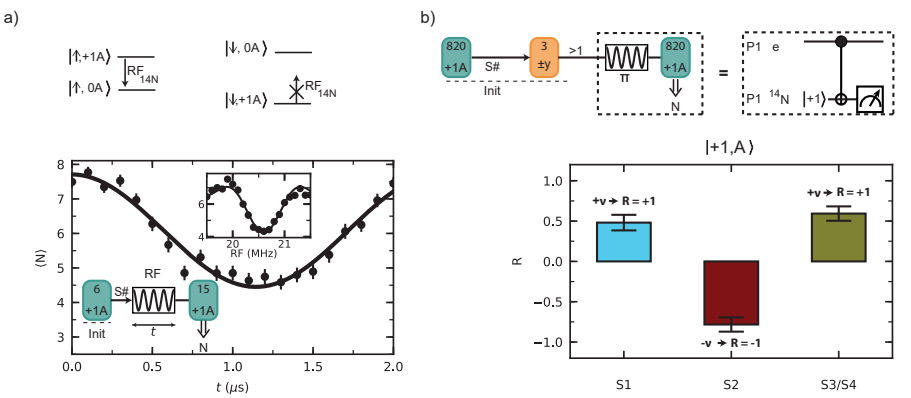

Figure A.1: **Coupling sign of NV-P1 dipolar interaction for different P1 centers in the $|+1,\mathrm{A}\rangle$ state.** a) Top: energy level structure of the P1 electron spin in the $\{0\mathrm{A},+1\mathrm{A}\}$ subspace. Bottom: A short initialisation sequence (K=6) prepares either S1, S2 or S3/S4 in $|+1,\mathrm{A}\rangle$ (without knowledge of which P1 is prepared in which run) and the length t of a pulse at frequency $RF = RF_{14N}$ = 20.55 MHz is varied. The nitrogen nuclear spin is driven conditionally on the electron spin state (top). Inset: NMR spectrum obtained by varying the frequency (RF) for a fixed pulse duration t. b) Value of R (see chapter 4, Methods) measured for the P1s in $|+1,\mathrm{A}\rangle$. Positive values correspond to a positive coupling sign.

A.4. NV-P1 coupling in $|+1,\mathrm{A}\rangle$

In Fig. 4.4a of chapter 4 the effective NV-P1 dipolar coupling (equation (A.12)) for S1, S2, S3/S4 in $|+1,\mathrm{D}\rangle$ is measured. Here, we measure the effective dipolar coupling of these spins in $|+1,\mathrm{A}\rangle$, see Fig. A.2. We initialize each P1 center by setting the requirement that the outcome of the DEER initialisation sequence is within the range for $|+1,\mathrm{A}\rangle$ (see Fig. 4.16a).

We obtain effective dipolar couplings ν of $2\pi \cdot 1.35(2)$, $2\pi \cdot 2.006(9)$ and $2\pi \cdot 1.06(2)$ kHz for S1, S2 and S3/S4 respectively, using the fit function in eq. 4.11 (see chapter 4, Methods). A comparison with the couplings for $|+1,\mathrm{D}\rangle$ (Fig. 4.4a in chapter 4) shows that the effective NV-P1 dipolar coupling strength differs for the two JT axes (see chapter 4, section 4.9.2 for the theoretical treatment).

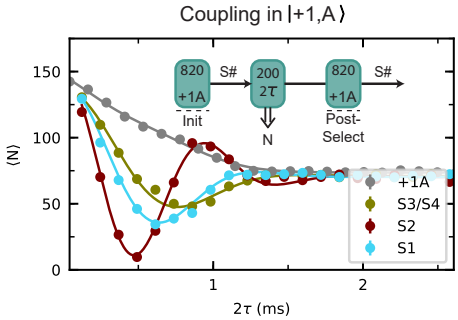

Figure A.2: **Measuring NV-P1 coupling strength in $|+1,\mathrm{A}\rangle$.** We initialize S1, S2 or S3/S4 in $|+1,\mathrm{A}\rangle$ and vary the interaction time 2τ of a DEER sequence (K=200). To improve the signal, the results are post-selected on again obtaining $|+1,\mathrm{A}\rangle$. Inset: experimental sequence. Grey: without P1 initialisation (data from Fig. 4.1c, chapter 4).

A.5. Magnetic field stability

Here we describe the magnetic field stabilisation used during the Ramsey and entanglement experiments in chapter 4, as well as during the data in Fig. 4.9b. We use three permanent magnets on motorized linear translation stages to create a static magnetic field. To compensate for magnetic field fluctuations we repeatedly measure the NV $|0\rangle \leftrightarrow |-1\rangle$ frequency (f_{NV}) and this signal is fed back to one of the magnet stages until (f_t - 1.5 kHz $\leq f_{NV} \leq f_t$ + 1.5 kHz), with target frequency $f_t = 2.749692$ GHz. We interleave this protocol (typically every 20 minutes) with repetitions of an experimental sequence.

Figure A.3a shows the time trace of f_{NV} before and after interleaved experiments. The two red lines indicate $f_t \pm 1.5$ kHz. The magnetic field can freely drift during the experimental sequences, but right before starting the next run the field is stabilized. From the histogram we infer that on average f_{NV} fluctuates with

A

$\sigma = 4.07$ kHz around $f = 2.749690$ GHz during feedback.

To monitor the complete magnetic field vector $\vec{B} = (B_x, B_y, B_z)$ during experiments with the stabilization protocol interleaved, we measure $f_{+1A}, f_{+1B}, f_{+1C}$ and f_{+1D} (see chapter 4, Fig. 4.1b). In a similar approach as in section 4.9.3 of chapter 4, we fit a parabola to the four frequencies and use the residuals consisting of the difference of the four fitted frequencies and the corresponding frequencies obtained from equation (A.1) to perform a least-squares minimization to find $\vec{B}$.

The obtained values for B_x, B_y and B_z are shown in Figs. A.3b,c,d. The standard deviations of these histogram verify a magnetic field stability during this protocol with σ_{B_x} = 20 mG, σ_{B_y} = 16 mG and σ_{B_z} = 3 mG. Note that the average values of $\vec{B}$ from Fig. A.3 show a discrepancy with the values obtained from the fit in chapter 4 and section 4.9.3, indicating that these measurements have been taken under slightly different conditions.

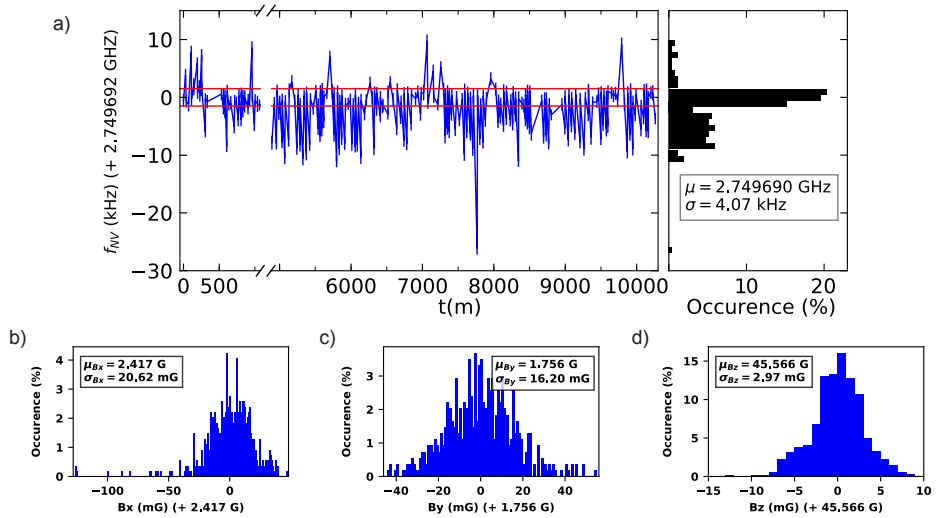

Figure A.3: **Magnetic field stability.** (a) Time trace of all measured NV resonance frequencies before and after performing repetitions of an experimental sequence. The red lines indicate the region ($\pm$ 1.5 kHz) to within which we stabilize before each measurement. (b,c,d) Distribution of measured B_x, B_y and B_z during 220 hours, while stabilizing f_{NV}.

References

[1] Smith, W., Sorokin, P., Gelles, I. & Lasher, G., *Electron-spin resonance of nitrogen donors in diamond,* Phys. Rev. **115**, 1546 (1959).

Acknowledgements

To all the great friends that I made over the years! Over the past years as a PhD student, I have learned a lot from all the people I worked with. For which I am truly grateful. Here I would like to express my gratitute to those people.

First of all, I would like to thank my supervisor **Tim Taminiau**. You are an amazing researcher and dedicated group leader. I started my PhD when the group was still relatively small but now it has grown into a larger group of motivated people, yet you still know almost every detail about what everyone is doing. During the past years, I liked your utter interest and enthusiasm towards the work, and also your devotion to understand data. You are a very critical thinker towards scientific work which was of great help during my PhD. I can really say that I have learned a lot from you during the past four years, and that this has helped me to become a better scientist. I will always be grateful for this guidance and support. I am sure you will lead the group towards exciting new projects in the future that I will definitely keep following. Thank you for the past years of guidance, discussions, experimenting and above all a lot of fun. **Ronald** thank you for bringing about the good environment for doing a PhD in, both for the welcoming group of Diamonds and QuTech in general. I have seen you become the scientific director of QuTech, a role which you have fulfilled very strongly, while still remaining a great group leader. Thank you for your supervision during my PhD, especially at the start when I was still trying to find my own path at QuTech and also thanks for the further support. **Slava**, thank you for helping me with the many questions about P1 centers. Thank you to my committee, professors **Caspar van der Wal**, **Sander Otte**, **Mete Atatüre** and **Yaroslav Blanter** for reading and assessing this thesis.

Team Diamond, both Tim's and Ronald's groups, I enjoyed it a lot to work in this team over the past years. I knew there was a lot I could learn here at QuTech and also have a lot of fun while at it. So I was really happy when I got the opportunity to start here. Over the years I got the chance to enjoy working on my PhD alongside numerous people from this team. **Mohamed** a.k.a. "the killer", over the past years we have become PhD buddies and it was nice to have such a good friend around. You are a great scientist and everything you have worked on during your PhD has seemed to turn into golden projects. Not so much for sports though, but who needs skiing (or any other sport) anyway. It was a lot of fun to spend so much time with you during numerous occasions such as trips, dinners and many more. We had all kinds of discussions ranging from physics to discussing/complaining about our PhDs to your famous broodje kaas. I am sure you will enjoy your post-doc in the US and we will continue to see each other there, in Egypt or elsewhere. See you in another life, my man ;). **Sjoerd**, we started working together intensively when I was getting closer to the end of my PhD and when you were starting yours. I can honestly say that it was a true joy to work with you in a team together with

Tim. Although our project sometimes seemed endless, you always kept a positive but critical attitude towards the work. I think this is very admirable and I am sure it will help you to bring your PhD to a very successful end. Outside work you are a lot of fun to hang around with and bring about a great new spark to the group. **Conor**, since the day of the QuTech Christmas party when you applied to the group it has always been a lot of fun with you around. One of the highlights being the spontaneous trip we made together with Arian to Norway, driving around the fjords and doing a lot of hiking. Also, you are a very dedicated researcher. Demonstrated not only by all the impressive work done, but also by showing up at early morning hot-topics meetings after first poisoning your lab mates and then yourself. I am sure you will do great after your PhD. **Dr. Joe**, one of the two British lads. Thanks for the fantastic but also the lame jokes you always made during occasions such as watching the soccer World Cup, pub quizzes or dress-up party as a peasant singing medieval songs. But most of all for being so willing to help during the last years and being such a nice and laid back person. You are a great researcher, and your future research group will definitely be lots of fun to work in. Thanks also to you and **Lucy** for helping me with the cover! **Arian** you are quite the character, in a very positive way. It has been a pleasure to have you as an office mate during most of the time of my PhD. Your strong views on nearly every subjects one can imagine as well as your sense of humor made our discussions quite entertaining. I am sure it will be soon that all the hard work you have put in the demonstrator project will fall into place and you will entangle the Hague and Delft. It was great fun to just hang out with you, watch F1 or visit various places and beaches during better times. Although you moving out of the office at the end of my PhD marked the end of an era, the saga will continue. **Suzanne**, thank you for all that that you have learned me. We worked together closely at the beginning of my PhD and at the time of the implantation project. During which we worked on several different setups and samples, and your skills, experience and patience have helped me during the rest of my PhD. Together we, in collaboration with our friends at MIT, reached conclusions that have changed the direction of my PhD. **Max**, we worked together during the beginning of our PhD's. It was nice to work with you during long cleanroom hours and to relax after working hours during beer, pizza or while visiting a random guy with a jar full of teeth and some maple syrup. Anyway, thank you for being so welcoming and taking initiative for social activities. I think you have worked hard during your PhD to get the nice results that you guys have now, which was a great challenge. All the best of luck in your future career, whatever it may be.

Hans Bartling, we worked together at the start of your PhD and later on had several discussions about similarities and differences between the P1 project and the pairs project. It was fun to share and gain insights which I think has helped us both, thank you for that. It was also quite funny to hear your (not so) slight discomfort with malfunctioning piezo's. I am sure you will continue to have fun during your PhD and after. **Matteo Senior**, thank you for your positive attitude and humorous reflection on several matters (especially lengthy projects). It was fun to explore New York with you after March meeting. I also enjoyed your Italian

pasta and the Mario Kart games during social events. With the demonstration of the three-node network you, Sophie and all others have achieved a new milestone for quantum networks. **Valeria**, it was nice to start out with you and together with Mohamed we had many laughs in the beginning of our PhDs. Thank you for the fun time in Rome, and for being so friendly in general. Although you had to break off your time in Delft before it was supposed to end, you made the right decision. I wish you and your family all the best for the future. **Sophie**, it was nice to see you start here as a master student working with Suzanne and thereafter continuing on cool three-node entanglement experiments. I really enjoyed the basketball tournements you organized. Thanks also for your outreach on quantum to the general public during podcasts, virtual lab tours and dinner with the one and only Willie the fourth. It is nice to see your excitement about research! **Aletta**, I learned a lot from you when we started on P1 centers. Finding them was not as easy as it looked, but the search with you was the start of one of the main projects of my PhD and a great experience for me. Thank you for you positivity and perseverance during your project. **Karima**, you were the first student I supervised, which was a good experience. It was nice to have you in our group, and good luck with your further studies! **Guido**, I like your spirit on science and chasing new ideas or extending existing ideas to their limits. Although the pandemic made us work from home mostly, it was fun to talk to you in the office on several occasions we were both there. Good luck with the rest of your PhD. **Damian**, I enjoy your enthusiasm about NV centers and defects in diamond in general. Also, you have a nice project going together with Guido which I think will be a lot of fun to explore further. I hope you enjoy the Netherlands while riding on your bike and once it will be organized again, I will definitely join you in the Dutch headwind championship on the afsluitdijk. **Simon**, thanks for the enthusiasm about research! It was nice to have you as a neighbour during my time in Delft. **Matthew**, it was great that you joined the diamonds as a post-doc and that you have contributed so much to the cavity project. Also, I always enjoyed discussing politics with you during lunch. All the best of luck for your future career. **Marie-Christine**, it was really nice to get to know you during your internship here in Delft and it was good to hear that you would come back as a post-doc. I am sure you have made a good choice to continue your career here in Ronald's group. All the best of luck for the future! **Takashi**, it must be hard to start basically from scratch and set up the complete CVD system to grow diamonds here in Delft. Nevertheless, very soon after you arrived you were already growing them with the first NV in a Delft grown diamond measured by Aletta. Great to see! **Norbert**, you have done an impressive amount of work in the diamond team. Thank you also for your guidance at the start of my PhD and the fun talks we had. While we were office mates it sometimes seemed like you could just not stop programming or writing. Therefore, I think you have found the right place to continue your career. Good luck in the future! **Peter Humphreys**, you are a great guy and we had a lot of fun learning to fly kites at the beach in Scheveningen. Even though it started with a long period in which our bodies uncontrollably followed any manoeuvres the kite made. Besides that, you were very helpful to me during the start of my PhD. Thank you for that and all

the best of luck with your new career. **Stefan**, it was nice to work with you. You are a real nice guy and take a lot of initiative for social activities. I also enjoyed the extensive lab tour at Harvard and your joy and eagerness to work in the field of quantum. I think you have found a really nice place to work now! **Julia**, we only had a very small time of overlap in the group. But also beyond this time I have enjoyed your great efforts to reach the general public with work in quantum, thanks. I am sure you will do great as a group leader in Leiden! **Bas**, although you were already gone when I joined the Diamonds. You have returned to Delft and I have always enjoyed your exciting talks here, thanks!

Nicolas D, we briefly shared office and it was nice to get to know you! I am sure you have chosen the right group to do a PhD in. **Nicholas Z**, cool that you started working on P1 centers during your masters. I wish you all of the best in your future career. **Asier**, good luck with your Master's project. **Ben**, nice to get to know you and great to see that in such a short time you got so involved with the pairs project! **Martin**, thanks for the help on several issues regarding setups. It was fun to talk with you about the many projects that you are involved with at TNO. **Matteo Junior**, it was great fun to hang around with you on several occasions. I think the research direction that you are pursuing in your PhD is very exciting. I am sure your exploration of tin's will learn the community a lot more about these exciting new defects. **Kian**, it was nice to share an office with you at the end of my PhD. I also really enjoyed the thuisje, which was great fun. I wish you all the best in the future and have no doubt that you will entangle Delft and The Hague in the gains team with Arian. **Hans Beukers**, I am very curious to see what will come out of tin-vacancy research together with Matteo. It was good to hear that after going back to medical research for a short time you still decided to do a PhD here in Delft. Also, great that Groningen alumni continue to be represented here as PhD students in Delft as well. **Yanik**, nice to get to know you and hear about your progress on the new cavity setup. More and more progress towards higher entanglement rates keeps building up and I hope you will also make steps in this direction! Good luck with your PhD. **Nina**, it was fun to meet you! I hope you have a great time here in Delft while working in two exciting groups. **Lorenzo**, it was a pleasure to meet you during the time you got stuck ;) in Delft. I wish you all the best in Ronald's and Dirk's group and success in the future. **Floris**, nice that you organized the pancake eating fest. It was fun with you in the group. Good luck with your future career. **Lisa**, **Kamiel**, **Laurens**, **Annick**, all the best of luck with finishing your Master projects. **Laura**, **Marianne**, **Airat**, **Mark**, **Chris**, **Guus**, **Thomas**, **Romy**, **Anais**, **Madelaine**, **Wouter**, **Jesse**, **Lisanne** thank you for the fun you brought to the diamond teams!

Also thanks to many more people for creating such a nice environment to work in. **Christian**, **Marta**, **Sjaak** and **Victoria**, thanks for all the laughs we had when visiting Texel twice. I had a lot of fun organizing the Uitje with you guys! Thanks to many group leaders at QuTech and QN from who I have learned in the past years and seen great talks: **Lieven**, **Leo**, **Stephanie**, **Menno**, **Giordano**, **Toeno**, **Barbara**, **David**, **Wolfgang**, **Johannes** and **Srijit**. I would like to thank **Caspar** for support during my master's and his support for new opportunities, also thanks to

Tamalika, **Jeff** and all others from the university of Groningen that have helped me during my bachelor's and master's. Thanks to the **Raymonds** and **Martijn** for teaching me more about electronics and **Jason**, **Olaf**, **Remco**, **Siebe**, **Roy**, **Mark**, **Jelle** for technical support and help with cryogenics. Thanks for the great administrative assistance **Chantal**, **Jenny**, **Marja** and **Helena**. Also thanks to many other people: **Jelmer**, **Adriaan**, **Stephan**, **Anna**, **Mariya**, **Joris**, **Guus**, **Josh**, **Nick**, **Nodar**, **Ruud**, **Remon**, **Jake**, **David**, **Nico**, **Damaz**, **Will**, **Nandini**, **Brian**, **Floor**, **Lukas**, **Kostas**, **Willemijn**, **Yang**, **Anne-Marije**, **Guoji**, **Jaap**, **Yves**, **Mario** and **Evert**. I would also like to thank the soccer team I have played in. Monday was always the best day of the week because it was great fun to play with you Kavli Warriors: **Captain Christian**, **Captain Gustavo**, **Captain Anta**, **Tim**, **Nikos**, **Mohsen**, **Michael**, **Alberto**, **Hany**, **Jorge**, **Thijs**, **Sebastian**, **Kaushik**, **Luca**, **Stefano**, **Fokko**, **Ruben**, **Adriaan**, **Jasper** and **Francesco**. The 1-hour tactics discussion at the end of every game have definitely resulted in more total soccer. To quote JC: if you always play in possession, you don't have to defend, there is only one ball. But most importantly, our team spirit has been good and helped us to go from last comer to a mid-league team. It has been a blast with all of you guys!

Additionally there are many more people that I would like to thank. Thanks to the friends that have supported me over the years: **Gelling**, **Leenstra**, **Sylvan**, **Steven**, **Jos**, **Seb**, **Melchior**, **Jerry**, **Dekens**, **Maarleveld**, **Bas**, **Lemaire**, **Wout**, **Pim**, **Brusse**, **Piter**, **Joris**, **Van Laar Sr.**, **Van Laar Jr.**, **Logist**, **R. de Vries**, **Keuning**, **Rutger**, **Niels**, **Quintin**, **Marijn** and **Daniël**. Thanks to my in laws **Ron** and **Hennie**, for their kindness and hospitality.

To my brothers and sister and their plus-ones **Sjouk**, **Roos**, **Nick** and the little **(OL)Senn**, thank you for all your love and support. **Henk**, **Peter** and **Anke** you are so much fun to be around and the best siblings I could ever wish for. Dear **dad**, thank you for showing me your perseverance ever since I was a little kid and for being just as stubborn as I am, which often makes me laugh. I am proud of you and of what you do for us. Dear **mom**, you are one bomb of joy. Thank you for your strong determination and your utter positivity. I am so grateful for all what you have done, and what you continue to do for family while achieving so many other things. You are great! Dear **Marieke**, you make me happy and proud every day and your support really means a lot to me. I am looking forward to our future with lots of new adventures. Lots of love.

List of Publications

This thesis:

7. *Entanglement of dark electron-nuclear spin defects in diamond.*
M. J. Degen[*], S. J. H. Loenen[*], H. P. Bartling, C. E. Bradley, A.L. Meinsma, M. Markham, D. J. Twitchen, T. H. Taminiau, arXiv:2011.09874 (2020).

6. *Atomic-scale imaging of a 27-nuclear-spin cluster using a quantum sensor.*
M. H. Abobeih, J. Randall, C. E. Bradley, H. P. Bartling, M. A. Bakker, **M. J. Degen**, M. Markham, D. J. Twitchen, T. H. Taminiau, Nature **576**,7787 (2019).

5. *A ten-qubit solid-state spin register with quantum memory up to one minute.*
C. E. Bradley[*], J. Randall[*], M. H. Abobeih, R. C. Berrevoets, **M. J. Degen**, M. A. Bakker, M. Markham, D. J. Twitchen, T. H. Taminiau, Physical Review X **9**, 031045 (2019). Highlighted in Nature and Physical Review X.

4. *Optical coherence of diamond NV centers formed by ion implantation and annealing.*
S. B. van Dam[*], M. Walsh[*], **M. J. Degen**, E. Bersin, S. Mouradian, A. Galiullin, M. Ruf, M. IJspeert, T. H. Taminiau, R. Hanson, and D. R. Englund, Phys. Rev. B, **99**, 161203 (2019).

Other:

3. *Coherence and entanglement of inherently long-lived spin pairs in diamond.*
H. P. Bartling, M. H. Abobeih, B. Pingault, **M. J. Degen**, S. J. H. Loenen, C. E. Bradley, J. Randall, M. Markham, D. J. Twitchen, T. H. Taminiau, arXiv:2103.07961 (2021)

2. *Pronounced Environmental Effects on Injection Currents in EGaIn Tunneling Junctions Comprising Self-Assembled Monolayers.*
M. Carlotti, **M.J. Degen**, Y. Zhang, R. C. Chiechi, J. Phys. Chem. C, **120**, 36, 20437–20445 (2016).

1. *Perovskite solar cells prepared by flash evaporation.*
G. Longo , L. Gil-Escrig, **M. J. Degen** , M. Sessolo, H. J. Bolink, Chem. Commun., **51**, 7376 (2015)

[*]Equally contributing authors

Curriculum Vitæ

Maarten Johannes DEGEN

25-04-1991	Born in Zutphen, The Netherlands.
2003–2009	Secondary School Isendoorn College, *The Netherlands*
2010–2014	BSc in Physics
2013–2014	BA in Philosophy of the natural sciences *University of Groningen, The Netherlands* 04/2014 - 07/2014: Internship at *ICMol, Spain*
2014–2016	MSc in Nanoscience *University of Groningen, The Netherlands* 02/2016 - 08/2016: Visiting student at *MIT, USA* Thesis: Engineering, control and effects of field amplitude distributions in solid-state devices with nanoscale optical emitters Supervisors: Prof. Caspar van der Wal, Prof. Dirk Englund
2016 – 2021	Doctorate in Physics *Delft University of Technology, The Netherlands* QuTech and Kavli Institute of Nanoscience
Thesis:	On the creation, coherence and entanglement of multi-defect quantum registers in diamond
Group:	Taminiau Lab, QuTech and Kavli Institute of Nanoscience
Promotor:	Prof. dr. ir. R. Hanson
Co-promotor:	Dr. ir. T. H. Taminiau